A Numerical Investigation into the Hemodynamics, Oxygen Transport, and Flow Stability of Cerebral Aneurysms

by

Michael J. Durka

MS in Mechanical Engineering, University of Pittsburgh, 2013

Submitted to the Graduate Faculty of

the Swanson School of Engineering in partial fulfillment

of the requirements for the degree of

Doctor of Philosophy

University of Pittsburgh

2020

UNIVERSITY OF PITTSBURGH

SWANSON SCHOOL OF ENGINEERING

This dissertation was presented

by

Michael J. Durka

It was defended on

February 26, 2020

and approved by

Anne M. Robertson, Ph.D.,Professor, Department of Mechanical Engineering and Materials Science

Juan R. Cebral, Ph.D., Professor, Department of Bioengineering, George Mason University

Hessam Babaee, Ph.D., Assistant Professor, Department of Mechanical Engineering and Materials Science

Giovanni P. Galdi, PhD., Professor, Department of Mechanical Engineering and Materials Science

Dissertation Director: Anne M. Robertson, Ph.D.,Professor, Department of Mechanical Engineering and Materials Science

A Numerical Investigation into the Hemodynamics, Oxygen Transport, and Flow Stability of Cerebral Aneurysms

Michael J. Durka, PhD

University of Pittsburgh, 2020

A cerebral or intra-cranial aneurysm (IA) is a pathological saccular bulge occurring in the cerebral arteries of the brain. These structures have a propensity to rupture due to their structurally deficient arising from their pathological nature. A ruptured IA can have disastrous or fatal consequence for a patient. Surgical intervention furthermore carries its own innate risks. Therefore, an understanding of IA initiation, growth and rupture remains imperative in the treatment of the disease. However, these processes remain poorly understood.

Hemodynamics, the mechanical forces imparted on the vessel wall from the flowing blood contained within, is thought to be a substantial contributing factor in the progression of the disease. The study of aneurysmal hemodynamics and their impact on the aneurysm wall remains challenging due to the inaccessibility from their location deep within the brain that clinicians are faced with. Therefore, computational fluid dynamics (CFD) studies are frequently utilized in the study of aneurysmal heodynamics.

The work herein focuses on advancing the study of aneurysmal hemodynamics in four major areas. The first is an extensive categorization of the blood flow waveforms found within the cerebral circulation from a uniquely large data-set of 272 cardiovascular patent waveforms that quantifies the impact on the hemodynamics from the variation in this large data-set. The second section focuses on quantifying the multi-parameter relationship between aneurysmal geometry and intra-saccular flow-structure via parametric study. The third section explores the impact of the pathological morphology of aneurysms on the blood's ability to transport oxygen to the wall tissue within the aneurysm. Finally, this work identifies geometric features additional to those previously known which initiate pathological high-frequency fluctuations in the blood flow and examines possible solution strategies in answering the open question as to what impact do these flow features have on the development of IAs.

Table of Contents

List of Tables

List of Figures

Preface

The work herein is a compilation of much of my efforts towards the computational modeling of cerebral aneurysms through my duration at the University of Pittsburgh as a PhD student under the advisement of Professor Anne Robertson. It was my intent, to produce this work with the aim of providing a further understanding of the fundamental physics governing the behavior of cerebral aneurysms which is, to this day, inadequately understood. It is my philosophy that, to have sufficient command over a problem, one must first dissect the principles which govern the physics of said problem, understand what parameters control its action, and only then, can one develop a strategy to decisively conquer the problem. As my work falls woefully short of the end goal, I have, as I believe, read what others have done, and taken an incremental step forward, as the problem of cerebral aneurysms is far too interdisciplinary and complex for any one person to be able to solve. It is my hope, therefore, that the work herein, like that of those before me which I have studied, will likewise serve as a starting place for others to read what I have done, and do with it what I could not, in the hope that, one day, though probably long from now, cerebral aneurysms will no longer be a burden to anyone. In the meanwhile, this work offers a small piece of the enormous task ahead of researchers who will work towards achieving a sufficient understanding of the underlying principles of cerebral aneurysm.

I could not have accomplished this work entirely on my own, and credit will be given to where it is owed. I first thank my advisor Dr. Anne Robertson, for her mentorship, guidance, insights, and in general, her ability to forge ones potential into ones useful ability. I must also thank my committee members, Dr. Hessam Babaee, Dr. Juan Cebral, and Dr. Giovanni Galdi for their time, insights, guidance, and input to this work. I must also thank (now Dr.) Zijing Zeng who in effect served as my first mentor within the lab when I was an undergraduate, who imparted onto me the many basic practical skills needed for me to get started with computational analysis.

I must give particular acknowledgment to individuals of two lab groups: the labs of Dr. Juan R. Cebral of George Mason University and Dr. Hessam Babaee of the University of Pittsburgh. Dr. Cebral, in addition to serving as a member of my dissertation, kindly provided the resources of FeFlow, a finite elements solver, with additional post-processing tools developed by his lab for use in work presented in the third and fourth chapters of this work. Two of his post-doc students, Dr. Bongjae Chung and Dr. Fernando Mut, additionally, provided me with excellent mentorship and support in using these analysis tools, in addition with Dr. Cebral. For all of their efforts, I am most grateful. In a similar manner, I must thank Dr. Hessam Babaee for providing me with Nektar, a h-p spectral elements solver, as well as pre-processing tools developed within his lab. His students Amirreza Hashemi and Prerna Patil were most helpful (and patient) with helping me build and use the codes. For their efforts, likewise, I am most grateful.

There are also those who have assisted me and provided insight over the years who must also be acknowledged, in chronological order: Wenran Chen, Dr. Bongjae Chung, Dr. Fernando Mut, Isaac Wong, Logan Tuite, Garrett Rettig, Qi "Alexa" Yang, Xingjian "Frank" Zhou, Sarah Knop, Amirreza Hashemi, and Prerna Patil. Also, I must thank my lab-mates (past and present) for their general insight and support: Michael Hill, Piwatt, Xinjie Duan, Piyusha Gade, Fangzhou Cheng, Chao Sang, and Yasutaka Tobe. From a financial aspect, I must thank the National Institute of Health, as well as the Swanson School of Engineering at the University of Pittsburgh for their financial support.

Michael J. Durka, February 13, 2020, Pittsburgh, USA

1.0 Introduction

An intra-cranial aneurysm (IA) is a pathological condition of the cerebral arteries defined by a localized bulging and weakening of the wall [16]. IAs have been estimated to occur within 2.0-8.5% of the general population [118, 161]. From initiation, the disease progresses are largely due to the degeneration of aneurysmal wall tissue resulting in enlargement of the wall - typically into a saccular or berry-like shape. IAs can either stabilize, or in the direst cases, the ultimate strength of the wall becomes insufficient to bear the loading in the wall, resulting in aneurysm rupture. This outcome is fatal 50 % of the time; if not fatal, the patient is left with a 60 % likelihood of permanent physical and mental impairment [17, 102]. Given the risk IAs pose, preventative surgical treatment may be viewed as a favorable if not imperative course of action. However; surgical intervention poses its own risks of morbidity (10 %) and mortality (2.6 %) [158]. Clinicians must therefore carefully evaluate the benefits/risk potential of preventative treatment. While IAs pose a potentially mortal threat to patients, the IA rupture rate is approximately 1/180 over the lifetime of an aneurysm-harboring individual [89]; the vast majority of individuals harboring IAs are unaffected by them, and will die from unrelated causes. Given the relatively low rupture rate, surgical intervention can pose a non-negligible risk to the patient as compared to the aneurysm itself. It is therefore imperative that the rupture risk be accurately determined. However, the mechanisms responsible for aneurysm pathology are poorly understood. In addition, non-invasive measurements of aneurysm wall structure/content in practice are currently unobtainable. It is therefore difficult, if not impossible, to directly determine what risk a given IA poses. As a result, clinicians are left to rely on information such as patients' medical history and aneurysm size – a metric non-evasively obtainable, for example, via angiography. However, size is not a universal indicator of rupture propensity; in a 20 year retrospective study on IA rupture status, 31.% of aneurysms less than 3mm in size ruptured, while 28.1% of aneurysms greater than 25mm in size did not rupture (n = 945) [204]. In this study, size was a particularly deficient predictor of the rupture status of small aneurysm ($\leq$ 3mm), in that only 68.7 % of the aneurysms in this group did not rupture. In response to

these findings, a substantial volume of work has been directed towards better understanding the mechanisms behind IA genesis, growth, and rupture to facilitate improved patient outcome.

Aberrant hemodynamics is generally accepted to be a mechanism responsible for the initiation and progression of IAs [72, 125, 176]. "Aberrant hemodynamics" here is defined generally as blood flows that produce wall shear stress fields on the lumen wall which deviate from those found on the lumen surfaces of (predominantly) straight arterial segments. In these segments, the wall shear stress vector acts dominantly in the downstream axial direction throughout the cardiac cycle provided a negligible change in diameter or curvature is encountered along the segment. Additionally, the gradient of the wall shear stress vector likewise varies negligibly. This is in contrast to the behavior of the wall shear stress vector in highly curved arterial segments, bifurcations, or at stenosed locations. For these geometries, the wall shear stress vector typically possesses a high degree of variation both spatially and temporally. Furthermore, the magnitude of the wall shear stress vector at these locations typically falls out of the bounds of healthy values. It has therefore been widely conjectured that aberrant hemodynamics is causal mechanism in aneurysm formation since most IAs occur at arterial bifurcations and highly curved segments [65, 129, 16]. The frequency of occurrence of IAs by locations is well depicted in Figure 1 of the work by Brisman et al. [16]. Here, the propensity of IAs formation at or near arterial bifurcations is evident.

The complexities of the IA geometry and parent vasculature combine to generate shear stress fields that are both qualitatively and quantitatively fundamentally different than those found in the simple cylindrical geometry of many healthy arteries. For example, a strong inflow jet may be present within the sac, impacting the wall and therefore producing a local region of elevated wall shear stress having a divergent directional pattern. The inflow jet typically drives a primary vortex – a region of circulating flow typically confined to the sac itself. In the same aneurysm, there may also be a slow-moving, driven vortex structure which shifts direction during the cardiac cycle. These features of intra-aneurysmal flow were well defined and categorized by Cebral et al. [23] who first associated these pathological flow structures with rupture status. Relative to the simple flows seen in straight arterial segments, flow in aneurysms can display both abnormally high or low wall stress (WSS, i.e.,

the magnitude of the wall shear stress vector), high oscillatory shear index (OSI), and high wall shear stress gradients (WSSG). These profound differences in wall hemodynamics in aneurysm versus straight arteries have given rise to the notion that wall hemodynamics such as WSS are driving factors in aneurysmal poathology.

The influence of WSS on the lumen wall in arteries has been extensively studied. The endothelium, acts as both a selective, protective membrane as well as mechano-transduction sensor. With respect to this latter role, studies have found that the presence of an endothelium is necessary for the vessel to maintain homeostatic values of wall shear stress following changes in flow rate. Over the short term, this response manifests through relaxation or contraction of the circumferentially aligned smooth muscle cells [47]. In animal models of rabbits and dogs [119, 103], it has been demonstrated that if the increased or decreased flow rate is maintained over a time period on the order of a week, a more permanent change ensues- the artery wall remodels the collagen fibers to maintain an increased or decreased vessel diameter, respectfully. However, if the changes to wall shear stress are too extreme, or the wall shear stress field is too spatially heterogeneous, then the vessel will not be able to achieve homeostasis, and pathological changes will be incurred.

Healthy values of WSS have been reported to be between 10 and 70 dyn/cm^2 by Malek et al. [124]. Malek et. al found that endothelial cells exposed to low WSS (< 4 dyn/cm^2) lose their alignment with the flow direction, and undergo an increased rate of proliferation and apoptosis. Thus, the endothelial permeability becomes increased; allowing for the infiltration of macromolecules such as low-density lipo-proteins (LDL), and thereby exposing the wall to the development of atherosclerosis. Within the setting of cerebral aneurysms, Ujiie et al. [192] noted that in this same low WSS regime, which can occur in regions of secondary vortices, can expose the wall to the aggregation of red blood cells and the adhesion of platelets and leukocytes to the lumen surface due to the dysfunction of shear stress-induced nitric oxide. High WSS however (above 100 dyn/cm^2), when focal, can also be detrimental to the wall. High WSS has been shown to facilitate the fragmentation and degeneration of the internal elastic lamina [183], as well as mechanical damage to the endothelium [182]. Both phenomena are thought to be found in early stages of aneurysmal initiation. Elevated WSS within aneurysms, once formed, has been observed in the existance of high speed inflow

jets, and are thought to drive aneurysmal enlargement [174]. Further supporting the theory of high WSS-mediated destructive remodeling is the association of cigarette smoking with IA formation. Cigarette smoking has been known to increase blood flow velocity within the brain while initiating vasoconstriction [36]. Such conditions would result in elevated WSS. Chalouhi et al [36]. noted that up to 80% of patients who sustain an aneurysmal subarachnoid hemorrhage have a smoking history, and 50-60% of IA patients are current smokers.

Because of the biomechanical significance of WSS on the endothelium, a large body of computational fluid dynamics (CFD) studies has been conducted with the aim of exploring the association between WSS and aneurysm growth/rupture [23, 177, 75, 31, 129, 21, 19]. CFD studies are the primary means of conducting hemodynamic studies of flow within cerebral aneurysms (particularly in the analysis of WSS) because the spatial temporal resolution of CFD studies is sufficient to resolve high spatial (and in some cases temporal) gradients in the velocity field necessary for accurate WSS calculations (for example, see Baek et al. [7], or Valen-Sendstad et al. [195] regarding CFD grid resolution). Even current in-vivo imaging techniques such as 4D MRI cannot provide sufficient resolution. For example, Zhao et al. [220] measured in vivo time-averaged flow rate using 1.5 T and 3T QMRA in cerebral vessels. The time averaged WSS could only be estimated using the Hagen-Poiseuille equation; which is valid for a straight pipe of cylindrical cross section under steady flow conditions, but insufficient to describe the wall shear stress vector in a driven cavity such as an aneurysm. Therefore, while this study excelled at measuring time-averaged volumetric flow rate in arteries, such methods are not suitable for providing wall shear stress distribution in aneurysms. Even 7 Tesla MRI only has a reported voxel resolution and interpolation of 0.90mm and 0.45mm respectfully. This length scale is still one order of magnitude higher than the aforementioned CFD studies of Baek et al.[7] and Valen-Sendstad et al.[195].

In addition to studying the magnitude of the wall shear stress vector, many numerical studies have been performed to understand the time-oscillatory component of the stress vector. He and Ku [77] proposed the oscillatory shear index (OSI) to describe the extent to which the wall shear stress vector deviates throughout the cardiac cycle from its average direction (which, in a straight artery, would be the axial direction), showing in this

study the value of this parameter for arterial disease as demonstrated by its correlation with atherosclerotic-prone regions of the wall. Elevated OSI has furthermore been associated with surgically-identified IA rupture location [149]. The time-average of the wall shear stress magnitude at these points, additionally, was significantly higher ($p = 0.031$). Similarly, Shimogonya et al. [176] proposed the definition of gradient oscillatory number (GON) to quantify the degree of oscillating tension/compressive forces on the endothelium caused by temporally changing wall shear stress gradient (WSSG). They demonstrated, in a patient-specific study of aneurysm initiation, that when the aneurysm was removed, the wall at that location where the aneurysm had been possessed a high GON in conjunction with high WSS magnitude relative to the parent-artery averaged WSS magnitude. Furthermore, positive WSSG, in conjunction with elevated WSS, has been linked with destructive remodeling in an in vivo study of surgically created canine arterial bifurcations [129]. These changes included fragmentation of the internal elastic lamina and were suggestive of aneurysm initiation.

More recently, hemodynamics within IAs have been associated with focal changes within IA walls [21]. In this study, Cebral et al. found an association between elevated WSS, elevated vorticity and increased levels of inflammatory cells within the sac. Increased inflammation was also associated with lost of integrity of the endothelium. Damage to the endothelium was found to be a common characteristic of ruptured aneurysms IAs in a study by Kataoka et al. [106]. This study identified macrophage infiltration in the walls of de-endotheliazed ruptured aneurysms. It is conjectured that without the protective barrier of the endothelium, that macrophage infiltration facilitated the loss of smooth muscle cells as well as the extra-cellular matrix proteins. Most recently, Cebral et al. [25] showed that local hemodynamic features are associated with local characteristics of the aneurysm wall that are visible in surgical videos. More specifically, slow, swirling flows within the sac were associated with sac wall features comparable to hyperplastic and atherosclerotic characteristics, while high flow conditions characterized by inflow jet impingement were associated with a local thinning of the wall. The study also associated many of the aforementioned hemodynamic metrics (and others) with wall rupture status. In a similar type of study, Kimura et al. [110] found an association between IA wall appearance (hypoplastic red regions versus thick white/yellow hyperplastic/atherosclerotic walls) and their novel parameter: wall shear

stress vector cycle variation. This parameter is a measure of the effect of the directional changes in the WSS and furthermore suggests the negative impact highly-temporal WSS imparts on the wall.

Despite the progress made in understanding the links between hemodynamic flows and IA rupture, the causes and mechanisms leading to formation, growth, and rupture currently remain poorly understood, as thus far, most results provide associations rather than specific mechanisms for wall changes. The coupling between hemodynamics and human aneurysm pathophysiology is indeed complex as well as difficult to study in vivo. Complex flow patterns within the IA sac form and change over time as the sac grows and remodels; these patterns in turn impact the wall via complicated processes involving cascades of biochemical reactions that are not yet well studied. Adding to these difficulties, the location of IAs is a major impediment to progress. Buried deep within the brain, IAs remain inaccessible for study by non-invasive means, and are almost exclusively physically accessible only during surgical treatment for IA repair. Non-invasive imaging leaves the community with incomplete information, lacking data on the wall structure and content as well as the biochemical processes occurring within the walls of the aneurysm. IAs are furthermore largely asymptomatic and many are detected incidentally; therefore, it is difficult to obtain data during the initiation phases of the aneurysm, as the patient is typically unaware that such a situation is occurring. The physical inaccessibility of IAs for study in conjunction with the challenges in awareness of their initiation gives rise to a lack of temporal data for a highly transient, multi-factorial analysis.

The body of this work is a compilation of multi-faceted studies on aneurysmal hemodynamics utilizing computational fluid dynamics. The first chapter describes a study identifying the variability in blood-flow waveforms within the aged population and provides guidance for addressing the challenge of approximating a patient waveform in the absence of patient specific data. These waveforms are essential for prescribing the pertinent time-dependent boundary-value data required for well-posed computational models of blood flow. The second chapter then uses the information obtained in the first chapter to investigate the impact of the broad set of waveform characteristics on intra-aneurysmal hemodynamics. This information is particularly useful for knowing what information can and cannot be obtained

when patient specific information is lacking. It furthermore provides insight into how the waveform alone can influence hemodynamic parameters and flow metrics which have been associated with aneurysm progression and rupture. The third chapter focuses on understanding intra-aneurysmal hemodynamics in a fundamental physical manner. Relationships between geometry and flow structures, as well as several hemodynamic metrics relevant to rupture status were obtained parametrically. These results are especially useful for assuring that animal models achieve flow fields that are relevant to the actual clinical problem. The information is likewise useful in determining how changes in sac geometry can alter hemodynamics – an understanding which is relevant for studies of wall remodeling, and is of particular importance given the typical dearth of data on changing aneurysm geometry over time. This chapter also addresses the question of why earlier attempts to correlate rupture status to one geometric parameter have not been successful. In particular, the results of this study highlight the multi-factorial dependence of flow on geometry. The fourth chapter is one of the few works of its kind that explores how the pathological flow structures inside aneurysms influence the lumenal transport of oxygen to the wall. Most, if not all metabolic processes within the wall require oxygen, Deficient oxygen supply is likely an important contribution to the pathological progression of the aneurysm wall. Finally, the fifth chapter addresses the topic of high-frequency flow oscillations which have been shown to be present in some (but not all) aneurysms. This chapter specifically focuses on identifying geometric characteristics of the internal carotid artery (ICA) which are capable of generating high frequency flow oscillations. The evolution of these structures as they flow downstream into the aneurysm is then considered, with the long range objective of understanding how these flow structures impact the wall biology. The chapter ends with a description of work demonstrating that these flow oscillations are most probably the result of a Hopf bifurcation to the solution of the governing equations. The final chapter summarizes the work described in the prior chapters and offers conclusions and recommendations for future work.

2.0 A Data-driven Approach for Addressing the Lack of Flow Waveform Data in Studies of Cerebral Arterial Flow in Older Adults

The work in this chapter was largely reproduced from the following manuscript: Michael J Durka, Isaac H Wong, David F Kallmes, Dario Pasalic, Fernando Mut,Manoj Jagani, Pablo J Blanco, Juan R Cebral, and Anne M Robertson. A data-driven approach for addressing the lack of flow waveform data in studies of cerebralarterial flow in older adults.Physiological measurement, 39(1):015006, 2018, which is a journal publication of the author's work. Gratitude is expressed to Issac Hong, who assisted the author in the pre-processing of the waveform data in this work.

SUMMARY - Blood flow waveforms - essential data for hemodynamic modeling - are often in practice unavailable to researchers. The objectives of this work were to assess the variability among the waveforms for a clinically relevant older population, and develop data-based methods for addressing the missing waveform data for hemodynamic studies. This work therefore analyzed 272 flow waveforms from the internal carotid arteries of older patients (73 ± 13 years) with moderate cardiovascular disease, and used these data to develop methods to guide new approaches for hemodynamic studies. Profound variations in waveform parameters were found within the aged population that were not seen in published data for young subjects. Common features in the aged population relative to the young included a larger systole - to - diastole flow rate ratio, increased flow during late systole, and absence of a dicrotic notch. Eight waveforms were identified that collectively represent the range of waveforms in the older population. A relationship between waveform shape and flow rate was obtained that, in conjunction with equations relating flow rate to diameter, can be used to provide individualized waveforms for patient specific geometries. The dependence of flow rate on diameter was statistically different between male and female patients. It was shown that a single archetypal waveform cannot well-represent the diverse waveforms found within an aged population, although this approach is frequently used in studies of flow in the cerebral vasculature. Motivated by these results, we provided a set of eight waveforms that can be used to assess the hemodynamic uncertainty associated with the lack of patient specific

waveform data. This work further provides a methodology for generating individualized waveforms when patient gender, age, and cardiovascular disease state are known. These data driven approaches can be used to devise more relevant in-vitro or in-silico intra-cranial hemodynamic studies for older patients.

2.1 Introduction

Various hemodynamic aspects of blood flow such as wall shear stress (WSS) and oscillatory shear index (OSI) have been implicated as important driving factors for the development of intracranial vascular diseases [37, 219, 125, 115, 126] and are therefore an active topic of study, both experimentally and computationally [97, 3, 208, 173]. Computational fluid dynamic (CFD) studies of hemodynamic phenomena, for example, are capable of providing non-invasive estimates of pressure and velocity information as well as flow-related parameters (e.g. WSS, OSI) at each of (potentially) millions of mesh nodes (analogous to non-obstructive sensors) within patient specific vascular domains. This capability is extremely important in the cerebral circulation where it is not yet possible to safely and accurately measure blood velocity and pressure in vivo using technologies such as MRA [220] with sufficient resolution to obtain hemodynamic parameters such as WSS and OSI.

Any computational model or experimental simulation of blood flow in finite regions of the vasculature requires specification of the shape of the vascular anatomy as well as the prescription of boundary conditions in terms of inlet/outlet flow/pressure data. When geometric data of the vessel lumen is obtained, the corresponding blood waveform data in the vessel is seldom measured in practice, and as a result, the inflow and outflow data for studies of intracranial blood flow are nearly always estimated from measurements obtained from population studies or representative subjects [23, 199, 127, 104, 177, 94, 208, 194, 209]. In doing so, it is inherently assumed that differences between such a one-fits-all representative waveform and patient specific waveforms (unknown) are small enough to be neglected. However, because of the large inter- individual variability of flow regimes relevant to different cardiovascular diseases and variability with age as well as disease, this hypothesis should be

confirmed for specific applications. There is therefore a critical need to carefully assess the variability among flow waveforms from a relevant patient population more likely to harbor cerebral aneurysms. In estimating the impact of inter-individual flow rate variability, it is critical to understand the range of flow waveforms within the population of interest. For example, while the waveform shape may be relatively similar across healthy, young adults [56, 85], a much larger variation would be expected in elder based populations, due to, for example, the decrease in arterial compliance with age [146, 81, 150]. A study by Hoi et al., [84] found substantial differences in the common carotid artery bifurcation waveforms among young and old patients. Furthermore, with increasing age, cardiovascular diseases are more common and have been found to substantially alter the cerebral vascular waveform [147]. These age associated variations in flow waveforms will be particularly important for hemodynamic studies of vascular pathologies, such as cerebral aneurysms [161, 34, 49] that are more common in older populations.

In this work, we identified and quantified the variability in both waveform shape and flow rate found in the left and right internal carotid arteries of an aged population with mild to moderate cardiovascular disease. Based on this analysis, we then produced results that can be utilized in one of two ways to incorporate the impact of waveform variability on hemodynamics in future hemodynamic studies with inflow from the ICA. We first provide eight waveforms from our ensemble which were found to be capable of capturing the range of waveform parameters found to strongly influence flow rate; such waveforms are well suited for use in parametric uncertainty studies. We then provide data which can be used to create an individualized waveform for a patient incorporating age, gender, and known disease factors.

2.2 Methodology

2.2.1 Waveform Generation

2.2.1.1 Doppler Data Acquisition Patients who underwent duplex, bilateral Doppler ultrasound of the carotid arteries at the Mayo Clinic from 1/1/2012 to 12/31/2012 were enrolled in the study. Of the 867 enrolled patients, those with greater than mild stenosis of the carotid artery, stent or patch placement, or lack of information regarding risk factors of interest were excluded from the study, leaving 352 patients for analysis.

Clinical data was collected for each patient including gender, age, hypertension status, and existence of the following cardiovascular diseases: aortic stenosis, aortic regurgitation, congestive heart failure, coronary artery disease, atrial fibrillation, diastolic dysfunction, systolic dysfunction, and paroxysmal atrial fibrillation (AFIB). Lifestyle and health information including cigarette smoking and BMI (averaged over three years prior to Doppler acquisition) were also obtained. Positive classification of hypertension was defined by a systolic blood pressure greater than 140 mmHg, or a diastolic blood pressure greater than 90 mmHg. Doppler ultrasounds were performed by dedicated sonographers. The Doppler ultrasound data in conjunction with the ICA diameters, determined to a precision of 1 mm, were obtained at a location approximately 3 cm distal to the origin of the ICA. Greyscale ultrasound images of the internal carotid arteries with velocity waveforms spanning three to eight cardiac cycles were saved by the sonographer for analysis.

2.2.1.2 Extraction of Velocity Waveform from Doppler Data The peak velocity over the cross section as a function of time, $V_p(t)$, was obtained from the waveform ultrasound images using custom scripts written in the MATLAB Release 2012a environment (The MathWorks, Inc., Natick, Massachusetts, United States.). The scripts were designed to automate the process of the detection of the waveform envelope so as to minimize user interaction and lessen human bias. The characteristic metrics for each period were visually checked in an automatically generated figure, e.g. Figure 2.1. Some of the images were either of too poor resolution to be analyzed or not possible to be analyzed using the automated software and

were thus excluded from the study. The metrics of the individual periods comprising the ensemble waveforms (consisting of three to eight periods per waveform) were simply averaged to produce period-averaged waveform metrics. Period-averaged waveforms which were produced for latter use in the study were produced by aligning the normalized waveforms by their maximum velocity to avoid artificial rounding or flattening of the systolic peaks which was otherwise unavoidable in many cases.

2.2.2 Definition of Characteristic Waveform Metrics

The waveform shape was characterized by eight metrics that were used for the young, healthy population in [85] as well as additional metrics $V_{3/4\,max}$,V_{DP}, $V_{Avg\,BDN}$, $V_{Avg\,ADN}$, $t_{V\,3/4\,max}$, t_{VDP}. Pulsatility index (PI) was additionally provided. The additional metrics were introduced primarily to distinguish features in our aged population that were not present in the young, healthy population in [85]. The definitions of each metric are listed in Table 3.2 and depicted in Figure 2.1. All velocity variables were normalized by the maximum velocity V_{max} , and all temporal variables by the cardiac period, T_{per}. The values of each characteristic metric - such as the maximum, and minimum velocities and the times at which they occurred - were automatically identified and recorded using the custom MATLAB script described above. The mean and standard deviation of each metric for each patient were then computed, as well as the population averaged means and standard deviations for the left and right ICAs. The dicrotic notch was defined as the local minimum of the waveform velocity directly following the completion of systole. More quantitatively, this is the point after the second systolic $V_{1/2\,max}$, where the second derivative in time of the velocity is maximum. The quantities $V_{Avg\,BDN}$, and $V_{Avg\,ADN}$, were then defined as the time averaged velocities for the regions before and after the dicrotic notch, respectively.

Table 2.1: Definitions of waveform characteristic metrics

Dimensional	
$V_p(t)$	Measured Doppler velocity (peak in space)
V_{max}	Maximum velocity over period
T_{per}	Duration of cardiac cycle
Non-Dimensional Velocity	
$V(t)$	Normalized velocity = $V_p(t)/V_{max}$
V_{min}	Minimum velocity over period
V_{avg}	Time-averaged velocity
$V_{1/2\,max}$	$1/2((V_{max} - V_{min}) + V_{min})$
$V_{3/4\,max}$	$3/4((V_{max} - V_{min}) + V_{min})$
V_{Amax}	Velocity at instant of maximum acceleration
V_{DN}	Minimum velocity of dicrotic notch
V_{DP}	Maximum velocity after dicrotic notch
$V_{Avg\ BDN}$	Time-average velocity before dicrotic notch
$V_{Avg\ ADN}$	Time-average velocity after dicrotic notch
V_{rec}	$V_{Avg\ ADN} - V_{Avg\ BDN}$
Acc_{max}	Maximum acceleration
PI	V^*/V_{avg}
Non-Dimensional Time	
t_{Vmax}	Time when $V_p(t) = V_{max}$
$t_{V\ 1/2\,max}$	Time when $V_p(t) = V_{1/2\,max}$
$t_{V\ 3/4\,max}$	Time when $V_p(t) = V_{3/4\,max}$
t_{VDN}	Time when $V_p(t) = V_{DN}$
t_{VDP}	Time when $V_p(t) = V_{DP}$

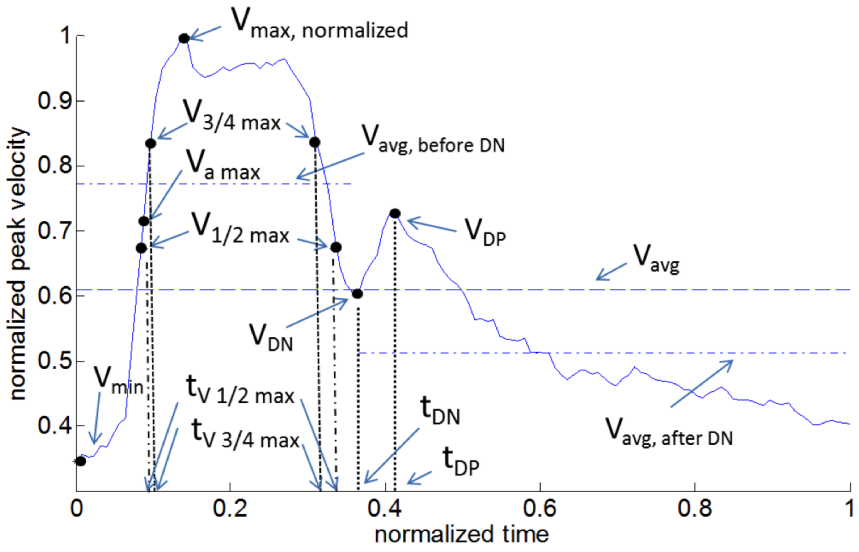

Figure 2.1: Representative waveform for the normalized velocity $V(t) = V_p(t)/V_{max}$, showing waveform metrics (see Table 3.2 for definitions).

2.2.3 Special Treatment of the Dicrotic Notch

Special care is needed when processing the velocities of the dicrotic notch. It was found that some waveforms did not contain a discernible dicrotic notch (to within the resolution of $1.\frac{cm}{s}$. These waveforms were excluded from metrics directly measuring the dicrotic notch velocities V_{DN}, V_{DP}, and V_{rec}. In patients where only one of the carotid vessels had an identifiable dicrotic notch, V_{rec} was set to zero for the side with no dicrotic notch.

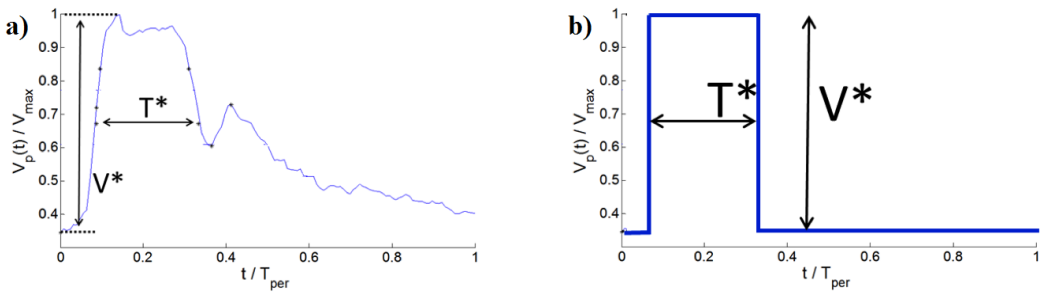

Figure 2.2: Representative normalized velocity waveform with non-dimensional metrics V^*,T^*. Shown are (a) Velocity waveform with metrics, (b) Corresponding square waveform with equivalent values of V^*,T^* used to estimate $\overline{\mathrm{Q}}$.

2.2.4 Contralateral Variability

The contralateral variability of a given waveform metric between the left and right ICAs in each patient was quantified as the contralateral difference ($\mathrm{m_{diff}} \geq 0$) defined as

$$m_{diff} = 2|(m_l - m_r)/(m_l + m_r)| \tag{2.1}$$

where abs stands for the absolute value of the quantity, m_l and m_r are the left and right side values of the metric, respectively. This metric was used to compare the magnitude of the difference in waveform metric between left and right vessels relative to their mean value.

2.2.5 Relationship between Velocity Flow Rate Waveforms

Flow rate Q(t) and time averaged flow rate $\overline{\mathrm{Q}}$ were defined as

$$\mathrm{Q(t)} = V_p(t)\,\pi \mathrm{d}^2/8, \qquad \overline{\mathrm{Q}} = \frac{1}{T_{per}} \int_0^{T_{per}} \mathrm{Q(t)}\; dt \tag{2.2}$$

where, in Eq. 3.4(left), the velocity profile has been approximated as parabolic in space, and d is the arterial diameter, which was assumed to be constant in time. As the information to directly obtain $V_p(t)$ was contained within the ensemble data, we first made use of 3.4 (left) to transform our data from a velocity quantity to a flow rate quantity. We could then make use of Eq. 3.4 (right) to obtain a flow quantity that is averaged in time, $\overline{\mathrm{Q}}$.

2.2.6 Representative Waveforms for Parametric Studies

To explore the impact of waveform shape on flow in downstream vessels, it is helpful to identify representative waveforms from a feasible, manageable number of parameters that can be used in parametric studies. These representative parameters should be chosen in a way that they are able to capture the most basic features of the waveform. As motivated below, after providing a qualitative evaluation of the range of waveforms in the older population, we concentrate on three primary waveform parameters, rather than the more extensive list given in Table 3.2. These are (V^*, T^*, V_{max}, Figure 2.2). V^* is defined as the difference between the maximum and minimum normalized velocities, or

$$V^* = (1 - V_{min}). \tag{2.3}$$

V^* is therefore, the same as the commonly referenced resistance index [56, 84, 206, 18]. T^*, is the non-dimensional time interval between the first and second occurrences of $V_{1/2\,max}$, Fig. 2.1 .

These metrics are defined as high or low if they are, respectively, above or below the mean value for the population. On this basis, each waveform was placed into one of eight sub-populations consisting of combinations of low and high values of (V^*, T^*, V_{max}) for which averages of $\overline{\mathrm{Q}}$, V^*, T^*, and V_{max}, were computed.

2.2.6.1 Choice of V^*, T^*, V_{max} as Primary Variables for Parametric Studies

With the expectation that the dependence of average flow rate on waveform shape is dominated by the parameters (V^*, T^*, V_{max}), we introduced an idealized square waveform with equivalent values (V^*, T^*, V_{max}), Figure 2.2(b). The time averaged flow rate for such an idealized square wave is

$$\overline{\mathrm{Q}}\,' = V_{max}(T^* + (1 - V^*)(1 - T^*))\pi d^2/4 \tag{2.4}$$

where we have again approximated the flow as parabolic at each instant in time. The closeness of this approximation to the measured flow rate $\overline{\mathrm{Q}}$ was evaluated by determining a correction factor (i.e., a slope $\overline{\mathrm{Q}}$ / $\overline{\mathrm{Q}}\,'$, and the correlation coefficient of the resulting linear equation.

2.2.6.2 Selection of Representative Waveforms for Parametric Study

Representative waveforms for each of the eight sub-populations were then determined by selecting the waveform within each sub-population with values of (V^*, T^*, V_{max}) collectively closest to the sub-population averages of (V^*, T^*, V_{max}). In particular, the waveform was chosen with the minimum value of the sum of the magnitude of these differences, each normalized by the sub-population average for that variable.

2.2.7 Generation of Individualized Waveforms

In many cases, although the patient waveform is not known, the vessel geometry and some patient data is known, for example age, gender, heart rate and existence of various types of cardiovascular diseases. As described below, this patient specific information can be used to select individualized values of $\overline{\mathrm{Q}}$, V^*, T^*, and V_{max}. As for the parametric studies, these values can then be used to obtain a individualized waveform by morphing a standardized waveform such as the population averaged waveform to match these values.

2.2.7.1 Obtaining Individualized Values of $\overline{\mathbf{Q}}$, V^*, T^*, V_{max}

In this method of generating individualized waveforms, individualized $\overline{\mathrm{Q}}$ was first determined by curve-fitting a $\overline{\mathrm{Q}}$ versus diameter relationship for the ensemble. Then, to determine how age, disease, and the cardiovascular risk factors described in Section 2.3.5 affected waveforms, the ensemble was divided into patients with and without each disease or risk factor. If a statistically significant difference ($\mathrm{p} \leq 0.05$) in the mean values of (V^*, T^*, V_{max}) was found between the groups with and without a disease characteristic, then a disease-specific mean was identified. A multiplicative scaling (defined as the mean of the disease group divided by the mean of the group free of that particular disease), was then created for the purpose of adjusting the waveform parameters to better tailor the waveform for patients harboring the disease. In the case of $\overline{\mathrm{Q}}$ being significantly influenced by a disease, a unique diameter flow rate curve was fit for the population harboring the disease.

2.3 Results

2.3.1 Range of Patient Characteristics across the Aged Adult Database

The analyzed population consisted of 53 males and 83 females between the ages of 51 and 94 with a mean age of 73 ± 13 years; 68% of whom were hypertensive. The prevalence of various cardiovascular diseases is tabulated in Table 2.2.

Table 2.2: Prevalence of cardiovascular risks/disease within ensemble (as % of population (Note UW = underweight, NW = normal-weight, OW = overweight, O = obese).

Risks Factors	
BMI	UW: 3%, NW: 30%, OW: 38%, O: 29%
Tobacco use (smoking)	Never: 54%, Smokes: 5%, Quit: 41%
Hypertension	68%
Cardiovascular Disease	
Aortic Stenosis	13%
Aortic Regurgitation	1%
Mitral Valve Regurgitation	10%
Congestive Heart Failure	6%
Coronary Artery Disease	28%
Atrial Fibrillation	11%
Diastolic Dysfunction	4%
Systolic Dysfunction	3%
Paroxysmal Atrial Fibrillation	2%

2.3.2 Range in Waveforms Across the Aged Adult Database

2.3.2.1 Aged Versus Young Adult Populations The range in waveform shape across the ensemble of 272 vessels from older adults can be seen in Figure 2.3(a) where a subset of 32 waveforms are chosen to reflect the range of variability of V^* and T^*, without crowding the figure. The aged population (a) shows relatively large variability across waveforms compared with the young, healthy adult population, (b). This is most evident in the region of peak velocity, V_{max}, (P1 in Fig. 2.3(b)).

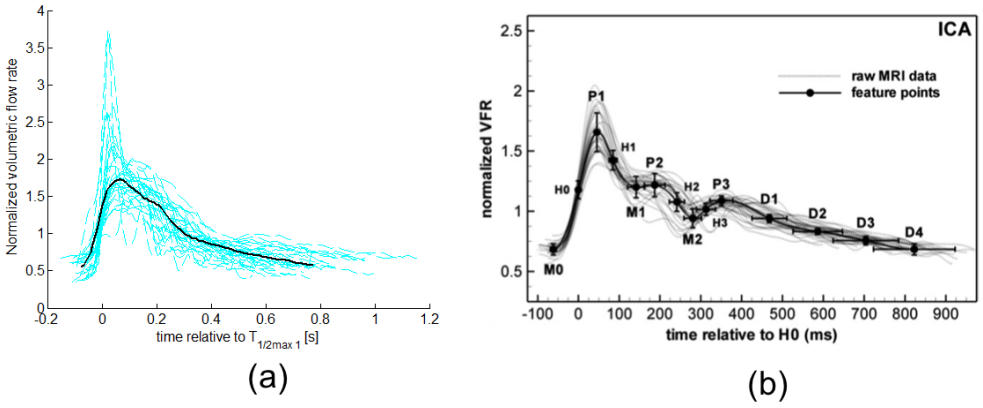

Figure 2.3: Normalized velocity waveforms (dashed lines) and mean waveform (solid line) for (a) representative subset of older population from this study, and (b) healthy, young adults, reproduced from [56] with permission of IOP Publishing. All rights reserved. Only a subset of the 272 waveforms from aged adults and the corresponding average are shown in (a) to avoid crowding the figure. For comparison with the results in [56], the older population velocity waveforms in (a) are normalized by their respective mean velocity. The volumetric flow rate was calculated by assuming Poiseuille flow, and therefore, the normalization in (a) and (b) are equivalent, though it should be noted these axis are scaled differently. Collective patient waveforms in both (a) and (b) are aligned by the point of mid-acceleration $V_{1/2\,max}$, denoted as H0 in (b).

The flow rate beyond this point decays more slowly in the aged population. Furthermore, the dicrotic notch, which is visible in the averaged curve for the young, healthy population, is absent in the average curve for the aged population. This point will be discussed in more detail in Sec. 2.3.2.3.

2.3.2.2 Waveform Metrics for Aged Population The average, standard deviation, and extrema of the normalized characteristic metrics for each of the 272 analyzed waveforms are given in Table 2.3. All kinematic variables were normalized by the vessel specific V_{max} and all times were normalized by their respective period, T_{per}. A Wilcoxon rank sum test

revealed no significant differences in any of the metrics considered here between the contralateral vessels (lowest p value was 0.13 for V_{DP}). Though variation between the left and right side was appreciable, this signifies that there is no *preferred* side for extreme values to occur. The range and frequency of the key waveform quantities (V^*, T^*, V_{max}) over the entire population are shown in Figure 2.4. In the following sections, this dataset will be used to guide the selection of the parametric and estimated individualized waveforms for this aged population

Table 2.3: Average characteristic parameter values for data ensemble.

Variable	Average ± SD	Min,Max
Primary Waveform Parameters		
$\overline{Q}$ [cm^3/s]	3.94±.61	[0.91, 12.3]
V_{max} [cm/s]	70.7±8.5	[18, 134]
T^* []	0.28±.06	[0.07, 0.42]
V^* []	0.71±.07	[0.50, 0.92]
Dimensional		
V_{avg} [cm/s]	38.2± 10.5	[7.64, 73.9]
Acc_{max} [cm/s^2]	5260± 2460	[1880, 16700]
T_{per} [s]	0.92± 0.15	[0.55, 1.35]
Non-Dimensional Velocity, Acceleration		
V_{min}	0.29± 0.07	[0.08, 0.50]
V_{avg}	0.55± 0.07	[0.25, 0.71]
$V_{1/2\,max}$	0.65± 0.03	[0.55, 0.75]
$V_{3/4\,max}$	0.82± 0.20	[0.77, 0.87]
V_{Amax}	0.57± 0.11	[0.27, 0.87]
V_{DN}	0.45± 0.18	[0.18, 0.75]
V_{DP}	0.52± 0.19	[0.33, 0.79]
V_{rec}	0.06± 0.05	[0.03, 0.34]
$V_{Avg\ BDN}$	0.73± 0.07	[0.40, 0.84]
$V_{Avg\ ADN}$	0.41± 0.08	[0.18, 0.62]
Acc_{max}	73.7± 23.2	[30.3, 171]
PI	1.34 ± 0.37	[0.73, 3.67]
Non-Dimensional Time		
t_{Vmax}	0.19± 0.06	[0.09, 0.50]
$t_{V\ 1/2\,max1}$	0.08± 0.02	[0.02, 0.17]
$t_{V\ 1/2\,max2}$	0.37± 0.06	[0.15, 0.55]
$t_{V\ 3/4\,max1}$	0.11± 0.03	[0.04, 0.21]
$t_{V\ 3/4\,max2}$	0.31± 0.07	[0.10, 0.47]
t_{VDN}	0.38± 0.13	[0.28, 0.54]
t_{VDP}	0.43± 0.15	[0.33, 0.70]

.

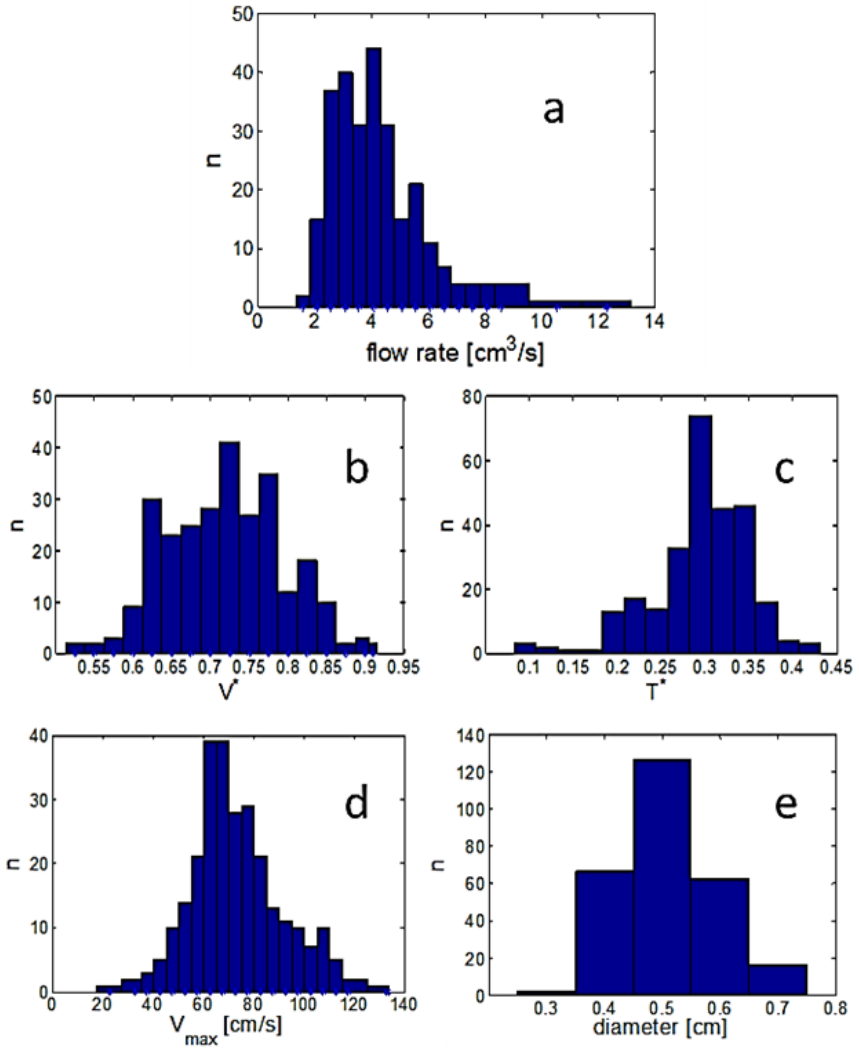

Figure 2.4: Distribution of (a) flow rate (b-d) primary waveform parameters, and (e) vessel diameter across the aged population. Here, n is the number of occurrences within the 272 waveforms.

2.3.2.3 Lack of Dicrotic Notch Twenty-three of the ICA waveforms from the 136 patients did not contain a discernible dicrotic notch, Figure 2.5. Sixteen of these patients had no discernible dicrotic notch on either side, while seven had a discernible dicrotic notch on only one side. Of these seven, three dicrotic notches were missing from the left and four dicrotic notches were missing from the right. A significant difference using a Mann-Whitney test (p = 0.007) was found between the average age of the subgroup missing at least one dicrotic notch (80 ± 9.8 years) versus the mean age of the ensemble (73 ± 13 years).

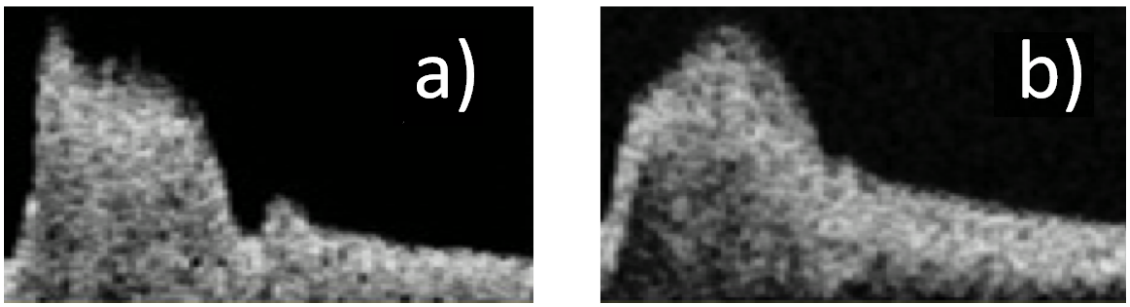

Figure 2.5: Doppler velocity waveforms selected to illustrate the extremes in the aged population showing (a) marked dicrotic notch and (b) undiscernible dicrotic notch.

2.3.3 Coupling of Waveform Contour to Flow Rate

The ability of the square waveform (introduced in Section 2.2.6) to approximate the actual waveform flow rate, $\overline{\mathrm{Q}}$, through the waveform metrics (V^*,T^*,V_{max}) was evaluated for the ensemble waveforms. The relationship between the time averaged flow rates obtained from the Doppler images and their corresponding square waveform flow rates was found to be remarkably close to linear with a scaling factor of 1.11, Figure 2.6,

$$\overline{\mathrm{Q}} \quad = 1.11\overline{\mathrm{Q}}\,' \pm 0.18cm^3/s, \qquad r^2 = 0.987. \tag{2.5}$$

$$\overline{\mathrm{Q}} \quad \approx 1.11\, V_{max}(T^* + (1-V^*)(1-T^*))\pi \mathrm{d}^2/8 \pm 0.18\mathrm{c}m^3/s \qquad r^2 = 0.987. \tag{2.6}$$

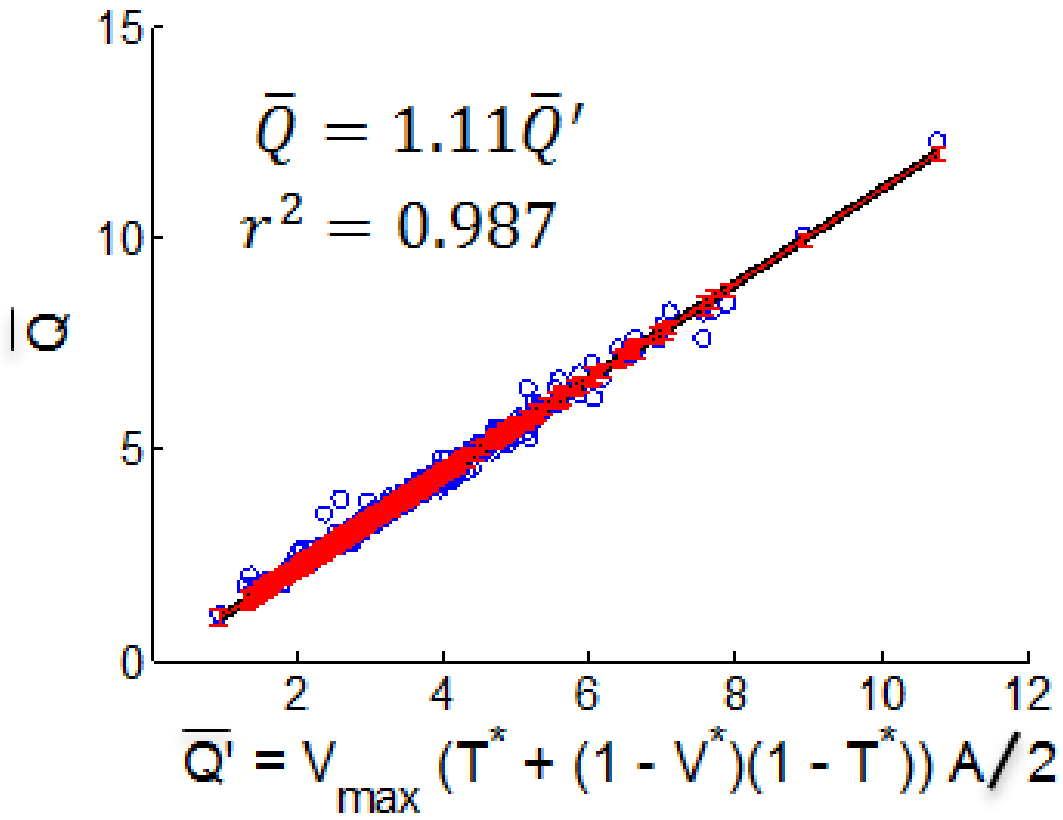

Figure 2.6: Time averaged flow rate obtained from Doppler velocity waveforms versus the estimated flow rate $\overline{Q}'$

2.3.4 Selection of Representative Waveforms for Parametric Studies

2.3.4.1 Prototypical Waveforms As described in Section 2.2.6, the ensemble of all waveforms was organized into eight groups, defined through combinations of high and low values of the parameters (V^*, T^*, V_{max}), Table 2.4. High or low values and combinations of V_{max} , T^* , and V^* were found to influence $\overline{\mathrm{Q}}$ as predicted by Equation 3.2.

Table 2.4: Eight waveform groups characterized by high/low values of (V_{max}, T^*, V^*). In column 2, H = "high", L = "low". $\overline{\mathrm{Q}}$ is determined from Eq. 3.4 and well estimated by Eq. 3.2. Group numbers are ordered from maximum to minimum $\overline{\mathrm{Q}}$.

NGroup	V_{max}, T^*, V^*	N	V_{max}	T^*	V^*	$\overline{\mathrm{Q}}$ [cm^3/s]	Age [yr]
1	H, H, L	25	85.4±7.8	0.33±0.03	0.67±0.05	4.95±1.89	71.6±7.8
2	H, H, H	44	87.7±15.8	0.31±0.04	0.76±0.04	4.74±2.36	78.2±8.6
3	H, L, L	23	83.5±12.7	0.26±0.03	0.65±0.04	4.60±1.73	65.1±17.6
4	H, L, H	28	88.7±14.6	0.20±0.06	0.80±0.06	3.87±1.58	72.5±15.9
5	L, H, L	48	58.8±8.6	0.33±0.03	0.63±0.04	3.79±1.42	69.9±9.2
6	L, L, L	43	58.6±8.3	0.24±0.03	0.64±0.04	3.49±1.04	67.4±13.3
7	L, H, H	31	56.8±8.4	0.31±0.02	0.76±0.03	3.44±1.22	83.2±9.2
8	L, L, H	30	56.8±12.6	0.24±0.03	0.76±0.05	2.88±1.07	74.1±17.0

The most representative waveform for each category is shown in Figure 2.7. Namely, for each of these categories, a waveform is provided that has the closest fit of V^*, T^*, and V_{max} , to the respective averages for that category. Hence, these waveforms collectively function as a parameter-motivated representation of the ensemble. To demonstrate the rather weak dependence of V_{max} on diameter for these groups. The lower right panel of Figure 2.7 contains the ensemble data for $\overline{\mathrm{Q}}$ as a function of d, which can be used to inspect the likelihood of any of the eight waveforms of Figure 2.7 occurring for any given vessel diameter.

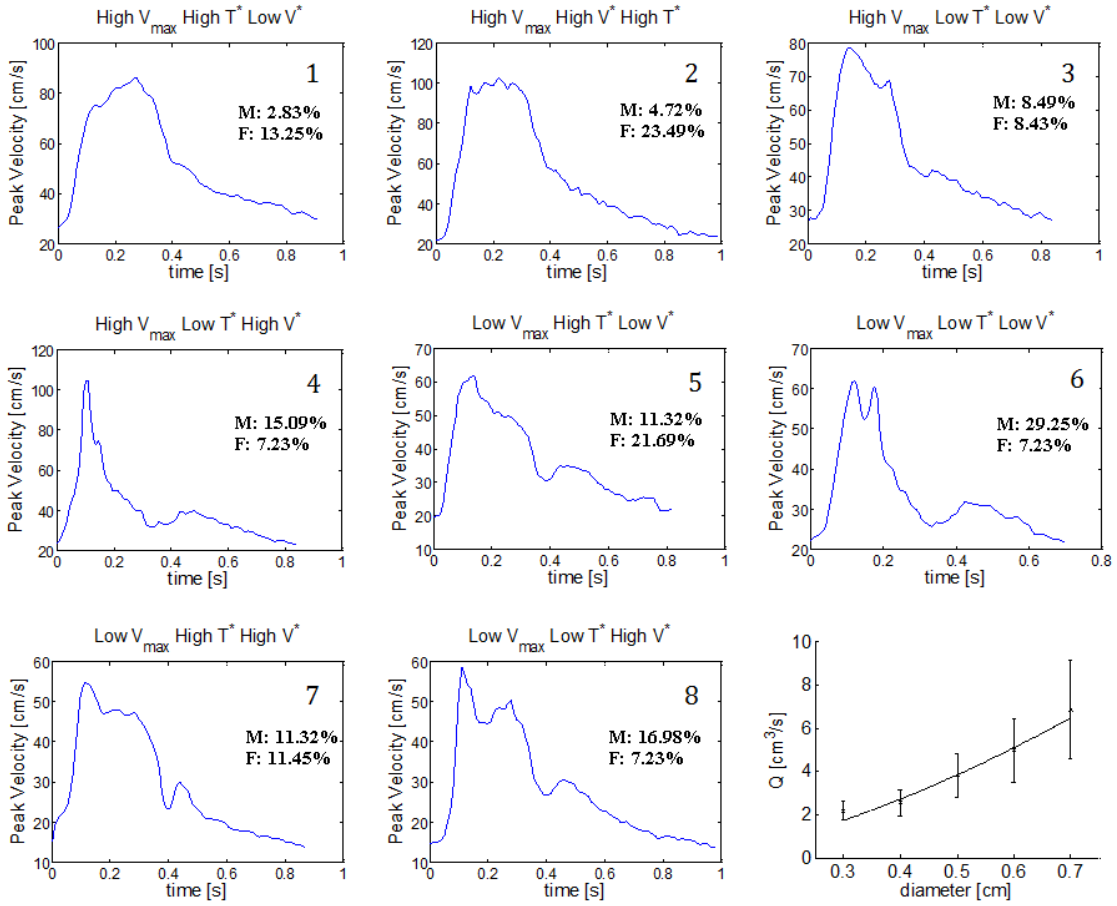

Figure 2.7: Representative patient-specific waveform for each of the eight groups identified in Table 2.4. Percentage of the overall male/female population represented in each group are shown with each waveform. The flow rate as a function of diameter for the ensemble is shown in the lower right panel of the figure.

2.3.5 Generation of Individualized Waveforms

In this section, we provide a methodology to generate an *individualized flow rate* and *individualized waveform shape* using patient information such as the diameter, age, gender, cardiovascular disease and risk factors. In the absence of patient specific waveforms and flow rates, most hemodynamic studies of the cerebral vasculature use a polynomial function of diameter to estimate the average flow rate and an idealized waveform shape from healthy, young subjects In this section, we introduce a method to use patient information combined with the database for older patients to better estimate both average flow rate and waveform shape for this older population. In particular, patient information and vessel diameter in conjunction with Equation 3.2 will be used to provide an individualized value for the flow rate $\overline{\mathrm{Q}}$ as well as the descriptive waveform metrics (V_{max}, V^*, T^*) needed to generate an individualized patient waveform. A schematic of the methodology used to estimate these four parameters is given in Figure 2.8 and described in detail below.

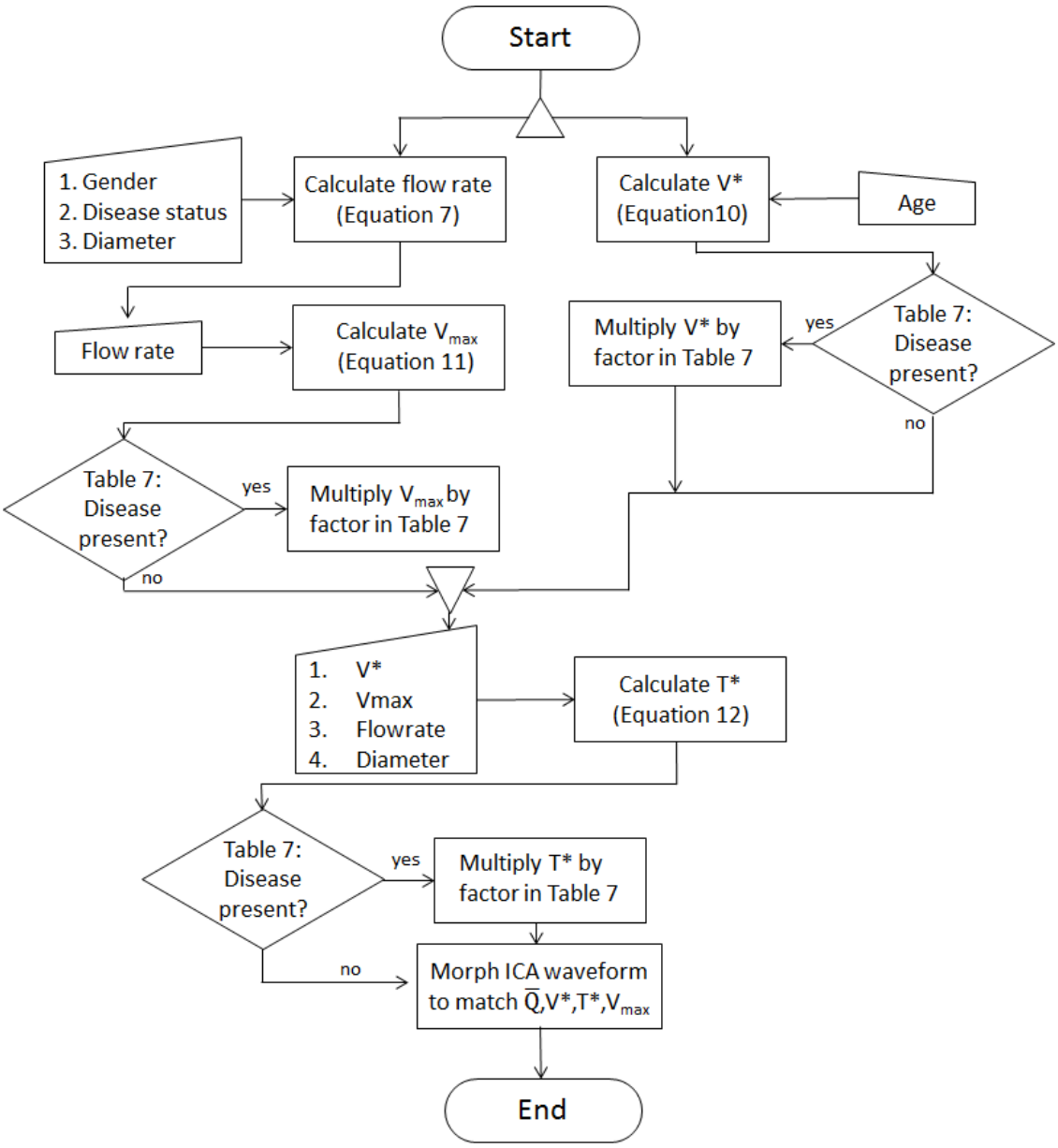

Figure 2.8: Flowchart depicting algorithm for generating individualized waveform (individualized flow rate and individualized waveform shape) waveform.

2.3.5.1 Patient Individualized Flow Rate Estimation from Diameter and Disease Condition A power law relationship between $\overline{\mathrm{Q}}$ and d, was obtained for the entire ensemble as well as all sub-populations defined by disease state,

$$\begin{array}{lll} \text{Ensemble} & \overline{\mathrm{Q}} = 11.25\ \mathrm{d}^{1.55} \pm \sigma(\mathrm{d}), & r^2 = 0.97 \\ \text{Aortic Stenosis} & \overline{\mathrm{Q}} = 11.88\ \mathrm{d}^{1.82} \pm \sigma(\mathrm{d}), & r^2 = 0.99 \\ \text{Atrial Fibrillation} & \overline{\mathrm{Q}} = 9.05\ \mathrm{d}^{1.52} \pm \sigma(\mathrm{d}), & r^2 = 0.82 \end{array} \tag{2.7}$$

where d is in units of cm and $\overline{\mathrm{Q}}$ is in units of cm^3/s. The units of the multiplicative constant are not shown. The ensemble data was well fit with an exponent of 1.55 ($r^2 = 0.97$), Figure 2.9(a). The difference in flow rates for patients with aortic stenosis and AFIB compared with the ensemble average approached, but did not reach, statistical significance with a 95% CI (p = 0.06 in both cases), Figure 2.9(a). No other diseases or factors considered in the study (see Table 2.2) were found to have a statistically significant impact on flow rate. Vessel diameter, additionally, was found to depend on age. For patients older than 73 years, the ICA diameter averaged 0.497±0.090 cm. In contrast, for patients younger than 73 years, the diameter averaged 0.517±0.083 cm with 94% CI.

2.3.5.2 Influence of Gender on the Individualized flow Rate The estimation of flow rate was further patient tailored by considering the influence of gender. The ensemble was divided into two gender-based sub-populations (53 males and 83 females) whose mean ages were not significantly different (p = 0.52). Notably, the mean flow rates for each gender-based sub-population were significantly different with 3.64±1.34 cm^3/s for males and 4.13±1.73 cm^3/s for females (p = 0.018), Figure 2.9. The power-law fits of flow rate to diameter were substantially different as seen in the difference in powers of 1.41 for males versus 1.95 for females,

$$\begin{array}{lll} \text{Ensemble, Male} & \overline{\mathrm{Q}} = 8.90\ \mathrm{d}^{1.41} \pm \sigma(\mathrm{d}), & r^2 = 0.99 \\ \text{Ensemble, Female} & \overline{\mathrm{Q}} = 15.53\ \mathrm{d}^{1.95} \pm \sigma(\mathrm{d}), & r^2 = 0.99 \end{array} \tag{2.8}$$

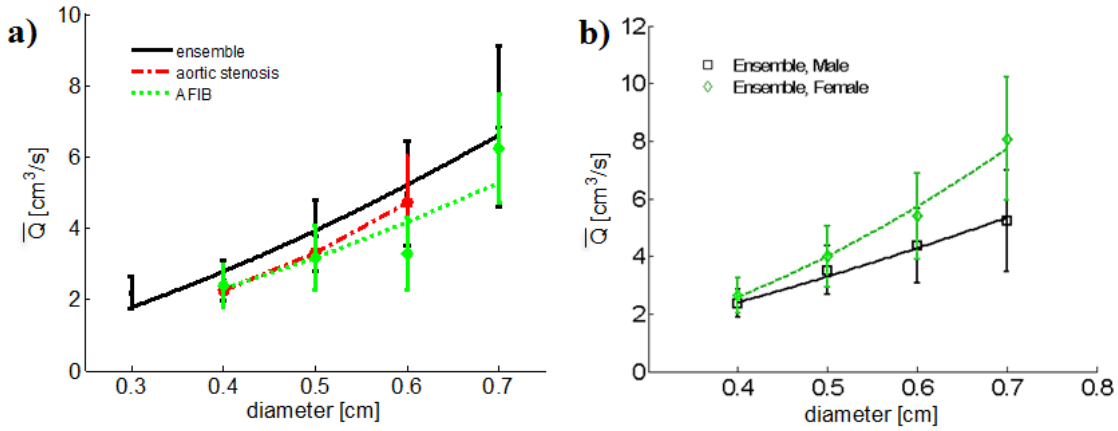

Figure 2.9: (a) Data for average flow rate as a function of diameter for the entire ensemble, the aortic stenosis sub-population, and the AFIB sub-population and, b) Difference in flow rate diameter relationship due to gender.

The best fit power-law models for the subpopulations that include the combined influence of both disease and gender are:

$$\begin{aligned}
&\text{Aortic Stenosis, Male} && \overline{\mathrm{Q}} = 7.75\ \mathrm{d}^{1.31} \pm \sigma(\mathrm{d}), && r^2 = 0.99 \\
&\text{Atrial fibrillation, Male} && \overline{\mathrm{Q}} = 5.74\ \mathrm{d}^{1.05} \pm \sigma(\mathrm{d}), && r^2 = 0.82 \\
&\text{Aortic Stenosis, Female} && \overline{\mathrm{Q}} = 17.54\ \mathrm{d}^{2.23} \pm \sigma(\mathrm{d}), && r^2 = 0.99 \\
&\text{Atrial fibrillation, Female} && \overline{\mathrm{Q}} = 4.85\ \mathrm{d}^{0.60} \pm \sigma(\mathrm{d}), && r^2 = 0.37
\end{aligned} \tag{2.9}$$

The influence of gender on $\overline{\mathrm{Q}}$, V^* , T^* ,V_{max} and d is shown in Table 2.5. It was found that V_{max} and T^* are primarily responsible for the gender-based difference in flow rate (refer to Equation 2.5), while no significant gender based relationship was found for $V^*$and d . The period of the cardiac cycle also differed significantly between genders (p = 0.03) with an average of 63±8.5 beats per minute (BPM) for males versus 67±9.3 BPM for females.

Table 2.5: Gender-based sub-population flow rate parameters

Parameter	Males	Females	p-value
$\overline{Q}$ [cm^3/s]	3.64±1.34	4.13±1.73	0.018
V_{max} [cm/s]	66.5±18.1	73.2±17.8	0.010
T^*	0.26±0.05	0.30±0.05	1e-9
V^*	0.71±0.08	0.70±0.07	0.98
d [cm]	0.51±0.08	0.51±0.08	0.88

2.3.5.3 Individualized Estimates for V^* Of the waveform parameters (V^*, T^*,V_{max}), only V^* was found to vary significantly (95% CI) with age, Table 2.6. A scatter plot is provided for this data in Figure 2.10(a) with a best linear fit of

$$V^* = 0.0036 \times age + 0.43, \qquad r^2 = 0.24. \tag{2.10}$$

This relationship can be used to obtain an individualized estimation for V^* (age is given in years). Also shown in Figure 2.10(b) are the ensemble means from Hoi 2010 [84] (mean

Table 2.6: Impact of age on waveform parameters

Parameter	Age>73 y	Age $\leq$ 73 y	p
$\overline{Q}$	3.76±1.44	4.08±1.71	0.33
V_{max}	68.4±18.0	72.2±18.3	0.055
T^*	0.28±0.06	0.28±0.05	0.69
V^*	0.73±0.07	0.67±0.08	1e-12

age 68±8 years) and Ford [56] (mean age of 28 ± 7 years). These data show reasonable agreement with the trend in V^* with age found in this work, further supporting the use of Eq. 2.10.

The influence of diseases and risk factors on the flow rate parameters V^*, T^*, and V_{max} are tabulated in Table 2.7 where a disease based scaling factor is provided. In particular, the values given are multiplicative factors equal to the mean for that population relative to the mean of the average from the entire population. Carrying out the multiplication better-tailors the waveform for that particular sub-population of patients.

Table 2.7: Modifiers of waveform parameters by cardiovascular diseases which produced significant differences ($p < 0.05$) between patient with and without each condition

Parameter	Afib	AortSten	CAD	DiaDysf	SysDysf	Quit Smoking	Under Weight
V^*	1.06	1.06	-	1.09	1.10	-	-
T^*	-	-	-	0.89	-	-	-
V_{max}	0.85	-	0.93	-	0.96	0.97	1.27

2.3.5.4 The Influence of Hypertension on V^* The prevalence of hypertension was found to be significantly higher in patients older than the mean age of 73, compared with those younger than the mean (79% versus 48%, respectively, p = 7e-5). V^* was significantly higher in the hypertensive group (0.71±0.07 versus 0.69±0.08, p = 0.009). Since this is only a modest influence on V^* and redundant with the increase in V^* due to increasing age, we do not consider hypertension as a modifying factor for V^*.

2.3.5.5 Individualized Estimates for V_{max} Motivated by the dependence of $\overline{Q}$ on V_{max} in Equation 3.2, a scatterplot of V_{max} is shown for $\overline{Q}$, Figure 2.10(a). Of V^* , T^*, and V_{max} , only V_{max} by itself showed substantial dependence on $\overline{Q}$. A linear fit was used here, though recognizing the appreciable scatter in the data expected for a older, diseased population. Using the individualized value of $\overline{Q}$, Equation 2.11 can be used to obtain a

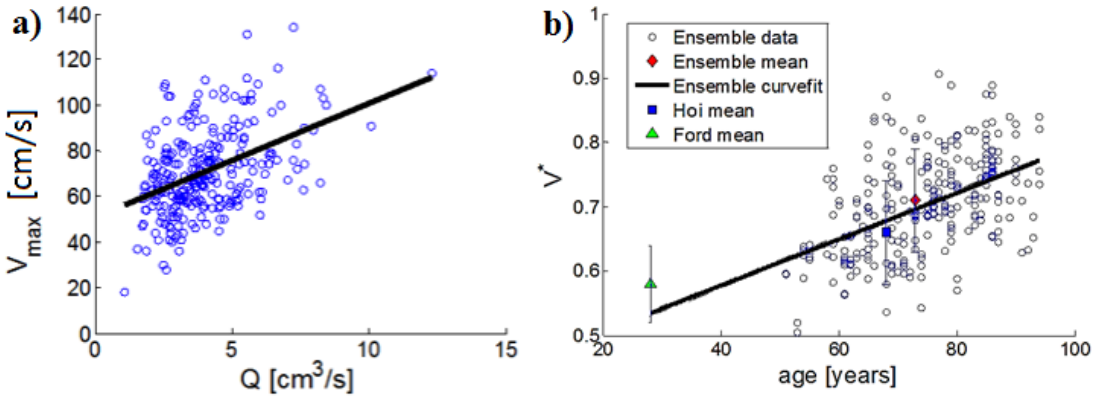

Figure 2.10: (a) Scatterplot of V_{max}, (r^2=0.19) as function of time averaged flow rate, showing data and linear fit and (b) Distribution of V^* with age and comparison with data reported by Ford et al. [56] and Hoi et al. [84].

patient individualized estimation for the maximum velocity, V_{max}.

$$\begin{aligned} V^* &= -0.0048\ \overline{\mathrm{Q}}\ + 0.72, & r^2 &= 0.01 \\ V^* &= -0.0048\ \overline{\mathrm{Q}}\ +\ 0.72 & r^2 &= 0.01 \\ T^* &= 0.0071\ \overline{\mathrm{Q}}\ +\ 0.25 & r^2 &= 0.04 \\ V_{max} &= 5.0\ \overline{\mathrm{Q}}\ +\ 51 & r^2 &= 0.19 \end{aligned} \tag{2.11}$$

2.3.5.6 Estimation of T^* Once V^*, V_{max}, $\overline{\mathrm{Q}}$ and d are determined, Eq. 2.12 can be used to estimate T^*,

$$T^* = \frac{2\overline{\mathrm{Q}}}{1.1V^*V_{max}} - \frac{1}{V^*} + 1, \qquad \text{where} \qquad A = \pi \mathrm{d}/4 \tag{2.12}$$

which, upon accounting for diastolic dysfunction (Table 2.7) finally provides all descriptive waveform parameters [1]. At this point, the parameters required to morph an existing waveform into a more patient-tailored waveform are known. The resulting morphed waveform will have a data driven flow rate with a corresponding data driven shape appropriate for the age, gender, and disease state of the patient. Motivated by the p values in Table 2.6, we chose to estimate V^*based on age through Equation 2.12.

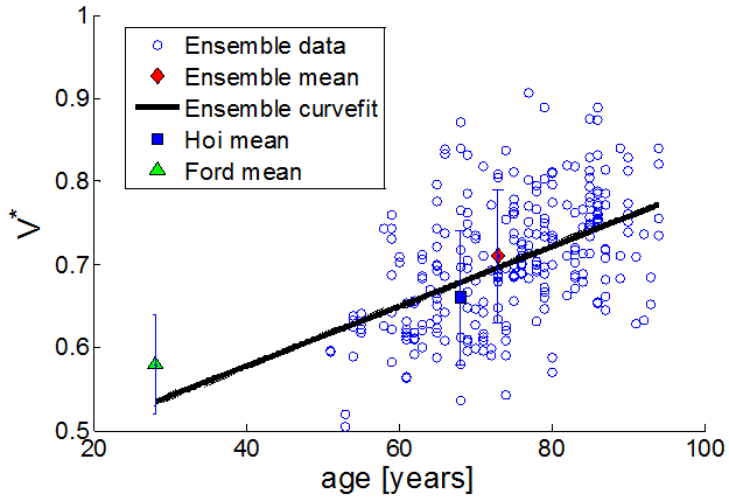

Figure 2.11: Distribution of $V^*$with age and comparison with data reported by Ford et al. [56] and Hoi et al.[84]

[1] As a side point, we note that larger T^* is associated with a faster pulse rate. In particular, the subpopulation with a faster than average pulse (66PBM), has a significantly higher T^* than the average, though it is a very minor difference (0.29 versus 0.28).

2.4 Discussion

2.4.1 Waveforms in the Aged Adult Population

In the current study, we demonstrated both qualitatively and quantitatively that there are profound differences in both ICA waveform shape and the degree of intra-population variability between healthy young adults and older adults with mild to moderate cardiovascular disease. The healthy young adult data were drawn from published literature and the older adult data from our study population of 136 patients with an average age of 73±13 years. We used existing metrics for young adults and also introduced new metrics to quantify additional waveform features relevant to the older population. As elaborated on below, the most notable qualitative differences between the healthy young ensemble and aged population were features defining the waveform shape, including the older population's larger systole - to - diastole flow rate ratio, increased flow during late systole, and the absence of a dicrotic notch. A parameter perhaps most critical to hemodynamic studies, the flow rate, was found to be 3.94±1.61 cm/s^3 for the aged ensemble of the current study versus 4.58±0.97 cm/s^3 for the left and right ICA average flow rate reported in Hoi et al. [84] for young, healthy subjects. Between these two populations, the $\overline{Q}$ coefficient of variation is nearly double. This decline in $\overline{Q}$ with age could be supported by the findings reported in Scheel et al. [168] of an age dependent decline in flow velocity and increase in resistance index (V^*). Equation 3.2 can be used to reference how these two aspects can cause a decrease in $\overline{Q}$.

2.4.1.1 Augmented Secondary Systolic Peaks Similar to the findings in this study, Hoi et al. [84] reported a conspicuous second systolic peak in older adults that existed in young adults, but was much lower in magnitude (e.g. Fig. 3 in [84])). This increased magnitude of the secondary peak is believed to be caused, at least in part, by the early return of wave reflections from the upper body circulation to the aorta, which can arise from age-related arterial stiffening [81, 140, 187]. For the present study as well as that of Kallman et al. [100], increased age and aortic stenosis were associated with additional systolic peaks. While the augmented secondary systolic peak was a common finding in the

current population, a considerable number of waveforms did not possess this characteristic during systole, displaying instead systolic waveform shapes such as a single spike of short duration Figure 2.12(a), a long-duration flat, plateau (see Figure 2.12(c)), or shapes such as seen in Figure 2.5. For this reason, we chose to make use of T^* over the more commonly used flow augmentation index (FAI) [81]. Though not equivalent, T^* is qualitatively similar to FAI in that it captures late systolic flow augmentation.

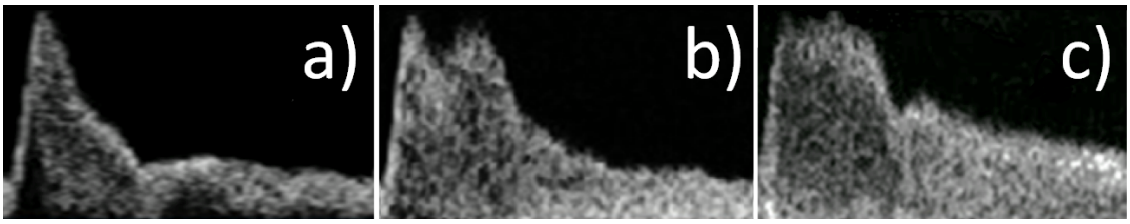

Figure 2.12: Variations in waveforms at late systole having: a) no augmented secondary systolic peak, b) augmented secondary systolic peak as described by Hoi et al. [84], c) plateau-like systolic peak.

2.4.1.2 Lack of Dicrotic Notch We identified waveforms without dicrotic notches in 17% of patients, in some cases missing only on one side. O'Boyle et al. [147] considered absence of a dicrotic notch in the internal, common and external carotid arteries of patients with different grades of aortic stenosis that included 23 men, 1 woman with a mean age of 72 as well as 11 male age matched controls. In this male dominated cohort of a relatively small size, they found 9% of the combined population lacked a dicrotic notch, and there was statistical difference between control and study group. In a study of 26 patients with aortic valvular disease, Kallman et al. only identified one ICA waveform without a dicrotic notch [100]. This patient had moderate aortic regurgitation and a 50-75% ICA stenosis. We did not find any correlation between lack of dicrotic notch and aortic stenosis, nor did we find a correlation with aortic regurgitation. Of all the disease/risk factors considered in the present study, only increasing age was found to be a significant factor associated with the absence of the dicrotic notch. This suggests, as one possibility, other vascular age related factors at the systemic level affect the presence of the ICA dicrotic notch.

2.4.1.3 Contralateral Differences The magnitudes of the waveform metric contralateral differences were substantially larger in the aged population compared with those reported for a young, healthy population. For example, the average intrasubject difference in $\overline{Q}$ between the left and right ICAs was 1.26 cm^3/s, or 32% of the ensemble $\overline{Q}$ average for our older population. This difference is twice that reported in [56] for 17 young, healthy individuals. In addition to differences in $\overline{Q}$ between left and right ICAs, the older population studied here showed average contralateral differences in V_{max}, V^* (resistance index), and T^* of 12 cm/s (17%), 0.04 (5.6%), and 0.03 (10.7%), respectively. We have not found reports of contralateral differences in these parameters in younger patients. The dierences that we found for the older population did not demonstrate a preference with a particular side.

2.4.2 Design of Hemodynamic Studies

Having shown that, unlike young adults, there is no single prototypical ICA waveform for older patients, we addressed the question of how to design in vitro and in silico studies of the hemodynamics in the anterior cerebral circulation, in the absence of patient specific inflow boundary conditions for the ICAs. We developed two approaches for producing ICA flow waveforms driven by the study population data. One approach involves the use of eight identified prototypical waveforms (Section 2.3.4.1) which capture an appreciable range of waveform characteristics defined by V_{max}, V^*, T^* found within the ensemble. Referring to Table 2.4, it is also seen that the eight waveforms capture an appreciable range of variability for $\overline{Q}$. These waveforms could be used in parametric in-vitro or in-silico hemodynamic studies as inflow data to evaluate the impact of the waveform signatures in simulated hemodynamics. The value of these eight waveforms would then be harnessed, in that for such a study, rather than imposing an arbitrary, assumed, or hypothetical set of flow conditions, one would instead impose a set of conditions which accurately simulate the range of conditions found within our data ensemble. By imposing flow conditions from each waveform onto each vascular geometry in question, one could develop a margin of uncertainty pertaining to the absence of knowledge of the actual waveform. One could also evaluate the sensitivity of each hemodynamic parameter to the choice of waveform for each vessel, and could distinguish the

hemodynamic metrics which are relatively insensitive to the choice of waveform from those which are more sensitive. Alternatively, it may be of interest to run parametric studies with $\overline{Q}$ held fixed; this could be achieved for a given vessel geometry by appropriately scaling $V_p(t)$ for each of the waveforms in Figure 2.7. The bottom right panel of Figure 2.7 could be used to provide an appropriate $\overline{Q}$ for a particular vessel in question. In the case of some studies however, it may not be desirable or practical to consider multiple waveforms for each geometry; rather, it may be desirable to construct a waveform which more likely represents the actual patient waveform as opposed to a waveform taken from, for example, a young healthy subject. The second approach we developed, presented in Section 2.3.5, is well suited for such a task. The average older waveform obtained for this population (shown in Figure 2.3) can be used to generate an older patient waveform with desired values of V^* , and T^* using a morphing technique. An example is shown in Figure 2.13 where an older adult waveform was created with prescribed values of (V^*, T^*) = (0.91, 0.08). To illustrate the effectiveness of this method, a patient waveform was chosen with low and high values of V^* and T^* relative to the population average, (V^* = 0.71, T^* = 0.28). While there is

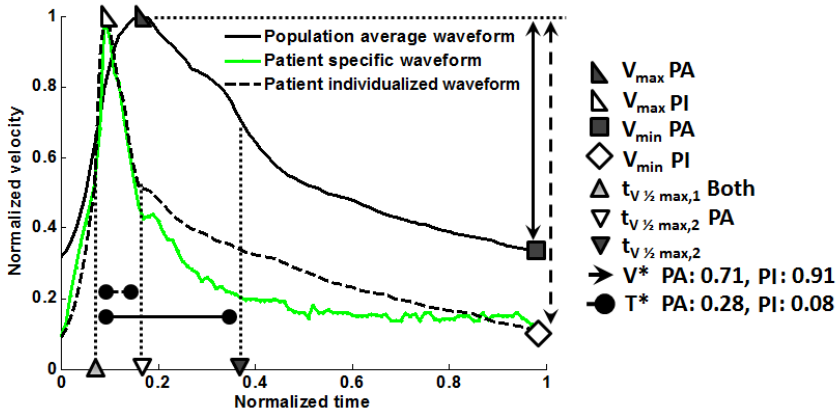

Figure 2.13: Example of morphing the population averaged velocity waveform to obtain a waveform with prescribed values of (V^*, T^*). Shown are the morphed normalized velocity waveform compared with the older population averaged waveform and the patient specific waveform. Only the values of (V^*, T^*) were prescribed to match the morphed and patient waveform. In the legend: PA = Population averaged; PM = individualized.

no unique method for morphing the average waveform, a straightforward method employing linear interpolation was used here. Briefly, the waveform velocities were first normalized with respect to V_{max} and T_{per} . In the mapped waveform, the values of $V(t)$ over the domain (0,t_{Vmax}) were linearly interpolated from the original waveform with $V(t_{Vmax})$ specified as one (based on the normalization) and $V(0)$ chosen so that the desired V^* was achieved, Equation 2.3. Similarly, the values of $V(t)$ over the domain (t_{Vmax},1) were obtained through a linear interpolation of the data defined such that $V(1) = V(0)$ with the diastolic $t_{V\ 1/2\,max}$ shifted to achieve the prescribed T^*. If the population averaged waveform (solid black line in Figure 2.13) had been considered for the patient, the normalized flow rate would have been over-predicted by 129% in contrast with a discrepancy of 22% when considering the morphed waveform (green curve in Figure 2.13) created using the prescribed (V^*,T^*).

2.4.3 Limitations and Future Directions

The current study is by no means intended to be, nor should it be utilized as, a replacement for patient-specific flow data. There are still uncertainties present even in the most-representative individualized waveforms which could potentially have a substantial impact on any hemodynamic study. Furthermore, this study makes no estimates of the impact of even key waveform parameters on hemodynamics in the ICA. This will be a subject of further investigation. The use of V^* and T^* to characterize the waveform shape has largly been adopted solely on their collective ability to reproduce a square waveform such that the time-averaged flow rate of both the patient-specific and the square waveform is largely preserved. Though this is an encouraging finding that such a condition can be remarkably-well accomplished by two parameters, this is not meant to imply that other, higher-order features of the waveform do not have their own clinical significance. Another direction of intended future work involves the use of machine learning for analysis of the ensemble to obtain more accurate descriptions of the waveform shape that include more localized shape parameters and their relationship to flow rate and disease state. This approach has been forgone at the moment since the impact of even the large scale flow features (e.g., V^* , T^*) on hemodynamics have not been well explored. Furthermore, the patient population for

this study consists of older adults with mild to moderate cardiovascular disease and could be extended in the future to include severely diseased groups. Here, we have focused on waveforms from the ICA obtained from routine screening of cardiovascular patients. In a future study, it would be valuable to apply this approach to the posterior cerebral circulation, for example the basilar artery. Finally, the standard limitations of Doppler ultrasound apply here, including the precision of typical clinical Doppler systems and the approach for estimating velocity profiles from measurements at a single location.

2.5 Conclusions

In this work, we have introduced data and methods to address the often unavoidable challenge of addressing the lack of patient specific waveform data when performing in-vitro or in-silico hemodynamic studies. We have provided an extensive analysis of the waveform shapes and flow rates in the ICAs of 136 older adults with mild cardiovascular disease - a population of clinical relevance where hemodynamics are believed to play an important role in the onset and progression of diseases (e.g. cerebral aneurysms, atherosclerosis). This study has demonstrated that there is a substantial degree of variation in flow rate and waveform shape in this aged adult cohort that cannot be represented by a single archetypal waveform. With this in mind, we have provided two approaches to design patient specific hemodynamics studies in the absence of such data. With the results obtained here, we are poised to move forward to study the impact of range of waveform shape and flow rates on vascular diseases in the aged cerebral circulation.

3.0 The Impact of Waveform Variability on Intra-Aneurysmal Hemodynamics

The author at this point wishes to express gratitude to Dr. Juan Cebral as well as Dr. Bongjae Chung and Dr. Fernando Mut from the Cebral lab group for their advisement, support, and guidence with the use of their in-house solver FeFlow and corresponding post-processing software utilized in this chapter.

SUMMARY - Blood flow inside the sac of intracranial aneurysms (IAs) spans a wide range of abnormal flow types that are believed to in part drive IA pathology. However, the small size of IAs and their location internal to the skull prevent routine, high resolution measurements of IA flow. Therefore, computational fluid dynamics (CFD) modeling is an important tool for studies of IA pathology. Numerous hemodynamic parameters are being explored as potential markers for risk assessment as well as for their importance in representing the mechanisms coupling abnormal flow and wall pathology. However, it is not yet known how robust these parameters are to uncertainly in inflow waveforms, which are not generally available on a patient specific basis. The objective of the present work was to determine which, if any, hemodynamic parameters have robust spatial distribution and magnitude over the range of waveforms associated with clinically relevant older patient populations. Aneurysm flow parameters were compared in 96 CFD simulations using 32 waveforms drawn from a recently published and highly relevant data base of internal carotid artery waveforms of older adults with mild cardiovascular disease. The spatial distribution of wall hemodynamic parameters was found to be relatively robust to changes in waveform shape and flowrate an important finding for studies analyzing the relationship between extremes in flow variables and local wall characteristics. While the magnitude of some parameters had large coefficients of variance ($<$ 25%), hemodynamic parameters that were normalized by intra-saccular values were relatively insensitive to waveform variation. The results presented here provide guidance for selecting hemodynamic parameters for investigations of the role of flow in cerebral aneurysm pathology when patient specific inflow data is not available.

3.1 Introduction

Endothelial cells are highly sensitive to spatial and temporal variations in wall shear stress [51, 48, 52, 9] and transmit the necessary information about flow to intramural cells so that the arterial diameter can be modulated to maintain homeostatic levels of wall shear stress [120, 215, 148]. Various vascular disease such as atherosclerosis are associated with regions of the vascular system where these values cannot be maintained [124, 175, 64]. For example, the substantial qualitative and quantitative flow abnormalities within cerebral aneurysms are believed to play a critical role in the further degeneration and possible rupture of the aneurysm sac [128, 20]. As direct measurements of blood flow inside the aneurysm are generally not of sufficient resolution to estimate the hemodynamic stress on the lumen of the aneurysm wall, computational fluid dynamics (CFD) provides an important tool for investigations of the role of hemodynamic stresses in cerebral aneurysm pathology.

Ideally, patient specific flow waveforms would be used at the inlet to the flow domain for these studies. However, measurements of arterial flow are typically not part of clinical routine for IA patients [207, 84, 23, 199], though there are some exceptions [14, 76, 184, 95]. In the absence of this data, the flow waveform imposed as the inlet condition in the CFD studies is often taken from young healthy subjects with flowrates chosen based on assumptions about the time averaged wall shear stress (WSS) in the vessel. These idealized boundary conditions however may not be appropriate for cases involving aneurysm patients; particularly older adults [83, 54]. Both waveform shape and flow rate vary across this population and generally differ from those of young adults [147, 168, 84, 83].

Regular access to patient specific waveform data will likely continue to elude researchers as Doppler ultrasound and phase contrast magnetic resonance imaging are not routinely performed on cerebral aneurysm patients. As a result, a pressing question remains - How to perform patient specific studies in the absence of such patient specific flow data. Patient specific CFD studies have two main areas of application for cerebral aneurysms i.) investigations of the relationship between intra- aneurysmal flow and features of the aneurysm wall directed at understanding the role of flow in the IA pathology [26, 27, 98, 107, 21] and ii.) identification of differences in flow inside ruptured compared with unruptured aneurysms directed

at identifying flow features that can guide rupture risk assessment for patients presenting with unruptured aneurysms [28, 94, 172, 19]. For the first area of study, wall characteristics are identified either through ex vivo analysis of IA samples, harvested during open brain surgery [21] or from intra-operative video [61, 60]. The role of hemodynamics in IA pathology can then be explored by looking for statistical correlations between wall characteristics and global flow variables (e.g. mean wall shear stress, rate of flow into the sac [21]). More recently, new tools have been developed [27, 30] so that local flow variables can be correlated with local wall properties (e.g. local wall thickness, collagen fiber orientation [22]). This latter approach more directly explores the relationship between changes to the IA wall and flow. In the absence of patient specific inflow data, it is then critical to determine the degree to which the spatial distribution of the hemodynamic parameters is robust to the range of inflow data found in the relevant patient population. This question is addressed using a subset of 32 waveforms from a recently published database of 272 waveforms, obtained by routine clinical procedures for aged cardiovascular patients (not presenting for treatment of IAs) [54]. The subset represents the spectrum of waveforms found in the aged population relevant to IAs. In the second area of application, correlations are sought between rupture risk and flow variables [31, 94, 51, 172, 19, 50, 39]. For such studies, it is important to develop approaches that address the uncertainty in hemodynamic waveform that can potentially impact the study. In this regard we determine the variability in hemodynamic parameters associated with the physiologically relevant range in patient waveforms using the same subset of waveforms. These results are then used to categorize the robustness of hemodynamic parameters to this variability. In order to identify an approach that can be used for parameters that are not robust, we explore how these flow parameters depend on waveform shape and flow rate. Finally, approaches are introduced that can be performed in the absence of patient specific data for the less robust parameters.

3.2 Methods

3.2.1 Selection of Geometries

The impact of flow waveform choice on intra-aneurysmal hemodynamic metrics was analyzed in three ICA bifurcation aneurysm geometries (Figure 3.1). The geometries, G1,G2, and G3 are displayed in Figure 3.1A, and corresponding geometric information is given in Table 3.1. The aneurysm geometries were chosen to display appreciable diversity: G1) a small, somewhat spherical aneurysm, G2) a larger aneurysm with a noticeable bleb, and G3) an elongated, tubular-shaped aneurysm.

Table 3.1: Geometric parameters for three geometries where AR = aspect ratio (height / neck diameter), BF = bottle-neck factor (max sac diameter/ neck diameter), N = neck diameter, D = parent artery diameter at inlet, Max sac size = largest diameter in aneurysm.

Geometry #	Sac volume [cm^3]	Sac area [cm^2]	Max size [cm]	D [cm]	AR	BF	N/D
G1	0.020	0.34	0.41	0.40	1.3	1.2	0.66
G2	0.11	1.1	0.71	0.47	1.8	1.7	0.87
G3	0.17	0.35	0.52	0.48	2.3	1.1	0.62

3.2.2 Selection of Waveforms

As described below, a subset of waveforms were selected from a database of 272 ICA waveforms obtained using Doppler ultrasound from aged patients with mild cardiovascular disease [54]. Hemodynamic results for the steady waveform are then used as an extreme limit with regards to independence of patient waveform. In addition, a steady state waveform was considered for each geometry, where the steady state flow rate was chosen as a function of the ICA diameter based on data from the older patient population Equation 7 in [54]. In what follows, we will first briefly review information from [54] that is pertinent to the present methodology, then move on to incorporate this material into the present study.

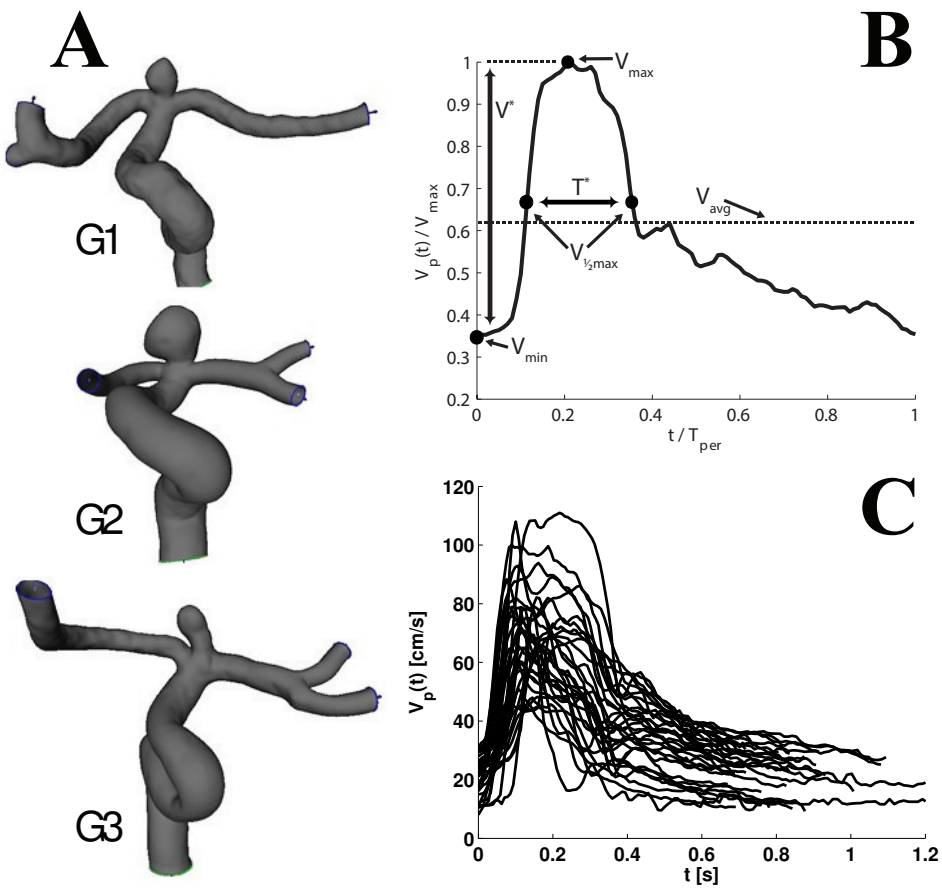

Figure 3.1: A. Three patient-specific ICA bifurcation aneurysm geometries (G1, G2, G3) selected for the evaluation of impact of waveform variation on hemodynamics. Entire computational domain is shown. (B) Non-dimensional waveform metrics used for selection of waveform cohort in the current study. (C) The subset of 32 velocity waveforms from Chapter 2 used in the present study. These waveforms are collectively representative of an older population with moderate cardiovascular disease. The waveforms are aligned so that corresponds to time zero.

3.2.2.1 Descriptive Waveform Metrics Our previous work [54] identified three dominant waveform parameters, V^*, T^*, $V_p(t)$ that could be used to estimate the dimensional time averaged flow rate $\overline{\mathrm{Q}}$ through Equation 3.2 from Chapter 2, where D is the parent vessel hydraulic diameter. The ICA waveforms identified from the prior study are imposed as inflow conditions on the parent artery feeding the aneurysm, and therefore we denote the non-dimensional time averaged flow rate as Q_p, where $Q_p = \frac{Q_{avg}}{V_{max}}$. We denote the time averaged intra-aneurysmal flow rate as Q_a.

Table 3.2: Definitions of waveform parameters

Dimensional	
$\mathrm{V}_p(t)$	Measured Doppler velocity (p = Measured Doppler velocity (spatial peak across the diameter))
V_{max}	Maximum in time of V_{max}
T_{per}	Duration of cardiac cycle
V_{min}	Minimum in time of V_{max}
V_{avg}	Average of $\mathrm{V}_p(t)$ *overonecardiaccycle*
Non-Dimensional	
V(t)	Normalized Doppler velocity = $\mathrm{V}_p(t)/V_{max}$
V_{min}	Minimum velocity, / V_{max}
V_{avg}	Normalized time-averaged velocity, / V_{max}
V^*	1 - V_{min}
$\mathrm{V}_{1/2\ max}$	$\frac{1}{2}(\mathrm{V}_{max}-)/V_{max}$
T^*	Fraction of cardiac cycle when $\mathrm{V}_p(t)$ $/V_{max}¿V_{1/2\ max}$

The parameters V^* and T^* are instrumental in quantifying the waveform shape (e.g. nondimensional waveform) while V_{max} assigns magnitude to the velocity waveform envelope, Figure 3.1. Pulsatility index (see Equation 3.1) can be utilized to capture the waveform features described by these parameters, and has been used previously for such a role; for example, see [84, 54, 62, 92, 56]. To a this end in the current work, we manipulate PI in the following manner:

$$PI = (V_{max} - v_{min})/v_{av} = V^*/V_{av} \tag{3.1}$$

where v_{min} , v_{av} and V_{av} are defined in Table 3.2. We can further appreciate the influence of T^* in this definition in the sense of an approximation if we realize that, through Equation 3.2,

$$\overline{\mathrm{Q}} \approx 1.11\, V_{max}(T^* + (1 - V^*)(1 - T^*))\pi \mathrm{d}^2/8 \pm 0.18 \mathrm{c}m^3/s \qquad r^2 = 0.987. \tag{3.2}$$

$$V_{avg} \approx 1.11(T^* + (1 - V^*)(1 - T^*)) \tag{3.3}$$

It thus follows from 3.1 and 3.3 that PI is a function of V^* and T^*.

3.2.2.2 Selection of 32 Representative Waveforms Thirty-two velocity waveforms from the prior study (Figure 3.1 C) were selected for use as time varying flow boundary data for the three geometries. The waveforms were selected based on their collective ability to span the ranges of both V^* and T^* reported in the prior study and to capture and quantify the influence of these parameters on intra-saccular flow. For the 32 selected waveforms, V_{max} ranged from 51 to 111 cm/s, covering a range of approximately three standard deviations in V_{max} , as reported in [54].

In this work, the time-averaged flow rate over one cardiac cycle, Q_p will receive substantial consideration. We therefore converted our data, in terms of $V_p(t)$, into Q_p by the following where we have assumed Pouiselle flow:

$$Q_p = \frac{\pi D^2}{8T_{per}} \int_0^{T_{per}} V_p(t)dt \tag{3.4}$$

The Q_p ranges in resulting flow rates (Table 3.3) spanned between approximately 1.5 to 2.0 diameter-dependent standard deviations found in [54]. As a point of reference, the corresponding ensemble predicted flow-rates for such geometries are 2.72, 3.49, and 3.61 $\mathrm{cm/s}^3$ as determined by Equation 7 in [54], and the resulting maximum peak velocities at the models' ICA inlets (ref Table 3.3) were within their corresponding range identified in our previous study [54]. The current study therefore did not require any re-scaling of the peak velocity according to vessel diameter.

Table 3.3: Ranges of waveform metrics for the 32 waveforms using in this study

$\overline{\mathrm{Q}}$ or Q_p [cm/s^3]	1.2 $\leq$Q$_p$ 5.4
PI	$0.70 < \mathrm{PI} < 4.0$
V^*	$0.50 \leq V^* \leq 0.91$
T^*	$0.07 \leq T^* \leq 0.42$
V$_{max}[cm/s]$	$51 \leq V_{max} \leq 111$
Acc$_{max}$	$43 \leq Acc_{max} \leq 171$

3.2.3 Computational Methodology

Numerical simulations of rigid-wall pulsatile Newtonian blood flow governed by the unsteady 3D Navier-Stokes equations were conducted for each geometry using the 32 waveforms plus a steady-state flow, totaling 99 simulations (3 cases x 32 waveforms + 3 steady state). The original Doppler ultrasound velocity waveforms were converted into time-varying flow waveforms through Equation 3.4. Flow waveform boundary data were then imposed in the form of time-varying Womersley profiles on all vessel outlets, assuming a flow division via Murray's law [151]. All simulations were conducted over two cardiac cycles discretized by 100 timesteps. The spatial domain was discretized by tetrahedral finite elements having a maximum element length scale of 0.15 mm. The timestep size for each model depended on the period of each waveform, which varied between 0.67 to 1.27 seconds, and was found to be sufficient for resolving the models for the purposes of this study. The finite element models with boundary conditions and discretization described here were solved as described in [24].

3.2.4 Spatial Sensitivity of Hemodynamics to Waveform Shape and Magnitude.

The sensitivity of the hemodynamic parameters in Table 4.1 to waveform are considered in this study. Qualitative analysis was first considered, beginning with visualization of streamlines and vortex corelines. Contours of WSS, normalized by the sac maximum, and OSI were represented. Furthermore, we included for each geometry, as an aid and a metric for

assessing the qualitative similarities among cases, the maximum surface distance separating the locations of maximum WSS resulting from all waveforms. The standard deviations of the sets of the maximum WSS locations for each geometry are furthermore given. The same location measurements are likewise provided for MaxOSI.

Table 3.4: Definitions of waveform parameters. Note: WSS = time averaged wall shear stress magnitude.

Parameters quantifying flow at lumen surface	
WSSMax	Maximum WSS in aneurysm
WSS	Temporally and spatially averaged WSS in aneurysm
WSS	Minimum wall WSS in aneurysm
OSIMax	Maximum OSI in aneurysm
OSI	Spatially averaged OSI in aneurysm
SCI	Shear concentration index [32]
LSA	Low shear area [32]
Parameters quantifying bulk flow	
CORELEN	Aneurysm vortex core line length [19]
PODENT	Proper orthogonal decomposition entropy in aneurysm [19]
Q_{an}	Time-averaged aneurysm inflow rate
ICI	Inflow concentration index [32]
VMax	Maximum velocity in aneurysm
VMaxMean	Time-averaged maximum velocity in aneurysm
KER	Kinetic energy ratio [172]
SRR	Shear rate ratio [172]
VER	Velocity ratio [172]
VOR	Vorticity ratio [172]
VDR	Viscous dissipation ratio [172]

Moving to quantitative analysis, the sensitivity of each hemodynamic metric was assessed by ranking them by standard deviation per mean for each of the three geometries using the 32 waveforms. To then quantify the dependence of each metric on both flowrate and waveform shape for each geometry, regression equations for each metric were fit as functions of the relevant waveform parameter(s). Waveform parameters considered in this fitting process were Q_p ,V^* , T^* , V_{max} , A_{max} , and PI. Further, the goodness of a steady-state approximation was assessed by comparing flow metrics such as time- averaged wall shear stress magnitude (WSS) between the steady state and pulsatile solutions.

Table 3.5: Summarizing spatial deviations (cm) between MaxWSS locations resulting from differences in the 32 waveforms. The maximum dimension of G1, G2, G3 are (0.41 cm, 0.71 cm, 0.35 cm), respectively.

	G1		G2		G3	
Parameter	Max	StDev	Max	StDev	Max	StDev
Max WSS	0.058	0.020	0.016	0.002	0.13	0.032
OSIMax	0.082	0.028	0.077	0.021	0.023	0.008

3.3 Results

3.3.1 Impact of Waveform on Flow and Wall Hemodynamic Patterns

Streamline and vortex core line plots at systolic deceleration remain generally consistent among multiple waveforms, with the exception of Waveform D in G1, which is more similar to the steady flow solution. The time- averaged wall shear stress (normalized by the sac maximum) and OSI contours are provided in Figure 3.2B,C and Figure 3.3A, B. With this normalization, the WSS contours remain qualitatively similar, even over this wide range of flow rates from 15 - 60 dyn/cm^2. Quantitative measures of the shift in maximum WSS and MaxOSI that include all 32 waveforms confirm this relative insensitiviy to flow rate Table 3.5. Most notably, the largest standard deviations of the maximim WSS locations occuring for G3, and the maximim OSI locations occuring for G1, are 0.0316 cm and 0.0849 cm respectfully. The explanation for the selection of Waveforms A-D in in Figure 3.2 is deferred to Section 3.4.2.

3.3.2 Ranking Quantitative Hemodynamic Sensitivity

In Table 3.6, the flow parameters are grouped with respect to their sensitivity to the choice of waveform for each geometry. Sensitivity is presented using the ratio of the standard deviation to the mean, or coefficient of variance (CV), averaged over the 32 waveform cases shown in Figure 3.1C. Intrasaccular parameters that are, by definition, normalized by a

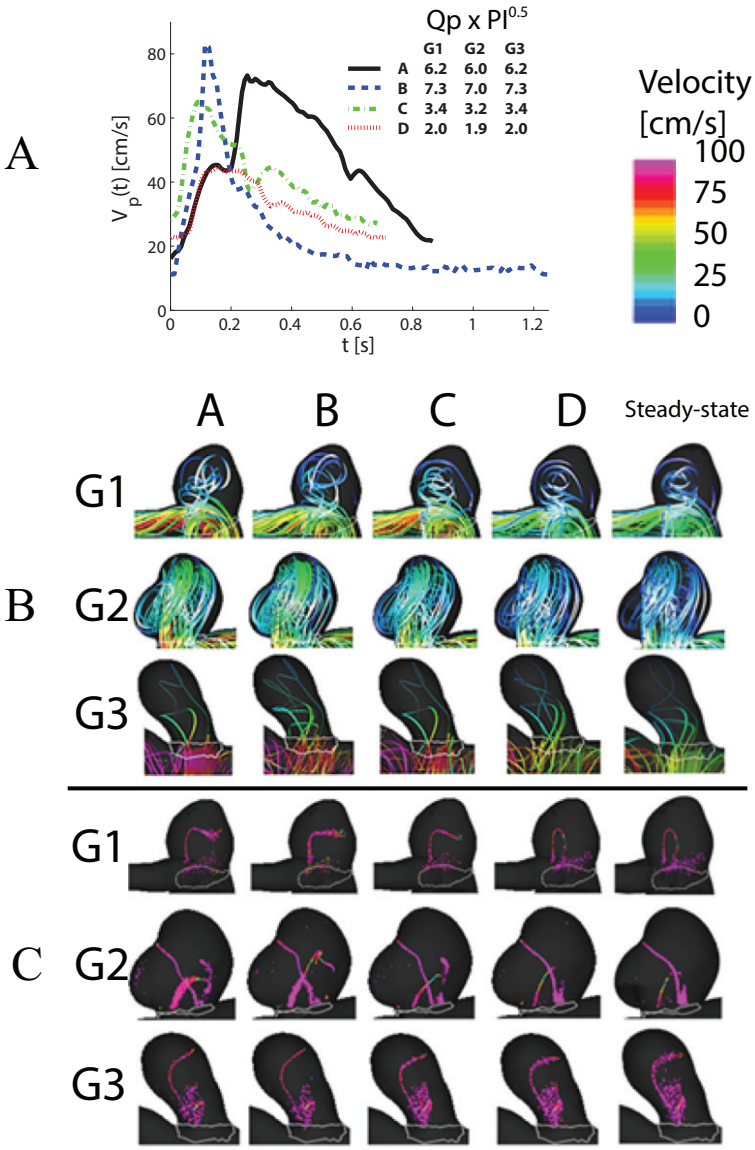

Figure 3.2: A. Representative waveforms A,B,C,and D, selected for their span of the range of Q_p x PI, were used in the cases plotted B. Streamlines resulting from waveforms A-D (plus steady state) for each geometry at late systole. Qualitative similarity in flow structure is noted despite appreciably different ranges in velocity present among each geometry (0 - 100 cm/s). C. Vortex core lines resulting from waveforms A-D (plus steady state) for each geometry at late systole. Qualitative similarity among the cases is appreciable despite the differences in waveforms.

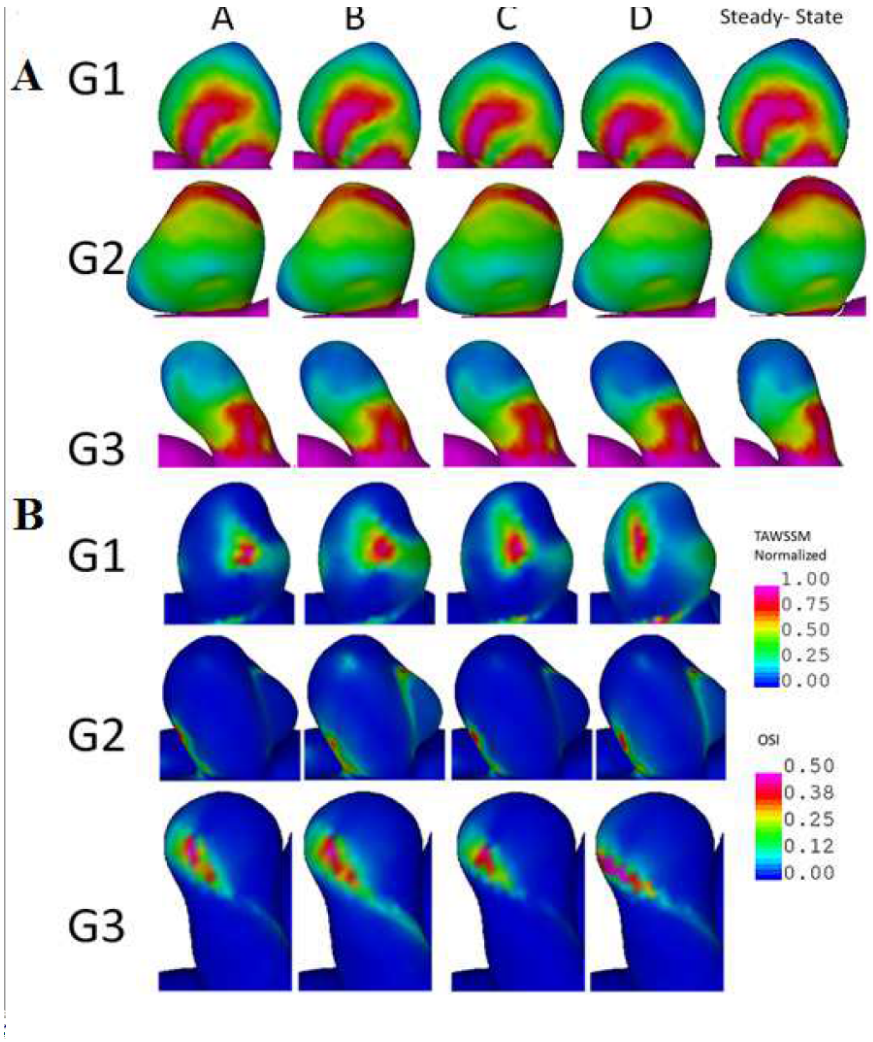

Figure 3.3: A. Time-averaged wall shear stress magnitude (WSS) resulting from waveforms A-D (plus steady state) for each geometry. Each contour is normalized by the maximum WSS present in the aneurysm. Such a normalization is shown to robustly preserve regions of high/low WSS under different parent flow conditions. B. OSI resulting from waveforms A-D. Though (as in row G2, columns B vs A or D vs C) the location of maximum OSI is different, the regions of elevated OSI remain consistent.

parent-artery values (e.g. LSA, VDR) were found to be less impacted by the choice of waveform than parameters which are not normalized in this way (e.g. OSIMax, WSSMax), Table 3.6 . The sole exception to this is KER for Geometry 3.

Parameters that were independent of waveform shape (Fig. 3.4) were compared with steady flow results, Table 3.7. The standard deviation normalized by the sac average, was less that 10% for 7 out of the 18 parameters and less than 25% for 10 out of 18 parameters.

Table 3.6: Hemodynamic metric averages and standard deviations of all 32 cases for Geometries 1-3. Parameters with a "*" are normalized by the corresponding parent artery value.

	Parameter	G1 Mean±SD	G2 Mean±SD	G3 Mean±SD
SD/AVG	LSA*	91.6±0.41	86.5±2.87	77.1±1.57
$< 5\%$	ICI	0.37±0.02	1.27±0.03	0.44±0.01
	VDR*	0.15±0.0050	0.15±0.015	0.24±0.013
	SRR*	0.34±0.023	0.35±0.025	0.46±0.033
SD/AVG	KER*	0.055±0.0041	0.11±0.010	0.096±0.0075
$< 10\%$	VER*	0.18±0.016	0.30±0.020	0.25±0.023
	VOR*	0.30±0.026	0.35±0.029	0.42±0.036
SD/AVG	SCI	6.32±0.78	8.15±1.49	3.69±1.38
$< 25\%$	VMax[cm/s]	55.8±10.4	99.2±17.0	89.5±22.33
	CORELEN [cm/s]	1.09±0.12	2.18±0.58	1.74±0.30
	OSIMax	0.29±0.12	0.40±0.03	0.25±0.05
	WSSMax [dyn/cm^2]	155±32	294±65	288±78
	VMaxMean [cm/s]	26.0±5.65	47.0±10.5	50.2±14.4
SD/AVG	Q_{an} $[cm/s^3]$	0.19±0.04	0.72±0.16	0.41±0.12
$\geq 25\%$	PODENT	0.38±0.09	0.42±0.13	0.11±0.04
	OSI	0.03±0.01	0.02±0.01	0.01±0.01
	WSS[dyn/cm^2]	10.4±3.1	16.0±5.3	37.5±14.2
	WSSMin	0.01±0.01	0.01±0.01	0.01±0.01

Table 3.7: Comparison between steady-state and pulsatile metrics for corresponding Q_{PA}. Categorization is based on metric difference average over all three geometries.

	Parameter	G1 dif	G2 diff	G3 diff
$\text{diff}_{Steady-Pulsatile} < 5\%$	LSA	1.4%	-2.5%	1.4%
	SRR	0.04%	3.5%	1.9%
	VOR	0.8%	3.2%	2.4%
	Q_{an} $[cm/s^3]$	-4.5%	1.5%	0.90%
	VER	-4.8%	1.1%	-2.7%
	VMaxMean [cm/s]	-3.7%	-2.4%	-5.3%
$\text{diff}_{Steady-Pulsatile} < 10\%$	WSS [dyn/cm^2]	0.60%	11%	5.3%
	VDR	-1.2%	12%	4.9%
$\text{diff}_{Steady-Pulsatile} < 20\%$	SCI	-0.70%	9.6%	-23%
	ICI	-33%	-7.1%	-19%

3.3.3 Characterization of Relationships between Waveform Parameters and Hemodynamic Metrics

The degree to which the hemodynamic parameters were found to depend on waveform shape and flow rate varied, (Figures 3.4 - 3.7. For some parameters, dependence was primarily on parent artery flow rate, Fig. 3.4, while for other parameters, dependence included both flow rate and waveform shape (Figures 3.5 - 3.7). In general, hemodynamic parameters dependent solely on Q_p (Figure 3.4) generally expressed higher r^2 values than parameters dependent on both flowrate and waveform shape e.g., Figure 3.4 versus Figure 3.6. Parameters impacted by both flow rate and shape, as seen in the r^2 values in Figs. 3.5 - 3.7, generate a wider spread of data when plotted against waveform parameters.

The more complex waveform-hemodynamic relationships involving both flowrate and waveform shape can be quantified by a single parameter that is a multiplicative combination of Q_p and shape parameters. For example, WSS (dependent on both flowrate and shape) can be captured through a single parameter, Figure 3.5. Particularly, WSS showed a linear dependence on the product $Q_p PI^{0.5}$. In general, many of the time-sensitive hemodynamic parameters with a dependence on waveform shape were found to exhibit a unique dependence on $Q_p^N PI^M$ (N = 0,1; M = 0, 0.5, 1), Figures 3.5, 3.6, 3.7. Regression models where M = 0

often incorporated one or more of the fundamental waveform parameters (V^* for example) which comprises PI (according to Equations 3.1, 3.3) as an alternative to PI itself (e.g., Figure 3.6, OSI_{max} for G3). One exception, PODENT, was found to best model hemodynamic dependence on waveform by incorporating A^* into the regression model (Figure 3.7B). On a per-case basis, alternative values of M and N often produced no meaningful fit $r^2 < 0.05$), indicating the physical significance of the dependent variables (discussed later). To obtain improved fits, it was found useful for several regression models to divided the ensemble of cases between those with low T^* and those with high T^* , which indicate a waveform having a T^* below or above the ensemble mean of 0.28.

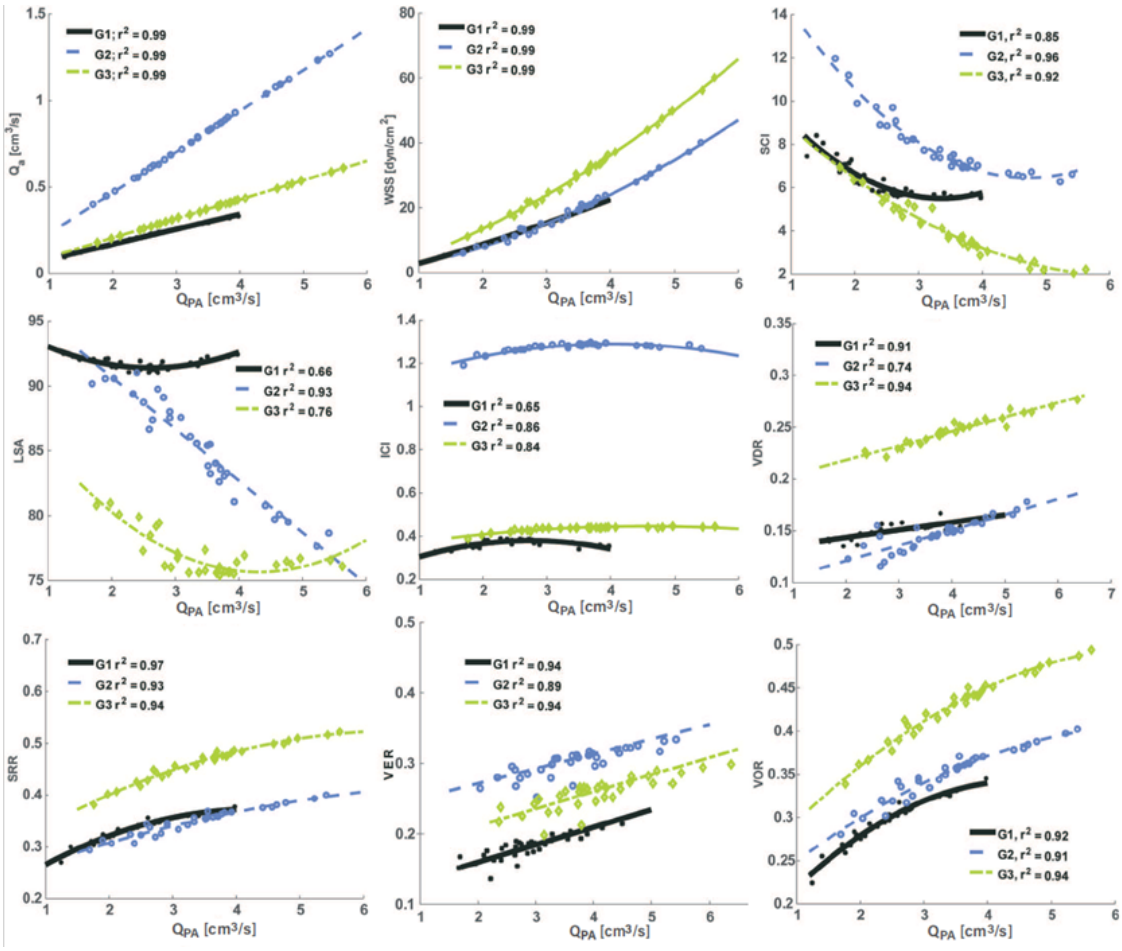

Figure 3.4: Several time-averaged hemodynamic metrics are largely independent of waveform shape and dependent only on Q_p. With few exceptions, the general manner in which these metrics respond to Q_p is reasonably well described by a simple polynomial which can be used in evaluation the uncertainty in a parameter in the absence of a patient specific waveform.

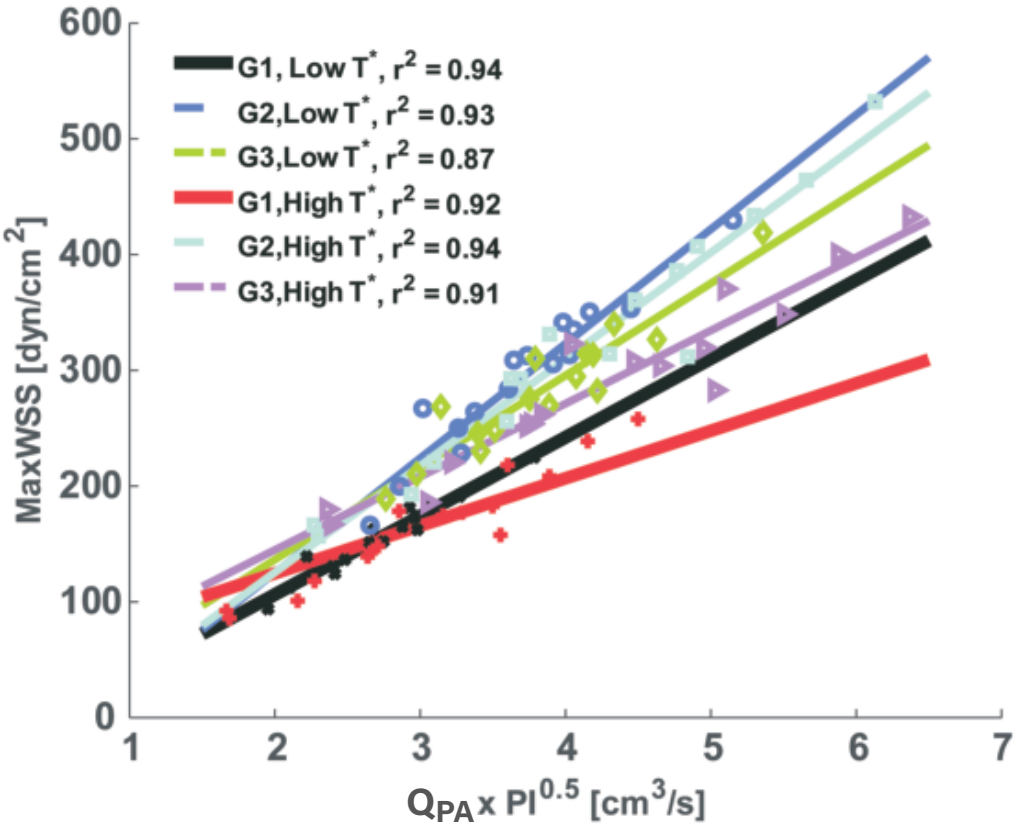

Figure 3.5: WSSMax, unlike its time-averaged counterpart WSS, is dependent on both Q_p and PI. While this relationship is more complex and less robust than that for Q_p, all data-points in the figure are well above their respective time-averaged values.

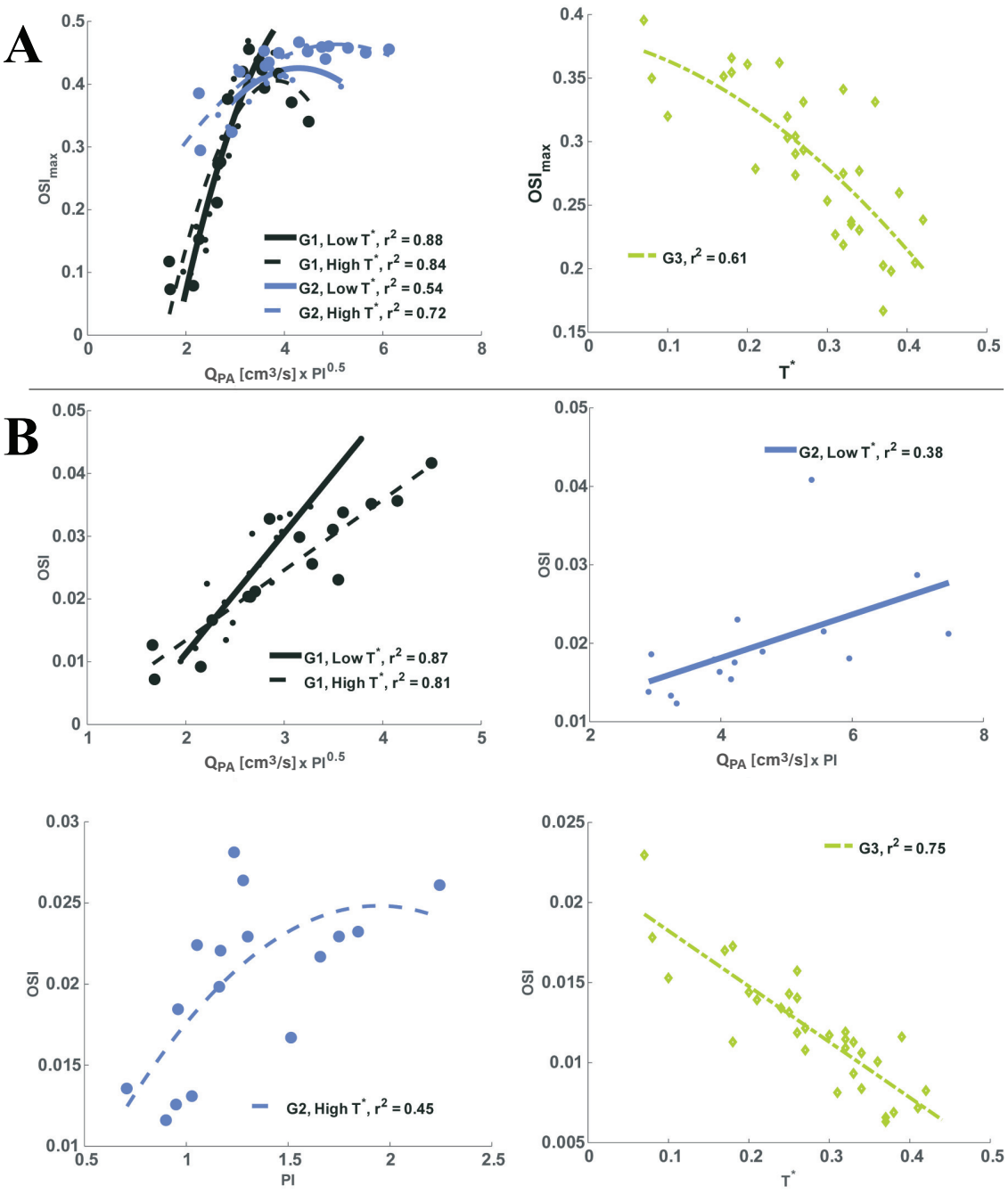

Figure 3.6: Influence of waveform on A. Maximum OSI B. spatially averaged OSI are strongly influenced by both flow rate and waveform shape. Note that, although PI itself does not influence maximum OSI for G3 in a manner which can be described by a simple polynomial, T^* by definition can (though not necessarily) influence PI (see Equations 2,3).

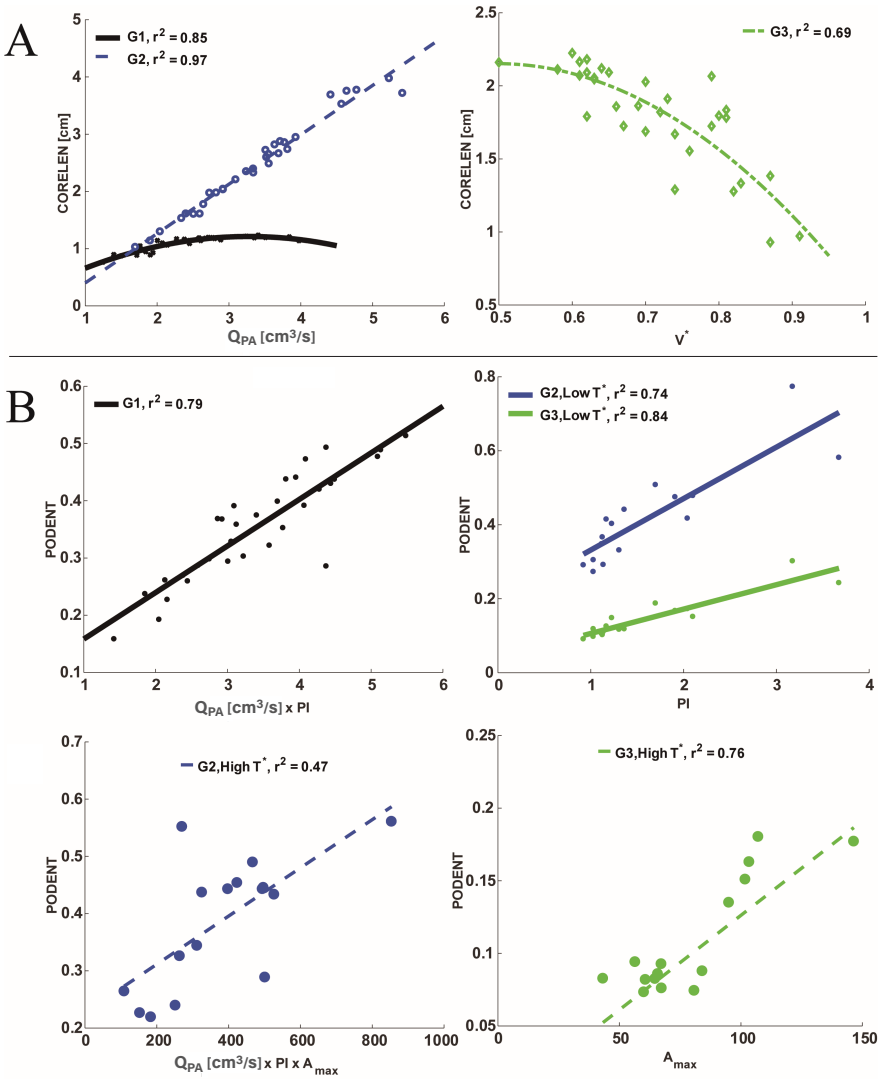

Figure 3.7: A. Vortex core line length and B. PODENT are strongly influenced by both flow rate and waveform shape. Furthermore, the influential waveform parameter(s)are dependent on the aneurysmal and vessel geometry, demonstrating the the general complexity of the waveform-hemodynamic relationship between these parameters and the need to consider multiple waveform parameters to sufficiently identify the hemodynamic uncertainty in the absence of the patient specific waveform.

3.4 Discussion

Patient specific waveform data in the cerebral circulation is often not available to researchers conducting hemodynamic studies of cerebral aneurysms. To address this commonly encountered scenario, we explored the robustness of hemodynamic metrics to waveform shape and magnitude. Such work is vital to support ongoing research correlating focal changes in wall structure (e.g., lipid accumulations, calcification, collagen fiber structure) to local extremum in the hemodynamics between hemodynamics and wall pathology [21, 22, 190, 60, 61]. Most importantly to this end, the current study has demonstrated the robustness of the spatial distribution of hemodynamic quantities to an extensive, diverse waveform set (see Figure 3.1). More specifically, the largest shift in the maximum WSS location between any two cases among all three geometries was 0.13 cm (G3). On average, this shift was 0.032, 0.020, and 0.002cm for G3, G1, and G2 respectfully. The preservation of the spatial distribution of wall hemodynamics, as opposed to their absolute magnitudes, has been conjectured to be of particular relevance for influencing wall properties [21, 22, 190, 60, 61]. This notion of an *adaptive* homeostatic set point (as opposed to a universal hemodynamic strict threshold) has been conjectured and supported by Bond et al.[13], who found from a study of mice that the set point in shear stress was dependent on body weight, and therefore the animal the animal must have an adaptive set point that changes over its lifespan. Therefore, if this holds in humans, the assumption that the magnitude of dimensional wall shear stress can be interpreted similarly across individuals may not hold. The existance of adaptive homeostatic lumenal hemodynamics in humans is further supported by Cebral et al. [22], who found a strong correlation between physical changes in the aneurysm wall (e.g. atheroma) and flow parameters when flow parameters were normalized by the intrasaccular average value. This suggests that the wall biology is responsive to the locally normalized hemodynamics; i.e., the qualitative distribution of hemodynamic values as opposed to a discrete threshold. These results motivated us to repeat the study of normalized flow parameters in Figure 3.3 using the sac average rather than maximum values as a normalizing parameter, Figure 3.8.

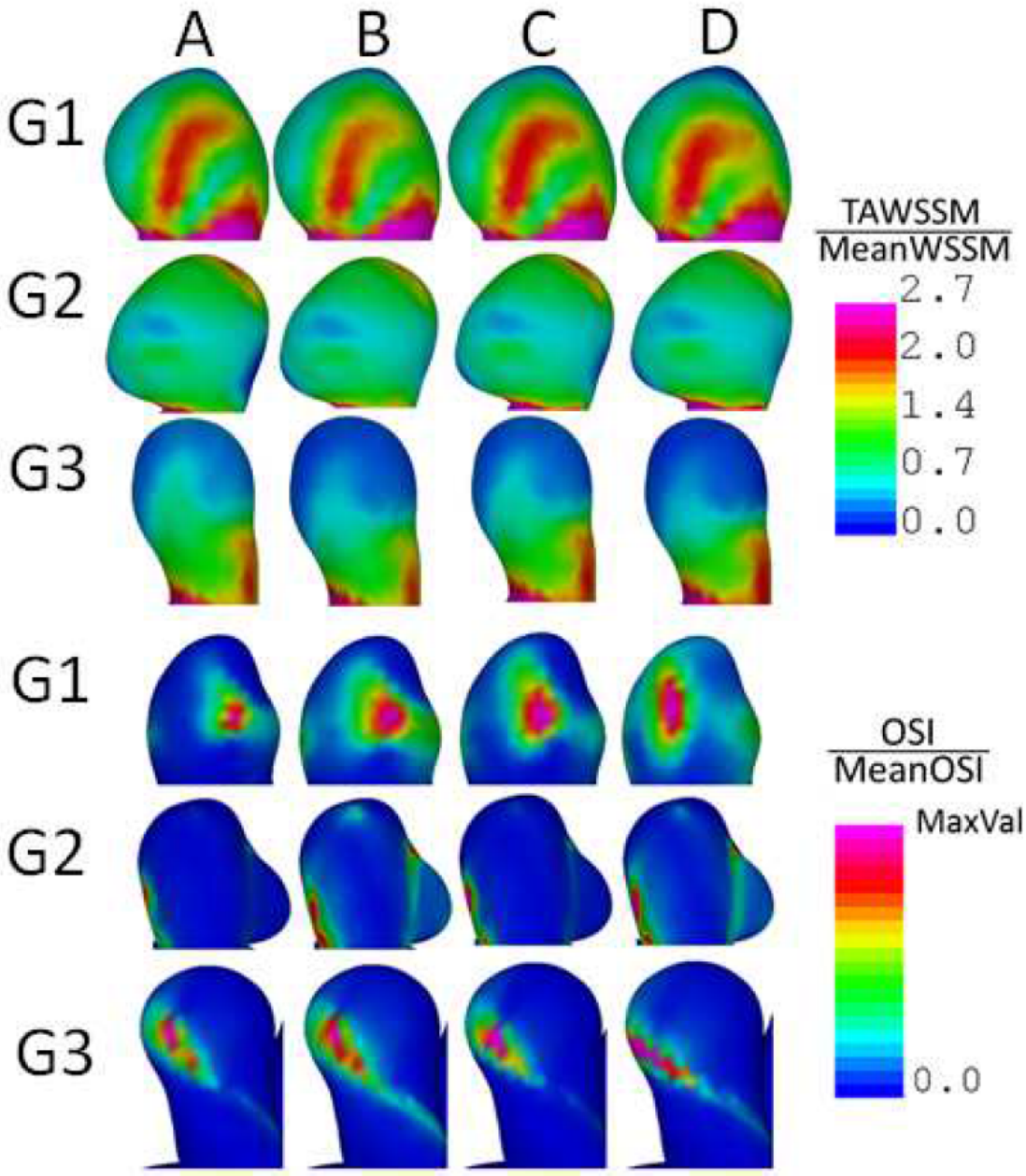

Figure 3.8: A. Both the qualitative and qualitative aspects of WSS are minimally impacted by the choice of waveforms A - D when normalized by the sac-averaged value. B. OSI normalization by sac-averaged OSI preserves the regions of elevated OSI. The maximum OSI values (shown as MaxVal) for the cases shown range from five to 18 times the sac average.

In doing so, we have furthermore identified waveform parameters responsible for influencing intra-aneurysmal hemodynamics in a manner that can be represented by polynomial functions. Collectively, this work provides a means to identify for future studies which hemodynamic metrics are robust enough for use in the absence of patient specific waveforms and how to address the sensitivity of metrics which are strongly impacted by waveform.

3.4.1 Ranking Sensitivity and Waveform-Hemodynamic Characteristic Curves

In other IA studies, quantitative flow information has been correlated to aneurysm pathology and rupture status. For example, global hemodynamic features like ICI and PODENT have been associated with increased wall stiffness [26], and degenerated walls with loss of mural cells [21], while studies such as [19, 32, 39, 31] have associated quantitative hemodynamic metrics (e.g., WSS, PODENT, SCI) with aneurysm rupture status. Relevant to these studies, the current study ranks the variability of several quantitative hemodynamic parameters. For example, Table 3.6 data suggests that the absence of waveform data in large data correlations utilizing ICI would not likely be a confounding factor within such a study, while metrics such as PODENT may require extra attention to attain similar certainty. For the latter instance, the current study demonstrated that intra-saccular hemodynamic quantities are influenced by waveforms parameters which can often be characterized in a manner (similar to work by Morales [136] that is well described by simple polynomials. Such relationships have been previously introduced by Xiang et al. [207], who demonstrated the possibility of MaxOSI prediction via linear relationship with pulsatility index. This encouraging ability is highly useful when addressing the waveform uncertainties in large data correlation studies. In this process, an appropriate sample space of waveforms must first be determined. Rather than selecting or perturbing waveforms randomly, one can select waveforms parametriclly (e.g., by V^* , T^* , PI, etc.). The parameters chosen should show that the selected waveform parameter(s) predominately control the underlying physics of the flow, and should span their expected physiological range (for example, as reported in [54]. An appropriate choice of waveform parameters should form relationships such as those shown in Figures 3.4 - 3.7. For example, the MaxOSI in G1 varies dramatically over

a comparitively small range of $Q_pPI^{0.5}$ as compared to G2 (Figure 3.6); one could therefore can be reasonably confident in the MaxOSI for G2 but not for G1. One can furthermore determine whether the hemodynamics between geometries are statistically distinguishable. For example, (referencing Figures 3.7B) two-sample Kolmogorov-Smirnov tests reveal that the PODENTs of G1 and G2 are indistinguishable (p = 0.23) when considering the potential variability in waveform; however, the PODENTs of G2 and G3 as well as G1 and G3 are indeed distinguishable from one another regardless of waveform choice (p = 1.1e-12 and 1.5e-13 respectfully). As another example, by simply considering the characteristic curves in Figure 3.4, it is inconceivable that the choice of waveform could be a confounding factor in distinguishing ICI between G1 and G2 (see Figure 3.4). These methods can be applied, for example, to large groups of aneurysms stratified between ruptured an unruptured to determine whether statistical differences exist between hemodynamic metrics while accounting for the potential impacts of unknown waveforms. Additionally, the characteristic curves of Figures 3.5-3.7 demonstrate an appreciable contribution from the waveform to the hemodynamic metrics relative to aneurysmal geometry (e.g., Figure 3.6, G1 MaxOSI). Since many of the hemodynamic metrics considered here have previously been implicated as detrimental to cerebral aneurysms (i.e., high or low values), knowledge of the waveform may itself may provide relevant clinical risk-factors for cerebral aneurysm patients.

3.4.2 Selection of appropriate regression models

The parameter $Q_pPI^{0.5}$ was the first choice for use in both our regression models and for selecting representative cases in Figure 3.2 for physical reasons. In our previous work [54], we evaluated the ability of a simple square wave model (see Figure 2 in [54]), having a manageable number of parameters, to approximate the flow rate of a given waveform through a given cross-sectional area. The ensemble fit for this model is given by Equation 3.2. As seen by Equations 3.1 and 3.3, the shape parameters of Equation 3.2 can be combined to approximate PI, making PI a natural choice to use as a model-fitting parameter for relating the waveform to hemodynamics. To aid in the design of the current study, numerical studies involving parametric manipulations of the square wave were implemented as inflow bound-

ary conditions in a simple bifurcation geometry were first conducted. These pilot studies resulted in near- noiseless, smooth characteristic curves relating $Q_pPI^{0.5}$ to Q_{an}, as well as $Q_pPI^{0.5}$ to WSS, highlighting the physical impact of systolic duration and difference in systolic-to-diastolic velocity on hydrodynamics in general. Of course, the square wave is a simplification of a physiological waveform, and therefore $Q_pPI^{0.5}$ should not be expected to be the best choice of fit in all instances for hemodynamic metrics (though despite this, it is remarkable that $Q_pPI^{0.5}$ or any of PI's components are still usable in such analysis). Indeed, regression models chosen, such as CORELEN for G3 (see Figure 3.7A), if fit to a second order polynomial in $Q_pPI^{0.5}$, produces an unfruitful r^2 value of 0.0107. In general though, $Q_pPI^{0.5}$ serves at least as a starting point of isolating and capturing the intra-saccular flow physics influenced by the waveform with respect to a single input parameter based on the approximations undertaken in Equations 3.2, 3.3. In practice, as the results have demonstrated, the characteristic curves relating waveform and hemodynamics are generally applicable only on a per- aneurysm basis and therefore must always be obtained for each geometry within a study. In this manner, the patient-specific range in quantitative hemodynamic uncertainty can be estimated. Further uncertainty quantification may be accomplished through information regarding the distribution of waveform parameters within the population (see, for example, our previous work on this subject [54]. While we have not particularly considered the distributions of our input parameter sample space for the cases displayed in this work, we have considered the full range of parameters, for the purpose of demonstrating the physics of the hydrodynamic system under consideration. To this end, it is furthermore reassuring that reasonable r^2 coefficients to regression models can be obtained even when applying more weight to the less-frequently occurring outliers in the input parameter space.

3.4.3 Impact of Waveform on Flow and Wall Hemodynamic Patterns

Perhaps the most reassuring result obtained from this study is Selection of waveforms based on parameterization of the kind demonstrated (as opposed to random perturbations of a representative waveform) increases the physical relevance of the input parameters to the study. For a nonlinear problem of this type, it is particularly important to explore the impact

of the full range of input parameters. This is evident, for example, in Section 3.3.3 where it is clear that the variation to input parameter is highly nonlinear. The impact of waveform on qualitative features of the flow in cerebral aneurysms had also been previously considered. For example, consistency of flow structure across a $\pm 25\%$ variation in flow rate was reported by Cebral et al. [24]. Qualitatively, these results graphically summarized in Figure 3.3 are in general agreement with the qualitative similarities in the WSS and OSI contours of Figures 3 and 5 in Xiang et al. [207]. Furthermore, we add to these contributions in that the current study considered a comparatively sizable 32 waveforms per geometry selected from a recently-published data- base such that the magnitude and shape parameters span a range reported for an aged population with cardiovascular disease. This population has been shown to have a much greater waveform variability compared with young healthy subjects [54] and would therefore generate a more exhaustive pool of waveform variability.

To a similar end, the current study demonstrated that qualitative information on the wall can be well approximated by a steady-state simulation rather than the considerably more costly transient simulation. For example, this is true of WSS, as shown quantitatively in Table 3.6 and qualitatively in Figure 3.7A. These results are in good agreement with [207] and [62], which similarly found WSS to be accurately approximated by a steady flow. This is useful for studies involving a large number of cases when particularly qualitative information is sought.

The current study therefore supports the notion that even under a wide range of waveforms relevant to an aged cardiovascular patient population having less than 40% ICA stenosis, the qualitative distribution of some of the commonly used hemodynamic quantities are effectively insensitive to the choice of waveform, provided appropriate protocol to address the potential mild shifting of qualitative distribution as per Table 3.5 is adhered to.

In a similar manner, albeit toward a somewhat different aim, Jansen et al. [90] compared the intra- aneurysmal hemodynamics of patient specific flow boundary conditions versus generalized boundary conditions (i.e., comparing the impact of waveform shape on hemodynamics), and had found that quantitatively (as opposed to qualitatively), waveform shape significantly impacts IA maximum and mean WSS. Our study did identify, however, parameters which are much less impacted by waveform, such as ICI for example, with an

overall CV of less than 5%. It may be reasonable to assume that the conclusions of hemodynamic studies involving these parameters would not be confounded by the choice of waveform in the models.

Our approach in selecting the waveform variation is somewhat a contrasting approach to that of Sarrami-Foroushani et al. [166], where the inlet waveform variation was selected based on a statistical model of intra-patient waveform variability versus our extra-patient variability approach. For the purposes of this study, we believe an extra-patient approach was more justified in that the aims of the current study addressed the assumption that the unknown waveform may be of any kind belonging to the general population rather than some perturbation of a waveform about which is known a priori. The intra-patient variation of the waveform (e.g., sleeping versus walking) however is still an important topic of consideration in that the hemodynamic state of a patient's aneurysm is accounted for during the full range of the patient's lifestyle habits.

3.4.4 Limitations

The current study has several limitations. The blood is modeled as a single phase Newtonian fluid and wall motion is neglected. These choices are based on the size of the blood vessels under consideration [163] and the fact that cerebral aneurysms have reduced elastic toe regions, due to the loss of elastin, in the loading curve, resulting in very little wall motion under the pressure variation of a typical cardiac cycle [162]. Only three aneurysm geometries have been considered here, although as noted above, these choices were made in effort to span a reasonable range of ICA bifurcation aneurysm geometries. As with previous work [54], the conversion of doppler ultra-sound waveforms to volumetric flow rate waveforms was accomplished by simple Poiseuille scaling of the peak-velocity data. Such assumptions could have the effect of underestimating flow rate waveform [143]. While it is most probable that as a result, quantitative values within the present study may be impacted. However, it is most likely that, as demonstrated earlier, that the locations of maximum and minimum values as well as the manner in which quantitative values are dependent on waveform parameters (e.g., Figures 3.4-3.7) would not be impacted by this error in measurement. It is furthermore

important to place the scope of the current study into the broader context of hemodynamic sensitivity. The current work establishes that it is possible to characterize the response of hemodynamic metrics to individual waveform parameters. The current study does not directly address evaluating the probability of a particular hemodynamic state within the IA under an unknown waveform, nor does it address the impact of different flow splits at the bifurcation. The current study however, in conjunction with our previous work [54], could be extended to address both of these issues. For example, if a desired output were the range in WSS corresponding to $\pm$1SD of Q_p , then the regression model for WSS in Figure 3.5 could be employed to adjust the expected range in WSS accordingly. If the impact of flow split were to be considered, relationships that were established for G1-G3 would need re-established for a different flow split. The impact on hemodynamics from flow split has been previously studied by [199] and [24]. In the former, qualitative distributions of WSS seem to change minimally (Figures 3.3 and 3.8) although there is appreciable differences in quantitative information.

3.5 Conclusions

In this work, we addressed the important question regarding the extent to which patient-specific hemodynamic studies can be meaningfully conducted in the absence of patient-specific waveforms. Location of extremum in hemodynamic parameters such as WSS and OSI were found to be fairly insensitive to flow rate and waveform shape, implying that it is still possible to correlate local qualitative hemodynamic information to aneurysm wall pathology in the absence of patient specific waveforms. Further, the quantitative value of parameters which are normalized by intrasaccular values are also relatively insensitive to waveform. By contrast however, discrete values of non-averaged, non-normalized hemodynamic metrics do not display the same degree of insensitivity to the waveform, and in the absence of patient-specific flow information, require further attention. To this end, we have shown that it is possible to meaningfully characterize the impact of waveform variation on hemodynamics using simple functions. Such information can then be used to determine whether the use of

a surrogate waveform has the strong potential to modify a study's conclusion. Such findings are important for designing studies and interpreting results from investigations of the role of flow in cerebral aneurysms.

4.0 An Investigation into Quantifying the Relationships between Aneurysmal Geometry and Hemodynamic Metrics towards Improving Risk Assessment

Like with the previous chapter, the author at this point wishes to express gratitude to Dr. Juan Cebral as well as Dr. Bongjae Chung and Dr. Fernando Mut from the Cebral lab group for their advisement, support, and guidence with the use of their in-house solver FeFlow and corresponding post-processing software utilized in this chapter.

SUMMARY - The pathological flow-structures within intra-cranial aneurysms (IAs) can have a simple to highly-complex nature, dependent on both the aneurysm and parent-vessel geometries. These flow structures not only are time-dependent at the timescale of the cardiac cycle, but also at the aneurysmal growth/remodeling timescale through which often little clinical information is available. The current study utilizes a parametric computational fluid dynamics (CFD) approach to systematically unravel the relationship between multiple IA flow structures and geometry metrics. Four non-dimensional aneurysmal geometric parameters of a bifurcation aneurysm were systematically varied (both individually and simultaneously) to produce a vast family of geometries for CFD analysis while maintaining constant parent vasculature. Relationships between geometry and the number of vorticies, inflow-jet impact-zone, and quantitative flow metrics such as vortex coreline length were obtained. Three of the four geometric parameters were found to influence the number of vorticies present, and all parameters were found to have substantial impact on the location and strength of inflow-jet impact zone and location. Particularly interesting is that the maximum POD entropy in the flow field was found to be attained in cases possessing aneurysm geometries facilitating flow in the transition regime between one and two intrasaccular vorticies. The results presented here provide a means of obtaining a quick estimation of intra-aneurysmal flow structure from clinical imaging, and can also serve as a means of understanding the influence of flow on aneurysmal growth and development by providing estimates on likely past-configurations of the flow structures and hemodynamic fields. The methodology used in work, guided by the results, can also be used as a tool for designing animal models of aneurysms in order to achieve a desired wall shear stress pattern.

4.1 Introduction

The exact role of hemodynamics in cerebral aneurysms remains an open question. Hemodynamic stresses, particularly wall shear stress, are thought to be partially responsible for the growth, progression, and rupture of IAs [128, 14, 130]. Wall shear stress (WSS) experienced by the lumenal wall of the aneurysm, by its own definition, is in part determined by the intra-saccular flow structure. Flow-structures within intra-cranial aneurysms range from being simple to highly complex; possessing anywhere between one single stable vortex, to multiple transient vortices. These flow-structures, being deviant from the Womersley flow of healthy arteries, are responsible for pathological hemodynamic stresses within the sac.

The clinical significance of the number of IA vortices was first proposed by Ujiie et al [192]. Aneurysms possessing a height to neck diameter ratio, or aspect ratio (AR), greater than 1.6, were found to harbor a slow-moving secondary driven vortex that induces hemodynamic conditions thought to facilitate wall inflammation. While some clinicial studies have identified a positive correlation between AR and rupture [191, 165, 144, 82], other studies have not found such an association [10, 204]. Furthermore, the AR threshold values used to distinguish ruptured from unruptured aneurysms is inconsistent [55], presenting the question as to whether AR is a sufficient predictor of multiple vorticies; or furthermore, whether multiple vortices are a sufficient description of "safe" versus deleterious flows.

Cebral et al. further classified IA flow-structure by both the number and transient nature of vortices, as well as the diffuse versus narrow structure of the inflow jet. Such considerations found that ruptured IAs were more likely to contain flows characterized by multiple, transient vorticies and narrow, high-speed inflow-jets than unruptured aneurysms [23]. Moving from this more qualitative description of IA flow structure, metrics used to quantitatively describe the IA flow such as vortex core line length (CORLEN) and proper orthogonal decomposition entropy (PODENT)[19], mean viscous dissipation ratio (VD)[32], and energy loss (EL) [156] were introduced in part to distinguish the flow structures of ruptured from unruptured IAs. Collectively, the studies found that longer vortex core-lines, higher POD entropy, lower viscous dissipation, and higher EL are associated with IA rupture. While these metrics are far less subjective to the definitions of classification as with the number and type of

vorticies, these metrics do not directly characterize the volumetric flow at the scale of its localized influences on the IA lumen. Rather, these metrics are descriptors of the flow on the global (saccular) scale.

The impact of IA flow structure on aneurysm pathology has also been demonstrated in studies associating flow-structure characteristics with the intraoperative appearance of IAs [190, 60, 61, 184]. For example, Tobe's [190] findings suggest that wall thinning is a result of inflow-jet impact, while thickened atherosclerotic-like walls are a result of slow-moving flow.

Though much evidence suggests IA flow-structure (in part) drives IA pathology, studying and clearly identifying the role of hemodynamics on IA development remains challenging. IAs are located within the brain, which limits their accessibility for in-vivo research due to the inherent risks involved with invasive procedures within the brain. Furthermore, the pathology of IAs is highly transient in nature. IA geometry evolves over the lifetime of the aneurysm. Due to the dependence of flow-structure on geometry, a substantial change in sac geometry can alter the flow-structure. It is therefore conceivable that a particular flow feature responsible for inducing a change in wall morphology/content may substantially alter itself in a transient feed-back cycle, creating challenges in establishing a causative relationship between hemodynamics and the state of the aneurysm wall. In this work, computational fluid dynamics (CFD) was used to parametrically study and map the impact of five geometric parameters on intra-aneurysmal flow structure; including the number of vorticies and the jet impact zone. The current work is a continuation of previous work by the author [53], in which it was demonstrated that the number of vorticies present within the sac cannot in general be adequately predicted by a single parameter, but in fact, depends on multiple geometric parameters, thus providing more robustness and generalization to the aforementioned work on AR by Ujiie et al. [192]. The current work, utilizing higher-fidelity methods, refines this relationship. This work furthermore maps the manner in which the jet impact location the wall can be moved by changes in geometry, and demonstrates that the jet impact on the wall can be enhanced or diminished throughout saccular remodeling. Furthermore, this work quantifies the relationship between sac geometry and quantitative flow metrics associated with rupture status [32, 19], aneurysm stability/growth [172], and wall inflammation [21]. In addition to obtaining a physical understanding into the nature of

saccular flow for studies of human aneurysms, this work provides design information for the production of surgically-created animal aneurysm models (for example, see [41, 101, 218]), so that the aneurysm may be created to achieve a desired flow field for study. Such animal models are advantageous in that they offer the ability to collect and analyze aneurysmal tissue exposed only to a particular flow, and thus can serve as a snapshot in time of the transient sac growth process.

4.2 Methods

4.2.1 Geometry Creation

The geometry of a single-lobed saccular aneurysm located at the tip of the basilar bifurcation was selected for use in the parametric flow study. The development of the utilized technique was, to the author's knowledge, first pioneered by Zakaria et al. [214] for application to arterial bifurcations, and later extended towards cerebral aneurysms (both sidewall and bifurcation) by Zeng [218]. Briefly, the 3DSA data of the original lumen, M0, was first converted to a steriolithography (STL) format using the commercial software package Mimics 13.0 (Mimics; Materalise, Brussels, Belgum). The STL M0 lumen data was then converted to a parametric-based CAD model constructed in the CAD software Pro/ENGINEER (PTC., Needham, MA, USA) such that the surface could be parameterized via a lumen centerline, and several best-fit cross-sectional lumenal diameters normal to the centerline. The resulting cross-sections were then blended via a sweep function to form the lumen surface. This resulting model, M0p, could then be generated via parameter input to a CAD package, thus allowing the systematic manipulation of the M0p lumen.

4.2.2 Selection of Geometric Parameters

Five geometric parameters on IA flow were considered in this study, demonstrated in Figure 4.1. The aneurysmal lumen geometric parameter set consisted of aneurysm height (H), maximum width (W), neck diameter (N), and height from the neck to the location of

maximum width (S). Additionally considered was the parent artery diameter (P), defined at the location in the Basilar artery immediately upstream of the bifurcation. To fulfill the study objectives, the aneurysmal parameters were varied (both singly and simultaneously for separate phases of the study), while P was held fixed for all models. To keep the current study consistent with previous work, the five dimensional parameters H,W,N,S,and P were combine in ways to form non-dimensional parameters H/N (aspect ratio, AR [192]), W/N (bottle-neck factor), BF [82], S/H (conicity parameter, CP, (also bulge location) [82], and P/N (PN, aneruysm to parent artery ratio [82]), which served to relate the lengthscales of the aneurysm with its parent vasculature. These parameters are identified in Figure 4.1 and the impact of their variation on sac geometry is shown in Figure 4.2.

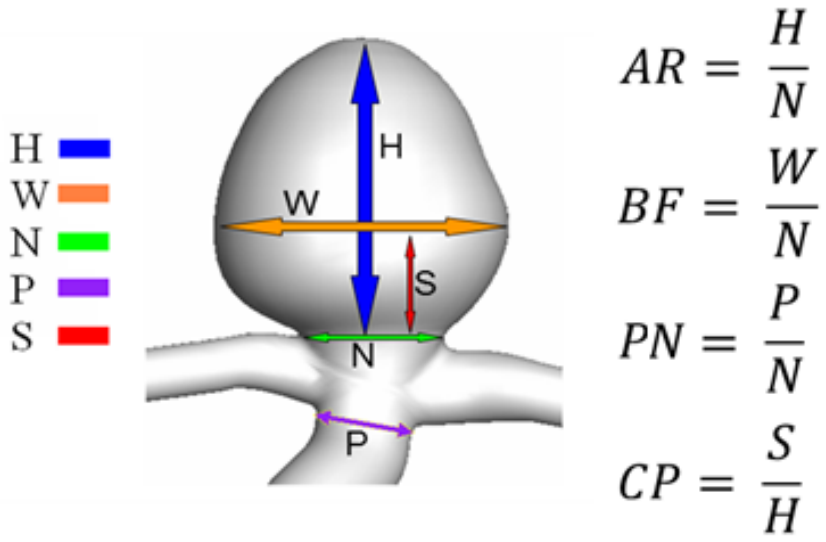

Figure 4.1: Definition of non-dimensional geometric parameters; each corresponding to one of the four sets of models which varied only one of these parameters throughout the models within each parameter's respective set.

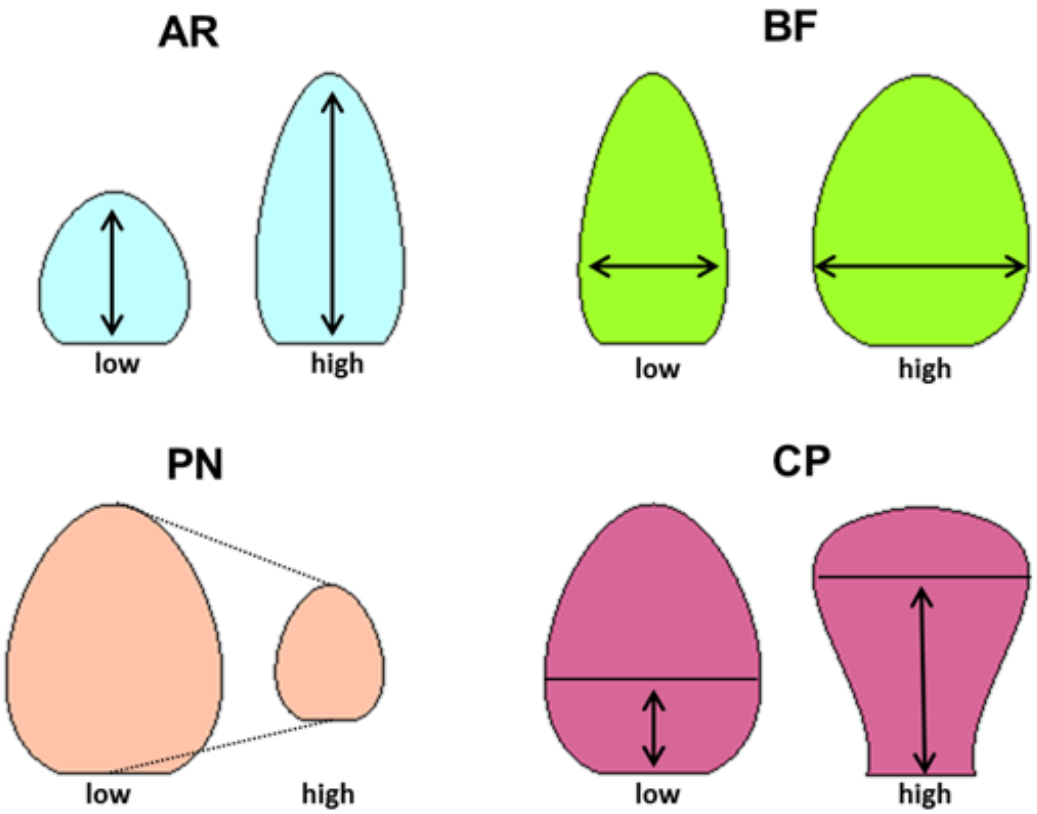

Figure 4.2: Demonstration of impact on aneurysm geometry from varying each of the four non-dimensional parameters.

4.2.3 Variation of Geometric Parameters

The impact of the four non-dimensional parameters AR, BF, CP, and PN on IA flow-structure was studied in two phases: 1.) varying each parameter independently, and 2.) varying the parameters simultaneously. For the first phase, four sets of parametric models were produced; each set varied one of the four nondimensional parameters. The ranges and number of models of each set needed to be determined iteratively based on each set's ability to capture changes in IA flow-structure within physiologically relevant geometries [217], and thus could not be decided a priori. In addition to considering the calculated flow structure, quantitative hemodynamic metrics Table 4.1 for each model were calculated to observe the relationship between each geometric parameter and each hemodynamic metric. For the second phase, combinations of AR, BF, CP, and PN were created to identify critical combinations of the parameters for which the flow structure transitioned from containing one vortex to two vortices.

4.2.4 Quantification of Impact Jet Type and Influence

In this work, we utilized a unique methodology to analyze the physical nature of the intra-saccular inflow jet with the creation of a parameter jet influence factor (JIF). This parameter is intended to quantify the action of the inflow jet with respect to the wall. JIF is broken into a normal and tangent component (JIFN and JIFT respectfully). This purpose is to distinguish whether the inflow jet is acting more normal or tangent to the wall at a particular location. Furthermore, a magnitude is assigned to these metrics. JIFN is calculated by projecting the systolic velocity vector onto vectors normal to the wall at all locations. The gradients along these wall-normal vectors are then evaluated only along the direction of the wall normal-vectors. The maximum absolute value is then identified along with its normal distance from the wall. JIFN is then the maximum absolute value of the velocity gradient along the wall-normal vector divided by the normal distance from the wall. The maximum JIFN value on the wall is the location where the velocity vector is most normal to the wall in a near-wall proximity, causing flow impingement previously conjectured to be detrimental to the wall (for example by Cebral et al. [23]). JIFT, conversely, populates

the wall-normal vectors with the magnitudes of the maximum velocity component tangential to the origin of the wall-normal vector on the wall. The magnitudes of gradients of these velocities along the wall-normal vector are, like with JIFN, divided by their distance to the wall. The location on the wall where JIFT is maximum corresponds to the location nearest to the most concentrated inflow jet that is shearing (rather than impinging) against the wall. JIFN and JIFT can be used to quantitatively distinguish the influence of inflow jets which impinge on the wall versus those that shear against the wall.

Table 4.1: Definitions of hemodynamic parameters. Note: WSS = time averaged wall shear stress magnitude.

Parameters quantifying flow at lumen surface	
WSSMax	Maximum WSS in aneurysm
WSS	Temporally and spatially averaged WSS in aneurysm
WSS	Minimum wall WSS in aneurysm
OSIMax	Maximum OSI in aneurysm
OSI	Spatially averaged OSI in aneurysm
SCI	Shear concentration index [32]
LSA	Low shear area [32]
Parameters quantifying bulk flow	
CORELEN	Aneurysm vortex core line length [19]
PODENT	Proper orthogonal decomposition entropy in aneurysm [19]
Q_{an}	Time-averaged aneurysm inflow rate
ICI	Inflow concentration index [32]
VMax	Maximum velocity in aneurysm
VMaxMean	Time-averaged maximum velocity in aneurysm
KER	Kinetic energy ratio [172]
SRR	Shear rate ratio [172]
VER	Velocity ratio [172]
VOR	Vorticity ratio [172]
VDR	Viscous dissipation ratio [172]

4.2.5 Computational Study Methodology

Numerical simulations of rigid-wall pulsatile Newtonian blood flow governed by the unsteady 3D Navier-Stokes equations were conducted for every parametric variant of the M0p. The parent artery flow conditions were identical in each model: the parent artery geometry was kept identical as well as the time-averaged flow rate of 1.81 cm^3. The Womersley profile was applied normal to the model outlets such that the time-averaged wall shear stress magnitude was 15 dyn/cm^2. The peak velocity waveform shape was assigned as reported in [197] for the basilar artery. Each simulation consisted of two cardiac cycles of 0.857 second periods discretized by 100 timesteps. The simulations were conducted on unstructured tetrahedral finite elements with a near- uniform grid resolution of approximately 0.1 mm. The the finite element models were solved using the finite element solver described in [24].

4.3 Results

4.3.1 Single Parameter Studies

4.3.1.1 Flowstructure and Aspect Ratio (AR) Streamline plots colored by velocity magnitude at systole and diastole are presented in Figure 4.3. Here, variants of M0p are shown ranging from 1.1 to 2.3 (in increasing order from left to right), in increments of 0.1. Three distinct flow regimes were produced in this set. Below an AR of 1.4, there was one stationary vortex in the cases. At systole, a secondary flow-structure initiates at an AR of 1.4. At diastole, there is an AR-mediated flow-type transition regime between 1.4 and 1.7, in which the secondary vortex is transient. As AR is increased past 1.7, there were two stationary vortices observed in all cases. For all cases consistently or partially involving a secondary vortex, the primary vortex remained consistent in size and the remainder of the sac volume was occupied by the secondary vortex.

4.3.1.2 Flowstructure and Bottleneck Factor (BF) Streamline plots colored by velocity magnitude at systole and diastole are presented in Figure 4.4. Here,variants of

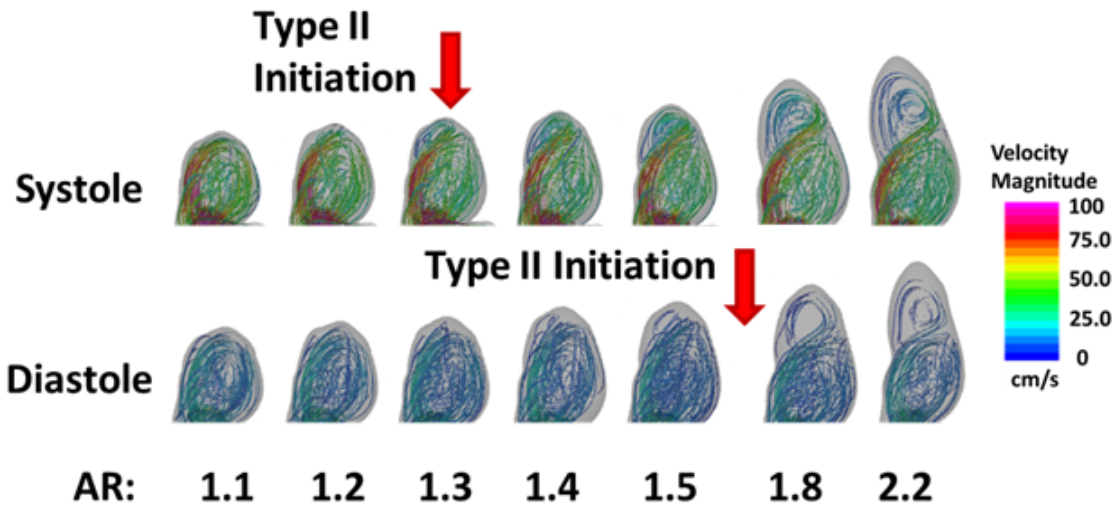

Figure 4.3: Transition between Type I flow (one vortex) and Type II flow (two vortices) for the AR group. Between AR 1.3 and 1.7 (not shown) there is a transitory flowtype between systole and diastole. In these cases, BF = 1.1, PN = 0.67 and CP = 0.33.

M0p are shown possessing an AR of 2.0, and BF ranging from 1.0 to 2.0 in increments of approximately 1/6. The selection of an AR of 2.0 for this group was particularly selected to demonstrate the finding that different flow structures are possible with a constant AR, even for the simple bifurcation geometry case as M0. The same distinct flowtypes that were found in the AR family were found in the BF family. For BF less than 1.5, two stationary vortices are present. At a BF of 1.5, the flowtype transitions from two stationary vortices to one stable and one transient vortex. The single-vortex flowtype is finally achieved for a BF of 1.85.

4.3.1.3 Flowstructure and Parent-Artery to Neck-Diameter Ratio (PN)

Streamline plots colored by velocity magnitude at systole and diastole are presented in Figure 4.5. Here,variants of M0p are shown possessing an AR of 1.0, and PN ranging from 0.33 to 2.0. An AR of 1.0 for this group was selected to demonstrate the finding that through the range of a 20-fold increase in sac volume that the flowtype remained unchanged

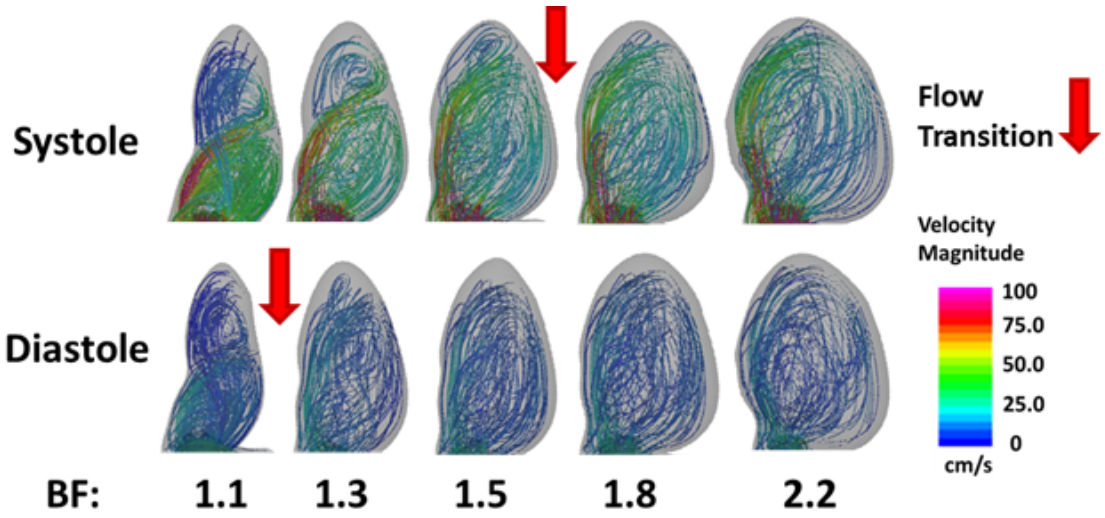

Figure 4.4: Transition between Type II flow (two vortices) and Type I flow (one vortex) for the BF group. Between BF 1.3 and 1.7 (not shown) there is a transitory flowtype between systole and diastole.In these cases, AR = 2.1, PN = 0.67 and CP = 0.33.

for PN less than 1.5. As the diameter of the parent artery approaches twice the diameter of the aneurysm neck however, a change in the flow structure begins to emerge. The single vortex increasingly recedes from the sac into the parent artery bifurcation, and a stationary secondary driven vortex begins to develop, as the inflow jet is redirected back into the parent artery. In general though, the PN set of models demonstrates that the flowstructure scales uniformly with a uniformly-increase scaling of the sac geometry.

4.3.1.4 Flowstructure and Conicity Parameter (CP) Streamline plots colored by velocity magnitude at systole and diastole are presented in Figure 4.6. Here, it is seen that except for the most extreme case of CP = 0.75, the Type I flow-structure remains unchanged.

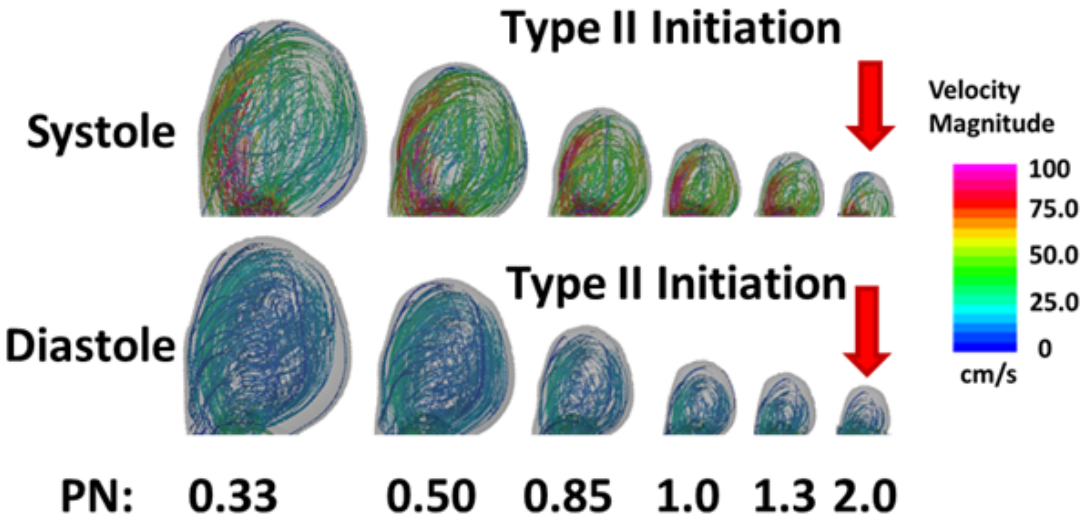

Figure 4.5: Flow-type is largely maintained with the scaling of the aneurysm with the parent vessel. In the smallest sac however (i.e., the largest parent-artery to neck-diameter ratio (PN) case),the circulation zone is seen to migrate into the parent vessel bifurcation, leaving volume for the development of the secondary vortex. In these cases, AR = 1.0, BF = 1.1, CP = 0.33.

4.3.2 Multi-Parameter Relationship to Determine Flow-Structure

The principles gained from the previous section on single-parameter manipulation of the sac are shown in Figure 4.7. The flow structure type is given in terms of aspect ratio (AR) as a function of bottle neck factor (BF) and parent aretery to neck diameter ratio (PN). As found in the previous section, changes in CP only alter the size and shape of the vortex/vortices present within the sac, and CP was thus omitted from this section, being held constant at 0.33. For the simple saccular bifurcation aneurysm case studied in this work, a critical AR can be given as a function of BF and PN which can be used to determine the number of stationary vortices within the sac. Each line in the figure represents the critical AR, (AR_c), as a function of BF at a constant PN value. If the sac AR is greater than the critical AR lying in the space above the appropriate line, then the sac is predicted to contain

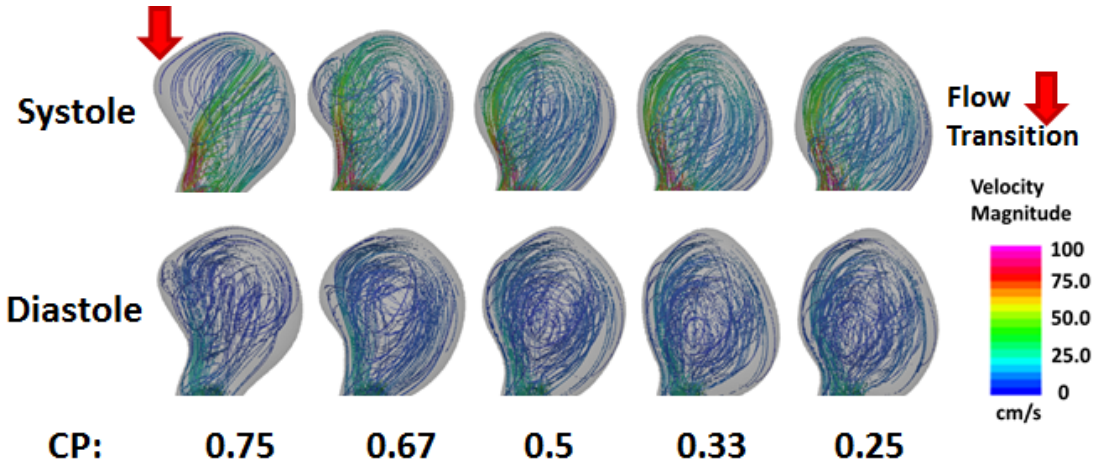

Figure 4.6: Flow-type is largely maintained with changing the location of the maximum sac diameter with respect to sac-centerline distance from the neck (i.e., CP). In the highest CP case however, the inflow jet migrates its impact location and the flow splits into two vortices. In these cases, AR = 2.3, BF = 2.2, PN = 0.67.

a secondary driven vortex; otherwise, the sac is predicted to contain a single stationary vortex. This can be generalized to fit the following regression model (Equation 4.1). The relationship is further plotted in Figure 4.7. Unilobular aneurysms at the tips of terminal bifurcations are therefor predicted to contain two vortices if their characteristic geometry parameters fall above their respective line given by Equation 4.1 and shown in Figure 4.7.

$$AR_c = 2.444BF - 0.2966PN^{-2.315} + 1.862 \tag{4.1}$$

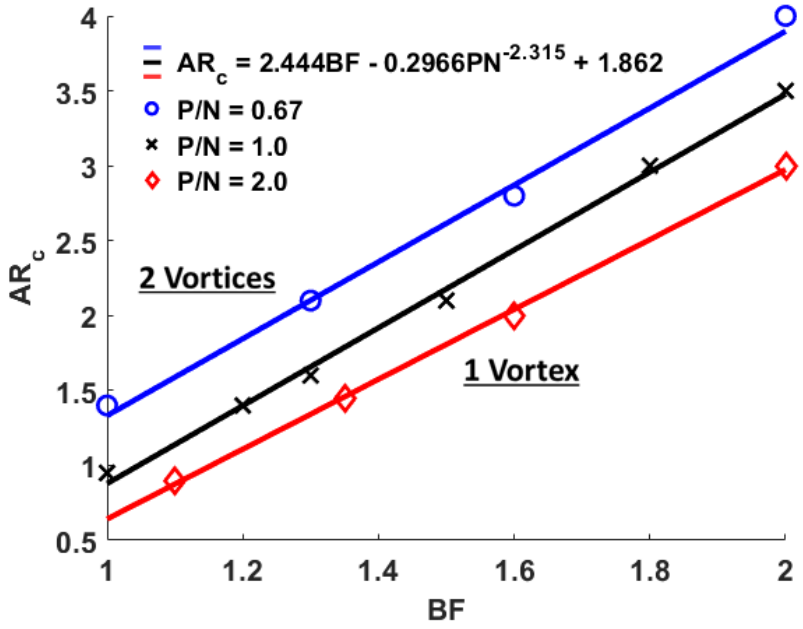

Figure 4.7: The critical aspect ratio AR_c is plotted for three values of PN. For a given PN, the space above the curve contains the pairs of AR and BF which produce a two-vortex flow structure; below the curve, contains the corresponding single-vortex space.

4.3.3 Relationships Between Quantitative Flow Metrics and Geometric Parameters

The proper orthogonal decomposition entropy (PODENT) is plotted for each of the parameters families Figure 4.8. Here, increasing PODENT manifests from two geometry-controlled situations. For the AR, and BF families, PODENT is seen to be be maximized in the transitional flowtype region: i.e., the flowtype when there are two intrasaccular vortices at systole and one intrasaccular vortex at diastole. The PN family gives insight into how PODENT increases with PN, i.e., as the aneurysm is scaled larger with respect to the parent vessel, PODENT increases. For the CP family, which did not undergo a flowtype transition (i.e., all cases possessed one vortex) except for the extreme case of CP = 0.75, PODENT remained fairly unaffected, although PODENT increased by a factor of two near this extreme

case approaching the upper morphological limit. In the case that a secondary vortex was present in a high CP case of 0.75 via the introduction of a larger distal lobe, the PODENT is seen to more than double as the inflow jet moved impingment locations and split into a second vortex.

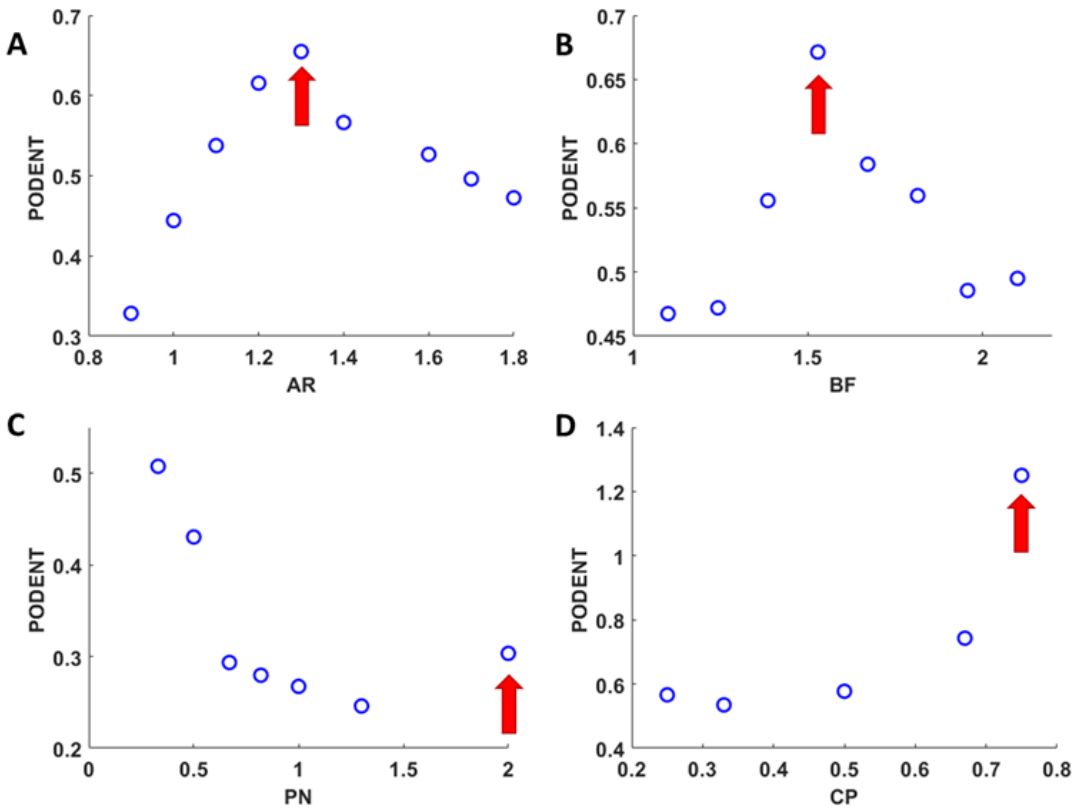

Figure 4.8: A-D: In each parameter family, PODENT is maximized at the critical parameter value for which, at systole, the flow structure transitions from one to two vortices, and at diastole, there is one vortex. Red arrows indicate the location where the transition of flow-type occurs at systole.

Vortex coreline relationships with the geometric parameters (Figure 4.9) show that CORELEN is indicative of the sac size and flowtype. CORELEN has substantial dependence on the sac volume as evident with the PN family: as the aneurysm size is uniformly scaled upward, the vortex size, and thus coreline, increases. Furthermore, as the sac approaches the tendancy to possess the dual-vortex flowstructure, CORELEN becomes elevated, as evident by AR and BF families. A large value of CORELEN relative to a population of aneurysms could therefore describe a large sac-volume possessing a single vortex, a smaller sac-volume possessing a complicated flowstructure, or a combination of both thereof.

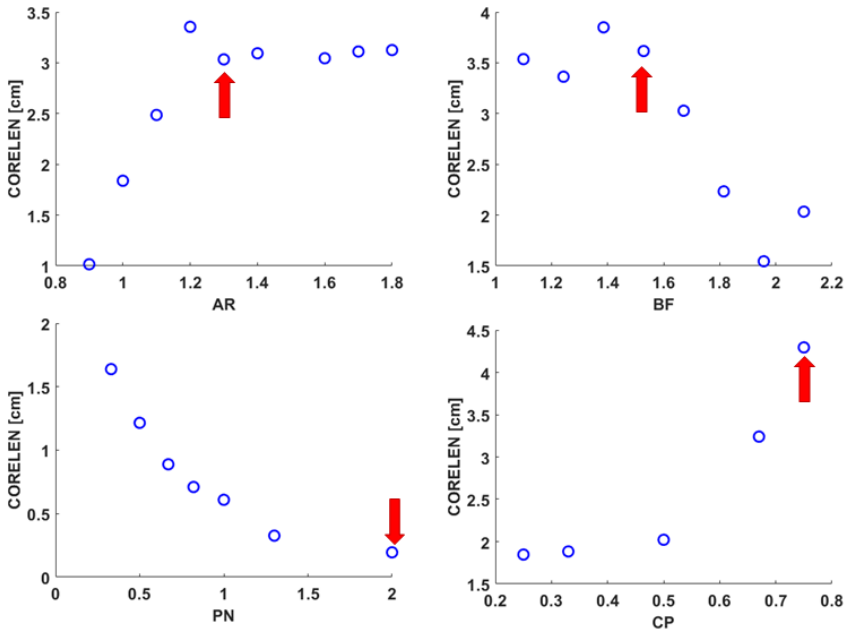

Figure 4.9: A,B: CORELEN is elevated in the Type-II vortex region. C: CORELEN increases with decreasing PN as the sac volume is increased, thus increasing the volume of the single vortex. D: CORELEN increases as the vortex shifts higher into the sac with increasing PN, and becomes maximum when the single vortex splits at CP = 0.75.

Plots of ICI as a function of AR, BF, PN, and CP are given in Figure 4.10. Collectively, these plots demonstrate that ICI is increased most notably by a larger neck area as evident by the PN relationship in the figure, in that ICI is doubled over the range of neck diameters from 1.6 mm to 9.5 mm. The shift in CP from its minimum to maxim value is the next largest contributor to changes in CP (approximately by a factor of 0.4. Changing flowtypes by increasing/decreasing AR or BF have a comparatively minimal impact on ICI.

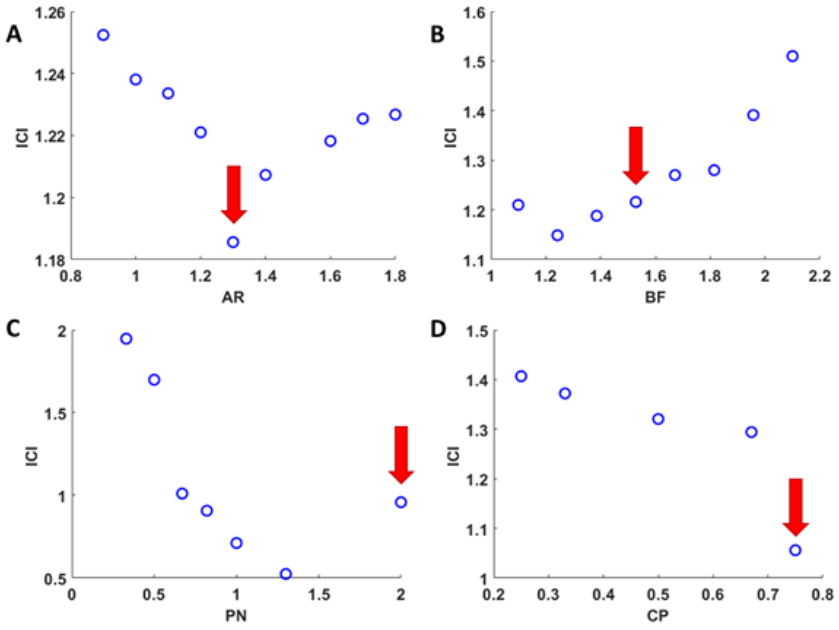

Figure 4.10: ICI is mainly influenced by a change in neck size with respect to the parent vessel, as the ICI varies most with PN (Panel C) as compared to AR, BF, and SH (Panels A,B,and D respectfully).

The mean OSI is given for all four groups in Figure 4.11. Relative to the ranges in OSIMean, the flow structure can be seen to maximize the mean OSI for three of the four families. In regards to the scaling of the aneurysm with respect to the parent vessel (i.e. PN), it is seen that a sac possessing a neck slightly larger than the parent vessel diameter is the factor tending to maximize the spatially- averaged OSI in the sac. Interestingly, this PN ratio corresponds to neither the PN ratio which maximizes the intra-aneurysmal flowrate as seen in Figure 4.14, nor the PN for which flow type transition is observed. Similarly, there is nothing striking regarding the flow-type transition in the AR family that increases or decreases flow into the sac, though the flow-transition zones seem to minimize the flowrate into the sac in the BF and CP groups. Unlike with OSIMean, there is a substantial decrease, by approximately a factor of 1.5, in the OSIMax for smallest aneurysms, seen in Figure 4.12. The maximum OSI, in the PN family, does indeed correspond to the case with the maximum intra aneurysmal flow rate. In regards to the other nondimesional sac paramters AR, BF, and CP, changing the aneurysm size with respect to the parent artery yields the most substantial change in OSIMax.

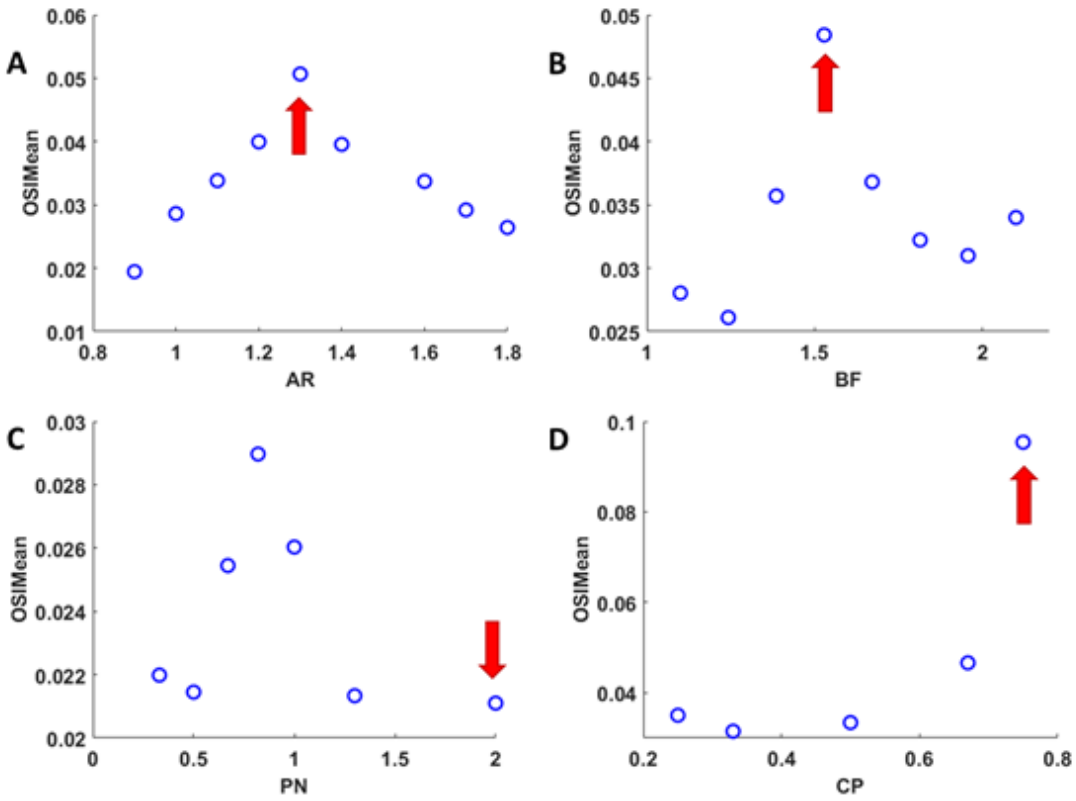

Figure 4.11: A,B,D: OSIMean is maximized by the systolic flow-structure transition AR, BF, and CP parameter. However, in regards to the sizing of the aneurysm relative to the parent geometry, OSImean is maximized by a PN of 0.875 rather than the PN of flow-transition.

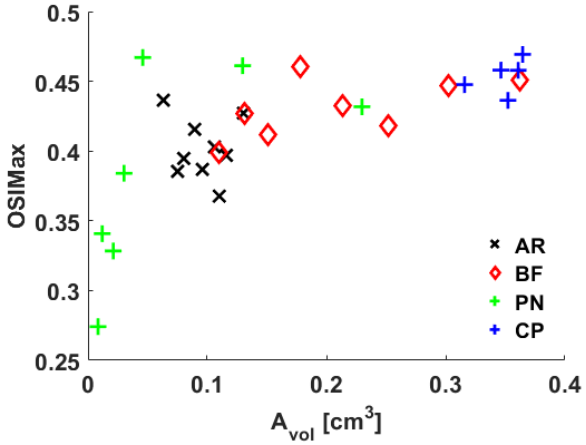

Figure 4.12: Unlike OSIMean, OSIMax follows no distinct trend for any of the parameter families, though there is a factor of approximately 1.5 decrease in OSIMax for the lowest sac volumes.

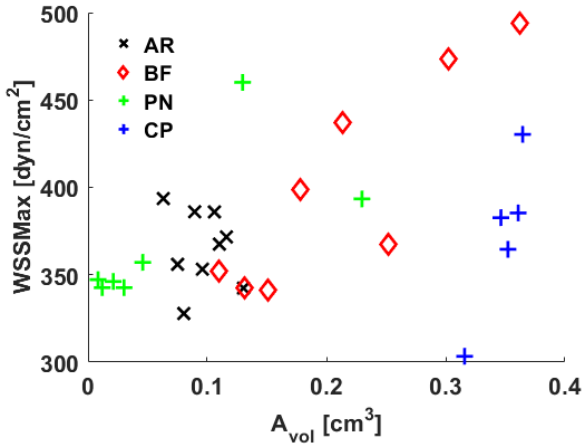

Figure 4.13: The maximum wall shear stress occurred at the location of jet impact in the neck region and roughly scales with aneurysm volume.

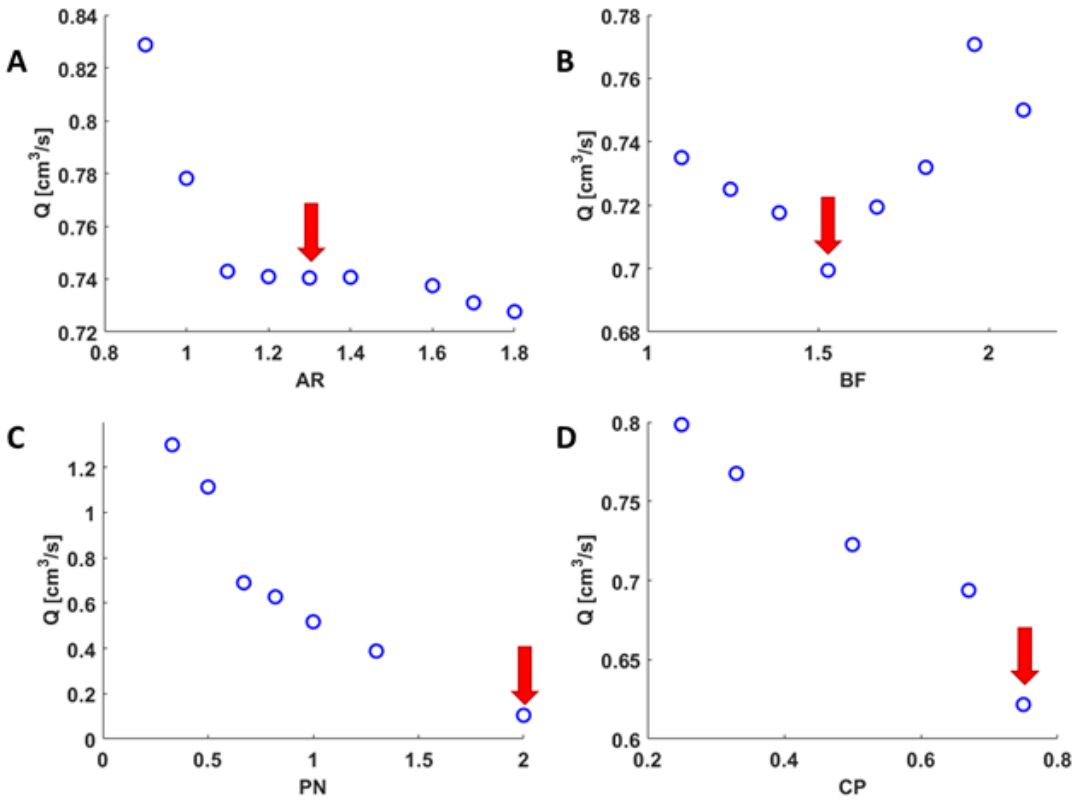

Figure 4.14: A-D: For the four parameter families AR, BF, PN, and CP, the size of the aneurysm, controled through PN, has the largest influence on intra-aneurysmal flow rate Q.

Plots of SCI, given in Figure 4.15, show that SCI is a unique parameter in which, for all four parameter families, can be approximated from the sac volume and the aspect ratio, by $SCI = 18.345 A_{vol} AR + 4.0, r^2 = 0.94$ This relationship implies that, per the definition of SCI, concentrations of high wall shear stress (high with respect to the sac) have a greater propensity to occur when the sac volume is larger and possessing a high aspect ratio giving way to slow-moving flows.

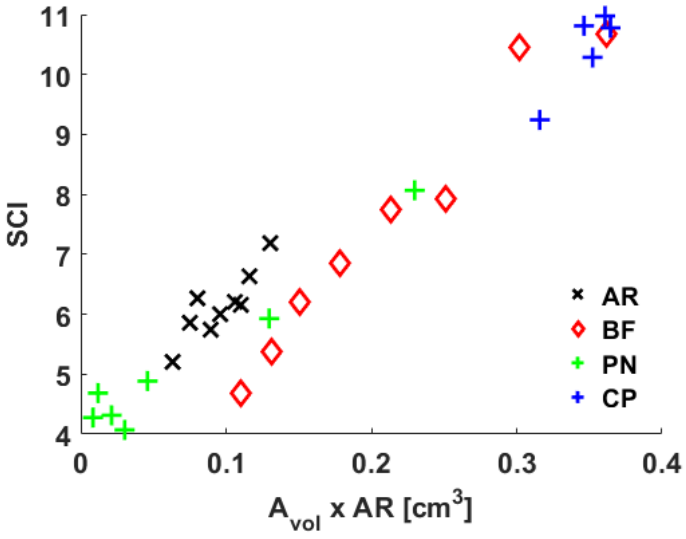

Figure 4.15: SCI roughly scales with sac volume times AR by $SCI = 18.345 A_{vol} AR + 4.0, r^2 = 0.94$

The intra-saccular flow metrics KE, SR, VD, VE, VO were all found to scale inversely with the aneurysm volume, independent of the parameter groups to which they belong. An exponential function of the form $C_1 e^{-C_2 A_{vol}}$ is capable of describing all of these relationships with a minimum r^2 value of 0.81 for the geometries in this study. These intra-saccular flow metrics were thus found to decay with sac volume per the fixed parent artery geometry and flow rate. The time and space averaged wall shear stress, WSS, was similarly found to decrease with aneurysm volume, except that a linear (versus exponential) fit was more suitable for this relationship ($r^2 = 0.82$ versus 0.74). However it is evident by Figure 4.17 that micro-trends exist among the AR, BF, PN, and CP families.

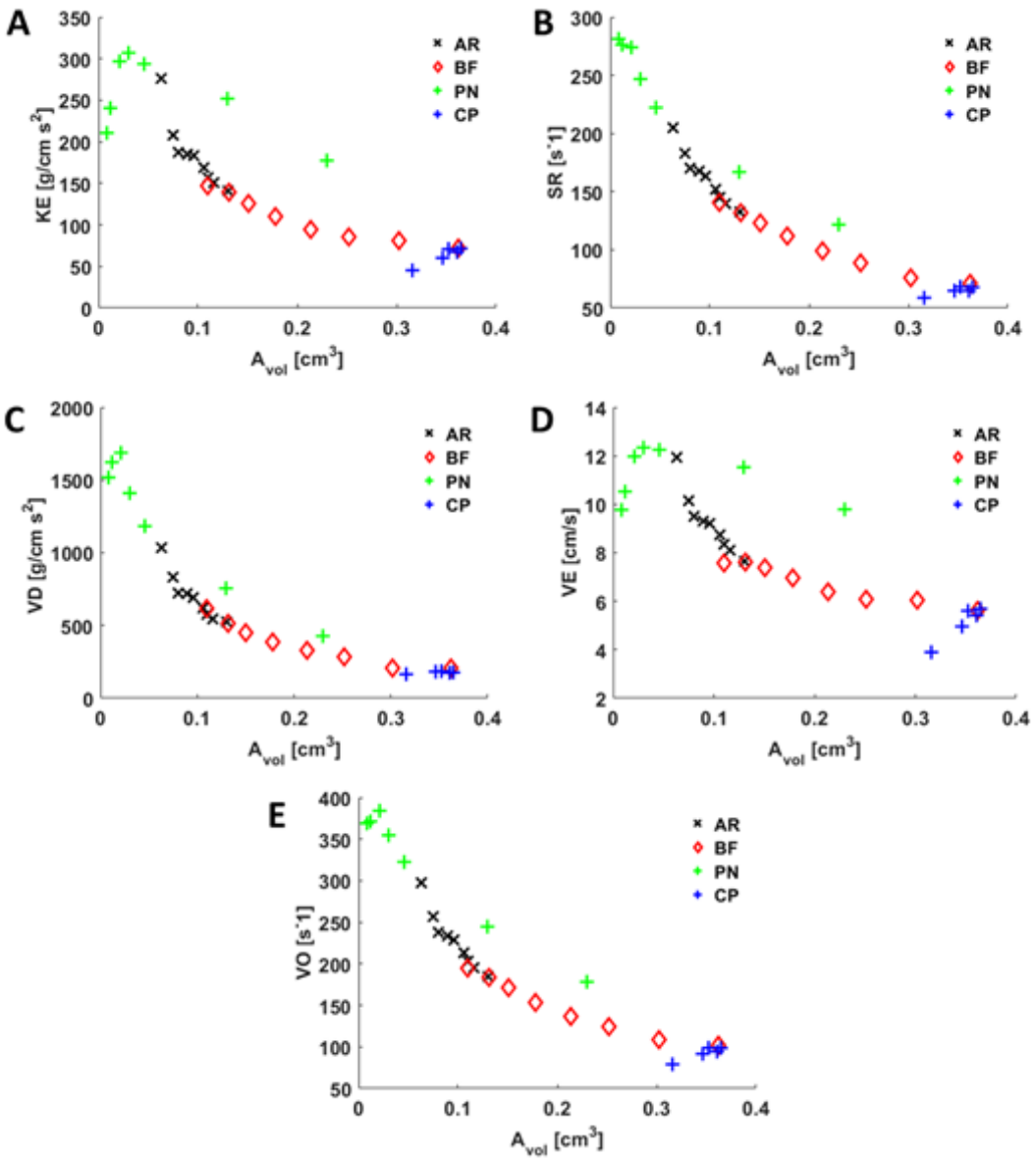

Figure 4.16: A-E: Intra-saccular bulk flow metrics KE, SR, VD, VE, and VO all generally increase conversely to aneurysm volume A_{vol}. CP however, can counteract this trend.

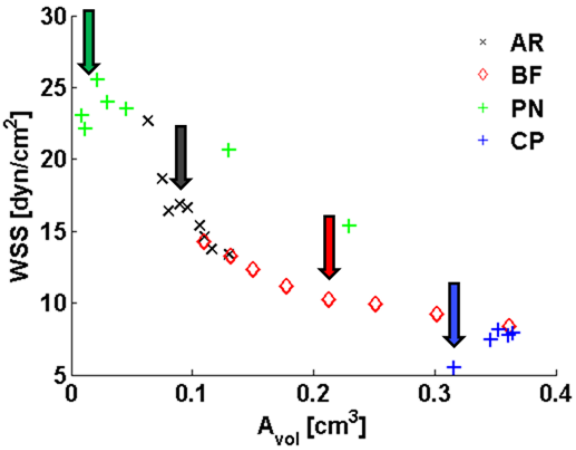

Figure 4.17: Temporally and spatially averaged wall shear stress magnitude (WSS) with respect to aneurysm volume (A_{vol}), grouped by parameter families. Colored arrows correspond to the flow-type transition for each parameter family.

4.3.4 Quantifying the Impact of the Inflow Jet with Changes in Sac Morphology

Two examples of how the jet impact zone changes in both intensity and location through hypothetical remodeling are presented. In Figure 4.18, the normal and tangent jet influence factor (JIF) is shown from the side which the jet enters the sac with increasing BF. As the maximum sac width enlarges, both the normal and tangential JIF decrease from their initial location and migrate from 1/3 to 1/2 the distance from the neck to the dome before dissipating. The tangential JIF however, intensified near the dome with increasing BF. On the reverse side of the sac, it can be seen that the normal and tangent JIF is most elevated at the site of jet impingement for BF = 1.1. As the BF is increased, JIF decreases. When BF attains a value of 2.25, the normal JIF is decreased by a factor of eight. In Figure 4.19, the region of highest tangential JIF is seen to migrate from the neck and mid-body region of the sac to the dome region betweem the PN = 2.0 and PN = 0.33 cases. The distance along the surface from centroid - to - centroid of this migration was 4.1mm. At the dome region, both the tangent and normal JIF values were seen to decline in magnitude as the sac enlarges.

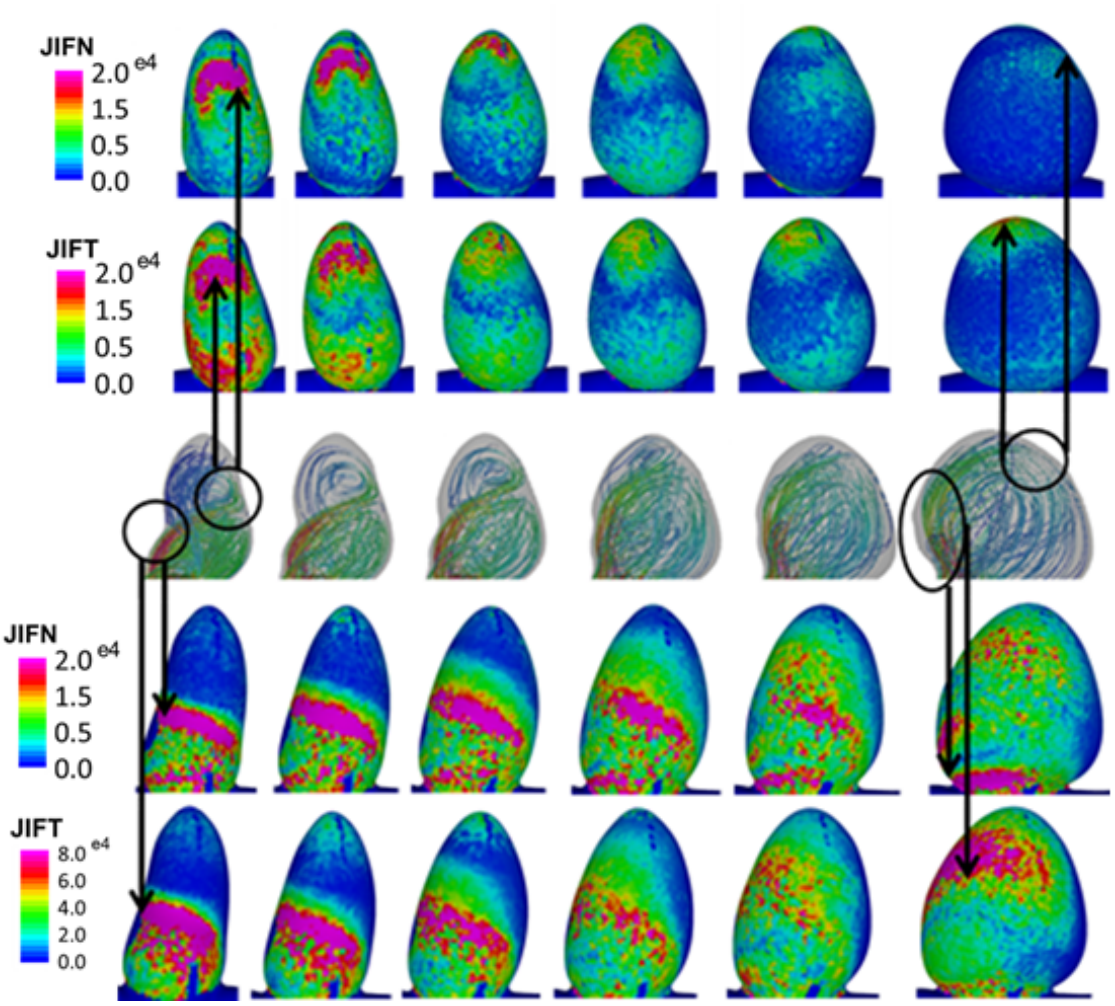

Figure 4.18: Demonstration of the weakening and disappearance of the jet impact on the upper sac wall as the flow structure transitions from two to one vortices with increasing BF. With respect to the JIF surface plots, the streamlines are shown rotated with 90 degrees about the axis perpendicular to the neck plane so that the normal jet impact can be visualized.

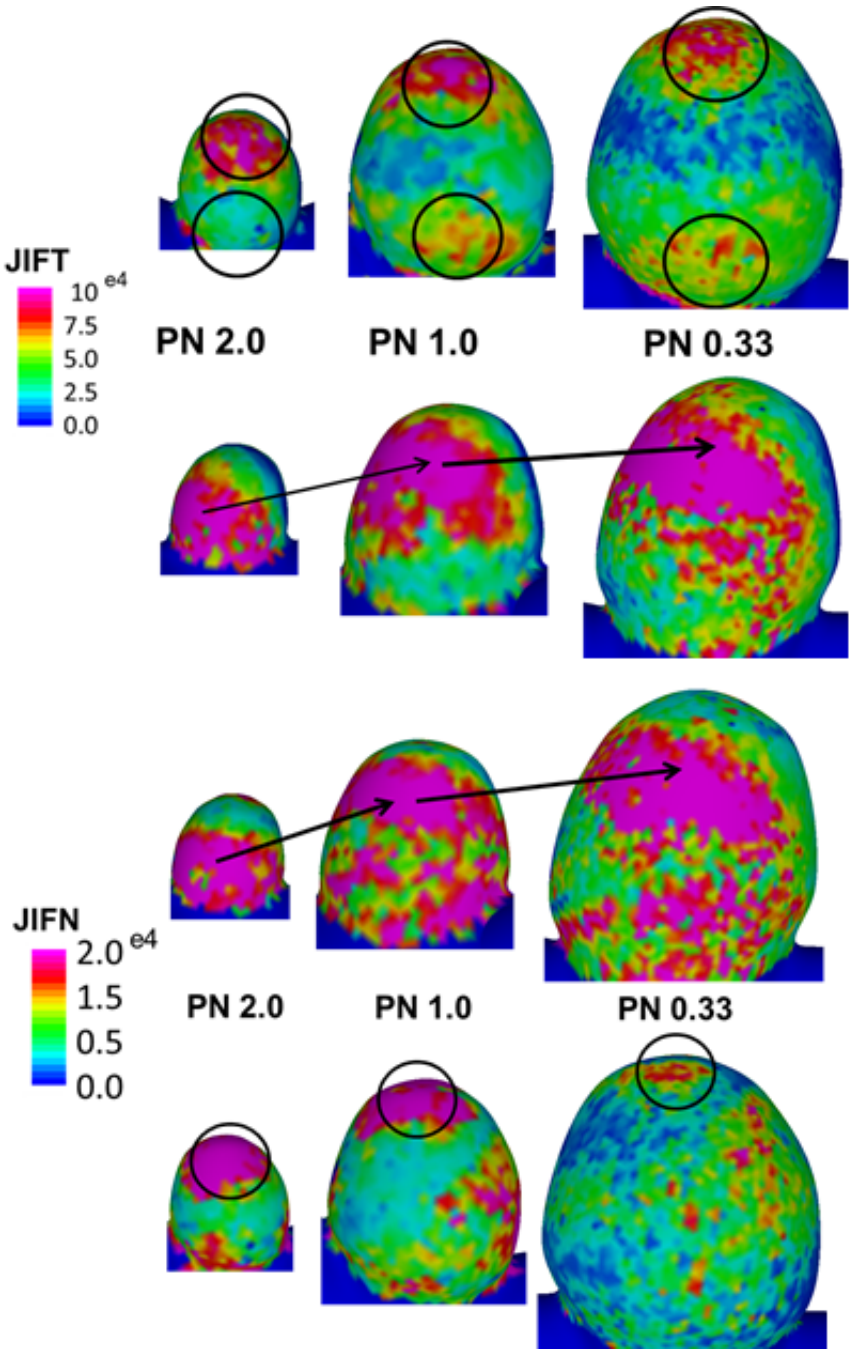

Figure 4.19: Shifting and dissipating jet influence on the wall with increasing sac volume (by decreasing PN).

4.4 Discussion

The focus of this work was to systematically understand how aneurysmal geometry impacts and determines the flow structure of a unilobular aneurysm located at a typical bifurcation location within the brain. The provided, improved knowledge of this aspect is important, perhaps most simply because clinically, aneurysmal geometry is almost solely the only known information pertaining directly to the aneurysm itself. This information is made available only through non-invasive imaging, as opening the brain of a patient carries non-trivial risks associated. As a result, many geometric indices have been proposed as a means of stratifying and categorizing rupture risk, having relevance partially due to the geometry's influence on the pathological flow found within the sac. Most of these methods however do not consider multiple geometric parameters simultaneously however. In this work, it was demonstrated that four non-dimensional geometric parameter can singly determine whether the aneurysm will possess one or two vortices. This finding improves the robustness of the use of surgical indices as suggested by Ujiie et al., who conjectured that aneurysms possessing an aspect ratio greater than 1.6 will harbor a slow moving vortex which triggers a negative biological cascade of events within the wall. The current study demonstrates that this 1.6 can be a critical aspect ratio; however, this is provided a number of other geometric parameters meet their required criteria. Aside from the conjectures discussed by Ujiie et al. [192], the next section discusses other possible motivations as to why understanding the behavior of the flow structure over time and its relationship to geometry can be of value.

4.4.1 Pathological Wall Shear Stress Features Influenced by Flow Structure

As demonstrated in this work, dual vortices can cause flow impingement/separation on the wall which establishes complex wall shear stress fields far from what is experienced in healthy arteries. The change in the wall shear stress vector qualities can be seen in Figure 4.20. Cebral et al. [23] previously reported on the clinical significance of narrow inflow jets with small impact zones in that these flow structures are associated with a higher incidence of IA rupture. Furthermore, Cebral et al. [25] associated the regions of jet impact zones

with thinned-wall regions. They furthermore identified thick, athelrocletrotic regions with the alignment of intra-saccular vorticies. A more complete understanding of how these features are facilitated through changes in geometry over time can therefore be a valuable asset, especially since harvested tissue samples in humans cannot reveal the pathological flow-mediated history of the sac. The secondary vortices within the study conducted are driven slower than the primary vortices, as shown, for example, with the AR family. This is in agreement with the observation made by Ujiie et al. [192], in that secondary vortices in aneurysms containing high aspect rations tend to posses these pathalogical flow features. However, the present study revealed that increasing the sac size under the condition of a single vortex, as with the PN family, can also have the impact of introducing slow-moving flow in the sac. Furthermore, the sac enlargement can facilitate a similar, albeit less-pronounced drop in WSS, as would increasing the AR induce. Therefore the secondary vortex as a facilitator of slow-moving flow may not be a complete explanation as to why clinicians and researchers should consider a multi-vortex IA to be particularly at risk in regards to hemodynamics. For this reason, the wall shear stress pattern formed by the creation of an impacting jet will be discussed.

4.4.1.1 Localized Initiation, Destruction, or Shifting of Divergent Wall Shear Stress Vector Pattern from Inflow Jet Impingement Figure 4.20 demonstrates how, for the AR cases, the introduction of the secondary vortex with increasing AR qualitatively locally modifies the wall shear stress field at systole. In the figure, it is demonstrated that, with the introduction of a secondary vortex, the wall shear stress vector field is altered from being unidirectional (indicated by the vector arrows) in the case of AR = 0.9, to being characteristic of a divergent vector field with AR of 1.4 and above (indicated by the arrows in the figure). This divergent-like flow pattern resembles what would be produced by impinging flow; specifically, the type of flow pattern one would expect to find at the apex of an arterial bifurcation where aneurysms typically form. This initiation is thought to occur from impinging flow with positive wall shear stress gradient away from the impingement zone [129]. A study by Cebral et al. [33], moreover, identified the location of bleb formation as being associated with regions of inflow jet impact. It may therefore be possiable to associate

the divergent wall shear stress pattern with destructive remodeling of the wall, which can be initiated (for example, increasing AR) or destroyed (for example, increasing BF) simple by the sac remodeling as demonstrated in this study. Furthermore, the current study highlights instances where in this regard hemodynamic mapping to post-operatively harvested tissue could lead to confounding or ambiguous conclusions. For example, if, as suggested in the Cebral study [33], if a bleb were to form within a jet impact zone, and then the aneurysm were to remodel such that its maximum diameter increased significantly, then the flowtype would change from possessing two vortices to a single vortex (for example, see Figure 4.4). This change in flowtype would then destroy the localized divergent wall shear stress vector at the impact site, and a uniform flow direction having decreased magnitude would likely take its place.

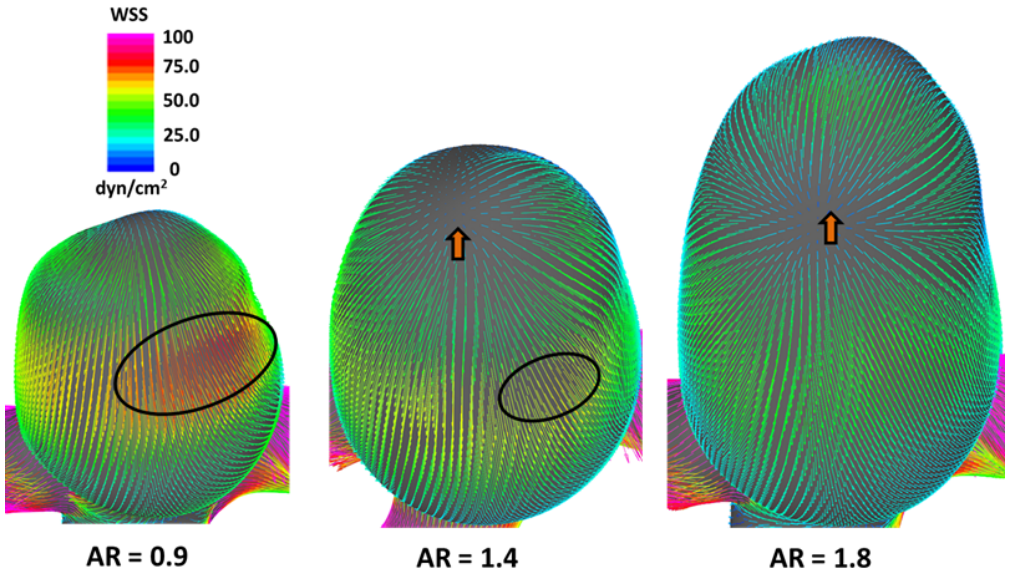

Figure 4.20: A: Systolic wall shear stress vectors from the AR 0.9 case from the AR family are unidirectional on the wall. B: When the AR is increased to 1.4, the jet impacts normal to the wall, splitting into two vortices creating a divergent WSS pattern (indicated by arrow). This pattern stays fixed in its location with distance from the neck plane as the aneurysm continues to grow to an AR of 1.8. The region of elevated wall shear stress (circled in the AR = 0.9 case) diminishes and vanishes as the AR, and aneurysm volume is increased.

4.4.1.2 Shifting of the Swirling Wall Shear Stress Pattern from the Vortex Center

The PN family furthermore presents information of the migration of the vortex center further into the sac as the neck is widened (Figure 4.21). Here, the wall shear stress vector is plotted at systole. As the aneurysm grows uniformly in size, the vortex center (marked by the thick arrow) shifts from the neck region to the center of the sac. At the vortex center, as shown by Figure 4.21, the wall shear stress vectors form a rotational pattern (in contrast to the highly unidirectional field experienced in a healthy artery). The shifting of this spiral WSS vector pattern with growth is an important finding as these regions have been associated with intra-operatively recognizable wall characteristics [190]. However, it is difficult to speculate at this time as to the nature of the impact had on the wall from the shifting over time of this particular pathological wall shear stress pattern.

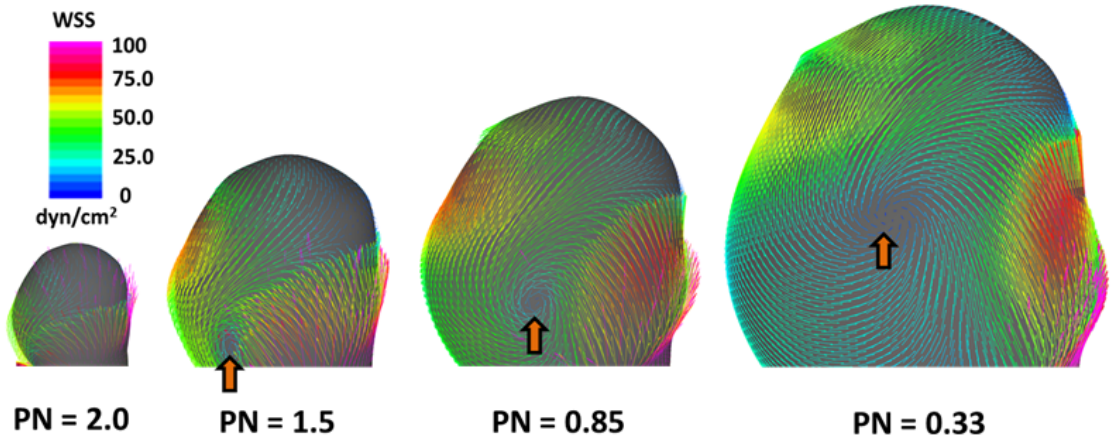

Figure 4.21: A: Systolic wall shear stress vectors plotted on selected cases from the PN family demonstrate that as the sac enlarges, the vortex core is elevated higher into the sac (indicated by the arrow). The vortex core is seen to create a swirling pattern of low magnitude on the wall.

4.4.2 High Wall Shear Stress Magnitude at the Neck in Small Aneurysms May Induce Neck Widening

Geometry-flow information also has its important uses in understanding how changes in geometry, i.e., remodeling, can potentially impact the flow structure and even how flow can potentially drive remodeling. For instance, for the PN family, the smallest aneurysm possesses elevated wall shear stress at the neck, due to the small neck diameter with respect to the parent artery's diameter, shown in Figure 4.22. The larger aneurysm however, possesses reduced wall shear stress at the neck, while the region of highest wall shear stress migrates towards the dome. This supports the conjecture that high wall shear stress can induce neck widening. The smallest aneurysm, additionally, can possess a region of low wall shear stress at the dome due to the flow restriction through the neck. This finding is agreement with the notion that pathologically high wall shear stress in excess of roughly 100 dyne/cm^2 (as given by experimental evidence in works such as that by Malek et al. [124]) induces destructive remodeling within the wall, potentially driving the neck to widen. Eventually, when the neck widens to the circumference of reducing the wall shear stress to normal levels, the neck enlargement potentially ceases,

4.4.3 Sac-Averaged Flow Metrics: Improving Their Predictive Capabilities

Insight is also provided into the flow-metrics used to characterize the intra-saccular flow. This is useful particularly because these metrics have been previously associated with growth [172], rupture [19], or the condition of the wall [21]. Moreover, hemodynamic-related and geometry-based metrics have used to construct rupture prediction models. A notable example of this type of work is that of Detmer et al. [50]. In this work, variables incorporating wall shear stress, oscillatory shear index, shear concentration index, maximum sac velocity, as well as several geometric shape parameters and age were found capable of constructing a rupture-predictor model with an AUC of 84%. In the Detmer study, more variables that were considered in the study were discarded from the predictive model rather than retained. In the current work, many of these same parameters have been considered and were found to possess a clear trend with sac geometry. This information may be useful in the treatment

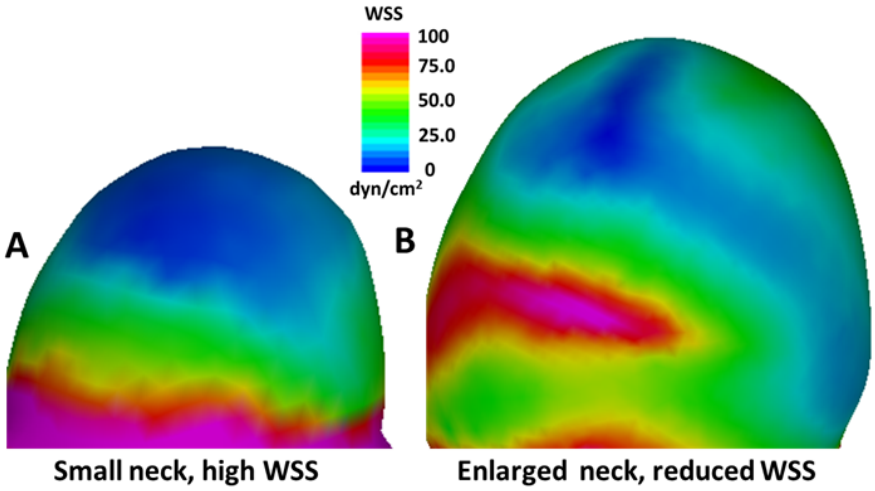

Figure 4.22: A: With a PN of 2.0, restricted flow into the sac causes flow impingement around the aneurysm neck, elevating the wall shear stress locally, while the wall shear stress in the dome is low. B: When the aneurysm grows (PN = 0.67), the enlarged neck experiences a reduction in wall shear stress.

of geometric and hemodynamic parameters for future such models - especially for parameters which possess multiple relationships with other parameters. For example, an increased PODENT has been previously associated with rupture [19]. The parametric studies in this work have shown that an aneurysm having geometric parameters that place its flow-structure possessing a transient nature; i.e., two systolic vortices and one diastolic vortex also has a maximized PODENT for the family, with the exception of the PN family. Here, sac volume was found to be the dominating driver of increasing PODENT, though PODENT was locally elevated for the smallest case that experienced a dual-vortex flow. The question then arises as to whether PODENT is associated with rupture because the hemodynamics of a large aneurysm volume versus the hemodynamics of an aneurysm having a flow-structure at or near a transitional state such as that given in Figure 4.7. One reasonable approach to addressing this, from the current findings, could be to consider PODENT per sac volume in an attempt to improve existing rupture-prediction models. Additionally, the current work found that CP near 0.75 would further increase the likelihood of elevated PODENT.

Several sac-averaged variables were found to correlate inversely with volume (Figures 4.15, 4.17, 4.16). Shear concentration index (SCI) correlates directly with aneurysm volume where as time and space averaged wall shear stress, as well as sac-averaged kinetic energy, strain rate, viscous dissipation, velocity magnitude, and vorticity, correlate inversely with aneurysm volume. In a study of growing versus stable aneurysms, Sforza et al. [172] found significant differences in many sac averaged parameters between growing versus stable aneurysms. In this study, VO, VD, and SR were found to be significantly larger in growing aneurysms versus stable aneurysms. In the current study (see Figure 4.16), these parameters were found to decrease with sac size for a constant parent geometry and flow rate. In a study by Cebral et al. [32], a higher SCI as well as ICI (inflow concentration index) was found be associated with aneurysm rupture. In the current study, it was found that SCI is directly related to sac volume and aspect ratio. It is probable that the larger neck area, which accompanied the larger sac volumes, is in part responsible for the increase in SCI and ICI.

Sac-averaged OSI (OSIMean) for the AR, BF, and CP families was found to be maximized, in each family, for the sac in which the flow structure transitions between having one and two vortices. This finding further suggests aneurysms having flow transitioning flow types are particularly at risk for rupture. Interestingly, the PN group however, experienced a maximum in OSI for a PN value around which no remarkable change in flow structure was found. This case of PN = 0.85 however contained the highest sac-averaged velocity in the PN group, suggesting that sac-avreaged velocity may be an indicator of the degree of OSI the aneurysm as a whole may experience. For the PN case, this value seemed to be maximized when the parent artery diameter just upstream of the Basilar bifurcation was 0.85 times that of the aneurysm neck diameter.

Collectively, the presented information on sac-averaged metrics provide motivation towards guidelines as to geometric parameters pertaining to cases which may be relevant for further study. Aneurysms containing the proper combination of height, maximum diameter, neck diameter, and parent artery diameter that facilitate the transition from one to two vortices are first of particular interest for rupture risk. Risk may be further elevated in cases containing a parent artery to neck diameter ratio of 0.85.

4.4.4 Potential Use in Understanding the History of Hemodynamic-Mediated Wall Remodeling

As aneurysms grow and remodel over time, the hemodynamic information has been shown in the AR, BF, PN, and CP families to change substantially. In any human tissue sample from a harvested aneurysm, only one timepoint - the timepoint at harvest - is physically capable of being available. Understanding on geometry and flow can help to improve the ability to understand how different means of the sac reaching its final configuration would have altered the flow along the journey. To understand the potential past flow structure configurations of a particular aneurysm, one could perform parametric studies on the sac, varying AR, BF, PN, and CP, to understand the likely possibilities of how the flow structure developed through time to its current state. Such information in large study cohorts could provide information on how the flow structure likely influenced the wall towards growth and remodeling. This procedure could also aid in explaining histological findings which do not correlate to the flow structure from the aneurysm at its harvested state.

4.4.5 Limitations

This study has several limitations which could be addressed in future work. While conclusions can be drawn from the results presented, they are limited to the aneurysm type and parameter ranges tested here. For example, the orientation of the sac to the parent vessel, child-vessel asymmetries, and bi or multi-lobular morphologies were not considered here. Furthermore, sidewall aneurysms were not explored in this work. The results herein can therefore be used only as guidelines for further studies, while they do provide an excellent starting point. Furthermore, the influence of flow rate or waveform shape has not been tested in this work, although the preceding chapter (Chapter 3) concluded that the waveform, in a qualitative sense, has a minimal impact on the intra-saccular flow-structure. Upon the creation of sufficient parametric studies to yield sufficiently-extensive geometry-flow information, the conjectures between flow-structure and rupture status and stability/growth status must then be tested. However, from this study, the results have shown that it is imperative to consider multi-variable correlation when associating a particular metric with

rupture. For example, as demonstrated in the study, a high PODENT could be indicative of a large sac, a transient flow-structure, or a possible combination thereof, all of which have different implications when considering the wall shear stress fields that accompany them. The trends identified in this work therefore may be further utilized in parametric studies of individualized clinical cases to understand how the metrics presented in this work may have progressed with the development of the sac, and which metric seem to drive the sac progression or rupture.

4.5 Conclusion

In this study, information regarding the relationship between multiple geometric parameters and flow structure was obtained. The results indicate that the relationship requires the consideration of multiple geometric parameters to adequately describe the nature of the flow field. The consideration of multiple geometric parameters are hence required to adequately study the flow and its impact on the wall. The work within this chapter provides crucial information regarding how these multiple factors can be considered so that risk-assessment from hemodynamic studies can be improved upon. These studies furthermore demonstrate how the intra-saccular flow may change during aneurysmal growth in several hypothetical scenarios in which the parent vasculature and inflow/outflow boundary conditions have been kept constant. In this manner, it is important to consider the possible temporal effects of flow-structure on the aneurysm wall when attempting to correlate local hemodynamics to wall structure/content. The work within this chapter provides a means of systematically accounting for such changes within the framework of a unilobular bifurcation aneurysm.

5.0 An Exploration of Oxygen Transport in Cerebral Aneurysms

5.1 Introduction

The hemodynamics contained within cerebral aneurysms deviate substantially from those in the parent artery due to the pathological sac shape that facilitates artery-deviant flows [73, 58, 203, 182, 172]. Often, these altered flow conditions are those which are thought to be detrimental to the wall biology [69, 192, 172]. For example, substantial research has been performed to study the association between altered wall shear stress in an aneurysm sac and detrimental changes to the aneurysm wall, [23, 177, 196, 94, 20]. In this regard, abnormally low wall shear stress has been associated with inflammatory-cell-mediated destructive remodeling [14, 192, 38, 164], whereas the combination of an abnormally high wall shear stress and a positive spatial gradient are associated with mural-cellmediated destructive remodeling [129]. CFD simulations of blood flow in aneurysms has been conducted under the assumption that both low and high WSS can lead to overall endothelial dysfunction [202, 128, 26]. While all the aforementioned effects of altered WSS on cerebral aneurysms are well supported, the question of the specific hemodynamics that leads to rupture remains. In fact, it is not definitive that abnormal values of the wall shear stress vector are the only flow related factors leading to wall degeneration. Namely, while hemodynamic wall shear stress and pressure directly impact the wall, the wall is not without other flow related influences including the need for adequate transport into and out of the wall. In particular, the biological processes within the wall require the proper conditions of mass and chemical equilibrium in order to maintain a healthy, homeostatic state. Molecular oxygen may be one of the most vital nutrients for the wall as oxygen is an essential element required for many vital intramural processes [179, 131, 188] ; most notably, the long-term production of sufficient energy necessary for cell function. Oxygen is essential for cellular aerobic metabolism to maintain intracellular bioenergetics through production of adenosine triphosphate (ATP), and to serve as an electron acceptor in many reactions [179]. The lack of electron acceptors can facilitate oxidative stresses deleterious to the wall in processes such as endothelial dys-

function and the migration of immune cells and vascular smooth muscle cells into the wall or cellular toxicity and apoptosis [8, 180]. Inadequate tissue oxygenation also initiates hypoxia-inducible factors (HIFs) which regulate the transcription of genes which are responsible for altering a cell's homeostatic state in response to a reduced oxygen supply, resulting in consequences such as an abnormal matrix metabolism, alteration of vascular smooth muscle cell phenotype, and immune responses [40]. Although mechanical forces can influence these processes through mechanotransduction and direct mechanical loading as discussed in many of the aforementioned works on WSS, they do not independently govern mass and chemical phenomena within the wall that ultimately are responsible for the wall's function.

While the mechanical stresses that result directly from hemodynamic loading and the chemical processes within the wall are two separate physical phenomena, they are not entirely uncoupled. lumenal-side advection maintains the concentration of lumenal-side free oxygen which dissociates from oxyhemoglobin. In cerebral aneurysms however, the blood flow is altered from that in a normal artery, which alters the advective conditions for oxygen transport found within a normal artery. Furthermore, an aneurysm wall that is undergoing remodeling will have altered diffusive properties and metabolic needs. Moreover, as the aneurysm enlarges, the wall often thickens, increasing the distance required for transport and increasing the metabolic needs of the wall. It is therefore conceivable that altered IA hemodynamics will result in insufficient oxygen transport from the interior of the sac into the IA wall and therefor create hypoxic conditions, despite the possible development of vasa vasorum.

Hypoxia has been associated with wall dysfunction and degeneration in arteries and the detriments from this condition have been found to be multi-faceted. When tissues receive insufficient oxygen, a plethora of chemical factors (e.g. hypoxia-inducible factors) will mediate a metabolic switch from aerobic energy generation to anaerobic glycolysis [86]. Anaerobic glycolysis in conjunction with decreased cellular demands for energy can maintain a cell through periods of intermittent hypoxia. However, if exposed to chronic hypoxic conditions, the cells will eventually lose function and die due to the inefficiencies of glycolysis relative to aerobic respiration [86]. The endothelium, in particular, has shown response to this state in ruptured cerebral aneurysms [117]. The failure of the endothelium can facilitate

increased wall membrane permeability, allowing for the entrance of macro-molecules such as low-density lipoproteins (LDL), and the wall's loss of ability to sense and adapt to changes in mechanical loading. Furthermore, there is evidence that on a systemic level that endothelial dysfunction in COPD (chronic obstructive pulmonary disease) patients is responsible for increased arterial stiffness and atherosclerosis [132]. Given the importance of adequate tissue oxygenation and outlined potential discrepancies between wall shear stress and lumenal oxygen, the consideration of aneurysmal oxygen transport could provide new understanding of previously unexplored facets of the disease necessary for gaining a thorough understanding of its behavior.

The only research known to the author on flow-mediated hypoxia in cerebral aneurysms is the dissertation work of Holland [86]. That work had the specific aim of investigating hypoxia in walls with lumenal thrombosis. In general, however, little has been investigated regarding the conditions required for hypoxia prior to the formation of a thrombus. It is known that the onset of hypoxia triggers a cascade of deleterious metabolic events that are distinct from the hemodynamic wall shear stress based changes described in prior chapters. The objective of the work described in this chapter is to determine the relationship between sac geometry and lumenal oxygen concentration via computational modeling. This objective was explored in three phases. The first section of this work utilized a fully-coupled lumen-wall model to demonstrate the ability of sac geometry to facilitate advective conditions which introduce hypoxic-prone conditions in one sac and fail to induce hypoxic-prone conditions in another sac using identical parent-artery geometries. The second section, once again utilizing a parametric modeling approach, explored geometric parameters which are capable of distinguishing the lumen's global oxygen state and identified a simple parameter that can serve this purpose. The third section of this work utilized parametric modeling to demonstrate that the aneurysm lumen, in the presence of wall shear stress considered as pathologically low, can in a localized manner experience a broad distributions of oxygen transport levels. Hence, wall shear stress state cannot be used as an indirect indicator of level of mass transport Collectively, this work provides insight into the link between pathological flow dynamics within cerebral aneurysms and flow-mediated oxygen transport into the wall tissue (particularly from the lumen side).

5.2 Ability of Sac Geometry to Influence Intra-Saccular Wall-Oxygenation

5.2.1 Methods

5.2.1.1 Geometry Creation Computational models for two distinct basilar tip bifurcation aneurysms were created using the same patient vasculature. The aneurysm for Model 1 was chosen to promote intra-saccular flow conditions favorable for advection whereas the aneurysm in Model 2 was chosen to be less favorable to advective transport. Both models considered aneurysms which were parametric reconstructions of the same clinical case; thus their parent geometries were identical, as were their parent-vessel flow rates. To create the blood domains, the lumen surface of the original case was extracted as described in Chapter 4, section and morphed to geometries chosen for the parametric study using methods described in Chapter 4, section to achieve the desired sac parameters: Aspect Ratio (AR), Bottle-Neck Factor (BF), Parent Artery to Neck Ratio (PN), and Conicity Parameter (CP) (see Figure 5.1). For a fuller discussion on these parmaeters reference Chapter 4, section 4.2.2. The wall domain was then created by offsetting the lumenal surface in the normal direction by a constant distance of 300 microns, a typical thickness for the basilar arteries [123].

5.2.1.2 Mesh Creation The lumens of both models (fluid domain) were meshed with hexahedral elements using ANSYS ICEM CFD (Ansys Inc, Canonsburg PA, USA). The average length scale for the mesh was 0.1 mm. To resolve the sharp spatial gradients of oxygen species near the wall, hexahedral boundarylayer mesh elements were utilized. For oxygen diffusion in blood, the Schmidt number, defined by the kinematic viscosity of blood divided by the mass diffusivity of oxygen in blood provides an estimate of the thickness of the mass boundary layer thickness relative to that of the momentum boundary-layer. For this work,

$$Sc = \frac{\mu}{\rho D} = 2777 \tag{5.1}$$

The boundary-layer elements were therefore kept to a ratio of less than 1/2900 of the average domain mesh length scale in both the original model meshes as well as in grid refinement

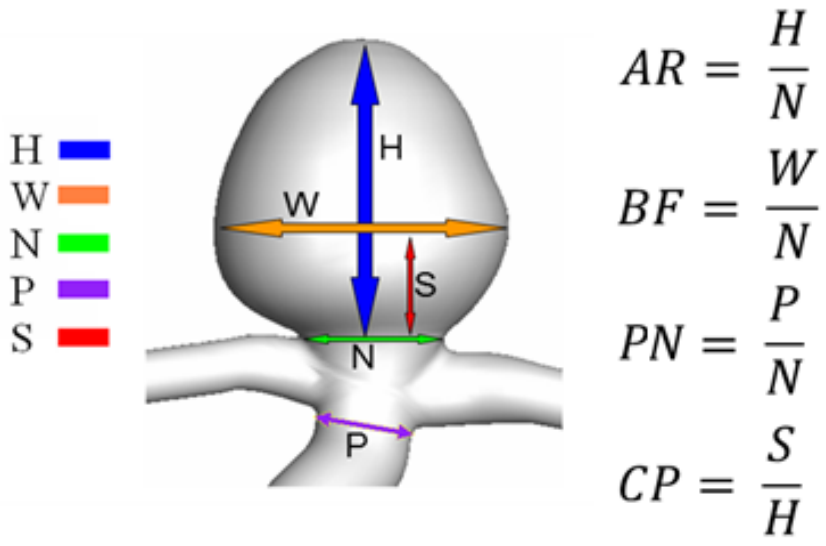

Figure 5.1: Definition of non-dimensional geometric parameters; each corresponding to one of the four sets of models which varied only one of these parameters throughout the models within each parameter's respective set.

studies. The near-wall grid spacing in the radial direction resulted in the off-wall grid spacing of the first node to be approximately $4.0e^{-4}$ artery diameters, which is in accordance to the spacing of $4.7e^{-4}$ artery diameters used by Moore and Ethier [135]. The vessel walls of each model (solid domain) were likewise meshed with hexahedral elements utilizing Ansys ICEM CFD. The grid spacing in the radial direction was kept consistent with the boundary layer element thickness while the element axial and angular distance spacings were kept consistent with the average mesh length scale in the blood domain.

5.2.1.3 Steady-State Treatment Due to the multi-order of magnitude difference in the advective versus diffusive time scales, only steady flow was considered. Kolandavel et al. [112] had previously investigated the impact of time-averaged versus transient steady wall oxygen transport, finding little qualitative difference between steady and transient conditions, even while considering wall motion in the transient case. A brief consideration of the advective velocity in the aneurysm lumen versus the wall allows one to draw this same

conclusion. Typical cerebral blood vessel velocities are on the order of 10-100 cm/s, whereas advective velocities through the wall are on the order of 0.1-1.0 μm/s. These velocities fluctuate periodically with the cardiac cycle at a frequency on the order of 1 Hertz. In contrast, the velocities within artery walls are $10e^{-6}$ cm/s and over a characteristic timescale ($D/Thickness^2$) of $1.0e^5$ s where D is the diffusivity of oxygen in the wall. The models were thusly studied under steady flow conditions.

5.2.1.4 Blood Oxygen Transport The modeling approach used herein for oxygen transport in arteries was previously employed in works such as those of Moore and Ethier [135] and recently, Murphy et al. [141]. The oxygen is transported through the circulatory system by two means- as free oxygen, where it is dissolved in solution (either plasma or inside RBC) and bound to hemoglobin molecules within the red blood cells to form oxyhemoglobin molecules. Approximately 98% of oxygen in blood is bound to hemoglobin molecules. The concentration of free oxygen (C_{free}) is assumed to be related to the oxygen tension or oxygen partial pressure (PO_2) in blood through Henry's law

$$PO_2 = \frac{C_{free}}{\alpha} \tag{5.2}$$

where α is the solubility of oxygen in plasma is solubility coefficient of oxygen in blood and is treated as a constant equal to 0.0031 mL O_2/(mmHg $\times$ 100 mL blood). All oxygen concentrations are typically given in terms of mL of O_2 per 100 mL of blood and the partial pressure of oxygen is given in mmHg.

Within each red blood cell, there are on the order of 270 million hemoglobin molecules, each with four heme groups that can reversibly bind to O_2 that has diffused across the RBC membrane from the plasma. The saturation of these heme groups (S) within the RBCs can be written as a function of PO_2 in the surrounding plasma, often represented in an oxygen dissociation curve. The functional form of $S(PO_2)$ is sigmoidal shaped and often approximated using the Hill Equation [79], given as

$$S = \frac{PO_2^n}{PO_2^n + PO_{2,50}^n} \tag{5.3}$$

where $PO_{2,50}$, is the PO_2 concentration in blood plasma at which the hemoglobin is 50% saturated with oxygen (S = 0.5) and n is Hill's coefficient, approximately 2.7 for hemoglobin in adults. While S is often represented as a percentage, here, it is represented as a saturation fraction so that S = 1 corresponds to the situation when all heme groups have bound O_2. Physical factors such as temperature and pH can shift the oxygen dissociation curve to the left or right. The concentration of bound oxygen will be the product of the total possible oxygen carrying capacity of hemoglobin is completely saturated ([Hb]) and the actual saturation of the hemoglobin (S)

$$C_{bound} = [Hb]S \tag{5.4}$$

[Hb] will be treated as a constant in space and time (no plasma skimming) and is given in units of mL $\frac{O_2}{100mL}$ of blood. The local values of C_{free} and C_{bound} will then be described through advection diffusion equations with diffusivity D_b and D_c, respectively. In this case,

$$\alpha\frac{DPO_2}{Dt} = \alpha\nabla\cdot(D_b(\nabla PO_2) + r \tag{5.5}$$

and

$$[Hb]\frac{DPO_2}{Dt} = [Hb]\nabla\cdot(D_b\nabla S) - r \tag{5.6}$$

where we have explicitly used the relationships for C_{free} and C_{bound} above. As already noted, 98% of oxygen is transported within the RBC. In equation 5.5, is the rate at which oxygen is released from hemoglobin into the plasma and $\frac{D}{Dt}$ is the material derivative with velocity $\boldsymbol{v}$ determined through the Navier-Stokes equations

$$\rho\frac{D\boldsymbol{v}}{Dt} = -\nabla p + \mu\nabla^2\boldsymbol{v} \tag{5.7}$$

$$\nabla\cdot\boldsymbol{v} = 0 \tag{5.8}$$

Namely, it is assumed blood behaves as an incompressible fluid with constant viscosity and density, so that the Navier-Stokes equations are uncouple from the equations describing the transport of oxygen. Here we use a blood density of 1050 $\frac{kg}{m^3}$ and a viscosity of 0.0035 $Pa\cdot s$. Once v is known from the Navier-Stokes equations, the mass transport equations reduce to three equations (two advection equations and Hill's equation) with three variables S, PO_2

and r. It is simple to eliminate r by adding the advection diffusion equations. We can then make use of Hill's equation to write S in terms of the PO_2 and thereby reduce the equations to one equation in terms of one unknown. Here we leave the term $\frac{dS}{dPO_2}$, (the slope of the oxygen dissociation curve) as an explicit expression,

$$(1+\frac{[Hb]}{\alpha}\frac{dS}{dPO_2})\frac{DPO_2}{Dt} = \nabla\cdot(D_b(1+\frac{[Hb]}{\alpha}\frac{D_c}{D_b}\frac{dS}{dPO_2}))\nabla PO_2 \tag{5.9}$$

where

$$\frac{dS}{dPO_2} = \frac{1}{dPO_{2,50}^n}\frac{nPO_2^{n-1}}{(1+(\frac{PO_2}{PO_{2,50}^n})^n)^2} \tag{5.10}$$

As the bound oxygen is physically located within the RBC, its transport depends on how the RBC travels within the blood vessel. Here, as in Murphy et al.[141], we do not explicitly model the transport of the individual RBCs. Rather, following Murphy, we use an effective value of D_c that implicitly depends on the RBC motion through a dependence on shear rate γ defined as

$$\gamma = \sqrt{(2\boldsymbol{D}:\boldsymbol{D})} \tag{5.11}$$

where

$$\boldsymbol{D} = \frac{1}{2}(\nabla v + \nabla v^T) \tag{5.12}$$

The functional dependence of D_c on γ is given in Table 5.1 and follows that of Murphy et al. [141] who made use of shear rate dependencies from three separate studies by Goldsmith [67], Goldsmith and Marlow [68], and Cha and Beissinger [35] and are described in Eqs 5 and 6 of Murphy et al. [141]. For computational purposes it is convenient to cast Equations 5.5 and 5.6 in the form of an advection-diffusion-reaction obtaining:

$$\frac{DPO_2}{Dt} = \nabla\cdot(D^{'}\nabla PO_2) + Reaction \tag{5.13}$$

where

$$D^{'} = \frac{(D_b(1+\frac{[Hb]}{\alpha}\frac{D_c}{D_b}\frac{dS}{dPO_2}))}{(1+\frac{[Hb]}{\alpha}\frac{dS}{dPO_2})} \tag{5.14}$$

and

$$Reaction = \frac{(D_b(1+\frac{[Hb]}{\alpha}\frac{D_c}{D_b}\frac{dS}{dPO_2}))}{(1+\frac{[Hb]}{\alpha}\frac{dS}{dPO_2})^2}\nabla PO_2\cdot(\frac{[Hb]}{\alpha}\cdot(\frac{[Hb]}{\alpha}\nabla\frac{dS}{dPO_s})) \tag{5.15}$$

Here $D^{'}$ serves as an effective diffusivity that depends on the diffusivity of both the bound and free oxygen. Thus, the transport of free oxygen in blood is dependent on the material constants: D_b, D_c, $[Hb]$, α, $PO_{2,50}$, and the local shear rate of the blood resulting from the velocity field $\boldsymbol{v}$. The material constants are tabulated in Table 5.1.

5.2.1.5 Transport of Oxygen in the Vessel Wall In this section we describe the governing equations for the transport of free oxygen within the wall as it travels through the interstitial fluid and is potentially consumed by the intramural cells. The model includes the distinct wall layers: intima, media, and adventitia with layer specific properties, Table 5.2. The oxygen consumption rate within each layer was modeled according to the Michaelis-Menten kinetics model, where the oxygen consumption rate in the tissue is proportional to the oxygen concentration within the interstitial fluid.

$$M = M_0 \frac{PO_2}{PO_2 + PO_{2,M}} \tag{5.16}$$

where M is the volumetric rate at which oxygen is consumed per unit volume of the wall layer with M_0 being the maximum rate according to Richardson et al. [160]. In that work, converting the oxygen concentration in the wall, given by the Michaelis-Menten equation requires division of the sink term by the oxygen solubility in the arterial wall [154]. The focus of this work is a parametric study of the influence of sac geometry on oxygen concentration. We therefore did not consider the added complexity of modeling additional factors that would modify oxygen consumption rate such as inflammation, plaque, age, loss or degeneration of interstitial tissue, and smooth muscle cell phenotype. The advective-diffusive-reactive equation including both diffusion and consumption is, for each wall layer,

$$\frac{DPO_2}{Dt} = \nabla \cdot (D_T(\nabla PO_2) - \frac{M}{\alpha_T} \tag{5.17}$$

where the subscript T refers to quantities within the wall tissue. As the velocity of fluid into the wall is one to two orders of magnitude smaller than the oxygen diffusion velocity the convective term is neglected (e.g. [135]), so we approximate the nonlinear material derivative with a simple time derivative,

$$\frac{dPO_2}{dt} = \nabla \cdot (D_T(\nabla PO_2) - \frac{M}{\alpha_T} \tag{5.18}$$

Table 5.1: Material properties pertaining to oxygen transport in the blood

Material property	Description	Value	Source
D_b	Kinematic diffusivity of free oxygen in blood	1.2e^{-9} m^2/s	[135]
D_b	Kinematic diffusivity of oxyhemoglobin in blood	$0 \leq \gamma \leq 100s^{-1}$ 5.00e^{-12}+4.00e^{-13} γ m^2/s	[67, 68]
		$\gamma > 100s^{-1}$ 3.60e^{-12}+1.96e^{-12} γ m^2/s	[35]
$[HB]$	Total oxygen carrying capacity of hemoglobin in blood	0.2 ml O_2/ml blood	[153]
α	Solution of oxygen in plasma	$3.0e^{-4}$ $\text{ml}_{O_2}/\text{ml}_{blood}$/mmHg	[135]
$PO_{2.50}$	The PO_2 value at which the hemoglobin is half-saturated	26 mmHg	[66]

The wall-oxygen transport is thus dependent on material properties M_0,$PO_{2,M}$,α_t,and D_T which are Tabulated in Table 5.2.

5.2.1.6 Boundary Conditions The time-independent boundary conditions for the models were chosen as follows. A parabolic velocity vector was prescribed at all the daughter vessel outlets such that the direction was normal to outlet and the magnitude was such that the wall shear stress on each outlet was 15 dyne/cm^2. At the inlet of the parent vessel, a reference pressure of zero was prescribed and the in plane components of velocity were set to zero. The velocity vector on the lumen surface was also set to zero. The oxygen partial pressure at the model inlet was set to 100 mmHg [154]. Diffusion at the outlets (in the axial direction) was set to zero (i.e., a zero-normal gradient condition was specified). The concentration of the cerebral spinal fluid on the adventitial wall was set to 39 mmHg as reported by Zaharchuck et al. [213]; in doing so, it was inherently assumed that the CSF is always able to meet any demanded amount of adventitial-side oxygen. At the lumen boundary, a continuity of the mass flux was enforced.

Table 5.2: Material properties pertaining to oxygen transport in the wall

Material Constant	Description	Value, Intima	Value, Media	Value, Adventitia	Source
M_0	Maximum oxygen consumption rate within the wall	$1e^{-6}$ ml_{O_2} $/ml_{tissue}$ /s	$1.21e^{-5}$ ml_{O_2} $/ml_{tissue}$ /s	$8.5e^{-6}$ ml_{O_2} $/ml_{tissue}$ /s	[160]
$PO_{2,M}$	PO2 value when reaction is at half the maximum rate	1mm Hg	1mm Hg	1mm Hg	[135]
α_t	Solubility of oxygen in the wall	$2.4e^{-5}$ ml_{O_2} $/ml_{tissue}$ /mm Hg	$2.4e^{-5}$ ml_{O_2} $/ml_{tissue}$ /mm Hg	$2.4e^{-5}$ ml_{O_2} $/ml_{tissue}$ /mm Hg	[160]
D_t	Diffusivity of oxygen within the wall	$9e^{-9}$ m^2/s	$5e^{-11}$ m^2/s	$5e^{-11}$ m^2/s	[160]

5.2.1.7 Metrics for Assessing Hypoxia It is not well established as to what concentrations of oxygen within the different layers of cerebral vessels are required to maintain healthy homeostasis. The question of proper tissue oxygenation becomes yet more complicated when diseased arterial tissues, such as tissues in cerebral aneurysms are considered, as metabolic needs could likely be altered by ongoing growth/remodeling, or the presence of inflammation. Two methods for assessing wall-oxygen content were therefore proposed. One method, utilized by Murphy et al. [141], reasonably considered the ratio of the Sherwood number to the Damkhöler number. Physically, the Sherwood number is a measure of the convective mass transport to the diffusive mass transport,

$$Sh = \frac{\partial PO_2}{\partial n_{wall}} \frac{d_{lumen}}{(PO_{2,in} - PO_{2,wall})} \tag{5.19}$$

where $PO_{2,in}$ is the PO_2 on the inlet, and $PO_{2,wall}$ is the PO_2 at the lumen surface and the first term is the gradient of PO_2 normal to wall, evaluated at the wall. The Damkhöler

number used here is a measure of the oxygen consumption rate relative to the mass transport rate into the wall given by:

$$Da = \frac{M_0 T d_{lumen}}{\alpha_T D_T P O_{2,in}} \tag{5.20}$$

where T is the wall thickness. Therefore, this ratio

$$\frac{Sh}{Da} = \frac{\frac{\partial PO_2}{\partial n_{wall}}(\alpha_T D_T P O_{2,in})}{M_0 T (P O_{2,in} - P O_{2,wall})} \tag{5.21}$$

describes the convective mass transport within the lumen across the lumen/wall interface with respect to the demand of oxygen within the wall with respect to the diffusive properties of the wall. As this ratio approaches one from above, the advective transport increasingly fails to meet the demands within the wall. The second method was to consider lumenal oxygen concentrations within the sac normalized to their respective spatially-averaged parent artery values. In this method, the mean value in the parent artery, plus or minus one standard deviation, is considered healthy in order for the vessel to maintain its homeostatic value. Values within the sac outside this range could be considered at risk for hypoxia. Such methods of parent-artery normalization are commonplace in assessing wall shear stress when patient specific waveforms are unknown. The concept of patient-specific homeostasis has been previously proposed [13].

5.2.2 Study 1: Impact of Sac Geometry on Lumenal Oxygen Concentration

5.2.2.1 Results - Study 1 The Case1 aneurysm lumen was found to be minimally impacted by the aneurysmal flow conditions (Figure 5.2 a,b). The sac average lumenal PO_2 was 0.995 $\pm$ 0.141 times that of the parent-vessel averaged PO_2. In contrast, the Case2 aneurysm lumen was appreciably impacted by the altered flow within the sac, having a sac averaged lumenal PO_2 of 0.771 $\pm$ 0.178 that of the respective parent vessel value. In this case, the minimal lumenal PO_2 was reduced to 0.348 times the parent vessel average; this reduction occurred in in the vortex region

In the Case 1 aneurysm wall, the oxygen concentration profile monotonically increased from its maximum at the lumen side to the minimum at the adventitial side. The oxygen concentration within the wall, therefore, never decreased below the oxygen concentration

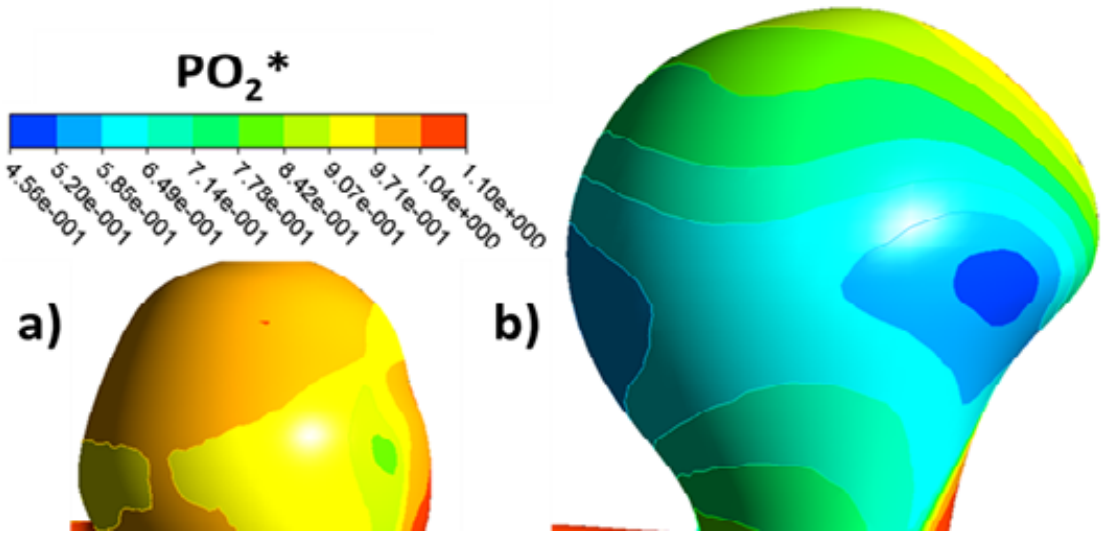

Figure 5.2: Lumen wall oxygen partial pressure normalized to the average parent artery oxygen partial pressure (PO_2^*) for a) Case1 and b) Case2. The view is opposite the side of the inflow jet entry, as decrease in lumen-wall PO_2^* is evident is Case2 versus Case1.

within the presumed CSF. In contrast, the Case 2 wall oxygen concentration fell below the CSF concentration in 38% of the wall tissue volume, indicating the requirement of oxygen diffusion from both the lumenal and adventitial sources. The role of advection in each case was further quantified by considering the Sherwood per Damkholer numbers; finding that this ratio was decreased by 17% in Case 2, where it was unaffected in Case 1.

In the Case 1 aneurysm wall, the oxygen concentration profile monotonically increased from its maximum at the lumen side to the minimum at the adventitial side. The oxygen concentration within the wall, therefore, never decreased below the oxygen concentration within the presumed CSF. In contrast, the Case 2 wall oxygen concentration fell below the CSF concentration in 38% of the wall tissue volume, indicating the requirement of oxygen diffusion from both the lumenal and adventitial sources. The role of advection in each case was further quantified by considering the Sherwood per Damkholer numbers; finding that this ratio was decreased by 17% in Case 2, where it was unaffected in Case 1, Figure 5.4, 5.5.

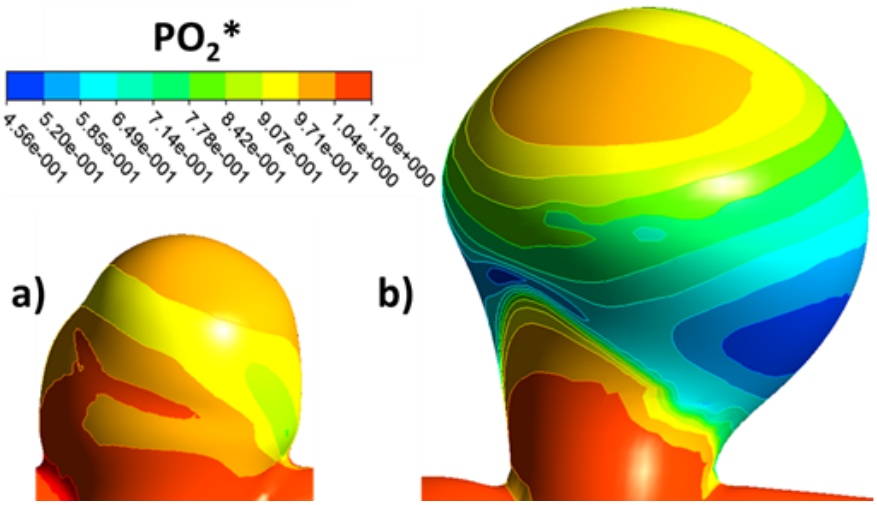

Figure 5.3: Lumen wall oxygen partial pressure normalized to the average parent artery oxygen partial pressure (PO_2^*) for a) Case1 and b) Case2. The view is opposite the side of the inflow jet entry, as decrease in lumen-wall (PO_2^*) is evident is Case2 versus Case1.

5.2.2.2 Flow Features Impacting Oxygen Transport Flow in the Case1 aneurysm was dominated by a single, well-defined circular vortex with a diameter close to that of the parent vessel, Figure 5.6. As the sac-averaged velocity was 0.47 times that of the parent vessel velocity, advective conditions were sufficiently well supported and, despite not possessing Pouiselle-like flow as what would be found in a healthy artery, the lumenal oxygen concentration in the sac was minimally impacted. However; the lumenal oxygen concentration was appreciably impacted near the vortex center, lowered to 81% that of the parent-vessel average. Case2, conversely, possessed a more complicated flow structure, having an elongated vortex with a long narrow inflow jet impacting the dome, as well as a smaller secondary vortex. The lower-than-Case1 aneurysmal velocity of 0.15 times that of the average parent vessel velocity in conjunction with a vortex deviating from a spherical shape facilitated the decrease in lumenal oxygen concentration. This was most notable in the vortex center, having lumenal PO_2 45.6% of the parent artery average. This low concentration was also prevalent at the vortex separation region. In contrast to vortex centers and separation re-

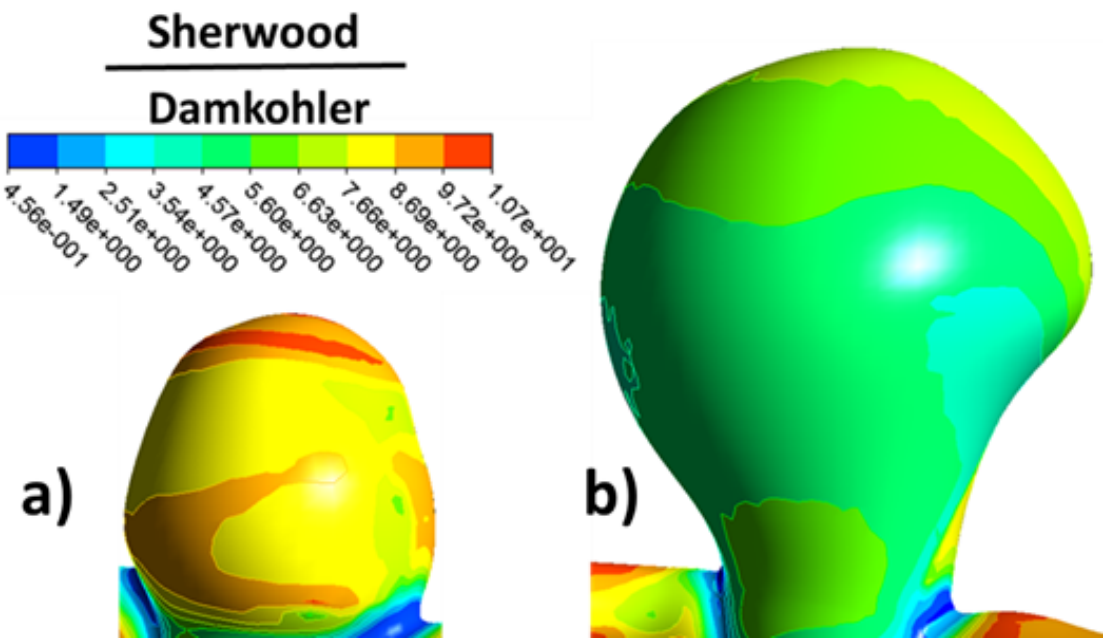

Figure 5.4: Ratio of $\frac{Sh}{Da}$ on lumen opposite to inflow jet entry for a) Case1 and b) Case2.

gions, the inflow jet was found to enhance lumenal oxygen transport in the dome around the impaction site. This effect was also found at locations where the inflow jet sheared the lumen as it traveled towards the dome from the ostium plane.

5.2.2.3 Wall Oxygen Content The Case1 aneurysmal tissue oxygen concentration was found to be greater than that of the cerebral spinal fluid at all points in the model. By contrast, 38% of the Case2 aneurysmal tissue contained a PO_2 concentration less than that of the CSF. These areas corresponded with regions around the centers of vortex circulation, region at the vortex separation zone, and regions of the sac farthest from the zone of jet impaction/shearing.

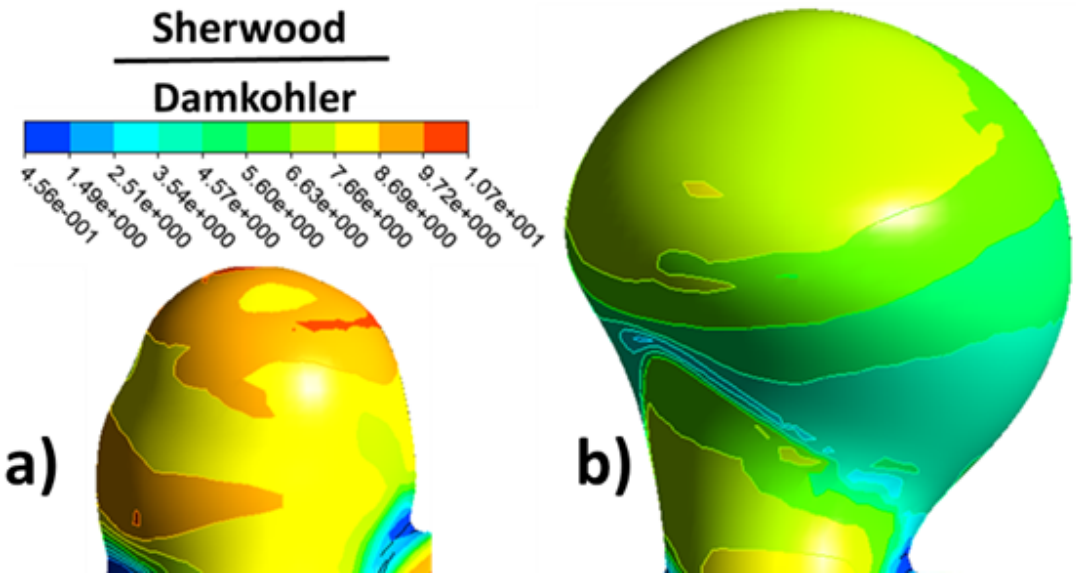

Figure 5.5: Ratio of Sh/Da on lumen near inflow jet for a) Case1 and b) Case2.

5.2.3 Discussion - Study 1

Hypoxia is a detrimental environment for most tissues of the body as it disrupts cellular respiration, induces oxidative stresses, and particular to the vasculature, can initiate angiogenesis. Furthermore, using in vitro studies, hypoxia in the vascular wall has been implicated as a driver of increased smooth muscle cell proliferation and apoptosis [159], altered Ca^{+2} levels within SMCs which impairs contractility [1, 185], decreased ability of SMCs to synthesize collagen [152], as well as SMC apoptosis [159]. In cerebral aneurysm tissue, all of the aforementioned consequences of hypoxia can be exceptionally problematic considering the diseased state of the tissue in conjunction with the increased mechanical loads resulting from the enlarged aneurysm geometry. While the impact of hypoxia in abdominal aortic aneurysms have been investigated, little attention has been given to the presence of hypoxia in cerebral aneurysms; despite the seemingly exceptionally critical role that wall tissue oxygen content can have in providing conditions in which the integrity of the IA wall can be maintained. To the author's knowledge, there are two previous works that have addressed oxygen transport in the context of cerebral aneurysms. The first, chronologically, is the work

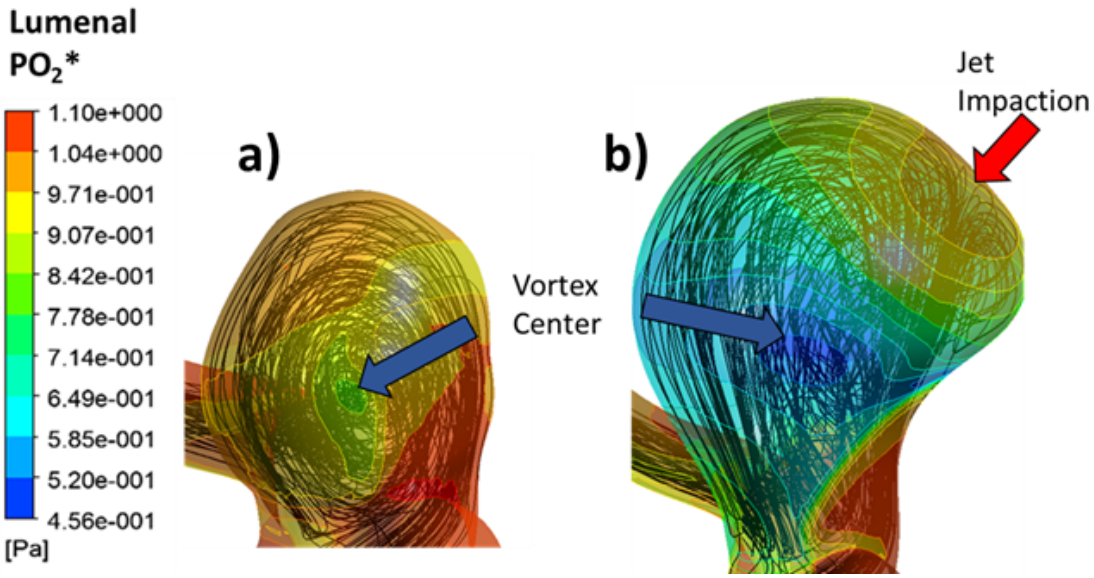

Figure 5.6: Jet impaction locally increases PO_2^* in both a) Case1 and b) Case2. This effect is more evident in Case2 where the inflow jet impinges in a region of low PO_2^*, causing a localized PO_2^* elevation. The vortex center is seen to decrease PO_2^* in both cases.

of Imai et al. [88], who conducted a numeric ATP transport study in parametrically created idealized aneurysms and vessels. The study focused on the impact to ATP transport through a wall-free model when an idealized spherical aneurysm was placed at different locations on a bent circular tube. This study demonstrated the possibility that sidewall aneurysms may harbor advective conditions detrimental to mass transport. The second study was from the work of Holland [86]. This work used a numerical model which incorporated the aneurysm wall and an intralumenal thrombus within the sac of patient specific geometries. The study found that for geometries considered in their work, oxygen transport to the dome regions was restricted, stenting had little impact, while the presence of a thrombus worsened the oxygen transport locally. The present work addressed the question of cerebral aneurysm wall hypoxia using a fundamental parametric approach to address the impact of sac morphology on wall oxygen levels. A parametric approach is particularly useful for gaining insight as to how the progression of sac geometry with time influences intramural oxygen levels. Further

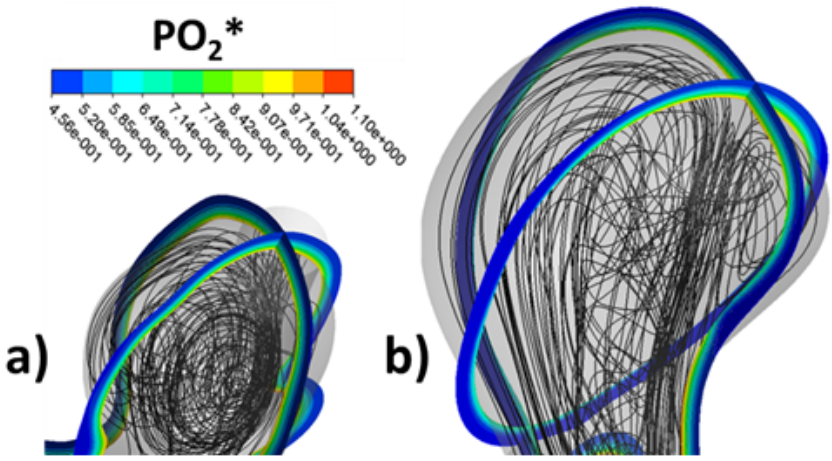

Figure 5.7: Cross-sectional PO_2^* contours within the aneurysm walls for a) Case1 and b) Case2. It is seen that PO_2^* within the wall interior is most impacted in vortex-center and post-inflow jet regions of Case2 more so than in Case1.

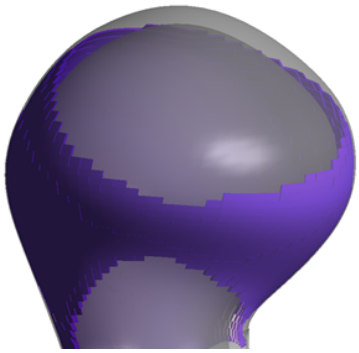

Figure 5.8: Volume rendering of wall regions in which the PO_2^* within the wall drops below the value of the cerebrospinal fluid. This criterion is never met in Case1.

work in this direction can provide insights as to whether growth/remodeling is a consequence of diminishing oxygen levels, and if so, at what point in the sac development oxygen concentration levels become a determining factor in the progression of an aneurysm towards rupture. There are many factors which can impact the oxygen supply that is available for

maintaining cerebral aneurysm wall integrity. These factors can be global (e.g., COPD) or localized (e.g., localized wall thickening). However, despite the numerous factors which can impact the level of free oxygen within the wall, the current work demonstrated that sac morphology alone can be a deciding influence on whether aneurysmal tissue will experience up to a 50% drop (or possibly greater) in lumen-side oxygen, all other parameters held constant. Most notably, this result kept the parent artery morphology fixed focusing on parametric changes to the sac geometry. The results suggest that hypoxia may shift over the timescale of an aneurysm's existence, depending on how growth and remodeling impacts the shape of the sac. Furthermore, as in the strict comparison between Case 1 and Case 2, this study's findings suggest that some aneurysms can be free (or mostly devoid) of hypoxia, while others can be impacted by it.

In both Case1 and Case2, despite notable differences in their average tissue-oxygen levels, one common feature was that the lowest levels of tissue oxygen occurred at the center of the vortex region. More critically, in Case1, this region is where the cascade of events triggered by hypoxia would be expected to initiate. Any subsequent impact of low tissue oxygenation within the sac's development would originate from this point (not considering any initiation of subsequent low oxygen regions resulting from continued changes in sac shape). In regards to hyperplasia, there is some clinical evidence to suggest a connection between low wall-oxygenation at the vortex center and wall thickening [189]. In particular, Tobe found that the locations of wall thickening in cerebral aneurysm tissue (resected following surgical clipping) corresponded to the site of vortex centers, estimated using patient specific CFD. The inflow jet also was found to dominate local tissue oxygenation. In Case1 and Case2, the lumen wall regions where the inflow jet shears possessed oxygen concentrations found in the core of the lumen flow due to enhanced mass transport. More particular to Case2, the dome region, surrounded in tissue having reduced oxygen content, was fully-oxygenated in the local region of the jet impaction zone. This effect reinforces the importance of the location of the inflow jet and highlights another role the flow structure possesses in aneurysm pathology. While the inflow jet has been implicated as a mechanism for causing mechanical damage to the endothelium, it can act as a delivery mechanism of oxygen in regions otherwise oxygen deprived. Further remodeling of the sac, as demonstrated in Chapter 3, has the ability

to relocate the point of inflow jet impaction. From here, one can conjecture that tissue oxygenation in more complicated sacs can be a strongly time-dependent factor over time scales of changes in geometry. The work of Tobe [189] has demonstrated an association between the jet impaction zone and localized wall thinning, suggesting the final stages of wall degradation, when associated with inflow jet impaction, are likely not driven by mass transport in the current instant, although a hypothetically different location of jet impaction at a previous time point would not allow the exclusion of oxygen concentration as a factor that contributed to the wall degradation.

At the time of conducting this work, to the author's knowledge, there are no available data on the oxygen requirements for homeostatic cellular function within cerebral arterial tissue. Nor, is the expected cellular response to changes in homeostatic oxygen concentrations available for cellular consumption known. As with the process of normalization of hemodynamic quantities such as saccular wall shear stress to parent artery values, the assumption was naturally made that the oxygen levels in the parent vasculature were sufficient for sustaining its oxygen needs, which could be patient-dependent. Further complicating the matter, there are many physical constants in the model, some of which can only be roughly estimated (Table 5.2, 5.1). Most, if not all of these parameters should, ideally, be chosen on a patient specific basis. Some parameters, such as wall thickness, are heterogeneous even within a single aneurysm [162]. As a result of these uncertainties, one can only predict relative changes or quantitative trends with regards to tissue oxygenation. However, even the well formulated governing equations enable important conclusions to be made about the impact of changes in some of the physical parameters, Table 5.3. For example, if the wall were to locally thicken, a greater gradient would be required to drive the same oxygen flux. Increased demands of oxygen due to wall remodeling or inflammatory changes could likewise cause a decrease in wall oxygen concentration due to a greater local sink term as oxygen is consumed. Wall structure, wall content (in the form of wall-oxygen diffusivity of each respective layer), as well as patient specific values of the cerebral spinal fluid oxygen content and blood-oxygen levels likewise substantially impact the sac-wall oxygen concentration. Regardless of the uncertainty in the material constants for the model, it is still straightforward to explore the impact of sac geometry on wall oxygen content. Such a study provides insights

Table 5.3: Table of wall-parameters which impact the wall tissue oxygenation, demonstrating the impact of changes in conditions on PO_2^*

Wall Parameter	Increase/ Decrease	Resulting Minimum PO_2
Wall thickness	↑ / ↓	↓ / ↑
Wall permeability	↑ / ↓	↑ / ↓
Cellular metabolic rate	↑ / ↓	↓ / ↑
Oxygen diffusvity	↑ / ↓	↑ / ↓
CSF PO_2	↑ / ↓	↑ / ↓
Lumen PO_2	↑ / ↓	↑ / ↓

into the implications of the evolving aneurysm shape over time, with respect to hypoxia. To this end, the next section of work in this chapter will focus on the lumenal-wall oxygenation resulting from the systematic parametric manipulation of sac morphologies for fixed parent geometry.

For example, if the wall were to locally thicken, a greater gradient would be required to drive the same oxygen flux than previously. Increased demands of oxygen due to wall remodeling or inflammatory changes could likewise cause a decrease in wall oxygen concentration due to a greater local demand. Wall structure, wall content (in the form of wall-oxygen diffusivity of each respective layer), as well as patient specific values of the cerebral spinal fluid oxygen content and blood-oxygen levels likewise substantially impact the sac-wall oxygen concentration. Regardless of the unknowns in the material constants relevant to the model, it is still straightforward to further explore the impact of sac geometry on wall oxygen content, which is an exploration into how remodeling of the aneurysm impacts its own oxygen transport. To this end, the next section focuses on the lumenal-wall oxygenation resulting from the systematic parametric manipulation of sac morphology.

5.3 Study 2: Impact of Sac Morphology on Lumenal Wall Concentration

In Chapter 4, it was shown that the intra-saccular flow was substantially influenced by aspect ratio (AR), bottle neck factor (BF), parent artery diameter to neck diameter (PN), and conicity parameter (CP). These parameters collectively determine the number and respective size of intra-saccular vortices, as well as the location of inflow jet impaction. In the previous section of this chapter, it was demonstrated that these aspects of the flow substantially impact wall oxygen transport. The objectives of this current section therefore will be realized by utilizing the information obtained in Chapter 3 on the influence of geometry on intra-saccular flow structure in order to develop a similar relationship between geometry and lumenal oxygen concentration. As described in Chapter 4, each non-dimension geometric parameter of interest, AR, BF, PN, SH, was varied within a range of physiologically relevant values, while keeping the other parameters and the parent geometry fixed. Therefore, the impact of each parameter on the flow could be clearly demonstrated free of confounding factors. Likewise, in this section, the manner in which sac geometry influences lumenal oxygen concentration will be analyzed and quantified.

5.3.1 Methods

The methods of geometry creation have been discussed in Chapter 4. To mesh the lumen geometry, tetrahedral elements were generated in ICEM CFD having an average minimum orthogonal quality of approximately 0.5, and having an average length-scale of 0.10 mm, which was previously found suitable for the grid independence of the solution. Prismatic wall-boundary layer elements were utilized on the lumen surface to resolve the steep oxygen concentration gradient on the wall; the first node was placed 1μm normal distance to the lumen wall. The modeling methodology between this section and the previous differs in that the wall was excluded from this analysis. The continuous interfacial PO_2 boundary condition at the lumen wall in the previous section was therefore replaced by a Neumann boundary condition for the PO_2 flux, q". Here, q" has been assumed to be constant on the lumen wall, and was set equal to the spatiallyaveraged q" on the lumenal wall obtained from Case1

and Case2 in the prior section. The flux, q", is therefore considered a representative oxygen flux which fulfills the metabolic requirements of a healthy cerebral artery. The lumenal wall oxygen concentrations obtained in the current sections therefore represent the lumen wall concentrations required to sustain oxygen transport for a healthy radial section of arterial tissue.

5.3.1.1 Justification The constant wall oxygen flux q" implemented in this section set the requirement for the lumenwall oxygen concentration required to sustain q" into the wall. In models harboring localized regions of poor advection, negative lumenal wall PO_2 values are predicted on the wall, indicating that a higher quantity of gaseous oxygen than what would be capable of dissolving in blood would be required to drive the oxygen transport through the wall, as the near-wall mass transport becomes diffusion dominant in regions of poor advection. Therefore, realistically, the hypothetical wall in the model would be required to lower its oxygen consumption, thus placing it at heightened risk for conditions resulting from oxygen deprivation. Scenarios in which q" would be an overrepresentation of the wall oxygen needs would pertain to wall-thinning or decreased metabolic needs. While the oxygen transport model in this section would falsely predict the occurrence of oxygen deficiency, the wall in that region would still be at risk for rupture due to the increased mechanical stress placed resulting from the localized thinning. Similarly, if q" under predicted the required oxygen flux, then any oxygen-deprived region predicted by the oxygen model in this section would in actuality exist in a state of greater oxygen deprivation due to the increase in wall thickness, decreased wall permeability, or increased metabolic needs of the increased tissue quantity. Furthermore, as seen in the previous section, the wall oxygen concentration (more so on the ablumenal side) is heavily influenced by the PO_2 in the cerebral spinal fluid – a patient-specific quantity. Permeability properties within the wall tissue could likewise be implicitly over or underestimated by the prescription of q"; however, this propagation of uncertainty is likewise selfrestricting, as a hypocellular wall would require less oxygen per unit tissue volume and a hypercellular wall would require more oxygen per tissue volume than the model accounts for.

5.3.1.2 Quantity of Interest

The influence of saccular geometric parameters was quantified by introducing a dimensionless characteristic diffusive length scale, L, normalized by the parent artery diameter, P, as $\frac{L}{P}$ for each aneurysm. Here, $\frac{L}{P}$ is equaled to

$$\frac{L}{P} = \frac{A_{vol}}{A_{neck}} max(\frac{H}{W}, \frac{W}{H}) \frac{1}{P} \tag{5.22}$$

where from Chapter 4, A_{vol} is the aneurysm volume and A_{neck} is the neck area. H, W and P retain their definitions as the aneurysm height and maximum width normal to the aneurysm centerline, and P as the parent-artery diameter before the bifurcation (Ref Figure 1). It is important to note that Equation 5.22 neither quantifies nor explains the number of intra-saccular vortices present in each case (this was covered in Chapter 4). Next, the lumenal wall PO_2 values in the aneurysm were normalized by the average parent artery lumenal PO_2, further denoted as PO_2^*. To distinguish between the parent artery and aneurysm lumen, the model lumen surface was divided by the neck plane. PO_2^* wall was then compared to L. In addition to relating geometric information to lumenal oxygen concentration, L serves as a means for quickly estimating the oxygenated state of the sac in a clinical setting.

5.3.2 Results

Figure 5.9 demonstrates the inverse relationship between $\frac{L}{P}$ and PO_2^*. All cases, having one or two vortices, generally obey the same rules of lumenal oxygen transport being inversely proportional to the aneurysm volume and ellipticity (H/W), and proportional to the aneurysm neck area and parent artery diameter.

Consideration of the number of vortices present in the sac both increased the strength of the correlation Figure 5.10a. Cases having one intra-saccular vortex possessed an inverse-linear relationship between $\frac{L}{P}$ and PO_2^* (Figure 5.10a), while cases having two intra-saccular vortices possessed a decaying power relationship for the range of $\frac{L}{P}$ values considered Figure 5.10b. The driven vortex has the effect of reducing the effectiveness of advection in the sac versus a singlevortex sac for moderate values of $\frac{L}{P}$; however, this effect tapers with larger values of $\frac{L}{P}$. The AR and BF groups warranted deeper examination. The impact of the vortex structure (i.e., the number of intrasaccular vortices) on PO_2^* is given displayed in

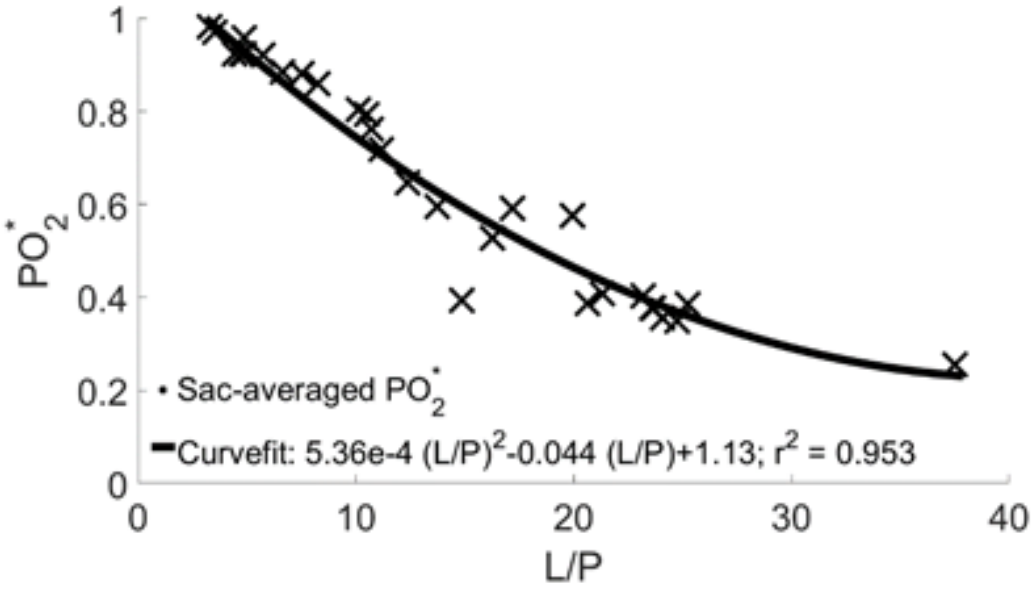

Figure 5.9: The ability of the geometric parameter $\frac{L}{P}$ to describe the sac-averaged oxygenation state of the lumen. This fit implies the dependence on wall oxygenation to be controlled by sac volume, ostium area, sac height, sac width, as well as the size of the parent harboring parent vessel.

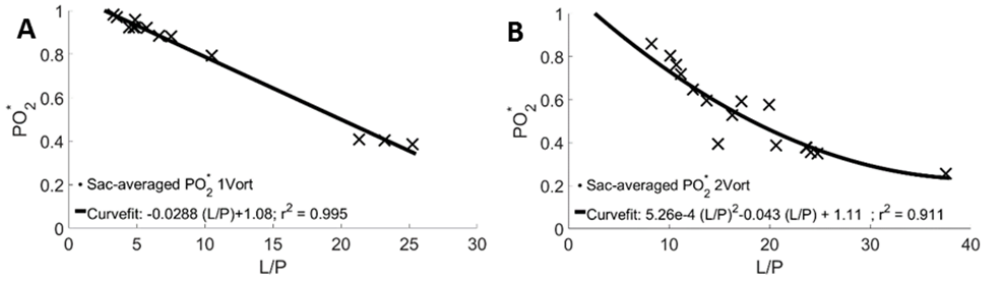

Figure 5.10: The $\frac{L}{P}$ with PO_2^* relationship divided between cases having A) one vortex and B) two vortices. The relationship becomes more complex when the driven secondary-vortex is present.

Figure 5.11a. In the AR model group, the transition from one to two vortices was found to increase the rate at which PO_2^* decays with increasing $\frac{L}{P}$ (Figure 11a). Here, the separated AR group case PO_2^* values are plotted with $\frac{L}{P}$. The AR family is divided by cases having one versus two vortices. Between the vortex subgroups, a linear curve fit $\frac{L}{P}$-PO_2^* slope decreases by a factor of 3.3 (i.e., from -0.0168 to - 0.0561) during the transition from one to two intrasaccular vortices. Similarly, the separated BF group case PO_2^* values are plotted with $\frac{L}{P}$ (Figure 11b). As for the AR group, a notable change in the $\frac{L}{P}$ PO_2^** relationship can be seen where the number of intra-saccular vortices transitions from two to one for a $\frac{L}{P}$ value of 16.7 (as an important reminder, $\frac{L}{P}$ does not determine the number of intra-saccular vortices present.). At this $\frac{L}{P}$ value, an inflection point occurs in the $\frac{L}{P}$ PO_2^* relationship as the increasing sac W initiates the flow field transition from two to one vortices at the expense of a greater sac volume. The impacts of one versus two vortices can best visualized in Figures 5.12-5.15. Figure 5.12 demonstrates the wall PO_2^* effects from flow-type transition in the AR group from one to two vortices when the AR exceeds 1.3 for a PN of 0.67 and BF of 1.2. As the second vortex grows in size, so does the area of decreased PO_2^*. As the jet impaction zone becomes more pronounced with increasing AR, the local PO_2^* is increased in this region. The BF group in Figure 5.13 demonstrates the transition from two to one vortex when the BF is increased by increasing the maximum sac width W while holding the neck area constant. While the secondary vortex is lost during the flow-type transition and the low PO_2^* area is diminished in the dome, it is done so at the expense of increasing the aneurysm volume, and thus lowering the PO_2^* magnitude downstream of the impaction zone, effectively redistributing the regions of poor oxygenation.

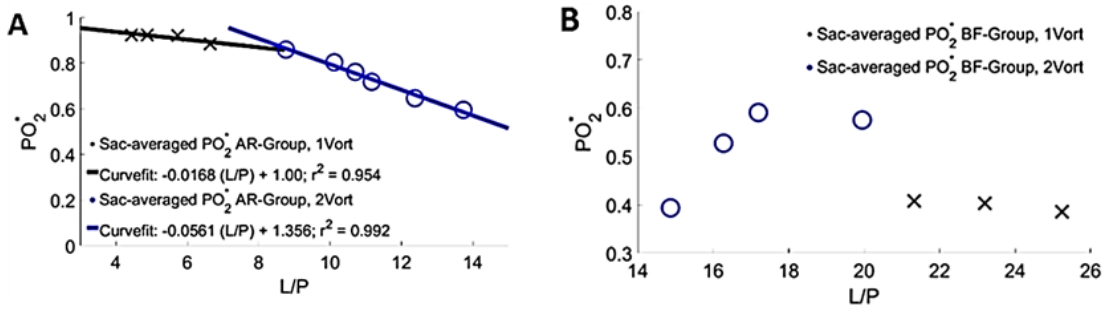

Figure 5.11: AR group divided between cases possessing one versus two vortices. The introduction of a secondary, driven vortex decreases the effectiveness of the blood to oxygenate the tissue. B) BF group divided between cases possessing one versus two vortices. There is a trade-off between increasing the aneurysmal volume to eliminate the secondary vortex and keeping the aneurysm volume as small as possible.

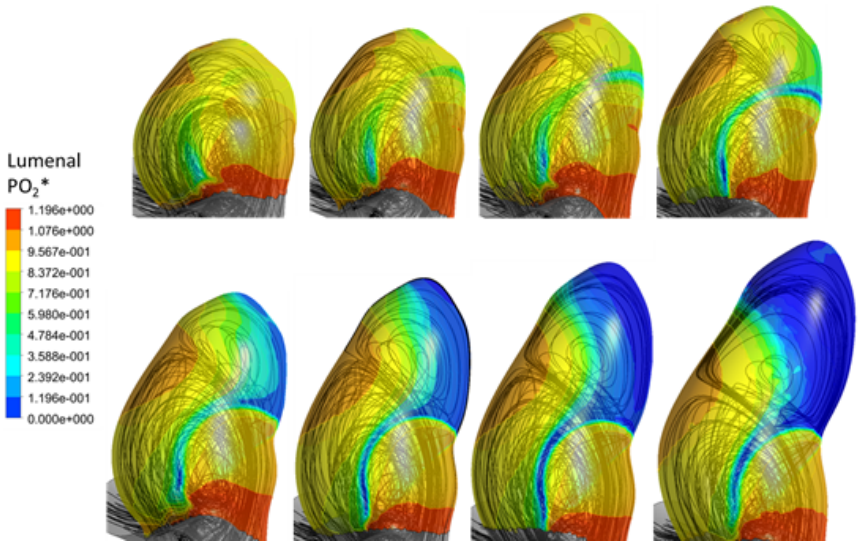

Figure 5.12: Lumenal PO_2^* relationship to geometry and flow-structure for the AR group. The PO_2^* within the driven vortex region decreases as this region grows. PO_2^* even for the largest AR case is still locally elevated in the region of jet impaction.

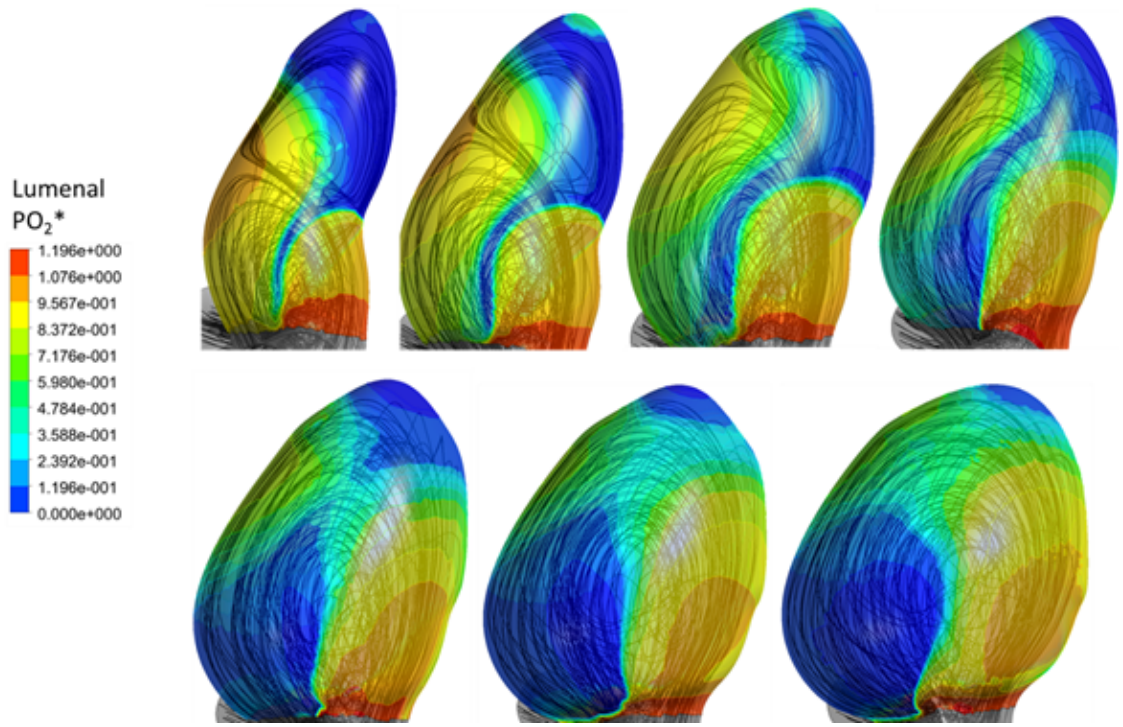

Figure 5.13: Lumenal PO_2^* relationship to geometry and flow-structure for the BF group. While the removal of the secondary vortex in the dome improves the dome oxygenation, it is done so at the expense of less oxygenation of the lower wall opposite to the side of jet inflow

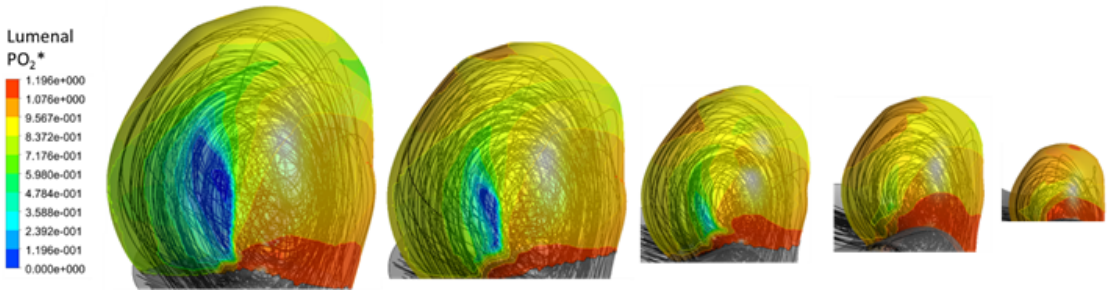

Figure 5.14: Lumenal PO_2^* relationship to geometry and flow-structure for the P/N group. Simply caling the sac size while retaining the sac shape has a limited impact on wall PO_2^* aside from ecreasing the wall oxygenation in the vortex core region of the larger cases.

Shown in Figure 5.14, as the sac is uniformly scaled in size (i.e., by manipulating P/N), little qualitative redistribution of low wall-oxygenation zone is observed. Rather, the PO_2^* is scaled inversely with size. This is most noticeable at the vortex center. It is critical at this juncture to emphasize that simply considering aneurysmal volume is not sufficient to describe lumenal oxygenation: while the largest BF and P/N group cases have volumes of 0.36 and 0.33 cm^3 respectfully, their sac-averaged PO_2^* are 0.39 versus 0.79. This emphasizes the importance of neck area, in that to provide sufficient advection in a given volume, the neck area must be appropriately sized.

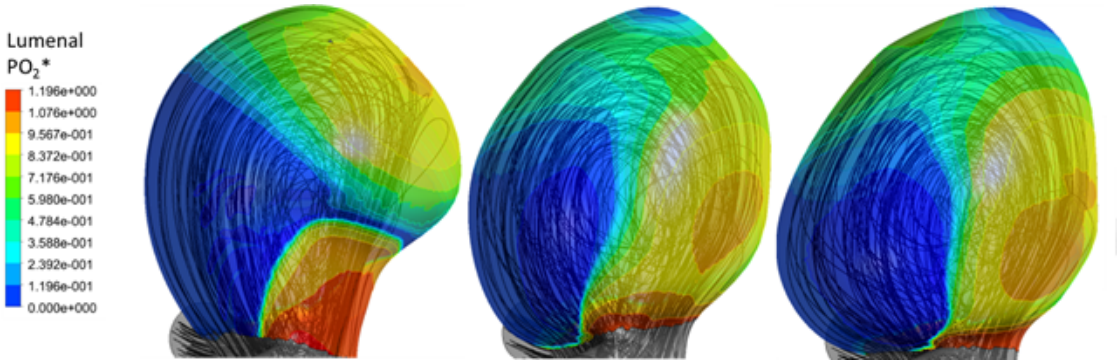

Figure 5.15: Shifting the maximum sac diameter closer towards the dome by increasing CP has the impact on moving the jet impaction location from the lower neck to the upper dome, and thus moving the region of high wall oxygenation correspondingly.

Modification of CP. i.e., modifying the location of the maximum sac diameter with respect to the sac centerline, resulted in shifting the jet impaction zone and thus a re-distribution of the localized sac PO^*, Figure 5.15.

5.3.3 Discussion

In this section, the behavior of lumen-wall oxygen partial pressure was explored when subjected to parametric modifications to the sac geometry. Sac geometry alone, all other parameters fixed, has a profound impact on the lumen wall oxygen concentration, which in turn, as shown in the previous chapter, impacts wall oxygen concentration. The state of wall tissue oxygenation in the sac relative to that in the parent artery was found to be able to be

approximated by a single geometric parameter. Additional qualitative information regarding the sac wall oxygenation state can be obtained by considering the number of vortices present within the sac, as well as the presence or absence of the inflow jet. The behavior of these flow features were extensively developed in Chapter 4. The current work yields important sac morphological descriptors for the sac harboring hypoxia. This work suggests that aneurysms having a large volume in conjunction with a constricted ostium are at risk for harboring hypoxic conditions. The presence of multiple vortices enhances the sac's propensity for hypoxic conditions. The most obvious value in such a parameter is that changes in sac geometry can be related to changes in available oxygen for wall tissue oxygenation. Such information is easily translatable for clinical use in image-based risk assessment for patients being temporally monitored. To the end of research, quantified geometric relationships such as $\frac{L}{P}$-PO_2^* are useful for assessing how sac remodeling impacts wall tissue oxygenation. For example if the aneurysmal volume were to increase without an increase in ostium area or change in the $\frac{H}{W}$ ratio, the wall tissue would trend towards being more oxygen deficient than previously, whereas if the ostium area were to increase without a change in the remainder of the sac geometry, the wall tissue would trend towards an improved state of oxygenation. This information is likewise useful for distinguishing whether a remolding process is either the cause versus the result of hypoxia, or whether another mechanism is likely the catalyst.

5.3.3.1 Wall Vasa Vasora and Implications for Hypoxia While typically absent in cerebral vessels [42], vasa vasora (VV)s have been previously been found in cerebral aneurysms [155]. The purpose of the VV is to oxygenate the ablumenal-side of the walls of large arteries (such as the aorta) where adequate lumenal-side diffusion of oxygen would otherwise fail. Cerebral arteries, however, possess thinner walls, and in addition, are surrounded ablumenally by oxygen-rich cerebral spinal fluid, which possibly eliminates the need of additional oxygen transport mechanisms. However, extensive VV networks have been found in diseased cerebral vessels, such as those being atherosclerotic, calcified [221, 137], or aneurysm-harboring vessels [155, 114, 113, 167, 133, 181, 111, 145]. Giant-sized cerebral aneurysms, for example, the intra-operative case study conducted by Iihara et al [111], are known for possessing extensive vasa vasorum networks. In this study, a 2 cm aneurysm in

the VA was treated by occlusion. The study noted that the VV network allowed for the aneurysm growth after its surgical occlusion, further demonstrating the ability for the VV to sustain aneurysmal growth. Similarly Nakatomi et al. [145] discovered a VV network via post-autopsy histology in a 3.2 cm diameter basilar artery bifurication aneurysm that fatally ruptured. In both studies, intimal hyperplasia was present. Krings et al. [113] reported on 20 patients with giant aneurysms and indicated the presence of VV found during surgery. They further determined the source of intramural throumbus in conjunction with bleeding as the VV network. In the aforementioned studies, it is not clear as to whether the wall thickening or thrombus had occurred before or after the formation of the VVs network; however, the formation of VVs has been suggested to be a result of hypoxia [78]. This mechanism may involve hypoxia-activated inflammatory processes, stimulating angiogenic factors [137, 74, 139]. Given this conjecture, the current work shows that, due to a large sac volume, lumenal-side oxygen deficiency could have been the initiating requirement for the VV network found in giant aneurysms. The discovery of bleeding from the VVs in giant aneurysm [111] in conjunction with their causation on the formation of intramural thrombus suggests that the VV in large aneurysms is prone to failure. This can be problematic in the sense of the ruptured VV acting as a conduit for inflammatory agents into the wall such as macrophages and enzymes in leukocyte production [114] which can aid in the degeneration of the extra cellular matrix, and severing the supply of oxygen to other wall tissues which rely on the VV due to insufficient lumenal-side oxygen transport. In a study of impaired VVs flow in the porcine descending thorasic aorta [5], it was found that impaired flow from the VV led to increased wall stiffness, and altered fiber morphology. The alterations included a loss of the normal sinuous pattern, as well as thinned and fragmented appearance in the outer media. The loss of smooth muscle cells was also reported. It was further suggested that this alteration in tissue characteristics could contribute to interlaminar shear stresses which contribute to rupture. It is furthermore reasonable to speculate that, if these effects are caused from oxygen deficiencies, oxygen deficiency in the wall tissue in general could instigate these deleterious changes.

5.3.3.2 Implications for Growth and Remodeling The current work reveals insightful behavior into how sac growth may impact the tissue oxygenation within the sac. For example, found relationship between PO_2 and the characteristic length scale $\frac{A_{vol}}{A_{neck}} max(\frac{H}{W}, \frac{W}{H}) \frac{1}{P}$ normalized by the parent vessel diameter suggest that smaller, newly formed aneurysms, having a neck diameter half that of the parent artery diameter, experience oxygenation levels comparable to their parent vessels regardless of what hemodynamic stresses may be present in the sac. In Chapter 4, it was shown that these aneurysms experience an elevated wall shear stress at the neck respective of the parent vessel, and lower wall shear stress in the dome region due to the constriction of flow into the sac. It then seems reasonable to conjecture that the initiation and early stages of aneurysms are mediated by hemodynamic stresses more so than oxygen transport. However, if the aneurysm were to enlarge to flow patterns prohibitive of oxygen transport, then under-oxygenated tissue may become a factor in aneurysm remodeling along with wall shear stress. Investigating these conjectures, even with harvested tissue, can be heavily confounded by growth and remodeling, as the results show. For example, if an aneurysm were to simply enlarge uniformly as investigated in the PN family (Figure 5.14), then regions of high and low PO_2 would scale in a similar manner. Neither the jet shear impaction regions nor the vortex center regions shift with the enlarging aneurysms. Therefore, the oxygen history of harvested tissue in this example would be relatively straight-forward to predict from known time point (i.e. time of harvest). However, in the case of an expanding BF or AR, regions that are well-oxygenated versus poorly-oxygenated shift locations with the changing flow structure. This situation can furnish scenarios where tissue once influenced by hypoxia is well-oxygenated at the time of harvest and vice versa. This work furthermore demonstrated that due to the shifting of well/poor oxygenated regions over a variety of geometric configurations, regions of poor oxygenations are not limited to any one region of the sac, as they have been shown to occur even in the neck region opposite to the inflow region. In the case of large aneurysms, as the $\frac{L}{P}$ PO_2 relationship predicts, wall oxygenation becomes unsustainable from the lumenal side. This is consistent with the observation that large aneurysms possess an extensive vasa vasorum network. Hyperplasic walls are typically encountered with large aneurysms [111, 145]; however, to the author's knowledge, there is no information available to conclude whether

the vasa vasorum was a result of a thickening wall or the thickening wall, nourished by the extensive VV network, was a result of a pre-existing VV network in place to cope with a volume that is too large for the neck area, or to compensate for an oxygen-deficient region as a result of a H/W away from unity.

5.4 Study 3: Discrepancies between Low Wall Shear Stress and Low Lumenal Oxygen Concentration

In studies of abdominal aortic aneurysms (AAAs), the locations of hypoxic wall tissue are frequently associated with wall regions possessing low wall shear stress (WSS) [15, 11, 200, 201]. It is thought that the low wall shear stress and high residence time of a circulation zone within AAA are responsible for the accumulation of platelets and other aggregates that create an environment suitable for development of an intra-lumenal thrombus. Hypoxia has therefore been thought to occur as a result of the thrombus being an obstruction to lumenal oxygen diffusion to the underlying tissue. It is however unknown as to whether hypoxia was a factor which preceded the formation of the thrombus. The same associations have been made with atherosclerotic plaque and hypoxia [216, 96]; and likewise, the question is open as to whether hypoxia is a causal or associative factor with the existence of these structures [178]. Applying the same principle to cerebral aneurysms may therefore seem permissible, though still with the open question as to the involvement of oxygen in wall degradation. It may seem, at a brief glance, straightforward and intuitive to associate low flow conditions with both low wall shear stress and low wall oxygen content given the nature of the governing equations. However, the previous two sections, as well as Chapter 4, suggest that caution is warranted when making conclusions regarding the PO_2 from the information on sac geometry and the WSS field. The relationship between geometry and flow structure can be complicated, and the relationship between PO_2 and WSS is even more complicated. Wall shear stress is defined (setting aside viscosity for the moment) only as the gradient of velocity normal to the wall at a point. The oxygen concentration on the wall, however, is described by the solution to an advection-diffusion-reaction equation having a non-linear

source term dependent on both oxygen concentration, and the local shear stress. Clearly, by this notion, it is not unreasonable to postulate that WSS may not always be a surrogate for PO_2. In cerebral aneurysms, low WSS has long been thought as a marker of endothelial dysfunction and inflammation within the wall [63, 124, 38, 99, 64, 59] potentially leading to aneurysm destabilization. However, to the author's knowledge, this association has only been conjecture, and has never been considered to be a complete explanation of the mechanism responsible for aneurysm growth or destabilization. Of the many possible reasons as to why this may be, one explanation may be that low WSS does not strictly correspond to hypoxia as previously implicitly assumed. The results from the previous section support the notion that such a WSS PO_2 relationship may not be so trivial, and therefore motivates the final section of this chapter, where the correspondence between time averaged wall shear stress magnitude (TAWSSM) and PO_2 will be explored.

5.4.1 Methods

In the previous section, four groups of models – parametric variations of a basilar bifurcation aneurysm sac - were created. Each group varied one of the four sac non dimensional parameters, H/N, W/N, P/N, and S/H, while having identical parent vessel geometries and boundary conditions. Numerical steady solutions to the Navier-Stokes equation were obtained, as well as to the advective-diffusive-reactive equation for species transport (oxygen and oxyhemoglobin). Time-averaged wall shear stress magnitude (TAWSSM) and wall oxygen partial pressure (PO_2) were therefore available at every node on the lumen surface. Each one of these nodes comprised the vertices of the triangular faces to each prismatic element comprising the lumen wall. The element-face averaged quantity was therefore computed by taking the average of the three nodes weighted by their distance to the face centroid. This process was taken over the entire sac-lumen surface. It was then possible to calculate an area percentage of the population sac surfaces containing a given range of TAWSSM or PO_2 range. If there were a perfect correlation between TAWSSM and PO_2, then a given value of TAWSSM inserted into a function should return a unique value of PO_2, regardless of the chosen boundary conditions in the model. Therefore, absolute values, rather than

the normalized values used in the previous sections of TAWSSM and PO_2, were compared. In this manner, a perfect correlation between TAWSSM and PO_2 should yield a curve of infinitesimal thickness; if there is any deviation in the relationship, there will be a spread in the data that deviates from a curve. Any deviation in multiple PO_2 values for a given WSS value can then be quantified by a probability distribution about a given TAWSSM value. As such, the objective of this section is to explore the accuracy of the association of low wall shear stress to the deleterious consequences of low- oxygen mediated processes within the wall. The TAWSSM and PO_2 values for each aneurysm lumen wall at every element face were concatenated into a single dataset. The TAWSSM values were then grouped over the range of TAWSSM into groups of 1.0 dyn/cm^2, starting from 0.0 – 1.0 dyn/cm^2 up to the maximum of 119 – 120 dyn/cm^2. The corresponding PO_2 values to each TAWSSM data point then formed a distribution within each TAWSSM group. The PO_2 distributions of each TAWSSM group where then assessed by separating the PO_2 values into 10 bins dividing the range of the PO_2 spread into 10 equal segments per every TAWSSM group. The assessment was based on noting two extreme possible outcomes related to the current topic in question. If the PO_2 perfectly corresponded with TAWSSM, then all PO_2 values within each TAWSSM group would fall into one bin. Conversely, if there were no correlation between TAWSSM and PO_2, the PO_2 would be equally distributed among the bins of each group, provided the PO_2 range in the highest-valued bins of each TAWSSM group are approximately equal. Therefore, in the case of perfect correlation, the PO_2 values would occupy one out of a potential ten bins, and in the converse case they would equally occupy ten of ten bins. A metric was therefore devised, ranging from 0.1 – 1.0 which measured the fraction of normalized area (with respect to the magnitude of the PO_2 bin containing the highest number of occurrences) occupied by the probability distribution. This metric provides a means of demonstrating for what values of TAWSSM, if any, PO_2 predictions via TAWSSM values would become confounded, and is noted as the area fraction of uniform distribution, defined as:

$$\text{AFUD} = \sum_{n=1}^{N} \frac{1}{N} \frac{(\%\text{Sac Area of } PO_2 \quad \text{in bin n})}{(\text{Largest } \%\text{Sac Area of } PO_2 \text{ bin})} \tag{5.23}$$

where $N \equiv$ the number of PO_2 bins and $n \equiv$ the n'th PO_2 bin, %Sac Area of PO_2 in bin n $\equiv$ percent of all sac areas containing PO_2 values belonging to the n'th PO_2 bin, and Largest %Sac Area of PO_2 bin $\equiv$ the maximum area percentage represented by any PO_2 bin.

5.4.2 Results

The TAWSSM-PO_2 data scatter for all cases is shown in Figure 5.16 A,B. It is seen that for TAWSSM of 15 dyne/cm^2 and above, the corresponding PO_2 lies predominately within the bin above 11000 Pa, indicating that for mean physiological TAWSSM and above wall oxygen needs are probably well satisfied. However, below the physiological time-averaged WSS value, the TAWSSM relationship with PO_2 becomes complicated, as seen in Figure 5.16B. Below a TAWSSM of 10 dyn/cm^2, PO_2 values at some locations begin to appreciably decrease while PO_2 remains unchanged at other locations. Below 5 dyn/cm^2 there is appreciable scatter in PO_2 values across its possible range.

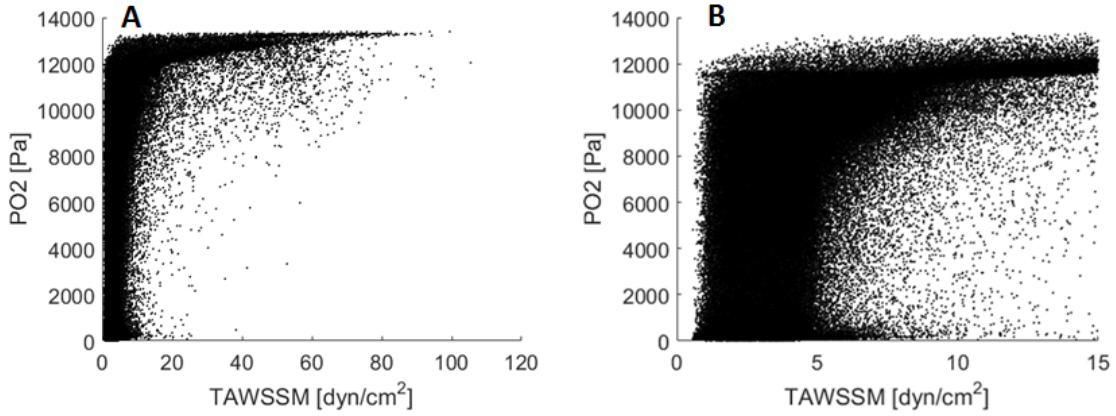

Figure 5.16: A: Scatter plot of the TAWSSM and PO_2 values at all sac wall nodes for cases shows appreciable scatter within the TAWSSM PO_2 relationship.B: While PO_2 seems well predicted by phisiological levels of TAWSSM, the relationship deterriorates appreciably below 5 dyn/cm^2

The PO_2 distribution was found to be closest to uniform at all the lumenal locations possessing TAWSSM between 1.025 and 2.025 dyn/cm^2 (Figure 5.17). In this TAWSSM group, the mean PO_2 was 6175 $\pm$ 3380 dyn/cm^2 giving a coefficient of variation (CV) of

0.547. Of the ten PO_2 bins, the maximum percent sac area to which any one of the PO_2 bins corresponded was 15.2%. The TAWSSM group having the highest standard deviation was the 0.0 – 1.0 dyn/cm^2 group (Figure 5.18); showing that while 57% of the sac area possessing 0.5 $\pm$ 0.5 dyn/cm^2 possessed the lowest category of PO_2, the remainder of the sac areas having this TAWSSM had a near-equally probable value of any other permissible PO_2. Between TAWSSM values of 15 $\pm$ 0.5 dyn/cm^2, 85.4% of the PO_2 fell in highest 10% of the PO_2 range (Figure 5.19), indicating that the vast majority of PO_2 values at locations of physiologically healthy TAWSSM in the aneurysms of all cases can probably be assumed to be healthy.

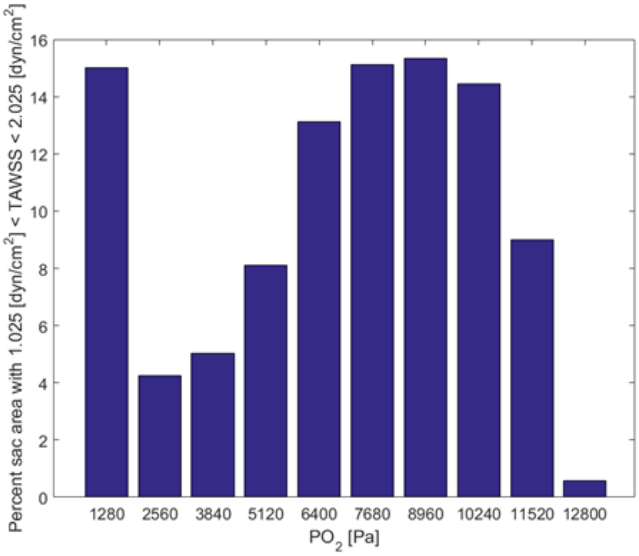

Figure 5.17: Distribution of sac area possessing PO_2 values falling in each of the ten PO_2 bins for TAWSS between 1.025 and 2.025 dyn/cm^2. PO_2 is the least predictable from TAWSSM within this TAWSSM range.

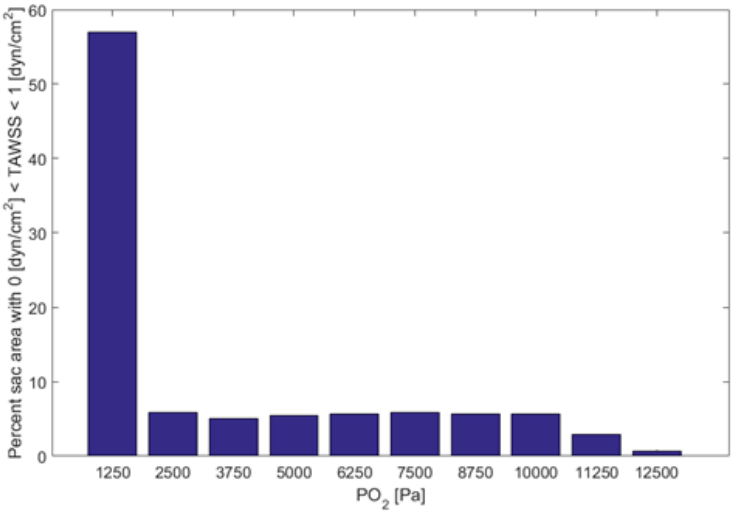

Figure 5.18: While TAWSSM below 1 dyn/cm^2 is mostly associated with hypoxic lumenal wall conditions, the presence of lumenal side hypoxia is not guaranteed.

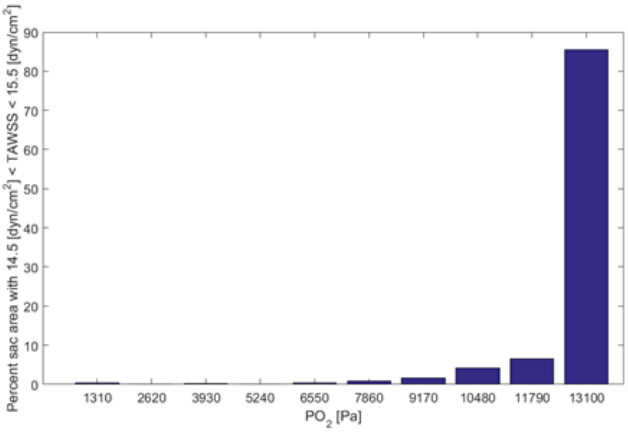

Figure 5.19: With TAWSSM in a physiologically healthy range, even within the aneurysm sacs modeled, lumenal-side oxygen transport is most likely adequate

An inspection into the deviation from PO_2 having a uniform probability distribution for a given range of TAWSSM values (Figure 5.20) reveals that centered around a TAWSSM value of 1.525 dyn/cm^2, the relationship between TAWSSM and PO_2 trends towards becoming random as the area fraction of uniform distribution metric attains its highest value of 0.67; indicating that 67% of the area bounded by the histogram in Figure 5.17 is occupied by PO_2 values. Away from this TAWSSM range, the predictability of PO_2 from TAWSSM increasingly grows, as the PO_2 distributions trend toward all PO_2 values falling within one bin rather than being distributed over many.

5.4.3 Discussion

This section investigated the relationship between time-averaged wall shear stress magnitude (TAWSSM) and the partial pressure of lumen wall oxygen (PO_2). The objective was to explore the validity of assuming the biological effects of hypoxia to be present at areas of low TAWSSM. An agreeable correspondence between the two quantities would imply that low TAWSSM can be used as a surrogate for hypoxia, and therefore, that the biological processes within the wall driving the growth and remodeling of the sac are, at least in part, hypoxia driven. The results however showed that the range of TAWSSM considered phys-

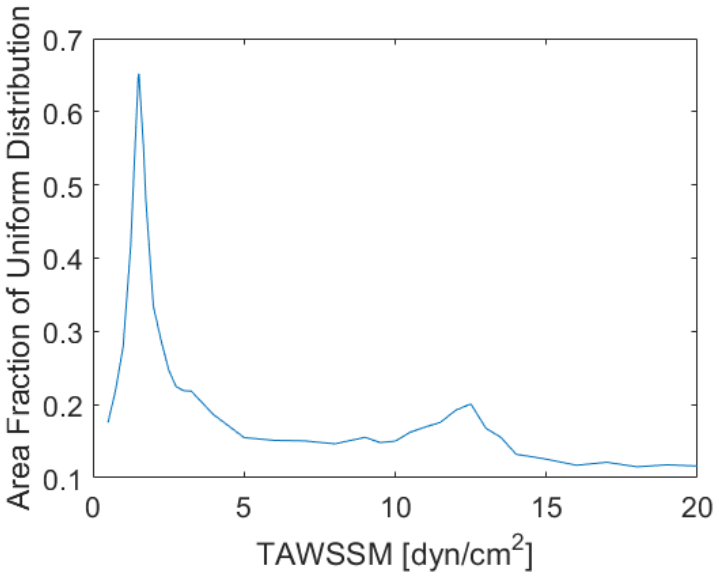

Figure 5.20: Plot of area fraction of uniform distribution (AFUD) for TAWSSM. An AFUD of 1.0 would signify that all phisiological values of PO_2 are equally likely to occur the corresponding TAWSSM, while a value of 0.1 would signify that the PO_2 at a location on the sac wall would be bounded to a range of $\frac{1}{10}$ of the full possible range of PO_2.

iologically unhealthy by Malek et al., i.e., below 4 dyn/cm^2 [124], is where the correlation between TAWSSM and PO_2 is the least predictable. Particularly, between 1.025 and 2.025 dyn/cm^2, five of the ten PO_2 value bins, 1280±640, 6400±640, 7680±640, 8960±640, and 10240±640 Pa, each represented more than 12%, or more than 50% total, of all the sac areas that contain TAWSSM between 1.025 and 2.025 dyn/cm^2. The roughly equal likelihood that the lumen wall PO_2 in this TAWSSM range can be 1280 Pa versus 10240 Pa could generate a substantial confounding factor when studying from a biological standpoint the impacts of low TAWSSM on the aneurysm wall

5.4.3.1 Separation of Low Wall Shear Stress and Hypoxic Pathology As previously introduced low wall shear stress on the arterial endothelium in general has been implicated as a probable cause for endothelium dysfunction. This is partially may be due to the

loss of cellular alignment among the endothelium [2, 109], allowing for the heavily increased infiltration of deleterious macromolecules such as lipids or macrophages [59, 2]. Furthermore, the reduced WSS results in a dysfunction of NO which is released via shear-induced stimulation; leading to the aggregation of red blood cells in conjunction with the accumulation of platelets and leukocytes along the intimal surface [71, 122, 134, 138]. This aggregation and accumulation may cause intimal damage and further infiltration and lead to subsequent inflammation which could then degenerate the structure of the wall [192, 191, 44, 45].

In the most extreme cases of chronic hypoxia, cells cannot function and will ultimately die. However, there are many more less-extreme impacts of hypoxia. Reactive oxide damage occurs when, under hypoxic conditions, the lack of O_2 mediates the increase of free radical production such as OH^-, which can facilitate the oxidation of lipids, nucleic acids, and proteins, possibly compromising the function of cells or facilitating cell death [86, 108, 171]. Nitric oxide levels are also increased from hypoxia, as NO is a potent vasodilator in response to low cellular oxygen levels. The intended consequence of increased NO production is that the vessels should dilate to increase blood flow to hypoxic areas. This effect is likely in part from increased smooth muscle cell contractility [142, 1]. Nitric oxide furthermore regulates SCM migration and proliferation, inhibits platelet adherence [43, 170], and low levels of NO can act as an antioxidant [93]. There also is the additional impact of neo-vascularization discussed previously, where the wall is degraded in order to allow the formation of neo vessels in the form of vasa vasora to proliferate through the hypoxic wall.

Clearly, the impacts of low wall shear stress and low cellular oxygen levels have pathways and effects which seem to either complement each other, contradict each other, or that act in their separate ways. For example, cellular damage seems to be a consequence of both conditions, albeit via different mechanisms. However with respect to nitric oxide production, vascular tone, or platelet adherence to the wall, these conditions seem to have contradicting consequences. The results in this work demonstrate that both conditions of low TAWSSM and hypoxia do not necessarily have to exist simultaneously. Rather, it is proposed hemodynamic studies comprising intra-cranial aneurysmal walls make the distinction between wall regions containing low TAWSSM under normoxic conditions versus wall regions containing low TAWSSM under hypoxic conditions.

5.4.3.2 Current Limitations

The limitations in previous sections of this chapter still generally apply to this section. However, it is of particular importance here to emphasize that the major limitation pertaining to this work is the lack of information on what PO_2 values correspond to normoxia, reduced oxygenation, or hypoxia. More particularly, knowledge of whether the aforementioned consequences of hypoxia occur as a continuous spectrum or by surpassing a threshold value would allow for vastly improved quantitative analyses of intra-saccular flow studies. Further, the modeling techniques utilized in this chapter do not consider the altered oxygen demands that would result from the aforementioned cascade of events resulting from hypoxia, low TAWSSM, or the combination of both. It is therefore more complicated to place strict quantitative bounds on what conditions may be present in the wall with respect to oxygen.

5.4.4 Chapter Overview and Discussion

This chapter covers a body of work that explored oxygen transport in cerebral aneurysms. The first aim was to determine what effects intra-saccular advection have on wall oxygen levels. It was found that sac geometry alone can indeed influence intra-saccular advection of oxygen to the lumenal side of the sac wall. This finding has the immediate implication that sac remodeling alone can have positive or detrimental consequences on wall oxygen levels. The next aim was to obtaining a more in-depth understanding of this process. On a general level, it was found that per a given parent geometry and flow rate, a proper ratio between the sac volume and ostium area must be kept in order for proper oxygenation to be maintained. Even with this criterion met, deviation from a spherical sac geometry (such as a sac possessing a high aspect ratio) can further impede oxygen transport. This has the immediate implication that as an aneurysm enlarges, its ostium must enlarge accordingly to accommodate the increased need for a higher intra-saccular volumetric flow rate. The early stages of aneurysm pathology may therefore be exceptionally important to understand – particularly the rate at which the ostium enlarges with respect to the sac volume as it may have a large impact on determining the future trajectory of the sac's remodeling. This is well demonstrated by the study of the aneurysm with the smallest sac volume (see Figure 5.14),

where the sac-averaged wall PO_2 is the same as that in the parent vessel, yet due to the large ratio of the parent artery diameter to the aneurysm neck diameter, the sac-averaged wall shear stress magnitude Is only 0.39 times that of the parent vessel. However, it was further found upon closer inspection that the relationship between localized wall oxygenation and sac geometry is too complex to be described by a single parameter. The location of the inflow jet impaction is an important factor in wall-oxygenation, yielding locally-elevated levels of PO_2 even when surrounded by regions of poor advection. The location of the impact jet furthermore can move with sac remodeling, and thus have a dramatic impact on localized wall oxygenation. As regions of low wall oxygenation were shown to shift with sac remodeling, the need for clinical data from multiple time points is made evident for studying both remodeling, and to have the information necessary for studying harvested tissue samples while placing the sample findings in the proper context of the sac history. The last aim of this study was then to determine to what extent hypoxic conditions coexist with low wall shear stress. Imai et al. [88] had noted in their study that regions of decreased ATP transport seemed to correspond with regions of low wall shear stress. The current study found that, while in general this is true, this notion can be refined. Hypoxia was least likely to occur for wall shear stress above the 10 dyn/cm^2 for healthy arteries (suggested by Malek et al. [124]) even in aneurysms; however, below this range of wall shear stress, the co-existence of low wall shear stress and low wall oxygen content becomes ambiguous within the current study. This was found particularly true at wall locations with wall shear stress values between 1.025 and 2.025 dyn/cm^2 where the PO_2 levels exhibited a relatively uniform distribution of values. A direct implication from this finding is that different wall biology may be present in regions possessing similar low wall shear stress values, due to substantially different levels of wall oxygenation.

5.4.5 Limitations

The work herein is subject to several limitations, originating from within and outside the scope of the framework of computational modeling. Perhaps the largest extrinsic limitation of the study is that it is difficult to quantify degrees of hypoxia when there is, to the author's

knowledge, no known data as to what the metabolic needs (and hence oxygen requirements) are of the cells comprising the arterial wall. This work attempted to address this by examining the ratio of the Sherwood and Damkholer numbers as well as considering partial pressures of oxygen normalized by those of the (presumably) healthy parent artery. However, there is not enough information known to make any direct claim that the predicted PO_2 values would indeed induce a state of hypoxia. The next limitation involves the question of patient-specific values. Many (if not all) parameters controlling oxygen transport within cerebral aneurysms can vary on a case by case basis, such as wall thickness/structure/content, the particular metabolic needs, blood flow rate, as well as blood and cerebral spinal fluid oxygen concentrations. The goal here however was not to analyze any patient-specific case, but to develop the framework and knowledge base for moving towards these analyses, provided the appropriate information is known (such as wall thickness, etc.). However, even if such information is not available or practical, this work provides guidance in understanding how geometry and flow impact wall oxygenation. Within the framework of the study itself, the models of the chemical kinetics are not a unique choice; however, their simple parameters are easily obtained under experimental conditions. It is however questionable as to the applicability of these models in the setting of the cerebral circulation, and particular, within the pathological conditions of aneurysms flow. The morphology of the blood for this study must also be called into question; specifically, with regards to the residence time of the hemoglobin within the sac. It is conceivable that as the diameter of the aneurysm approaches from above the diameter of a red blood cell that the assumption of the blood able to be approximated by a continuous medium becomes invalid. Long hemoglobin residence times not predictable via a Navier-Stokes fluid may occur due to blockage at the neck, thus rendering the current model under-predictive of hypoxic conditions. Such a model incorporating immersed particles would be warranted for future study, though computationally expensive.

6.0 High-Frequency Velocity and Wall Shear Stress Oscillations in Cerebral Aneurysms: Generation and Behavior

The author at this point wishes to express gratitude to Dr. Hessam Babaee as well as Amirreza Hashemi and Prerna Patil under his advisement for their support and guidence with the use of the Nektar code utilized in this chapter.

SUMMARY - High frequency velocity oscillations (HFVOs) have been previously identified in the cerebral arteries with frequencies that can be orders of magnitude higher than that typical of cardiac waveforms. HFVOs have been identified in the clinic [206], computationally [7], and experimentally [212]. Most HFVOs have been associated with cerebral-vascular diseases such as atherosclerotic stenosis. However, computational simulations have suggested of additional origins in vessels free of any such stenotic features but tortuous in nature (such as the internal carotid artery (ICA)). A central objective of the current work was to use high fidelity computational fluid dynamics to identify clinically relevant vascular conditions sufficient for generating HFVOs in ICAs, and to then explore the extent to which these HFVOs propagate downstream from the ICA into aneurysms harbored by the vessel. Using a computational parametric approach in idealized geometries, we found that a combination of sharp curvature immediately upstream of a vessel expansion could generate HVFOs; this combination was a necessary condition for HFVO generation in our scope. Furthermore, the HFVOs propagated downstream in a sidewall aneurysm with the most intense fluctuations in wall shear stress magnitude (WSSM) close to the inflow jet, whereas away from the impact jet, these WSSM fluctuations were largely dissipated. A comparison of the WSSM calculated by numerical techniques which resolve and fail to resolve HFVOS then showed that the locations of high and low time averaged WSSM within the sac are reasonably unaffected by the under-resolved HFVOs in lower resolution studies, though the magnitudes themselves differ appreciably. The results within this work offer key insights into the ongoing efforts to answer the open question as to how HFVOs impact cerebral aneurysm pathology.

6.1 Introduction

Hemodynamics within intracranial aneurysms (IAs) are believed to impact aneurysm pathology [58, 23]. A plethora of computational work on intra-aneurysmal hemodynamics has focused on the impact of spatial distributions of at least one metric pertaining to the wall shear stress vector. The most common of these is the magnitude of the wall shear stress (WSSM) - a time dependent scalar field [128, 177, 208, 26]. Examples of other field variables are the time averaged WSSM and various metrics involving the gradient of WSSM, denoted as WSSG [116, 51]. Alternatively, this information can be reduced to a single representative value for the entire sac, for example, the spatial maxima, minima or WSS averaged over both space and time. Other field variables have been introduced to more directly examine the temporal information within the WSS vector; e.g., the oscillatory shear index and the gradient oscillatory index [176, 186]. Alternative to analyzing WSS metrics on the wall, some studies directly analyse the flow that produces WSS. Examples of these type of studies include analysis of the inflow jet and the number and types of vortices [23, 32].

Most of the aforementioned works have used computational strategies that were chosen to resolve temporal features at frequencies on the order of the cardiac waveform. More recently, studies utilizing high-resolution numerical approaches [7, 121, 193, 194, 195, 198, 57, 211, 210] or in-vitro experiments [212] have suggested that high-frequency velocity oscillations (i.e., frequencies several orders of magnitude higher than one cardiac cycle) can exist in the cerebral vasculature at Reynolds numbers as low as 550. These findings could be relevant because there is evidence in biological studies that high-frequency velocity oscillations may pathologically impact the arterial wall. For example, high-frequency flow characteristics associated with turbulent-like flow have been found to significantly increase the endothelium turn-over rate, compromising the integrity and function of the endothelium mono-layer [46, 205]. Hsiai et al. [87] demonstrated in vitro that endothelial cell elongation and remodeling is significantly impacted by wall shear stress slew-rates by subjecting cultured endothelial cells to cardiac cycles of zero, one, and two Hz. Evidence from Himburg et al. [80] furthermore suggests that endothelial cells exhibit a pro-inflammatory response to shear stress frequencies greater than that of a normal heart rate (2Hz), especially at lower shear stress magnitudes.

The question must therefore be rightfully raised as to what the level of importance of the temporal fluctuations of wall shear stress on aneurysm wall pathology is. Future studies could assess the response of the wall to frequency content within the intra-aneurysmal blood-flow as well as the role that temporal changes in orientation of the stress vector in conjunction with the magnitude of the time averaged WSS plays in aneurysmal progression.

Performing computational studies that include high-frequency flow oscillations (HFVOs) remains challenging. Solving the coupled system of governing equations with appropriate methods to resolve the computational domain both in space and time requires extensive computational resources. Valen-Sendstad et al., for example, [195] noted the temporal resolution alone of their models was one to two orders of magnitude finer than that reported in CFD-based studies that neglect HFVOs. Simulations utilizing h-p spectral element methods conducted by Baek et al. [7] were reported to consume 15-20 h per cardiac cycle utilizing 512–768 cores. The motivation for tackling these computational challenges is clearly warranted as there is currently a poor understanding of the conditions under which HFVOs are generated, although there are some important prior works. For example, turbulent flow has been observed downstream of severe stenosis of the ICA in clinical studies such as that of Wood [206], which reports the existence of turbulent flows downstream of stenosis greater than 70%, where velocities are as high as 265 cm/s. Computational studies of flow in stenosed vessels (e.g., [12]) have demonstrated that HFVOs can be generated downstream of 50% contractions. However, this degree of stenosis is not typical in prior studies of HFVOs in patient specific geometries: neither those using computational methods (for example, [193, 195]) nor in-vitro studies [212]. Rather, Varble et al. [198] have conjectured that HFVOs can be initiated from the inflow jet at the ostia of bifurcation aneurysms, suggesting a dependence of HFVOs on aneurysm geometry. While such dependence may exist, Valen-Sendstad et al. [195] have identified HFVO initiation within the ICA itself, suggesting additional possible sources of HFVO generation may be those arising from]the tortuous geometry of the ICA. Furthermore, the authors noted that ICAs which generate the most prominent degree of HFVOs possessed sharp bends with local vessel narrowing in conjunction with sudden vessel expansions.

Motivated by the aforementioned work, the current study revisited the topic of HFVOs in the cerebral vasculature to systematically identify conditions in the ICA responsible for HFVO generation. The current study furthermore explored the behavior of HFVOs when present in an aneurysm harbored by this vessel. The ICA was selected as the target vessel because of its importance as the vessel upstream to the circle of Willis where most cerebral aneurysms are found [16], in addition to its tortuous geometry. The work was conducted in two distinct yet relatable studies with distinct objectives. The focus of Study 1 was to identify features of the ICA responsible for HFVO initiation by utilizing parametric computational models that isolate geometric characteristics of patient specific geometries: constrictions, expansions and tortuosity. A spectral element solver, Nektar [105] was used to address the challenge of modeling HFVOs. An idealized sidewall aneurysm was then added to this geometry to study how the HFVOs migrate downstream from the parent artery into the aneurysm sac. This study then addressed the question of whether a typical finite volume approach , specifically CFX (Ansys Inc., Cannonsburg PA, USA), could be as effective as the spectral element approach in simulations of HFVOs (at least, in identifying their existence). In Study 2, the focus shifted to the initiation of HFVOs in a patient specific vasculature. The results of Study 1 were leveraged in selecting a finite volume approach with suitable mesh and time steps to study HFVO initiation and propagation. The chapter concludes with a discussion of the possible ramifications of these high frequency oscillations on the endothelium and offers suggestions for further studies to answer the open question as to what, if any impact, do HFVOs have on IA walls and rupture risk.

6.2 Methods

6.2.1 Study 1: Geometric Conditions Sufficient to Initiate HFVOs

6.2.1.1 Geometry Selection Motivated by prior reports of flow instabilities in carotid arteries and cerebral aneurysms, (e.g. models C0001–C0005 in Figure 1 of [195]), the following geometric features were selected for parametric study: 1) Model A: constriction, 2)

Model B: expansion, and 3) Model C: curvature (see Figure 6.1). The combined impact of curvature and expansion (Model BC) was also considered. To isolate the independent effects of pure constriction, expansion, and curvature, simple straight pipes with circular cross sections were employed as the base geometry. Model diameters were chosen within the range reported for patient ICAs [54] to ensure that only physiologically reasonable mechanisms for HFVO initiation were considered. A single geometric parameter presumed responsible for initiating HFVOs was systematically varied in each model. The Model A study explored a stenotic geometry and varied the ratio of area reduction between the vessel and constriction. The Model B study considered a situation in which the artery included an asymmetric expansion. Examples of such expansions have been the topic of study in Schimansky et al. [169] (for example, see Figure 1 in the study) and are furthermore prominent features in the ICA cases studied in Valen-Sendstad et al. [195]). Here, we considered a vessel with a constant slope expansion in both a symmetric and asymmetric manner. The Model C study evaluated the impact of varying the ratio of the outer to inner radius of curvature of the idealized vessel. The Model BC study evaluated the impact of an expansion placed downstream of a 180 degree curve, as found in a model denoted as C0002 in [195]. Each geometric parameter of interest was varied until the initiation of HFVOs could be detected (if at all). In both studies, blood was modeled as an incompressible fluid with constant kinematic viscosity of 3.33e-6 m^2/s.

6.2.1.2 Inlet and Outlet Conditions The inlet condition in Study 1 is a Dirichlet condition with velocity normal to the inlet plane with a parabolic dependence on the radial position with a flow rate that depends on time through a prescribed waveform. For both studies, a waveform was chosen from a data base for patients with mild to moderate cardiovascular disease. In localized cylindrical coordinates with z as the inlet normal, this is can be expressed as:

$$\boldsymbol{v}(r,t) = V_p(t)(1 - (\frac{r}{R})^2)\boldsymbol{e}_z \tag{6.1}$$

where $V_p(t)$ is the magnitude of the waveform peak (maximum in circular cross section) velocity, R is the vessel radius, and $\boldsymbol{e}$ is the unit vector orthogonal to the inlet. Consequently, v_θ and v_r are zero on the inlet. In Study 1, this waveform was chosen from the bank of 272

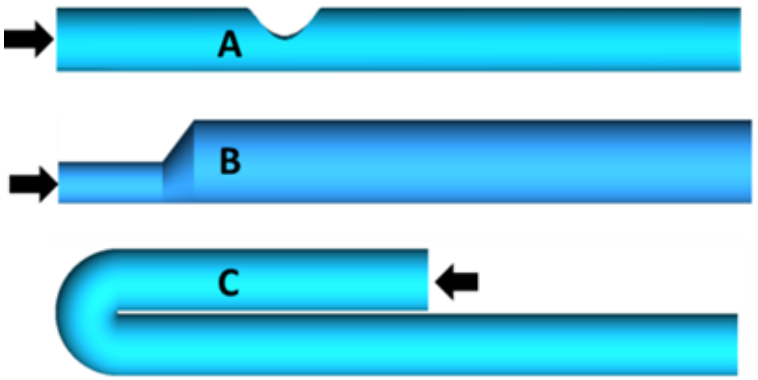

Figure 6.1: Simplified models of segments of the ICA used to study conditions needed for HFVO initiation. Model A: 4.1 mm diameter vessel with 50% stenosis. Model B: Asymmetric diameter expansion from 3 mm to 6 mm, Model C: 4.1mm diameter vessel with radius of curvature 0.1 times the centerline radius. Flow direction indicated by arrows.

waveforms for its production of a high PODENT [1] production within an aneurysm through the work presented in Chapter 2 within a bank of 272 patient specific waveforms for the ICA [54] as elevated PODENT numbers was expected to enhance HFVO formation (as discussed in Chapter 3). A higher PODENT number, as defined by Byrne et al. [19], means the waveform energy is distributed across a larger number of modes. The effect of modifications to the inlet waveform on the initiation of HFVOs was also considered by varying waveform parameters such as maximum velocity and maximum systolic acceleration (A_{max}). At the outlet, mixed conditions were applied with a reference pressure given (p=0) and the normal derivative of the velocity set to zero, or

$$p \equiv constant, \frac{\partial \boldsymbol{v}}{\partial \boldsymbol{n}} = 0 \tag{6.2}$$

Here, $\boldsymbol{n}$ is the outlet normal and is equivalent to $\boldsymbol{e}_z$ in Equation 6.1.

[1] PODENT, or proper orthogonal decomposition entropy, is a mathematical tool realized and implemented by Byrne et al. [19] to quantify the temporal flow stability within an aneurysm. Briefly, the entropy is the quantification of the average energy distributed across a number of orthogonal modes.

6.2.1.3 Numerical Methods and Computational Modeling The geometries and hexahedral meshes for Models A, B, C, and BC, were created using ICEM CFD (Ansys INC, Cannonsburg, USA). The wall velocity was imposed to be zero (i.e., rigid wall). To ensure high spatial and temporal accuracy, the Navier-Stokes equations were solved with the hp-spectral elements solver Nektar [105] using fourth-order spectral elements and third-order time integration, resulting in an effective spatial resolution of 0.06 mm (motivated by Valen-Sendstad et al. [195]) and a temporal resolution of 2.5 μs, selected to keep the CFL number below 1.

6.2.1.4 Comparison Between HP-Spectral Elements and Finite Volume Solvers in Model A With Sidewall Aneurysm An idealized aneurysm was placed downstream of the constriction feature in Model A with dual aims. The first was to determine whether HFVOs could propagate into an aneurysm in a simple model for further aneurysmal parametric study; and, if so, to study the dampening of HFVOs upon entering the idealized aneurysm. The second aim was to use the case as a comparison between Nektar and Ansys CFX. The motivation was to determine whether methods regarded as "low order" that have been commonly used in the majority of literature on the topic of CFD in cerebral aneurysms can be utilized, with the proper care, to detect HFVOs. The CFX model was meshed with linear finite volumes and discretized in space and time via central differencing and the second-order backwards-Euler method respectfully. A grid resolution of 0.06 mm and two coarser meshes were utilized. The maximum CFL number was not permitted to exceed 0.25. The CFX model CFL number corresponded to the maximum allowed Nektar CFL number, and the node spacing of the finite volume mesh approximately corresponded to the node and integration-point spacing of the 4'th order spectral elements.

6.2.1.5 Use of L-2 Vortex Criterion Vortex structures (sheets in particular) have been associated with the most unstable modes of fluid flow contributing to unstable motion [6]. We have used the λ-2 vortex region criterion (L-2 criterion) as a tool to visualize these structures and, in particular, their point of origin. We first denote S and Ω as the symmetric and skew-symmetric tensors, respectively, associated with the spatial velocity gradient where

$\boldsymbol{S} = \frac{1}{2}(\nabla \boldsymbol{u} + \nabla \boldsymbol{u}^T)$ and $\boldsymbol{\Omega} = \frac{1}{2}(\nabla \boldsymbol{u} - \nabla \boldsymbol{u}^T)$ and $\boldsymbol{u}$ is the velocity vector. The L-2 criterion is satisfied for incompressible flow when the eigenvalues $\lambda_1 \geq \lambda_2 \geq \lambda_3$ of the symmetric tensor $\boldsymbol{S}^2 + \boldsymbol{\Omega}^2$ satisfy the criterion that $\lambda_2 < 0$ as defined by [91]. When this criterion is satisfied, a local minimum in the pressure field is identified.

6.2.2 Study 2- HFVOs in Patient-Specific Vasculature in an ICA Including an Aneurysm

6.2.2.1 Numerical Methods and Computational Model A model of ICA Case C0002 (from Valen-Sendstad et al. [195], available from the Aneurisk dataset repository [4]) was meshed with tetrahedral finite volumes having spatial resolution of 0.08 mm using ICEM CFD. A prismatic boundary layer consisting of eight layers having a total layer thickness of 25 μm adjacent to the wall and exponentially increasing thickness across the other layers was employed to resolve flow in the boundary layer. The flow in Model C0002 was approximated with Ansys CFX (Ansys Inc, Canonsburg PA, US) using 1) a second-order discretization in space and time and 2) a first-order discretization in space and time. The second order model possessed spatial resolution of 0.08 mm motivated by results from Study 1 and, it is approximate to the 0.065 mm resolution in the Valen-Sendstad study [195] . The adaptive time step was chosen to enforce a maximum CFL number of 0.25, more than sufficient to meet the physical requirements for numerical stability in an explicit-in-time scheme) resulting in temporal resolution on the order of microseconds to tens of microseconds. The mesh Peclet number was on the order of 10. The first order model possessed spatial resolution of 0.15 mm and adhered to a maximum CFL number of 20. The choice of this discretization was intended to be roughly representative of discretization common to past literature when computational power was substantially limited in with respect to current standards [23, 76, 177, 196].

6.2.2.2 Inlet and Outlet Conditions Time-varying parabolic velocity profiles were applied to all outlets to satisfy the constraint of equal time-averaged wall shear stress at all outlets (i.e., Murray's Law), such that the corresponding flowrate in the ICA conformed

to Equation 8 in [54]. Therefore, at each of the model outlets, the tangential velocity components were set to zero and the normal velocity component, as a function of the outlet radial position and time, was prescribed to enforce the wall shear stress constraint that the time-average at the outlet be 15 dyn/cm^2. In local cylindrical coordinates where z is the outlet normal this can be written as

$$\boldsymbol{v}(r,t) = V_p(t)(1 - (\frac{r}{R})^2)\boldsymbol{n} \tag{6.3}$$

where r and R here are the radial coordinate and vessel diameter respectfully on the quasi-circular[2] outlet surface and $\boldsymbol{n}$ is the surface normal. It straightforwardly follows that, on the local surface, v_θ and v_r are zero. At the model inlet (i.e., the base of the ICA), the tangential components of velocity were prescribed to be zero and the pressure was set to a reference value of zero, or

$$v_\theta, v_r \equiv 0, p = p_{ref} \tag{6.4}$$

where again θ and r refer to the local coordinates on the quasi-circular inlet cross-section. Additionally, L-2 vortex core regions were again employed to visualize the initiation points of HFVOs both in the ICA and the aneurysm. Within the aneurysm, the temporal gradient of the WSSM, denoted as $\frac{\partial WSSM}{\partial t}$ was computed at locations impacted by the inflow jet, as well as in the dome, and within a small bleb located in the dome region.

6.2.2.3 Sensitivity to Waveform Variation The waveform used in the C0002 was modified for the purpose of a sensitivity analysis of the C0002 velocity solution to perturbations in the waveform data. This was accomplished by increasing the minimum velocity at diastole by 45 mm/s, corresponding to one intra-patient standard deviation from the set of 272 waveforms analyzed in [54]. The numerical solution to flow in C0002 was then obtained under the condition of using the modified waveform as boundary data. The solutions for the velocity field were compared at each time step by subtracting the solutions produced by the original and perturbed waveform.

[2]the term "quasi" is used here due to the nature of patient-specific vessels, which are in general circular but with minor deviation from a perfect circle

6.3 Resluts

6.3.1 Study 1- Geometric Features that Generate HFVOs Using Simple Parametric Models

Sudden constrictions, as those that might arise from plaque deposition, were found to initiate fluctuations, in a manner that depended on the acceleration in the waveform during systole, Figure 6.2. In these studies, the maximum inlet Reynolds number was 775 and the inlet velocity profiles were chosen so as to vary the systolic acceleration as quantified through the maximum acceleration (A_{max}) of the velocity waveform, Figure 6.2(a). The base value of maximum systolic acceleration of $A_{max,0}$ of 5260 cm/s^2 therefore was chosen as the ensemble average maximum systolic acceleration for a database of 272 human waveforms in [54]. Doubling this value while keeping the systolic velocity maximum constant, enhanced the HFVO content while halving this value eliminated the HFVO, Figure 6.2(b).

Both the independent and combined impact of expansion and vessel curvature were then explored. Neither a sudden asymmetric expansion of a diameter of 3mm to 6 mm nor a radius of curvature of 0.1 times the radius of centerline curvature were independently capable of initiating the high-frequency fluctuations at similar maximum Reynolds number (in the 700-800 range), Figure 6.3(a,b). However, when these features were combined in Model BC, they contributed synergistically to generate HFVOs, Figure 6.3(c).

The characteristic differences in HFVOs are more apparent when comparing Model A (analogous to stenosis) with Model BC, analogous to a sudden widening of the ICA vessel directly downstream of a curved segment (the C0002 C4 segment for example), Figure 6.4. With identical inflow waveforms, the velocity perturbations require less downstream distance to develop in the case of expansion following curvature (Model BC), and their frequency content is more multi-modal as compared to the easily recognizable mono frequency behavior seen after the stenotic case (Model A) in which frequency decreases monotonically with downstream distance while the amplitude of the fluctuating component increases with distance.

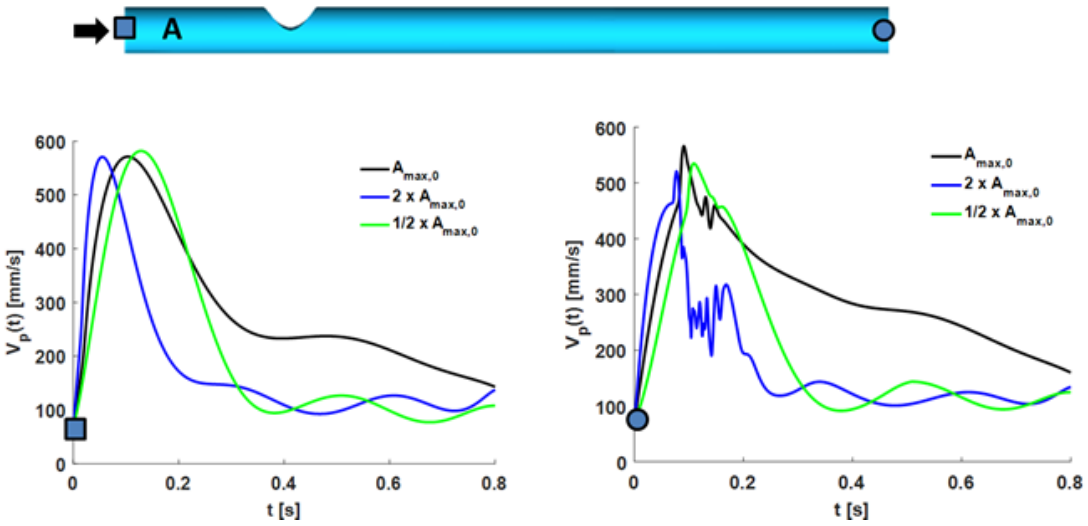

Figure 6.2: Importance of systolic acceleration in the generation of HFVOs due to a constriction. (a) Three inlet velocity profiles were chosen, differing in their systolic acceleration with fixed maximum systolic velocity. (b) The magnitude of systolic acceleration substantially impacts the HFVO initiation and intensity. Doubling the maximum systolic acceleration (blue) resulted in HFVOs in contrast to the base acceleration (black) and half the base (green). In all cases, the Reynolds number is 775 with a 50% stenosis.

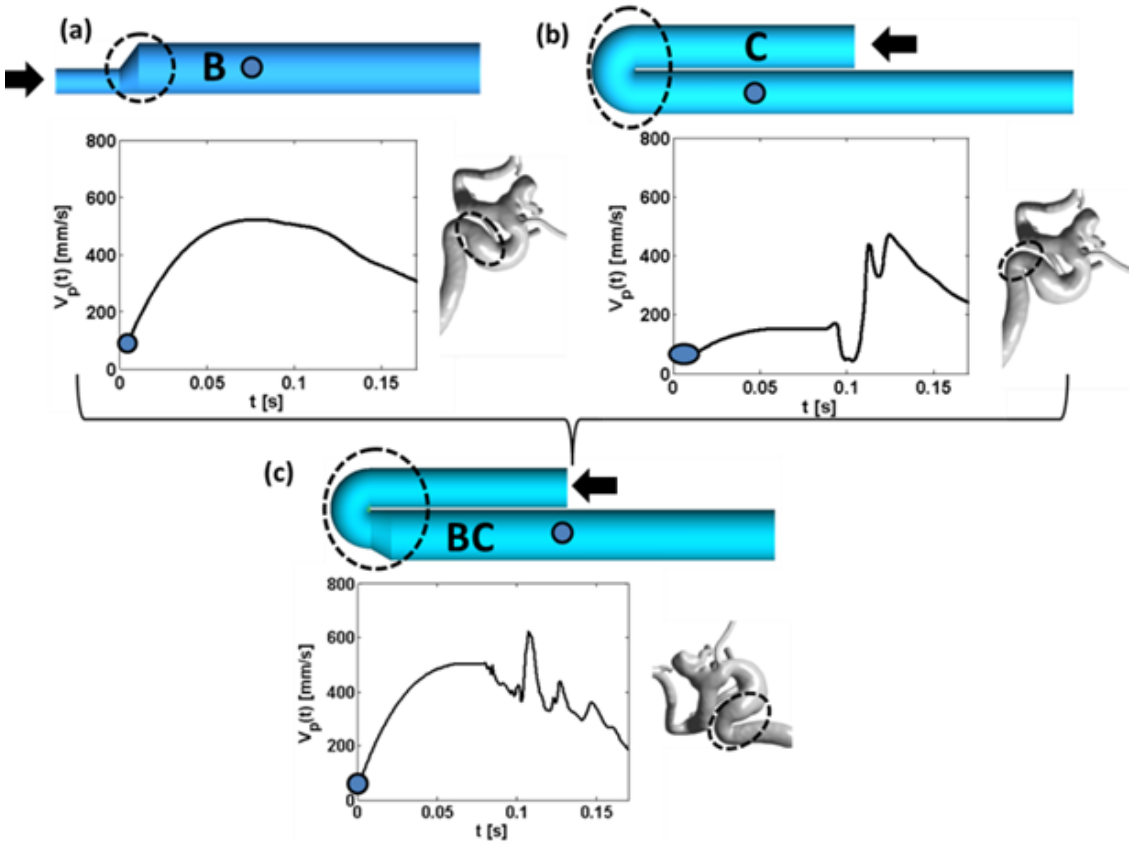

Figure 6.3: Study of the impact of a sudden expansion and curvature on the generation of HVFOs. The idealized model geometry (blue) is shown along with a human geometry with section of similar geometry type (grey). Velocity and marked location (filled circle) is shown as a function of time. a) Sudden expansion fails to induce HFVOs under physiological conditions. b) Sharp curvature fails to induce HFVOs under physiological conditions. c) Combined expansion following a sharp curve (model BC) induces HFVOs for conditions under which model B and model C failed to induce HFVOs.

6.3.1.1 High-Frequency Content in an Idealized Sidewall Aneurysm

The magnitudes and frequencies of the HFVOs in the aneurysm sac were found to be diminished compared to those in the parent artery, Figure 6.5. Once in the aneurysm, the magnitudes of the oscillations were found to progressively dampen from the ostium to the dome. The L2 vortex regions were seen to originate at the stenosis in the parent artery and intensify downstream. Within the aneurysm, the L2 vortex criterion was only satisfied in inflow-jet region.

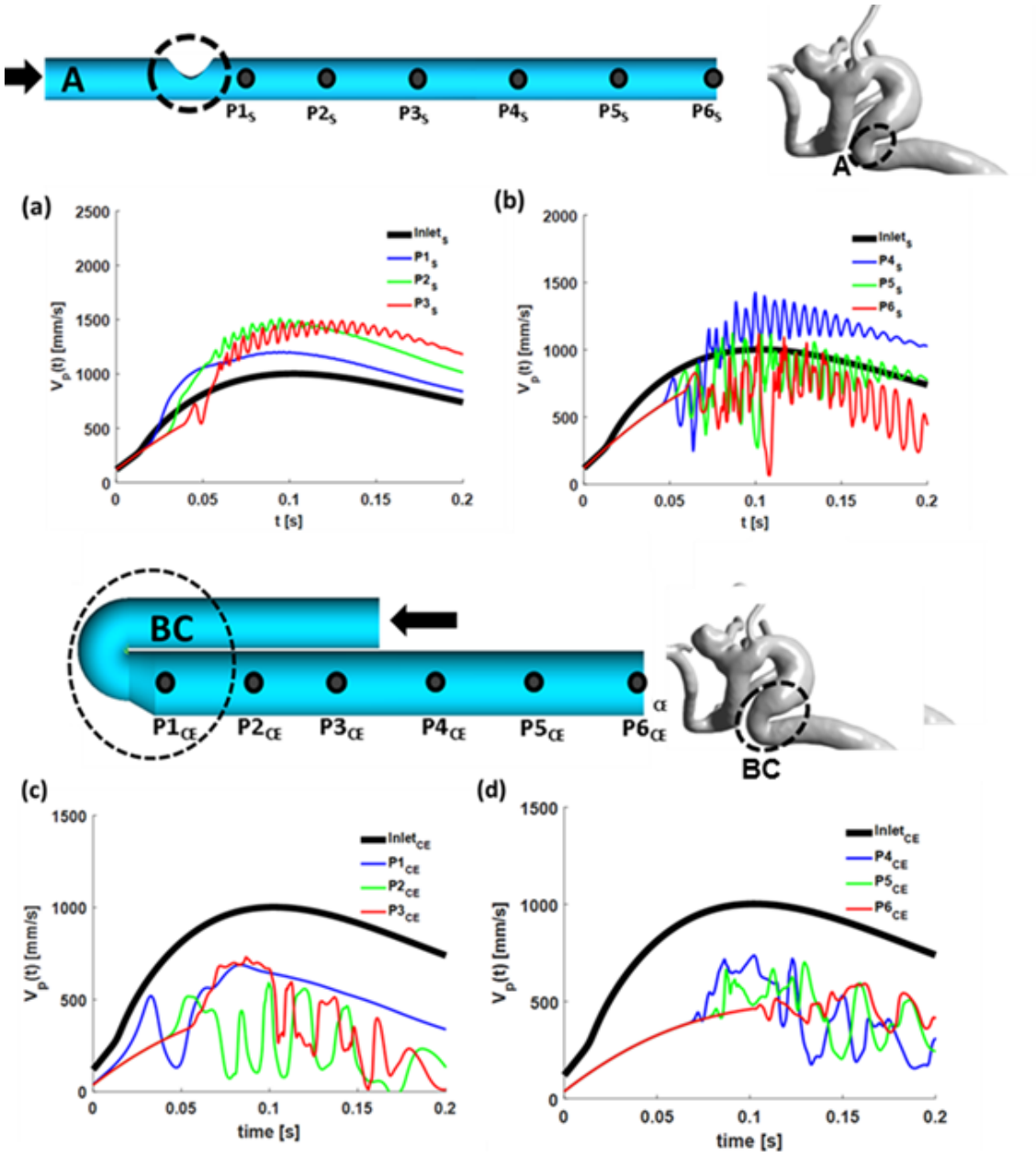

Figure 6.4: Comparison of HFVO characteristics (a,b) downstream of a stenosis (Model A) and downstream of a curved segment followed by an expansion (Model BC). (c) Model A produces HFVO's which increase monotonically with downstream distance while (d) Model BC produces multi-modal interactions with larger relative amplitudes with respect to those produced by Model A.

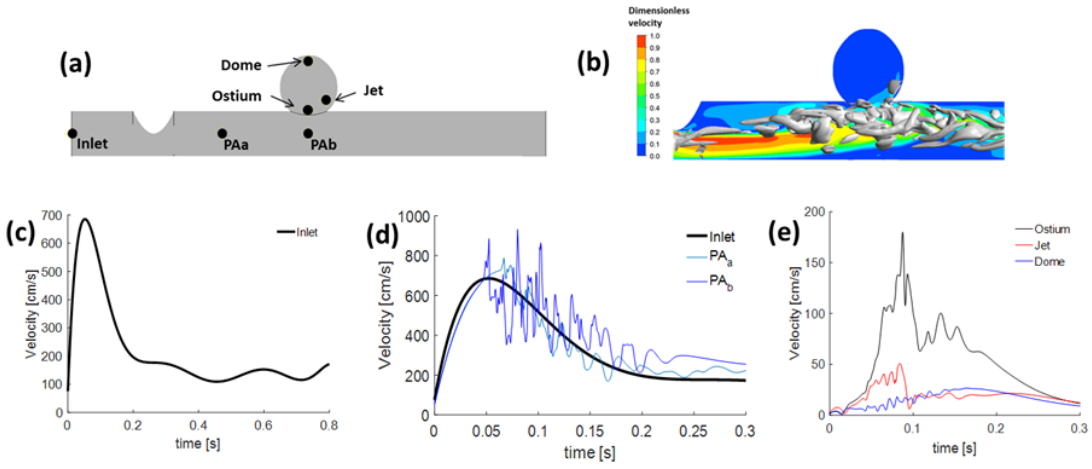

Figure 6.5: Convection of HFVOs into an idealized 3D sidewall aneurysm following HFVO generation at an upstreatm stenosis. (a) Locations in flow field where HVOs were analyzed. (b) Visualization of vortex structures in HFVOs that are generated at the stenosis, showing vortex intensification downstream and partial convection into the aneurysm by the inflow jet. The bulk of the vortices are convected downstream past the aneurysm. (c) Inflow waveform used for this study, corresponding Reynold number of 850. (d) HFOVs intensified with downstream distance from stenosis. (e) HFVOs dampen with distance into the aneurysm.

6.3.2 Study 2 - Initiation of High-Frequency Content within Patient Specific Model C0002

HFVO initiation upstream of the ICA of C0002 was found after the first curve followed by sudden expansion, Figure 6.6. In particular, the initiation occurred between the C4 and C5 ICA segments, with HFVOs continuing downstream (as seen at C6). This mechanism of generation is consistent with that found within the idealized model BC (curvature + expansion). Referencing Figure 6.7, in both Model BC and the C4-C5 segment of C0002, the velocity peak is seen to skew from the inner radius to the outer radius into a narrow jet when passing the C4-C5 bend. This narrow jet then enters the expansion into a stagnation zone against an adverse pressure gradient, as flow reversal is observed. This effect is not seen in Model C (curvature without expansion), where the expansion region, and hence the

adverse pressure gradient, are lacking. In patient geometry C0002, there is an additional curved region with a constriction region downstream of the Model BC features (curvature + expansion). The L2 vortex core was prevalent throughout the entirety of the downstream domain.

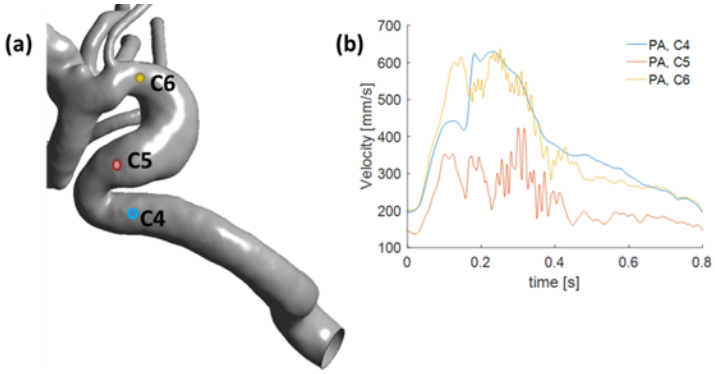

Figure 6.6: Flow in a patient specific model with expansion following a curved region generates HFVOs consistent with flow in Model BC. (a) 3D reconstructed patient specific vasculature C0002 with ICA showing labeled points of interest in the flow domain. (b) HFVOs seen at three points showing initiation between C4 and C5; HFVOs continue downstream at C6 through further curvature and narrowing of the cross section.

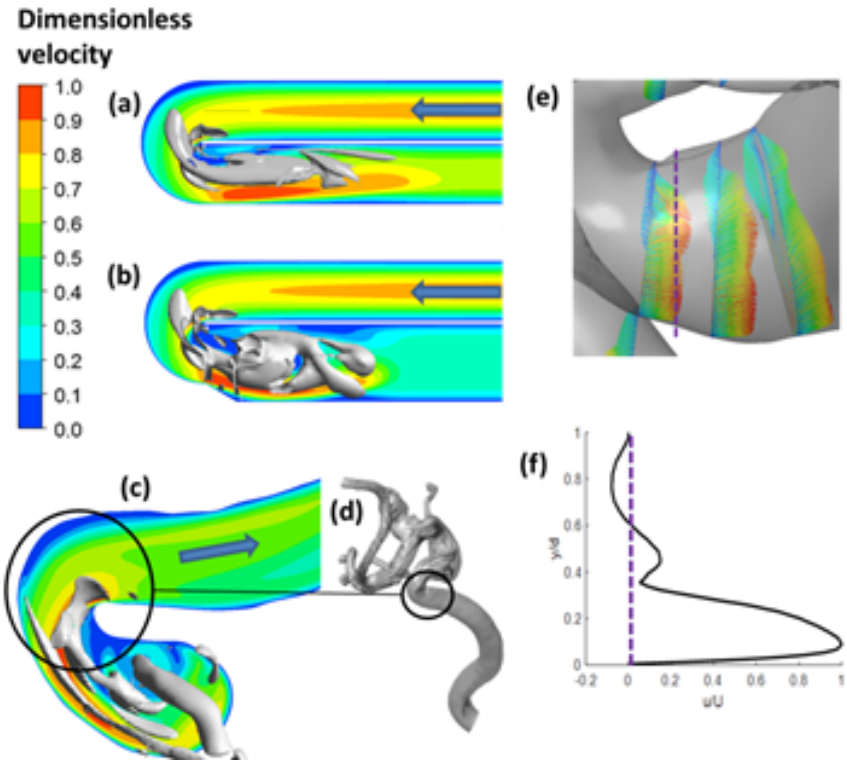

Figure 6.7: Flow in a patient specific model C0002 with expansion following a curved region and comparison with Models C and BC. (a) Dimensionless velocity contours for Model C with L-2 vortex zones (grey) and velocity contours (colored). Peak velocity is shifted from inner to outer radius as flow passes around sharp curve. (b) Expansion following curvature in Model BC drives the shift in peak velocity further outward, increasing size of stagnation region (blue); peak velocity in jet is further elongated (L-2 vortex regions in grey). (c) Substantial outward shift in peak velocity in Model BC is similarly observed in C4-C5 segment of C0002. L-2 vortex regions in grey seen to initiate at inner radius, then intensify in expansion. (d) Identification of location of constriction in (c) within the larger vascular segment. (e) Velocity vector plots in expansion confirm flow reversal and adverse pressure gradient in C5 expansion. (f) Velocity plot along dashed line as a function of distance from outer wall with diameter, providing quantitative plot of shift in velocity maximum and flow reversal.

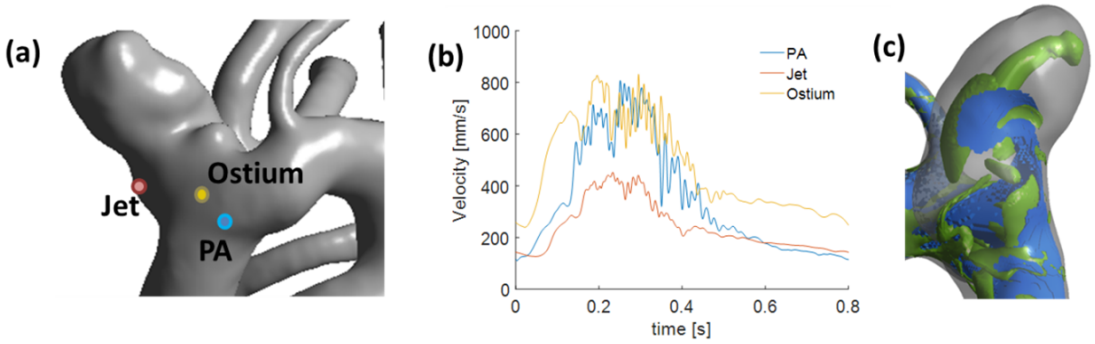

Figure 6.8: Convection of HFVOs into the patient specific ICA. (a) Locations of interest in parent artery and aneurysm. (b) Amplitude of velocity oscillations decreases with distance into the aneurysm. (c) L-2 vortex regions (green) are associated with inflow jet region (blue).

6.3.2.1 High-Frequency Content within C0002 ICA Aneurysm As with flow in the idealized sidewall aneurysm shown in Figure 6.5, the magnitude and frequency content of flow within the patient specific ICA aneurysm is seen to diminish relative to that in the parent artery, Figure 6.8. As for the sidewall model, the vortex regions in the patient specific ICA likewise are convected into the sac along the inflow jet. However, in the more complex patient specific geometry, the vortex structures were also present in other regions as well, Figure 6.8(c).

6.3.2.2 Impact of HFVOs on WSSM The HFVO impact on wall shear stress magnitude (WSSM), and the temporal gradient of WSSM (WSSTG), was most pronounced on the wall near the inflow jet (Figure 6.9). This impact then lessened with distance from the impact jet; most notably, the maximum WSSTG differed by an order of magnitude between the jet and dome regions and the amplitudes of the largest WSSM oscillations differed by two orders of magnitude between the respective regions. The WSSTG was notably minimal in the bleb.

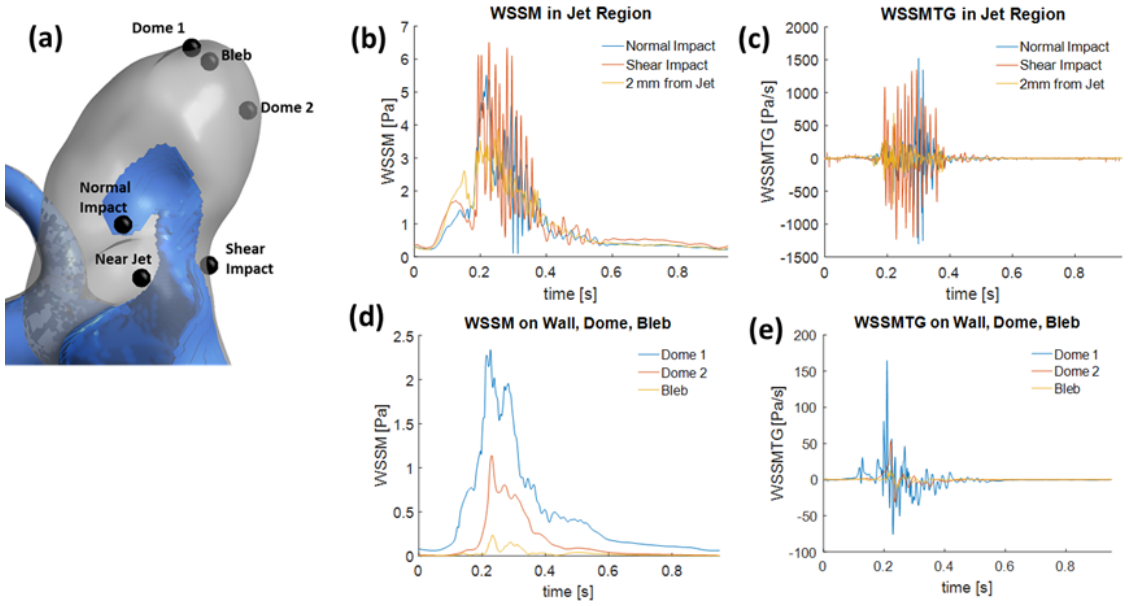

Figure 6.9: HFVO intensity is heterogeneous within the aneurysm. (a) Aneurysm and velocity magnitude isovolume visualizing the inflow jet (in blue) and locations at which WSSM and WSSTG were measured. (b,c) High frequency wall shear stress magnitude is most prevalent where jet shears against the wall as opposed to where jet impacts the wall; HFVO intensity diminishes with distance from inflow jet (in blue, see panel e for locations). (d,e) HFVO influence dampened in dome region; most notably, the time gradient of WSSM is on average an more than an order of magnitude less than in the inflow jet region.

6.3.2.3 Comparison of Results from Low versus High Resolution Studies in a Patient Specific Geometry The high resolution (HR) studies utilizing the CFX code that employed a second-order accurate numerical model with a mesh resolution of 0.08 mm and utilized a maximum CFL number of 0.25 were capable of predicting high-frequency fluctuations. These fluctuations were generated with a combination of constriction, curvature, and expansion that were less pronounced than those studied independently in the idealized geometry model BC using similar time/space resolution. The first order, low resolution (LR) studies with resolutions of 0.15 mm with maximum CFL numbers of 20 however did not capture the high frequency fluctuations. Nonetheless, the time-averaged wall-shear stress

magnitude (TAWSSM) showed reasonable qualitative agreement with the HR solution, Figure 6.10 (a,b). In particular, a region of elevated TAWSSM in the dome was seen with both resolutions, as well as the shearing of the jet against the wall. Furthermore, the region of diminished TAWSSM was seen in the aneurysm for both cases.

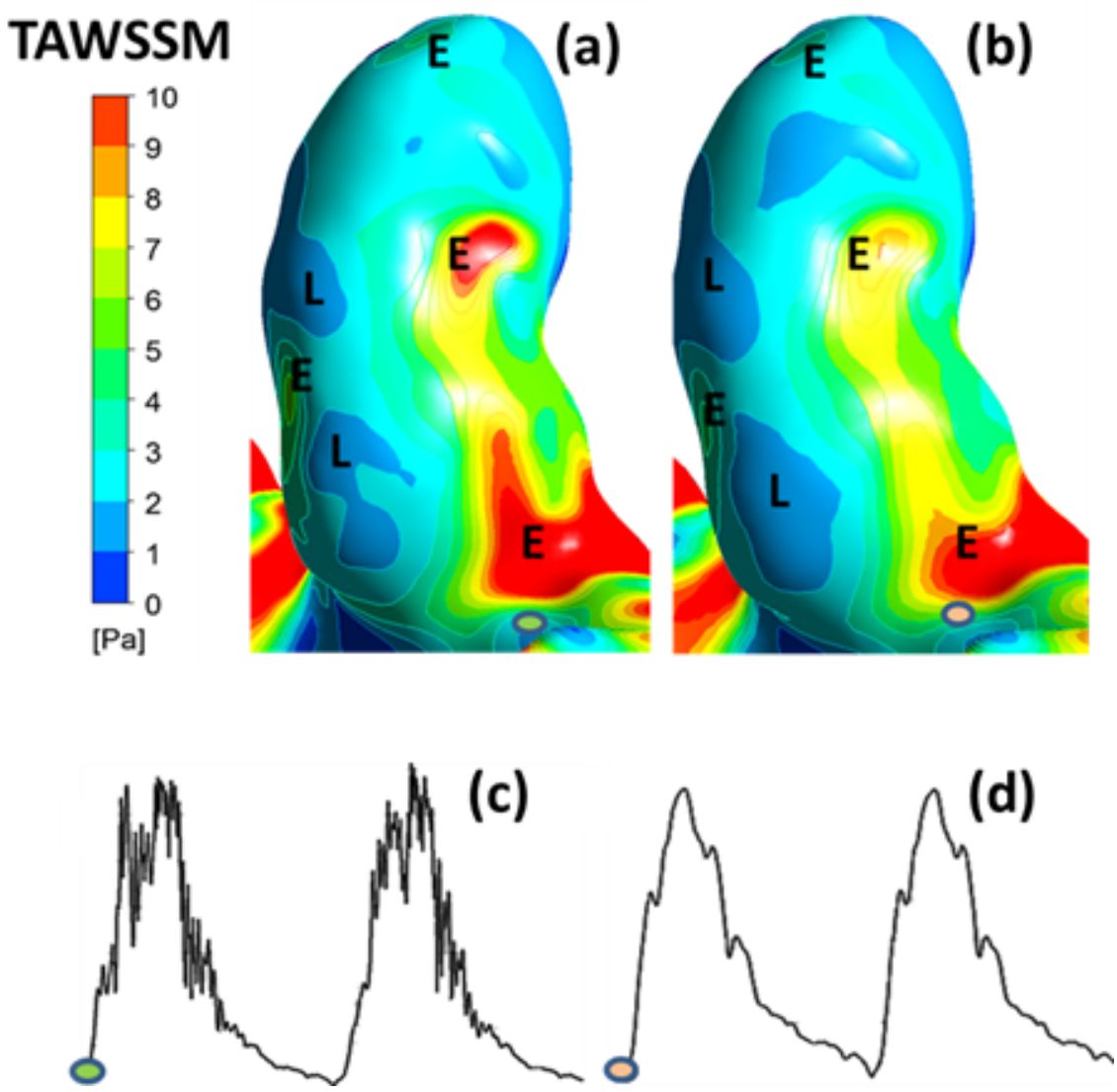

Figure 6.10: Contour plots of time-averaged wall shear stress magnitude (TAWSSM) for (a) "high resolution" and (b) "low resolution" models of C0002. Both studies predicted similar regions of elevated TAWSSM near the dome and the shear impact of the jet, as well as regions of lower TAWSSM regions (marked "L"). The ostium velocity however, is not time-periodic in the high resolution model (c) as opposed to that in the low resolution model (d).

6.4 Discussion

High frequency flow oscillations have previously been reported in high resolution CFD studies e.g., [7, 195, 211]. However, little attention was subsequently given to understanding the cause of HFVOs or understanding under what conditions they may arise in real vasculatures. The current study decomposed the complex 3D geometry of the ICA into simple components to identify features in this vessel (and possibly extendable to others) responsible for the initiation of these fluctuations. An important finding is that deviations from a straight vessel, such as curvature or sharp increase in diameter can synergistically work in tandem to produce HFVOs. Alternatively, if a constriction is sufficiently acute, it alone can lead to HFVOs. Although curvature and deviations in diameter have been previously speculated as a source of high frequency fluctuations [195], the current study, to our knowledge, is the first work to show this in a systematic manner. Later in this section, we offer additional insights as to how these oscillations can develop, and gain their temporally complex and volatile nature.

While more data is needed to be sure, it appears likely that high-frequency fluctuations have biological significance. In this case, special care is needed to resolve them, regardless of understanding their cause. As such, our results have import implications for cerebral vascular diseases such as atherosclerosis or cerebral aneurysms. Our results suggest that acute constrictions as well as the combination of curved regions with expansions are risk factors for HFVOs. As the factors can interact synergistically, it is possible that even in the case of a milder constriction that consideration of a single geometric attribute in the patient's vasculature is insufficient for predicting whether high-frequency velocity oscillations will occur. Therefore, analyses such as presented herein should be conducted on a wider range of vessels and vessel morphologies.

This study also demonstrated that the spatial distributions of maxima and minima for time-averaged quantities, such as TAWSSM, remain minimally impacted by HFVOs. Hemodynamic quantities such as TAWSSM have already been shown to have some association with aneurysm wall-pathology without the consideration of HFVOs [128, 29]. Considering this notion, it is conceivable that HFVOs will possibly impact aneurysm pathology by addi-

tional mechanisms in addition to those thought to be influenced by the spatial distribution of TAWSSM over the aneurysm sac. Hence, there is a great need for further study of the biological role of HFVOs on the vascular wall.

6.4.1 ICA Curvature and Expansion: a Possible Source of Detrimental Hemodynamic Environment

We have identified the fluid dynamic mechanisms by which a rapid expansion following a curved segment generates HFVOs in the ICA. Both features, curvature then expansion, are necessary in succession to create this effect. Of importance, this mechanisms was found to be similar to that for generating HFVOs downstream of a moderate to severe stenosis. The sudden increase in diameter downstream of the curved region, in conjunction with the adverse pressure gradient in this region, collectively create a dead zone adjacent to the jet, mimicking the effects of an obstacle such as a buildup of plaque. As a result, the velocity peak is augmented and shifted sharply to wall on both cases.

An immediate result of this finding is that we obtained a potential morphological discriminant for future analysis of aneurysms containing HFVOs. This result may offer insight into the role of HFVOs in creating a hostile hemodynamic environment for clinical ICA cases harboring aneurysms analyzed in a clinical study of ICA parent vessel expansion (excluding curvature). In this work [169] Schimansky et al. identified a link between the maximum distal-to-proximal ratio of ICA diameters, (R_{Mdp}) and aneurysm creation as found. In particular, they found that ICAs harboring IAs possessed a significantly higher R_{Mdp} than those without IAs ($R_{Mdp} = 1.17 \pm 0.1$ vs 1.03 ± 0.1). This difference was more pronounced in women than men. Though the published results do not include specifics on the R_{Mdp} locations or blood-flow velocities, results from the present study suggest that HFVOs could have been generated within these cerebral vessels based on reported values of R_{Mdp}, and furthermore could have increased the likelihood of aneurysm formation. Namely, the greater incidence of IA suggests that HFVOs may have contributed to a more hostile flow environment for the wall.

The presence of concentrated inflow jets has widely been associated with aneurysm rupture [23, 31] and more recently, with wall hypoplasia [22]. Our findings demonstrated that HFVOs originating in the parent vessel most strongly influence the aneurysm wall in the region of inflow jet impact. Here, the magnitude of WSSTG during the systolic phase is an order of magnitude higher than elsewhere in the aneurysm. It has been reported in computational studies such as [211, 198, 194] that HFVOs were not found in all aneurysms, even when using CFD capable of resolving HFVOs. For example, [198] reported that HFOVs occurred only in 5 of 16 aneurysms analyzed. It may therefore be of value to stratify aneurysms having concentrated inflow jets into groups with and without HFVOs to investigate the biological impact of high-frequency wall shear stress on the wall separately from the effects of the jet itself; more precicely, whether HFVOs are associated with a greater degree of destructive remodeling associated with intra-saccular jet impingement.

Furthermore, we have shown that WSSMTG can vary by orders of magnitude throughout the aneurysm sac. It is of especially interesting to note that the small bleb in the dome region of C0002 experienced no remarkable levels of WSSMTG compared to levels found within healthy arteries. Toward this end, it may be of value to consider WSSMTG on the sac wall in addition to TAWSSM, especially in studies with the aim of linking localized hemodynamics to localized wall pathology in harvested samples. Further, it may be useful to sub-categorize regions of low, physiological, and high levels of TAWSSM by the degree to which HFVOs are present: considering the magnitude of the oscillatory component, its frequency, and the duration of the cardiac cycle that the endothelium is exposed to high frequency flow.

6.4.2 Sensitivity to Waveform Variation

The application of a perturbation at early systole to the inlet waveform for C0002 led to downstream changes in the centerline velocity at the ostium of the aneurysm during the entirety of the systolic period, Figure 6.11. In particular, downstream, the magnitude of the perturbation was amplified up to a factor of 2.2 for a duration lasting 11.6 times longer than the original perturbation. The frequency content was consequently altered for the duration of

systole. This suggests that even seemingly small differences in patient inlet velocity profiles in the ICA can have substantial changes on the HFVOs at downstream aneurysms. It is clear from results in [54], that variability in the waveform of this magnitude and greater are to be expect across aged adults. Moreover, variation of the velocity profile in time in a single patient will similarly impact the downstream profile. It is therefore to be expected that the aneurysm sac wall would experience varied frequency content in a single patient in time as well as across patients in even the patient in resting state (versus a physically active state). The importance of these deviations are not yet understood as the sensitivity of the endothelial cell responses in this range of frequency information has not been investigated. Namely, at this time, it is unclear as to whether the wall is responsive to any particular WSSMTG, whether the wall responds to values simply beyond a particular threshold of WSSMTG, or whether the wall response to HFVO is a second order effect to WSSM once an aneurysm has formed.

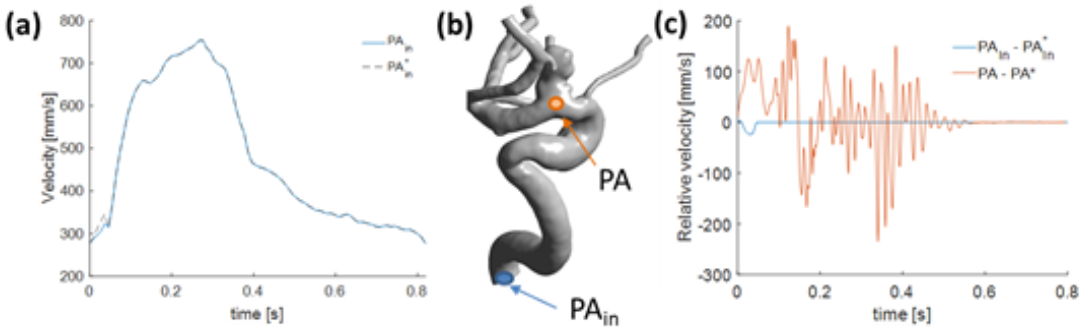

Figure 6.11: Changes in HFVO due to small perturbations in inlet velocity field. (a) Velocity perturbation at the inlet profile as prescribed at location PA_{in}. (b) 3D reconstructed patient specific with labeled positions of interest. (c) substantial deviation in velocity field in parent artery near entrance to aneurysm (PA) due to change in prescribed inlet velocity profile at PA (superscript star denotes original velocity field).

6.4.3 Comparison of Solvers and Resolution

Resolving HFVOs in the cerebral circulation is a computationally expensive undertaking. In addition to the stringent grid sizing and time stepping requirements, the numerical scheme with which the solution is obtained can also impact the solution in a strict sense. The question as to what type of code is required to properly conduct high resolution CFD in cerebral aneurysms has been previously raised. Particularly, the validity of the use of commercial CFD has come into question. Both a commercial finite-volume code (Ansys CFX) and a hp-spectral elements code (Nektar) were used in this work and it was demonstrated that special care must be adhered to if an implicit stabilized code is used (i.e., while numerically stable, a large CFL number will attribute to an under-resolved solution). In this work, comparisons were made between the solutions from Ansys CFX and Nektar for a simple vascular model with an idealized side wall aneurysm, Figure 6.12. The vessel centerline velocity obtained via four solution strategies at a point below the ostium is plotted. The magnitudes of the time-averaged acceleration and the maximum acceleration are used as metrics for comparison against computational times for each strategy. While appreciable differences are found, the general trend is similar - a lower fidelity solution under predicts the time gradients while saving computation time. However, even the cheapest of the solution strategies predicts the temporal gradients due to HFVOs will be an order of magnitude greater than the highest temporal gradient found with ICA waveforms of patients [54].

While it is clearly evident from Figure 6.12 and Table 6.1, that costly solution strategies will provide greater temporal resolution, an important question remains as to the importance of particular frequencies in the HFVOs on the wall biology. Without such knowledge, it is unclear which level of resolution is needed for a biofluid dynamic study. As an example, if an in-vitro study were to find that endothelial cells are detrimentally impacted simply by the mere presence of any HFVOs with frequencies greater than those normally associated with the physiological waveform, then a less-costly solution strategy that leverages this information may be reasonable. However, if the endothelium responds to HFVOs through a more complex functional dependence on frequency and amplitude, then more costly solution strategies may be required to conduct meaningful CFD studies involving hemodynamics

Table 6.1: Solutions obtained using the spectral-elements solver Nektar generally display higher maximum accelerations than those using the finite-volume solver CFX, while the average acceleration magnitude is predicted to be larger using the finite-volume solver. An appreciable difference in solve time with 16 3.4GHz cores is noted among the methods. All methods predict acceleration types an order of magnitude larger than that found in previously reported values for ICA waveforms in an aged adult population [54].

Numerical Stragety	$(\partial \boldsymbol{v}/\partial t)_{avg}$ mm/s^2	$(\partial \boldsymbol{v}/\partial t)_{max}$ mm/s^2	Runtime days
Nektar O(4)	48.1e^3	629e^3	24
CFX Fine	55.1e^3	416e^3	15
CFX Coarse	44.3e^3	375e^3	0.76
Inlet Waveform	61.0e^2	526e^2	-

in cerebral aneurysms or other vascular settings. Understanding the relationship between HFVOs and localized wall response remains to be realized, and experimental studies into this relationship would help guide further computational studies towards answering the open question as to what, if any impact, does high frequency flow have on aneurysmal tissue.

6.4.4 Mechanism for Fluctuation Generation: Hopf Bifurcation

We finally propose the mechanism which creates, controls, and dominates the high-frequency temporal nature of the flow. The geometric features (see case BC) discussed previously give rise to a Hopf bifurcation if the local Reynolds number has reached a critical threshold (for example, see Quaini et al. [157]). Under this condition, a stationary prescription of the velocity boundary conditions results in the departure from stationary behavior within the system downstream of the location of the C4-C5 curvature plus expansion. More precisely, the stationary solution to the Navier-Stokes system under the prescribed stationary boundary conditions takes on two solutions. The resulting system behavior is then a

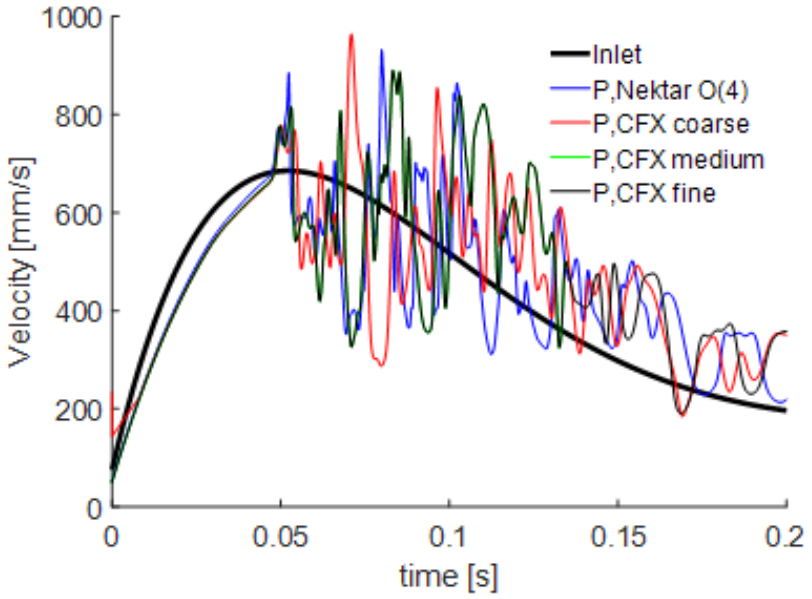

Figure 6.12: Variation in HFVO spectrum using different computational strategies. Finite-volume methods can produce qualitatively similar solutions to spectral elements solutions. "coarse", "medium", and "fine" refer to 0.15 mm, 0.10 mm, and 0.06 mm. The fourth order elements used in the Nektar model possessed integration points which approximately correspond to the fine meshing in CFX.

steady part plus a (relatively) small sinusoidal component with distinct frequency. In C0002, with distance downstream of the initiation of the unsteady behavior, the frequency within the fluid, while retained, shifted phase. The total kinetic energy within the domain likewise was oscillatory with the same frequency, although in general, the total kinetic energy of the system and velocity at any point were not in phase. We conjecture that as kinetic energy is added to the system via the oscillatory nature of the waveform, the energy being added at the cardiac frequency at different points in the system is, in general, added out of phase. The result is then the sporadic amplification and dampening of motion seen in the results of this work and in other works on this topic ([194, 195, 7] for example). For C0002, the first Hopf bifurcation frequency was found to be 74 Hz (Figure 6.13) at the marked locations in the

figure. While the velocity at each location possessed a considerable range of magnitudes (see Figure 6.13d), the frequencies among points were remarkably consistent. Figure 6.13a is included to aid the reader in visualizing the phasing of the velocity at these different locations. The amplitudes of the unsteady velocity components have been separated from their steady parts, and finally normalized so that the phasing at each point may be readily visual. Obtaining the first Hopf bifurcation mode in this case required a considerable degree of slowly incrementing the prescribed velocity boundary conditions at the vessel outlets (keeping all prescribed velocities in proportion to one-another) until only the first mode was observable, after tens of seconds of multi-modal behavior dampened from viscosity. Overestimations of the imposed steady velocity magnitudes resulted in velocity having a steady component plus an oscillatory component containing multiple frequencies (for example, see Varble2016 [198], Figure 6). The work herein clearly demonstrates the existence of this system state within the context of physiologically relevant velocity magnitudes within the ICA and that the geometry analyzed possessed a distinct first frequency. At this time, one can only speculate towards the biological significance of this quantity. It remains to be explored as to whether this first frequency correlates with any particular biological response on the lumenal wall (or within the wall). It can furthermore be conjectured that the Reynolds number at which the first frequency can be observed could serve as an index for indicating the propensity of an ICA to produce HFVOs.

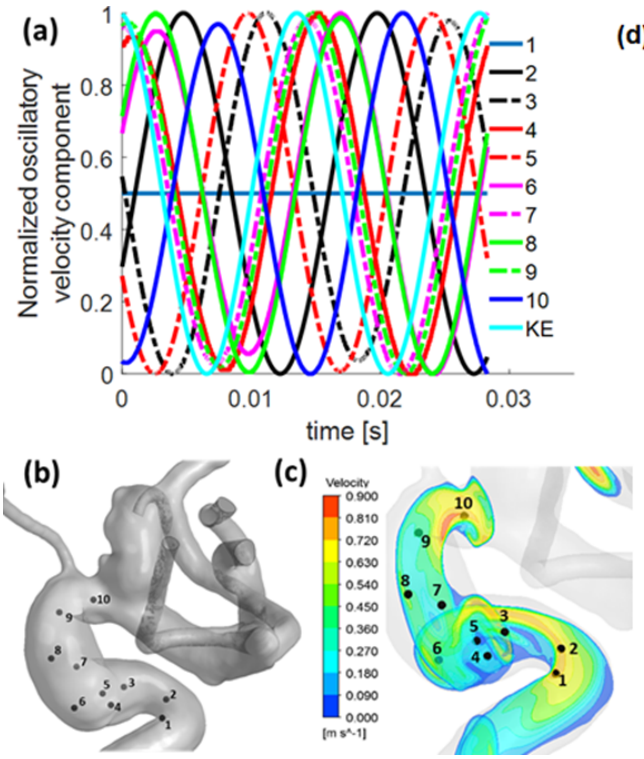

(d)

Sampling Loacation	Velocity Amplitude [mm/s]
1	0
2	1.79E-02
3	1.38E-02
4	5.31E-03
5	9.63E-03
6	6.44E-03
7	1.18E-02
8	6.89E-03
9	4.61E-02
10	3.09E-02
Global Quantity	Global KE Amplitude [J]
	3.90E-10

Figure 6.13: (a) Normalized oscillatory velocity components at locations in patient specific vasculature between inlet and aneurysm ostium. (b) 3D reconstructed vasculature of patient C0002 with labeled spatial locations of interest. (c) Contours of velocity magnitude close to the ICA centerline. It is conjectured that the phase-shift in velocity throughout the system under time-independent boundary conditions prohibits further addition of energy in a monochromatic manner, giving rise to the chaotic appearance of high frequency velocity fluctuations. (d) Amplitudes of oscillations at different locations.

6.4.5 Limitations and Future Directions

This work has both intrinsic and extrinsic limitations. Intrinsic to the current study, our scope of geometry was limited to the ICA; particularly, the curvature and changes in diameter along this vessel. This choice was motivated by prevalence of aneurysms in downstream regions of the ICA and also its importance in prior studies on HFVOs. Further, in an effort to identify the fundamental conditions needed for HFVOs, we did not consider complex

interactions between multiple curved segments. Furthermore, our study considered only one patient specific geometry; though in great depth. Expanding the current study to larger numbers of ICA cases as well as bifurcation aneurysms would provide the opportunity to explore the impact of WSSMTG on aneurysm pathology in a manner similar to past studies of other flow features such as WSSM and WSSG. We expect that such a study would identify geometric indicators that can be used to quickly assess risk for HFVOs in patients in a clinical setting. If high WSSMTG were found to be detrimental, such a geometric discriminant could serve as a biomarker of spots disposed to aneurysm formation or aneurysms prone to harboring vulnerable walls.

With respect to intrinsic limitations for modeling choices, once can consider the relevance of the constant viscosity, inelastic Navier-Stokes model for blood. While the viscoelasticity of blood has been measured in oscillatory shear flows, these experiments were performed as perturbations to the resting state. For the flows in the cerebral vasculature, the flow is far enough from the resting state to believe that this source viscoelasticity in these studies, storage and release of energy in rouleaux, will not be present (see Chapter 2 of [70]). It is furthermore unknown whether the red blood cells can serve to substantially dampen the kinetic energy associated with the higher frequency modes (for example, particle-particle interactions between red blood cells within the blood plasma). This should be the subject of future study.

With respect to choices for computational study, the resolution of the study could be enhanced even further by additional grid refinement in the finite volume models, and utilizing multiple p-refinement in the patient specific Nektar studies. As there is still little information regarding how WSS oscillations at high frequencies impact the endothelium or the wall- an extrinsic limitation of this and other works on HFVOs, the clinical significance of such a study is undetermined. In particular, the impact of frequencies and the amplitudes of oscillations on the biology of the wall need to be addressed in order to yield further meaningful information from CFD-based studies of high frequency blood flow in the cerebral circulation, as well as to guide the requirements for future CFD studies. Another fundamental question that remains unanswered is whether the walls of aneurysms and parent vessels responds differently to HFVOs. It seems unlikely that HFVOs could be detrimental to IAs without being detrimental to the parent vessel.

6.5 Conclusion

Through decomposing the complicated features of the ICA into simple parametric models, the combination of sharp curvature directly preceding a large diametric expansion of the vessel was found to be a source of high frequency velocity oscillations in the ICA. Velocity-time data at locations of a real ICA geometry, in conjunction with the use of the L-2 vortex criterion supported this finding even in the presence of physiologically normal velocities. The flow oscillations were subsequently found to infiltrate the aneurysm; the amplitudes and frequencies of the wall shear stress time-gradient were highest on the wall near the inflow jet, and dissipated with distance from the inflow jet; particularly in the aneurysm dome.

7.0 Conclusions and Future Directions

The sections herein have covered a broad range of topics pertinent to cerebral aneurysms. The work explored many facets of the cerebral aneurysm problem utilizing computational fluid mechanics, with the goal of providing insight to further understand the complex relationship between the pathalogical hemodynamics within the aneurysm and the aneurysm wall so that clinicians may one day be fully able to predict whether a cerebral aneurysm is in need of surgical treatment. While each section of work has its own stand-alone conclusions, the body of works herein highlight the multi-factorial nature of the problem, and motivate the imperative need to address the problem as a whole. Chapters 2 and 3 have highlighted the diversity in blood flow waveforms and the impact that diversity has on some metrics for assessing rupture risk. Chapter 4 demonstrates via parametric modeling the complex relationship between geometry and flow structure. A more complete understanding of the relationship between the intra-saccular hemodynamics requires the consideration of not just one but multiple geometric parameters that should be considered simultaneously to develop robust correlations between geometry and flow. Parametric modeling can also assist in retracing the possible previous hemodynamic configurations of the sac at an earlier time point, and help understand which sac parameter influenced change in the flow structure. Chapter 5 explored the oxygen transport characteristics in cerebral aneurysms. Here, it was demonstrated that sac geometry alone can have neutral or negative impacts on the ability for oxygen to be transported through the aneurysm wall tissue. By utilizing parametric modeling as in Chapter 4, it was determined which sac geometric parameters are responsible for placing the aneurysm at risk for lumen-side hypoxia. Perhaps most profoundly, Chapter 5 further revealed that low wall shear stress and low lumen-side oxygen content do not necessarily always coexist, and revealed that it is possible particularly for wall shear stress between approximately one and two dyn/cm^2 that a state of low wall shear stress and adequate wall oxygenation is not only possible but likely to occur locally in many aneurysms. To this end, the oxygenation of the wall was, in general, shown to be highly heterogeneous within the computational modeling. Many questions are left from this analysis. How do the

pathological states of the sac wall modify oxygen transport across the wall? Furthermore, how do oxygen demands change through the growth/remodeling processes of the wall? The most fundamental question needing to be answered is what constitutes a healthy range of oxygen concentration within the aneurysm wall tissue. Chapter 6 then revisited the topic of high frequency content within the cerebral circulation - particularly on how they can be generated (other than the simple stenosis situation) and how these flow features proliferate through the aneurysm. High frequency content was found to be particularly prevalent in the aneurysm inflow jet, raising the question as to whether there is a difference in the wall response to inflow jets with and without high frequency content. Further questions arise as to what particular information within the high frequency velocity fluctuations do the cells of the wall respond and what are those responses.

Appendix

Supplemental figures from Chapter 3

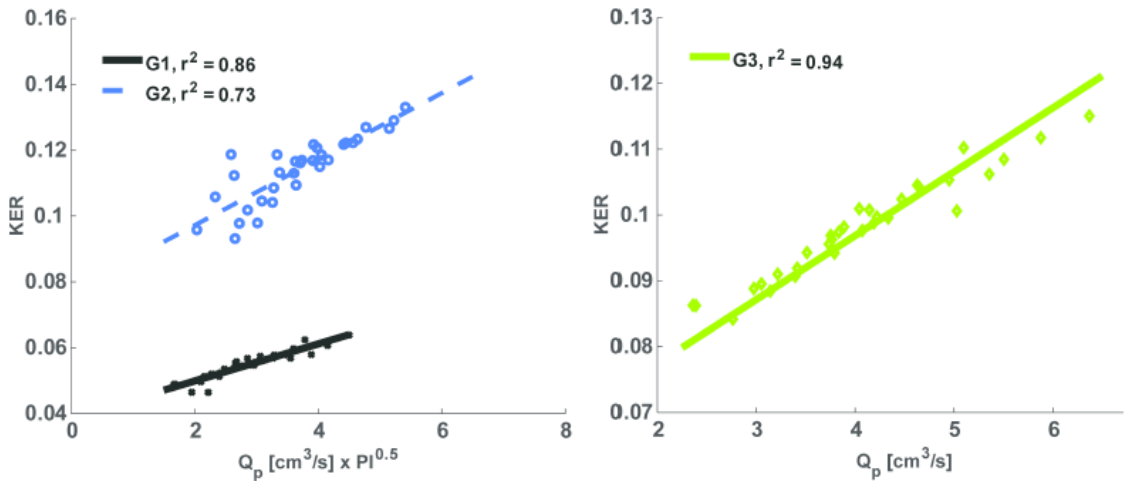

Figure A1: The KER for Geometry 3 is the only example in this work of a hemodynamic parameter normalized by the corresponding parameter found in the parent artery for which the waveform shape impacts the parameter. Here, KER is dominated by varying parent artery flow rate in the tubular-shaped Geometry 3, while waveform shape is an additional influence of KER for the saccular-shapped Geometries 1 and 2.

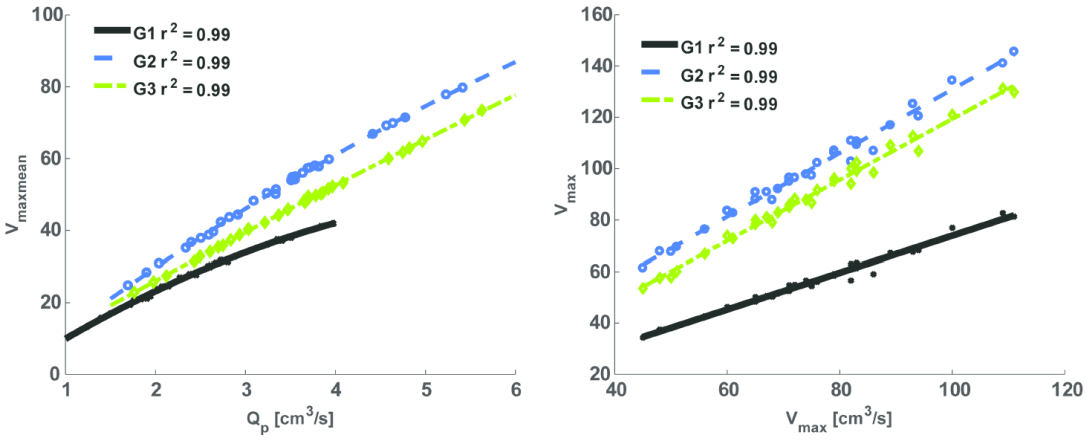

Figure A2: Time-averaged maximum velocity correlates well with parent artery flow rate, whereas the maximum velocity within the aneurysm is strongly dependent on the waveform shape.

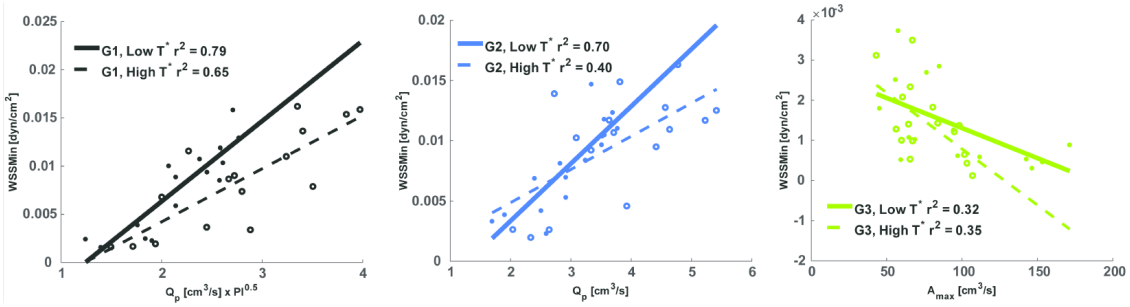

Figure A3: The WSSMin in the three geometries, while influenced by different waveform parameters, is seen to always be lower than two orders of magnitude than its time-averaged counterpart.

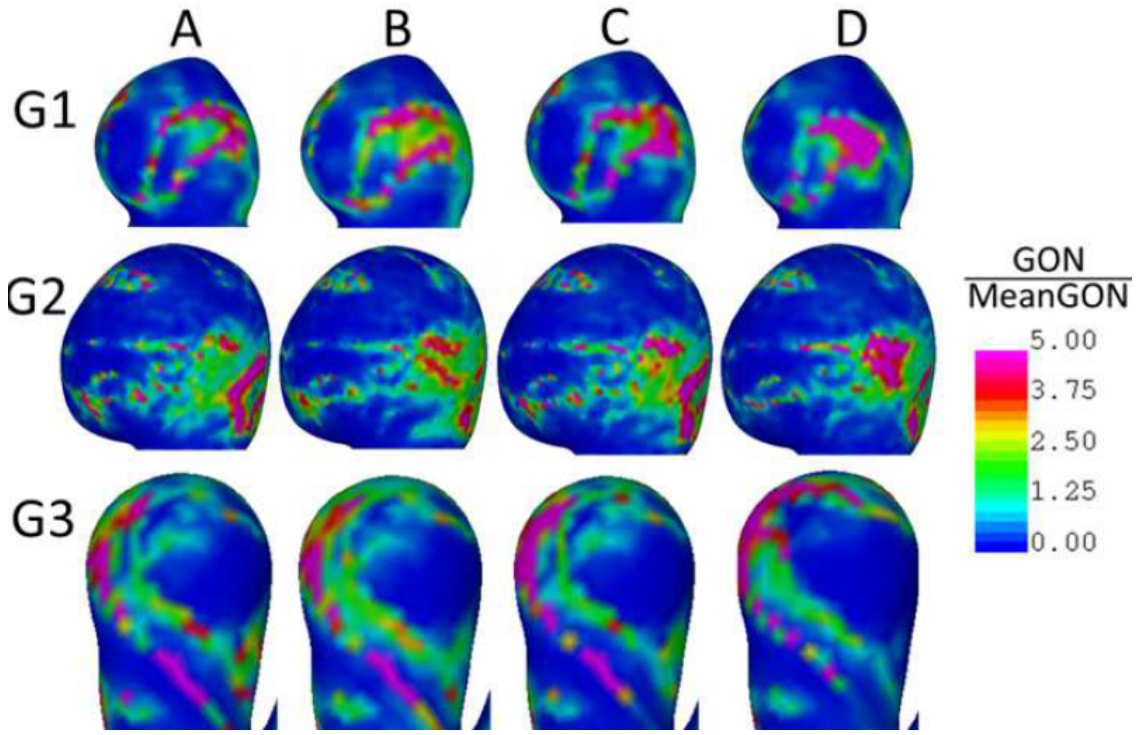

Figure A4: Regions of high and low Gradient oscillatory number (GON) are seen to be well predicted irrespective to the choice of waveform. Above, GON has been normalized by the mean GON value in the sac.

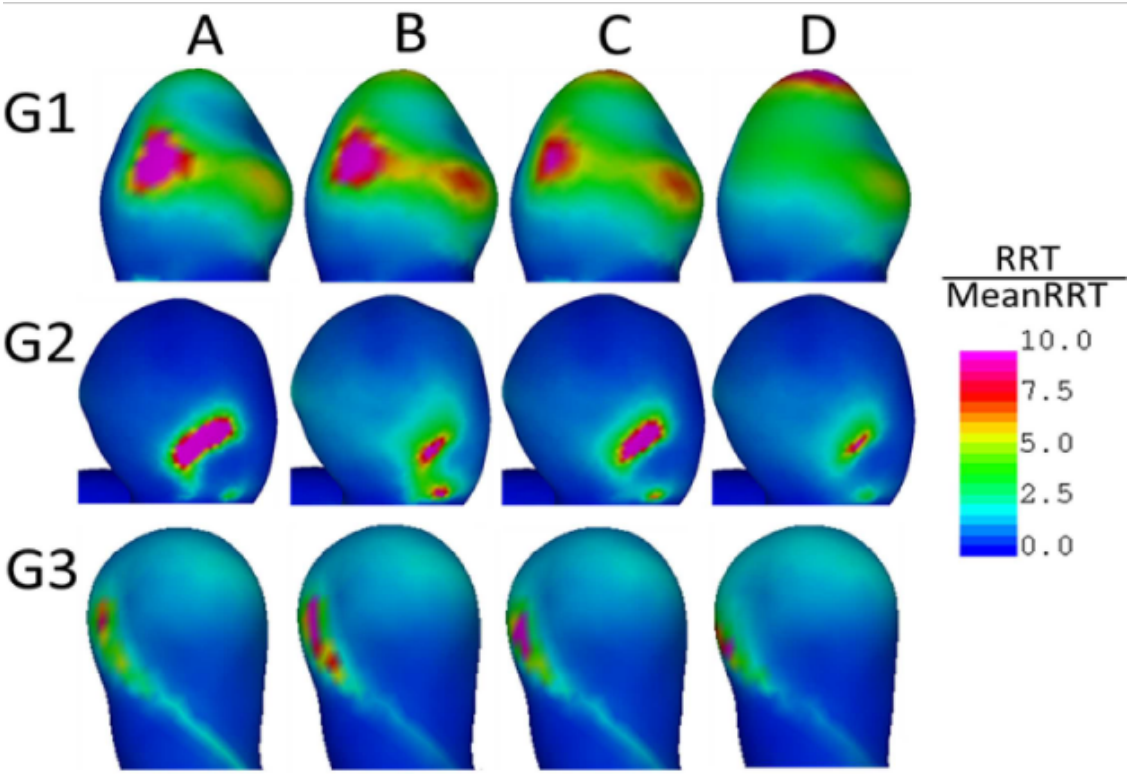

Figure A5: The above results suggest that regions of high and low relative residence time (RRT)rather well predicted irrespective to the choice of waveform. RRT predicted under flow conditions from Waveform D applied to Geometry1 however differs from the RRT predicted by Waveforms B-D, suggesting that the otherwise robust RRT trend begins to waver near minimum values of Q_p PI. Above, RRT has been normalized by the mean RRT value in the sac.

Bibliography

[1] Christian Aalkjaer and Julian H Lombard. Effect of hypoxia on force, intracellular ph and ca2+ concentration in rat cerebral and mesenteric small arteries. *The Journal of physiology*, 482(2):409–419, 1995.

[2] Mona Alimohammadi, Cesar Pichardo-Almarza, Obiekezie Agu, and Vanessa Díaz-Zuccarini. A multiscale modelling approach to understand atherosclerosis formation: A patient-specific case study in the aortic bifurcation. *Proceedings of the Institution of Mechanical Engineers, Part H: Journal of Engineering in Medicine*, 231(5):378–390, 2017.

[3] Ronny Amaya, Alexis Pierides, and John M Tarbell. The Interaction between Fluid Wall Shear Stress and Solid Circumferential Strain Affects Endothelial Gene Expression. *PloS one*, 10(7):e0129952, 2015.

[4] Aneurisk-Team. AneuriskWeb project website, ecm2.mathcs.emory.edu/aneuriskweb. Emory University, Department of Math and Computer Science, Web Site, 2012.

[5] Dimitrios Angouras, Dimitrios P. Sokolis, Theodosios Dosios, Nikolaos Kostomitsopoulos, Harisios Boudoulas, Gregorios Skalkeas, and Panagiotis E. Karayannacos. Effect of impaired vasa vasorum flow on the structure and mechanics of the thoracic aorta: Implications for the pathogenesis of aortic dissection. *European Journal of Cardio-thoracic Surgery*, 17(4):468–473, 2000.

[6] H. Babaee and T. P. Sapsis. A minimization principle for the description of modes associated with finite-time instabilities. *Proceedings of the Royal Society A: Mathematical, Physical and Engineering Science*, 472(2186):20150779, 2016.

[7] H Baek, MV Jayaraman, PD Richardson, and GE Karniadakis. Flow instability and wall shear stress variation in intracranial aneurysms. *Journal of the Royal Society Interface*, 7(47):967–988, 2009.

[8] Enikő Balogh, Andrea Tóth, Gábor Méhes, György Trencsényi, György Paragh, and Viktória Jeney. Hypoxia triggers osteochondrogenic differentiation of vascular smooth muscle cells in an hif-1 (hypoxia-inducible factor 1)–dependent and reactive oxygen species–dependent manner. *Arteriosclerosis, thrombosis, and vascular biology*, 39(6):1088–1099, 2019.

[9] Abdul I Barakat. A model for shear stress-induced deformation of a flow sensor on the surface of vascular endothelial cells. *Journal of theoretical biology*, 210(2):221–236, 2001.

[10] J Beck, S Rohde, M Beltagy, M Zimmermann, J Berkefeld, V Seifert, and A Raabe. Clinical Article Difference in configuration of ruptured and unruptured intracranial aneurysms determined by biplanar digital subtraction angiography. (September 1999):861–865, 2003.

[11] Jacopo Biasetti, T Christian Gasser, Martin Auer, Ulf Hedin, and Fausto Labruto. Hemodynamics of the normal aorta compared to fusiform and saccular abdominal aortic aneurysms with emphasis on a potential thrombus formation mechanism. *Annals of biomedical engineering*, 38(2):380–390, 2010.

[12] H. M. Blackburn and S. J. Sherwin. *Instability modes and transition of pulsatile stenotic flow: Pulse-period dependence*, volume 573. 2007.

[13] Andrew R Bond, Chih-Wen Ni, Hanjoong Jo, and Peter D Weinberg. Intimal cushions and endothelial nuclear elongation around mouse aortic branches and their spatial correspondence with patterns of lipid deposition. *American Journal of Physiology-Heart and Circulatory Physiology*, 298(2):H536–H544, 2009.

[14] Loic Boussel, Vitaliy Rayz, Charles McCulloch, Alastair Martin, Gabriel Acevedo-Bolton, Michael Lawton, Randall Higashida, Wade S. Smith, William L. Young, and David Saloner. Aneurysm growth occurs at region of low wall shear stress: Patient-specific correlation of hemodynamics and growth in a longitudinal study. *Stroke*, 39(11):2997–3002, 2008.

[15] April J Boyd, David CS Kuhn, Richard J Lozowy, and Gordon P Kulbisky. Low wall shear stress predominates at sites of abdominal aortic aneurysm rupture. *Journal of vascular surgery*, 63(6):1613–1619, 2016.

[16] Jonathan L Brisman, Joon K Song, and David W Newell. Cerebral aneurysms. *New England journal of medicine*, 355(9):928–939, 2006.

[17] Joseph P Broderick, Thomas G Brott, John E Duldner, Thomas Tomsick, and Alan Leach. Initial and recurrent bleeding are the major causes of death following subarachnoid hemorrhage. *Stroke*, 25(7):1342–1347, 1994.

[18] Ronald O. Bude and Jonathan M. Rubin. Relationship between the Resistive Index and Vascular Compliance and Resistance. *Radiology*, 211(2):411–417, 1999.

[19] G. Byrne, F. Mut, and J. Cebral. Quantifying the large-scale hemodynamics of intracranial aneurysms. *American Journal of Neuroradiology*, 35(2):333–338, 2014.

[20] Marcelo Castro, Christopher Putman, Alessandro Radaelli, Alejandro Frangi, and Juan Cebral. Hemodynamics and rupture of terminal cerebral aneurysms. *Academic radiology*, 16(10):1201–1207, 2009.

[21] Juan Cebral, Eliisa Ollikainen, Bong Jae Chung, Fernando Mut, Visa Sippola, Behnam Rezai Jahromi, Riikka Tulamo, Juha Hernesniemi, Mika Niemelä, Anne Robertson, et al. Flow conditions in the intracranial aneurysm lumen are associated with inflammation and degenerative changes of the aneurysm wall. *American Journal of Neuroradiology*, 38(1):119–126, 2017.

[22] Juan Cebral, Eliisa Ollikainen, Bong Jae Chung, Fernando Mut, Visa Sippola, Behnam Rezai Jahromi, Riikka Tulamo, Juha Hernesniemi, Mika Niemelä, Anne Robertson, et al. Local hemodynamic conditions associate with focal changes in the intracranial aneurysm walll. *American Journal of Neuroradiology*, 38(1):119–126, 2017.

[23] Juan R Cebral, Marcelo a Castro, James E Burgess, Richard S Pergolizzi, Michael J Sheridan, and Christopher M Putman. Characterization of cerebral aneurysms for assessing risk of rupture by using patient-specific computational hemodynamics models. *AJNR. American journal of neuroradiology*, 26(10):2550–9, 2005.

[24] Juan R Cebral, Marcelo Adrián Castro, Sunil Appanaboyina, Christopher M Putman, Daniel Millan, and Alejandro F Frangi. Efficient pipeline for image-based patient-specific analysis of cerebral aneurysm hemodynamics: technique and sensitivity. *IEEE transactions on medical imaging*, 24(4):457–467, 2005.

[25] Juan R Cebral, Felicitas Detmer, Bong Jae Chung, Joham Choque-Velasquez, Behnam Rezai, Hanna Lehto, Riikka Tulamo, Juha Hernesniemi, Mika Niemela, Alexander Yu, et al. Local hemodynamic conditions associated with focal changes in the intracranial aneurysm wall. *American Journal of Neuroradiology*, 40(3):510–516, 2019.

[26] Juan R Cebral, Xinjie Duan, Bong Jae Chung, Christopher Putman, Khaled Aziz, and AM Robertson. Wall mechanical properties and hemodynamics of unruptured intracranial aneurysms. *American Journal of Neuroradiology*, 2015.

[27] Juan R Cebral, Xinjie Duan, Piyusha S Gade, Bong Jae Chung, Fernando Mut, Khaled Aziz, and Anne M Robertson. Regional mapping of flow and wall characteristics of intracranial aneurysms. *Annals of biomedical engineering*, 44(12):3553–3567, 2016.

[28] Juan R Cebral, F Mut, D Sforza, R Löhner, E Scrivano, P Lylyk, and C Putman. Clinical application of image-based cfd for cerebral aneurysms. *International journal for numerical methods in biomedical engineering*, 27(7):977–992, 2011.

[29] Juan R. Cebral, F. Mut, J. Weir, and C. M. Putman. Association of hemodynamic characteristics and cerebral aneurysm rupture. *American Journal of Neuroradiology*, 32(2):264–270, 2011.

[30] Juan R Cebral, Fernando Mut, Piyusha Gade, Fangzhou Cheng, Yasutaka Tobe, Juhana Frosen, and Anne M Robertson. Combining data from multiple sources to study mechanisms of aneurysm disease: Tools and techniques. *International journal for numerical methods in biomedical engineering*, 34(11):e3133, 2018.

[31] Juan R Cebral, Fernando Mut, Jane Weir, and Christopher Putman. Quantitative characterization of the hemodynamic environment in ruptured and unruptured brain aneurysms. *American Journal of Neuroradiology*, 32(1):145–151, 2011.

[32] Juan R Cebral, Fernando Mut, Jane Weir, and Christopher Putman. Quantitative characterization of the hemodynamic environment in ruptured and unruptured brain aneurysms. *American Journal of Neuroradiology*, 32(1):145–151, 2011.

[33] Juan R. Cebral, M. Sheridan, and C. M. Putman. Hemodynamics and bleb formation in intracranial aneurysms. *American Journal of Neuroradiology*, 31(2):304–310, 2010.

[34] Emanuele Cecchi, Cristina Giglioli, Serafina Valente, Chiara Lazzeri, Gian Franco Gensini, Rosanna Abbate, and Lucia Mannini. Role of hemodynamic shear stress in cardiovascular disease. *Atherosclerosis*, 214(2):249–256, 2011.

[35] Woonou Cha and Richard L Beissinger. Evaluation of shear-induced particle diffusivity in red cell ghosts suspensions. *Korean Journal of Chemical Engineering*, 18(4):479–485, 2001.

[36] Nohra Chalouhi, Muhammad S Ali, Robert M Starke, Pascal M Jabbour, Stavropoula I Tjoumakaris, L Fernando Gonzalez, Robert H Rosenwasser, Walter J

Koch, and Aaron S Dumont. Cigarette smoke and inflammation: role in cerebral aneurysm formation and rupture. *Mediators of inflammation*, 2012, 2012.

[37] I Chatziprodromou, D Poulikakos, and Y Ventikos. On the influence of variation in haemodynamic conditions on the generation and growth of cerebral aneurysms and atherogenesis : A computational model. 40:3626–3640, 2007.

[38] Jeng-Jiann Chiu and Shu Chien. Effects of disturbed flow on vascular endothelium: pathophysiological basis and clinical perspectives. *Physiological reviews*, 91(1):327–387, 2011.

[39] BJ Chung, F Mut, CM Putman, F Hamzei-Sichani, W Brinjikji, D Kallmes, CM Jimenez, and JR Cebral. Identification of hostile hemodynamics and geometries of cerebral aneurysms: a case-control study. *American Journal of Neuroradiology*, 39(10):1860–1866, 2018.

[40] Tae Wook Chung, Hee Jung Choi, Cheorl Ho Kim, Han Sol Jeong, and Ki Tae Ha. Lipocalin-2 elicited by advanced glycation end-products promotes the migration of vascular smooth muscle cells. *Biochimica et Biophysica Acta - Molecular Cell Research*, 1833(12):3386–3395, 2013.

[41] Harry J Cloft, John G Short, Anjob Degast, Gregory a Helm, and David F Kallmes. Creation of Saccular Aneurysms in 1999 ARRS Executive Council the Rabbit : A Model Suitable for. (February):349–354, 2000.

[42] Ben R Clower, David M Sullivan, and Robert R Smith. Intracranial vessels lack vasa vasorum. *Journal of neurosurgery*, 61(1):44–48, 1984.

[43] John P Cooke, Jonathan Stamler, Nancy Andon, Peter F Davies, Gareth McKinley, and Joseph Loscalzo. Flow stimulates endothelial cells to release a nitrovasodilator that is potentiated by reduced thiol. *American Journal of Physiology-Heart and Circulatory Physiology*, 259(3):H804–H812, 1990.

[44] T Crawford. Some observations on the pathogenesis and natural history of intracranial aneurysms. *Journal of neurology, neurosurgery, and psychiatry*, 22(4):259, 1959.

[45] M Crompton. Mechanism of growth and rupture in cerebral berry aneurysms. *British medical journal*, 1:1138–1142, 1966.

[46] P F Davies, A Remuzzi, E J Gordon, C F Dewey, and M A Gimbrone. Turbulent fluid shear stress induces vascular endothelial cell turnover in vitro. *Proceedings of the National Academy of Sciences of the United States of America*, 83(7):2114–7, 1986.

[47] Peter F Davies. Flow-mediated endothelial mechanotransduction. *Physiological reviews*, 75(3):519–560, 1995.

[48] Peter F Davies. Hemodynamic shear stress and the endothelium in cardiovascular pathophysiology. *Nature Reviews Cardiology*, 6(1):16, 2009.

[49] N K de Rooij, F H H Linn, J a van der Plas, A Algra, and G J E Rinkel. Incidence of subarachnoid haemorrhage: a systematic review with emphasis on region, age, gender and time trends. *Journal of neurology, neurosurgery, and psychiatry*, 78(12):1365–72, 2007.

[50] Felicitas J Detmer, Daniel Fajardo-Jiménez, Fernando Mut, Norman Juchler, Sven Hirsch, Vitor Mendes Pereira, Philippe Bijlenga, and Juan R Cebral. External validation of cerebral aneurysm rupture probability model with data from two patient cohorts. *Acta neurochirurgica*, 160(12):2425–2434, 2018.

[51] Jennifer M Dolan, John Kolega, and Hui Meng. High wall shear stress and spatial gradients in vascular pathology: a review. *Annals of biomedical engineering*, 41(7):1411–1427, 2013.

[52] Helmut Drexler and Burkhard Hornig. Endothelial dysfunction in human disease. *Journal of molecular and cellular cardiology*, 31(1):51–60, 1999.

[53] Michael J. Durka. A computational parametric study of the relationship between the characteristic geometry, flow structure, and hemodynamics of intracranial bifurcation aneurysms. Master's thesis, University of Pittsburgh, 2013.

[54] Michael J Durka, Isaac H Wong, David F Kallmes, Dario Pasalic, Fernando Mut, Manoj Jagani, Pablo J Blanco, Juan R Cebral, and Anne M Robertson. A data-driven approach for addressing the lack of flow waveform data in studies of cerebral arterial flow in older adults. *Physiological measurement*, 39(1):015006, 2018.

[55] Neurosurg Focus. Unruptured intracranial aneurysms and the assessment of rupture risk based on anatomical and morphological factors: sifting through the sands of data. 26(May):1–7, 2009.

[56] Matthew D Ford, Noam Alperin, Sung Hoon Lee, David W Holdsworth, and David a Steinman. Characterization of volumetric flow rate waveforms in the normal internal carotid and vertebral arteries. *Physiological Measurement*, 26(4):477–488, 2005.

[57] Matthew D Ford and Ugo Piomelli. Exploring High Frequency Temporal Fluctuations in the Terminal Aneurysm of the Basilar Bifurcation. 134(September 2012):1–10, 2012.

[58] George N Foutrakis, Howard Yonas, and Robert J Sclabassi. Saccular aneurysm formation in curved and bifurcating arteries. *American Journal of Neuroradiology*, 20(7):1309–1317, 1999.

[59] Juhana Frösen, Riikka Tulamo, Anders Paetau, Elisa Laaksamo, Miikka Korja, Aki Laakso, Mika Niemelä, and Juha Hernesniemi. Saccular intracranial aneurysm: pathology and mechanisms. *Acta neuropathologica*, 123(6):773–786, 2012.

[60] Keiji Fukazawa, Fujimaro Ishida, Yasuyuki Umeda, Yoichi Miura, Shinichi Shimosaka, Satoshi Matsushima, Waro Taki, and Hidenori Suzuki. Using computational fluid dynamics analysis to characterize local hemodynamic features of middle cerebral artery aneurysm rupture points. *World neurosurgery*, 83(1):80–86, 2015.

[61] Kazuhiro Furukawa, Fujimaro Ishida, Masanori Tsuji, Yoichi Miura, Tomoyuki Kishimoto, Masato Shiba, Hiroshi Tanemura, Yasuyuki Umeda, Takanori Sano, Ryuta Yasuda, et al. Hemodynamic characteristics of hyperplastic remodeling lesions in cerebral aneurysms. *PloS one*, 13(1):e0191287, 2018.

[62] AJ Geers, I Larrabide, HG Morales, and AF Frangi. Approximating hemodynamics of cerebral aneurysms with steady flow simulations. *Journal of biomechanics*, 47(1):178–185, 2014.

[63] Gary H Gibbons and Victor J Dzau. The emerging concept of vascular remodeling. *New England Journal of Medicine*, 330(20):1431–1438, 1994.

[64] Michael A Gimbrone Jr, James N Topper, Tobi Nagel, Keith R Anderson, and Guillermo Garcia-Caredña. Endothelial dysfunction, hemodynamic forces, and atherogenesis a. *Annals of the New York Academy of Sciences*, 902(1):230–240, 2000.

[65] Seymour Glagov, Christopher Zarins, Don P Giddens, and David N Ku. Hemodynamics and atherosclerosis. insights and perspectives gained from studies of human arteries. *Archives of pathology & laboratory medicine*, 112(10):1018–1031, 1988.

[66] Daniel Goldman. Theoretical models of microvascular oxygen transport to tissue. *Microcirculation*, 15(8):795–811, 2008.

[67] HL Goldsmith. Red cell motions and wall interactions in tube flow. In *Federation proceedings*, volume 30, pages 1578–1590, 1971.

[68] HL Goldsmith and JC Marlow. Flow behavior of erythrocytes. ii. particle motions in concentrated suspensions of ghost cells. *Journal of Colloid and Interface Science*, 71(2):383–407, 1979.

[69] Carlos F Gonzalez, Young I Cho, Hector V Ortega, and Jacgues Moret. Intracranial aneurysms: flow analysis of their origin and progression. *American Journal of Neuroradiology*, 13(1):181–188, 1992.

[70] A M Robertson G.P. Galidi R. Rannacher and S Turek. *Hemodynamical Flows: Modeling, Analysis and Simulation*, volume 37. 2008.

[71] TM Griffith. Modulation of blood flow and tissue perfusion by endothelium-derived relaxing factor. *Experimental Physiology: Translation and Integration*, 79(6):873–913, 1994.

[72] George J Hademenos and Tarik F Massoud. Biophysical mechanisms of stroke. *Stroke*, 28(10):2067–2077, 1997.

[73] GJ Haldemenos. The physics of cerebral aneurysms. *Physics Today*, 48(2):24–30, 1995.

[74] Lorraine E Harry, Mrcs Edin, and Ewa M Paleolog. Modulating Angiogenesis. 292(8):6–11, 2019.

[75] Tamer Hassan, Eugene V Timofeev, Tsutomu Saito, Hiroaki Shimizu, Masayuki Ezura, Yasushi Matsumoto, Kazuyoshi Takayama, Teiji Tominaga, and Akira Takahashi. A proposed parent vessel geometry—based categorization of saccular intracranial aneurysms: computational flow dynamics analysis of the risk factors for lesion rupture. *Journal of neurosurgery*, 103(4):662–680, 2005.

[76] Tamer Hassan, Eugene V Timofeev, Tsutomu Saito, Hiroaki Shimizu, Masayuki Ezura, Teiji Tominaga, Akira Takahashi, and Kazuyoshi Takayama. Computational replicas: anatomic reconstructions of cerebral vessels as volume numerical grids at

three-dimensional angiography. *American journal of neuroradiology*, 25(8):1356–1365, 2004.

[77] Xiaoyi He and David N Ku. Pulsatile flow in the human left coronary artery bifurcation: average conditions. 1996.

[78] Donald D Heistad, Mark L Armstrong, and Susan Amundsen. Blood flow through vasa vasorum in arteries and veins: effects of luminal po2. *American Journal of Physiology-Heart and Circulatory Physiology*, 250(3):H434–H442, 1986.

[79] Archibald Vivian Hill. The possible effects of the aggregation of the molecules of haemoglobin on its dissociation curves. *j. physiol.*, 40:4–7, 1910.

[80] Heather A. Himburg, Scot E. Dowd, and Morton H. Friedman. Frequency-dependent response of the vascular endothelium to pulsatile shear stress. *American Journal of Physiology-Heart and Circulatory Physiology*, 293(1):H645–H653, 2007.

[81] Kozo Hirata, Toshio Yaginuma, Michael F. O'Rourke, and Masanobu Kawakami. Age-related changes in carotid artery flow and pressure pulses: Possible implications for cerebral microvascular disease. *Stroke*, 37(10):2552–2556, 2006.

[82] Brian L Hoh and Christopher L Sistrom. P Atients With Multiple Cerebral Aneurysms. *Neurosurgery*, 61(4):716–723, 2007.

[83] Yiemeng Hoi, Bruce A Wasserman, Edward G Lakatta, and David A Steinman. Carotid bifurcation hemodynamics in older adults: effect of measured versus assumed flow waveform. *Journal of biomechanical engineering*, 132(7):071006, 2010.

[84] Yiemeng Hoi, Bruce A Wasserman, Yuanyuan J Xie, Samer S Najjar, Luigi Ferruci, Edward G Lakatta, Gary Gerstenblith, and David A Steinman. Characterization of volumetric flow rate waveforms at the carotid bifurcations of older adults. *Physiological measurement*, 31(3):291, 2010.

[85] D W Holdsworth, C J Norley, R Frayne, D A Steinman, and B K Rutt. Characterization of common carotid artery blood-flow waveforms in normal human subjects. *Physiological measurement*, 20(3):219–40, aug 1999.

[86] Emilie C Holland. *Computational Modeling of transport phenomena in cerebral aneurysms*. PhD thesis, University of Oxford, 2012.

[87] Tzung K. Hsiai, Susan Hama, Henry M. Honda, Chih-Ming Ho, Sung K. Cho, Linda L. Demer, and Mohamad Navab. Endothelial Cell Dynamics under Pulsating Flows: Significance of High Versus Low Shear Stress Slew Rates. *Annals of Biomedical Engineering*, 30(5):646–656, 2002.

[88] Yohsuke Imai, Kodai Sato, Takuji Ishikawa, Andrew Comerford, Tim David, and Takami Yamaguchi. Atp transport in saccular cerebral aneurysms at arterial bends. *Annals of biomedical engineering*, 38(3):927–934, 2010.

[89] Timothy Ingall, Kjell Asplund, Markku Mahonen, and Ruth Bonita. A multinational comparison of subarachnoid hemorrhage epidemiology in the who monica stroke study. *Stroke*, 31(5):1054–1061, 2000.

[90] IGH Jansen, JJ Schneiders, WV Potters, P van Ooij, R van den Berg, E van Bavel, HA Marquering, and CBLM Majoie. Generalized versus patient-specific inflow boundary conditions in computational fluid dynamics simulations of cerebral aneurysmal hemodynamics. *American Journal of Neuroradiology*, 2014.

[91] Jinhee Jeong and Hussain Fazle. On the identification of a vortex. *Journal of Fluid Mechanics*, 285:69–94, 1995.

[92] Lisbeth G Jorgensen, Grazyna Perko, and Niels H Secher. Regional cerebral artery mean flow velocity and blood flow during dynamic exercise in humans. *Journal of Applied Physiology*, 73(5):1825–1830, 1992.

[93] Mahesh S Joshi, Julie L Ponthier, and Jack R Lancaster Jr. Cellular antioxidant and pro-oxidant actions of nitric oxide. *Free Radical Biology and Medicine*, 27(11-12):1357–1366, 1999.

[94] L-D Jou, D H Lee, H Morsi, and M E Mawad. Wall shear stress on ruptured and unruptured intracranial aneurysms at the internal carotid artery. *AJNR Am J Neuroradiol*, 29:1761–1767, 2008.

[95] Liang-Der Jou, Christopher M Quick, William L Young, Michael T Lawton, Randall Higashida, Alastair Martin, and David Saloner. Computational approach to quantifying hemodynamic forces in giant cerebral aneurysms. *American Journal of Neuroradiology*, 24(9):1804–1810, 2003.

[96] ER Jurrus and HS Weiss. In vitro tissue oxygen tensions in the rabbit aortic arch. *Atherosclerosis*, 28(3):223–232, 1977.

[97] Foad Kabinejadian, Fangsen Cui, Boyang Su, Asawinee Danpinid, Pei Ho, and Hwa Liang Leo. Effects of a carotid covered stent with a novel membrane design on the blood flow regime and hemodynamic parameters distribution at the carotid artery bifurcation. *Medical and Biological Engineering and Computing*, 53(2):165–177, 2014.

[98] Ramanathan Kadirvel, Yong-Hong Ding, Daying Dai, Hasballah Zakaria, Anne M Robertson, Mark A Danielson, Debra A Lewis, Harry J Cloft, and David F Kallmes. The influence of hemodynamic forces on biomarkers in the walls of elastase-induced aneurysms in rabbits. *Neuroradiology*, 49(12):1041–1053, 2007.

[99] Dirk Kaiser, Mark-Andre Freyberg, and Peter Friedl. Lack of hemodynamic forces triggers apoptosis in vascular endothelial cells. *Biochemical and biophysical research communications*, 231(3):586–590, 1997.

[100] Cindy E Kallman, Barbara B Gosink, and Douglas J Gardner. Carotid Duplex Sonography : in Patients with Bisferious Pulse Contour Aortic Valvular Disease. *Circulation*.

[101] David F. Kallmes, Naomi H. Fujiwara, Debbie Yuen, Daying Dai, and Shu Tung Li. A collagen-based coil for embolization of saccular aneurysms in a New Zealand White rabbit model. *American Journal of Neuroradiology*, 24(4):591–596, 2003.

[102] Makio Kaminogo, Masahiro Yonekura, and Shobu Shibata. Incidence and outcome of multiple intracranial aneurysms in a defined population. *Stroke*, 34(1):16–21, 2003.

[103] Akira Kamiya and Tatsuo Togawa. Adaptive regulation of wall shear stress to flow change in the canine carotid artery. *American Journal of Physiology-Heart and Circulatory Physiology*, 239(1):H14–H21, 1980.

[104] Christof Karmonik, Christopher Yen, Orlando Diaz, Richard Klucznik, Robert G. Grossman, and Goetz Benndorf. Temporal variations of wall shear stress parameters in intracranial aneurysms-importance of patient-specific inflow waveforms for CFD calculations. *Acta Neurochirurgica*, 152(8):1391–1398, 2010.

[105] George Karniadakis and Spencer Sherwin. *Spectral/hp element methods for computational fluid dynamics*. Oxford University Press, 2013.

[106] Kazuo Kataoka, Mamoru Taneda, Toshiharu Asai, Akira Kinoshita, Mamoru Ito, and Ryotaro Kuroda. Structural fragility and inflammatory response of ruptured cerebral aneurysms: a comparative study between ruptured and unruptured cerebral aneurysms. *Stroke*, 30(7):1396–1401, 1999.

[107] Tomohiro Kawaguchi, Shinjitsu Nishimura, Masayuki Kanamori, Hiroki Takazawa, Shunsuke Omodaka, Kenya Sato, Noriko Maeda, Yoko Yokoyama, Hiroshi Midorikawa, Tatsuya Sasaki, et al. Distinctive flow pattern of wall shear stress and oscillatory shear index: similarity and dissimilarity in ruptured and unruptured cerebral aneurysm blebs. *Journal of neurosurgery*, 117(4):774–780, 2012.

[108] James P Kehrer. Free radicals as mediators of tissue injury and disease. *Critical reviews in toxicology*, 23(1):21–48, 1993.

[109] Sungho Kim and Don P Giddens. Mass transport of low density lipoprotein in reconstructed hemodynamic environments of human carotid arteries: the role of volume and solute flux through the endothelium. *Journal of biomechanical engineering*, 137(4):041007, 2015.

[110] Hidehito Kimura, Masaaki Taniguchi, Kosuke Hayashi, Yosuke Fujimoto, Youichi Fujita, Takashi Sasayama, Akio Tomiyama, and Eiji Kohmura. Clear Detection of Thin-Walled Regions in Unruptured Cerebral Aneurysms by Using Computational Fluid Dynamics. *World Neurosurgery*, 121:e287–e295, 2019.

[111] Naoaki Yamada Koji Iihara, Kenichi Murao, Nobuyuki Sakai, Akio Soeda, Hatsue Ishibashi-Ueda, Chikao Yutani and Izumi Nagata. Continued growth of and increased symptoms from a thrombosed giant aneurysm of the vertebral artery after complete endovascular. *Journal of Neurosurgery*, 98:407–413, 2003.

[112] Maheshwaran K. Kolandavel, Ernst Torben Fruend, Steffen Ringgaard, and Peter G. Walker. The effects of time varying curvature on species transport in coronary arteries. *Annals of Biomedical Engineering*, 34(12):1820–1832, 2006.

[113] T Krings, H Alvarez, P Reinacher, A Ozanne, CE Baccin, C Gandolfo, W-Y Zhao, MHT Reinges, and P Lasjaunias. Growth and rupture mechanism of partially thrombosed aneurysms. *Interventional neuroradiology*, 13(2):117–126, 2007.

[114] Timo Krings, Ronie L Piske, and Pierre L Lasjaunias. Intracranial arterial aneurysm vasculopathies: targeting the outer vessel wall. *Neuroradiology*, 47(12):931–937, 2005.

[115] D. N. Ku, D. P. Giddens, C. K. Zarins, and S. Glagov. Pulsatile flow and atherosclerosis in the human carotid bifurcation. Positive correlation between plaque location and low oscillating shear stress. *Arteriosclerosis, Thrombosis, and Vascular Biology*, 5(3):293–302, 1985.

[116] Z. Kulcsár, Á Ugron, M. Marosfoi, Z. Berentei, G. Paál, and István Szikora. Hemodynamics of cerebral aneurysm initiation: The role of wall shear stress and spatial wall shear stress gradient. *American Journal of Neuroradiology*, 32(3):587–594, 2011.

[117] Mitja I. Kurki, Sanna Kaisa Häkkinen, Juhana Frösen, Riikka Tulamo, Mikael Von Und Zu Fraunberg, Garry Wong, Gerard Tromp, Mika Niemelä, Juha Hernesniemi, Juha E. Jääskeläinen, and Seppo Ylä-Herttuala. Upregulated signaling pathways in ruptured human saccular intracranial aneurysm wall: An emerging regulative role of toll-like receptor signaling and nuclear factor-κB, hypoxia-inducible factor-1A, and ETS transcription factors. *Neurosurgery*, 68(6):1667–1675, 2011.

[118] Elisa Laaksamo, Riikka Tulamo, Arto Liiman, Marc Baumann, Robert M Friedlander, Juha Hernesniemi, Marko Kangasniemi, Mika Niemelä, Aki Laakso, and Juhana Frösen. Oxidative stress is associated with cell death, wall degradation, and increased risk of rupture of the intracranial aneurysm wall. *Neurosurgery*, 72(1):109–117, 2012.

[119] B Lowell Langille and Frank O'Donnell. Reductions in arterial diameter produced by chronic decreases in blood flow are endothelium-dependent. *Science*, 231(4736):405–407, 1986.

[120] B LowellL Langille, Michelle P Bendeck, and Fred W Keeley. Adaptations of carotid arteries of young and mature rabbits to reduced carotid blood flow. *American Journal of Physiology-Heart and Circulatory Physiology*, 256(4):H931–H939, 1989.

[121] Seung E. Lee, Sang Wook Lee, Paul F. Fischer, Hisham S. Bassiouny, and Francis Loth. Direct numerical simulation of transitional flow in a stenosed carotid bifurcation. *Journal of Biomechanics*, 41(11):2551–2561, 2008.

[122] DW Liepsch. Flow in tubes and arteries-a comparison. *Biorheology*, 23(4):395–433, 1986.

[123] Donia J. Macdonald, Helen M. Finlay, and Peter B. Canham. Directional Wall Strength in Saccular Brain Aneurysms from Polarized Light Microscopy. *Annals of Biomedical Engineering*, 28(5):533–542, 2000.

[124] Adel M Malek, Seth L Alper, and Seigo Izumo. Hemodynamic shear stress and its role in atherosclerosis. *Jama*, 282(21):2035–2042, 1999.

[125] A. Mantha, C. Karmonik, G. Benndorf, C. Strother, and Ralph Metcalfe. Hemodynamics in a cerebral artery before and after the formation of an aneurysm. *American Journal of Neuroradiology*, 27(5):1113–1118, 2006.

[126] D. Martin, A. Zaman, J. Hacker, D. Mendelow, and D. Birchall. Analysis of haemodynamic factors involved in carotid atherosclerosis using computational fluid dynamics. *British Journal of Radiology*, 82(SPEC. ISSUE 1):33–38, 2009.

[127] Alberto Marzo, Pankaj Singh, Ignacio Larrabide, Alessandro Radaelli, Stuart Coley, Matt Gwilliam, Iain D. Wilkinson, Patricia Lawford, Philippe Reymond, Umang Patel, Alejandro Frangi, and D. Rod Hose. Computational hemodynamics in cerebral aneurysms: The effects of modeled versus measured boundary conditions. *Annals of Biomedical Engineering*, 39(2):884–896, 2011.

[128] H Meng, VM Tutino, J Xiang, and A Siddiqui. High wss or low wss? complex interactions of hemodynamics with intracranial aneurysm initiation, growth, and rupture: toward a unifying hypothesis. *American Journal of Neuroradiology*, 35(7):1254–1262, 2014.

[129] Hui Meng, Zhijie Wang, Yiemeng Hoi, Ling Gao, Eleni Metaxa, Daniel D Swartz, and John Kolega. Complex hemodynamics at the apex of an arterial bifurcation induces vascular remodeling resembling cerebral aneurysm initiation. *Stroke*, 38(6):1924–1931, 2007.

[130] Eleni Metaxa, Markus Tremmel, Sabareesh K. Natarajan, Jianping Xiang, Rocco A. Paluch, Max Mandelbaum, Adnan H. Siddiqui, John Kolega, J. Mocco, and Hui Meng. Characterization of critical hemodynamics contributing to aneurysmal remodeling at the basilar terminus in a rabbit model. *Stroke*, 41(8):1774–1782, 2010.

[131] Carine Michiels. Physiological and pathological responses to hypoxia. *The American journal of pathology*, 164(6):1875–1882, 2004.

[132] N. L. Mills, J. J. Miller, A. Anand, S. D. Robinson, G. A. Frazer, D. Anderson, L. Breen, I. B. Wilkinson, C. M. McEniery, K. Donaldson, D. E. Newby, and W. MacNee. Increased arterial stiffness in patients with chronic obstructive pulmonary disease: A mechanism for increased cardiovascular risk. *Thorax*, 63(4):306–311, 2008.

[133] Haruka Miyata, Hirohiko Imai, Hirokazu Koseki, Kampei Shimizu, Yu Abekura, Mieko Oka, Takakazu Kawamata, Tetsuya Matsuda, Kazuhiko Nozaki, Shuh Narumiya, et al. Vasa vasorum formation is associated with rupture of intracranial aneurysms. *Journal of neurosurgery*, 1(aop):1–11, 2019.

[134] SRMJ Moncada. Nitric oxide: physiology, pathophysiology, and pharmacology. *Pharmacol rev*, 43:109–142, 1991.

[135] J. A. Moore. Oxygen Mass Transfer Calculations in Large Arteries. *Journal of Biomechanical Engineering*, 119(4):469, 1997.

[136] Hernán G Morales and Odile Bonnefous. Unraveling the relationship between arterial flow and intra-aneurysmal hemodynamics. *Journal of biomechanics*, 48(4):585–591, 2015.

[137] Pedro R. Moreno, K. Raman Purushothaman, Marc Sirol, Andrew P. Levy, and Valentin Fuster. Neovascularization in human atherosclerosis. *Circulation*, 113(18):2245–2252, 2006.

[138] K Moritake, H Handa, K Hayashi, and M Sato. Experimental studies on intracranial aneurysms (a preliminary report): some biomechanical considerations on the wall structures of intracranial aneurysms and experimentally produced aneurysms. *No shinkei Sheka*, 1:115–123, 1973.

[139] K. S. Moulton. Plaque angiogenesis and atherosclerosis. *Current atherosclerosis reports*, 3(3):225–233, 2001.

[140] Dr IM Moxham. Age-related changes in carotid artery flow and pressure pulses: Possible implications for cerebral microvascular disease. *Stroke*, 37(10):40–42, 2003.

[141] Eoin A. Murphy, Adrian S. Dunne, David M. Martin, and Fergal J. Boyle. Oxygen Mass Transport in Stented Coronary Arteries. *Annals of Biomedical Engineering*, 44(2):508–522, 2016.

[142] Sae-Il Murtada, Martin Kroon, and Gerhard A Holzapfel. A calcium-driven mechanochemical model for prediction of force generation in smooth muscle. *Biomechanics and modeling in mechanobiology*, 9(6):749–762, 2010.

[143] Jonathan P Mynard and David A Steinman. Effect of velocity profile skewing on blood velocity and volume flow waveforms derived from maximum doppler spectral velocity. *Ultrasound in medicine & biology*, 39(5):870–881, 2013.

[144] Ali Nader-Sepahi, Miguel Casimiro, Jon Sen, and Neil D. Kitchen. Is Aspect Ratio a Reliable Predictor of Intracranial Aneurysm Rupture? *Neurosurgery*, 54(6):1343–1348, jun 2004.

[145] Hirofumi Nakatomi, Hiromu Segawa, Atsushi Kurata, Yoshiaki Shiokawa, Kazuya Nagata, Hiroyasu Kamiyama, Keisuke Ueki, and Takaaki Kirino. Clinicopathological Study of Intracranial Fusiform and Dolichoectatic Aneurysms. *Stroke*, 31(4):896–900, 2000.

[146] Wilmer W. Nichols. Clinical measurement of arterial stiffness obtained from noninvasive pressure waveforms. *American Journal of Hypertension*, 18(1 SUPPL.):3–10, 2005.

[147] Mk O'Boyle, Ni Vibhakar, J Chung, Wd Keen, and Bb Gosink. Duplex Sonography of the Carotid Arteries in Patients with Isolated Aortic Stenosis:Imaging findings and relation to severity of stenosis. *American Journal of Roentgenology*, 155:197–202, 1996.

[148] Søren-Peter Olesen, David Claphamt, and Peter Davies. Haemodynamic shear stress activates a k+ current in vascular endothelial cells. *Nature*, 331(6152):168, 1988.

[149] Shunsuke Omodaka, Shin-ichirou Sugiyama, Takashi Inoue, Kenichi Funamoto, Miki Fujimura, Hiroaki Shimizu, Toshiyuki Hayase, Akira Takahashi, and Teiji Tominaga. Local hemodynamics at the rupture point of cerebral aneurysms determined by computational fluid dynamics analysis. *Cerebrovascular Diseases*, 34(2):121–129, 2012.

[150] Michael F. O'Rourke and Junichiro Hashimoto. Mechanical Factors in Arterial Aging. A Clinical Perspective. *Journal of the American College of Cardiology*, 50(1):1–13, 2007.

[151] Page R Painter, Patrik Edén, and Hans-Uno Bengtsson. Pulsatile blood flow, shear force, energy dissipation and murray's law. *Theoretical Biology and Medical Modelling*, 3(1):31, 2006.

[152] Kari Pietilä and Olli Jaakkola. Effect of hypoxia on the synthesis of glycosaminoglycans and collagen by rabbit aortic smooth muscle cells in culture. *Atherosclerosis*, 50(2):183–190, 1984.

[153] Roland N Pittman. Regulation of tissue oxygenation. In *Colloquium series on integrated systems physiology: from molecule to function*, volume 3, pages 1–100. Morgan & Claypool Life Sciences, 2011.

[154] Aleksander S Popel. Theory of oxygen transport to tissue. *Critical reviews in biomedical engineering*, 17(3):257, 1989.

[155] Anthony Portanova, Niloofar Hakakian, David J Mikulis, Renu Virmani, Wael MA Abdalla, and Bruce A Wasserman. Intracranial vasa vasorum: insights and implications for imaging. *Radiology*, 267(3):667–679, 2013.

[156] Y Qian, H Takao, and M Umezu. Risk Analysis of Unruptured Aneurysms Using Computational Fluid Dynamics Technology :. 2011.

[157] A. Quaini, R. Glowinski, and S. Čanić. Symmetry breaking and preliminary results about a Hopf bifurcation for incompressible viscous flow in an expansion channel. *International Journal of Computational Fluid Dynamics*, 30(1):7–19, 2016.

[158] Theodora WM Raaymakers, Gabriel JE Rinkel, Martien Limburg, and Ale Algra. Mortality and morbidity of surgery for unruptured intracranial aneurysms: a meta-analysis. *Stroke*, 29(8):1531–1538, 1998.

[159] Julie Basu Ray, Sara Arab, Yupu Deng, Peter Liu, Linda Penn, David W Courtman, and Michael E Ward. Oxygen regulation of arterial smooth muscle cell proliferation and survival. *American Journal of Physiology-Heart and Circulatory Physiology*, 294(2):H839–H852, 2008.

[160] Richard B. Richardson. Age-dependent changes in oxygen tension, radiation dose and sensitivity within normal and diseased coronary arteries part b: Modeling oxygen diffusion into vessel walls. *International Journal of Radiation Biology*, 84(10):849–857, 2008.

[161] G J Rinkel, M Djibuti, A Algra, and J van Gijn. Prevalence and risk of rupture of intracranial aneurysms: a systematic review. *Stroke: a Journal of Cerebral Circulation*, 29(1):251–256, 1998.

[162] Anne M Robertson, Xinjie Duan, Khaled M Aziz, Michael R Hill, Simon C Watkins, and Juan R Cebral. Diversity in the strength and structure of unruptured cerebral aneurysms. *Annals of biomedical engineering*, 43(7):1502–1515, 2015.

[163] Anne M Robertson, Adélia Sequeira, and MV Kameneva. Hemorheology. hemodynamical flows. modeling, analysis and simulation, oberwolfach seminars, vol. 37, 63-120, 2008.

[164] Russell Ross. Atherosclerosis—an inflammatory disease. *New England journal of medicine*, 340(2):115–126, 1999.

[165] Takashi Sadatomo and D Ph. and U Nruptured C Ases in M Iddle C Erebral. 62(3):602–609, 2008.

[166] Ali Sarrami-Foroushani, Toni Lassila, Ali Gooya, Arjan J Geers, and Alejandro F Frangi. Uncertainty quantification of wall shear stress in intracranial aneurysms using a data-driven statistical model of systemic blood flow variability. *Journal of biomechanics*, 49(16):3815–3823, 2016.

[167] M Scanarini, S Mingrino, R Giordano, and A Baroni. Histological and ultrastructural study of intracranial saccular aneurysmal wall. *Acta neurochirurgica*, 43(3-4):171–182, 1978.

[168] Peter Scheel, Christian Ruge, and Martin Schöning. Flow velocity and flow volume measurements in the extracranial carotid and vertebral arteries in healthy adults: reference data and the effects of age. *Ultrasound in medicine & biology*, 26(8):1261–1266, 2000.

[169] Sarah Schimansky, Samir Patel, Jason Rahal, Alexandra Lauric, and Adel M. Malek. Extradural internal carotid artery caliber dysregulation is associated with cerebral aneurysms. *Stroke*, 44(12):3561–3564, 2013.

[170] G S Schultz and M B Grantt. N eovascular Growth Factors. 1991.

[171] Gregg L. Semenza. Life with oxygen. *Science*, 318(5847):62–64, 2007.

[172] Daniel M Sforza, Kenichi Kono, Satoshi Tateshima, Fernando Viñuela, Christopher Putman, and Juan R Cebral. Hemodynamics in growing and stable cerebral aneurysms. *Journal of neurointerventional surgery*, 8(4):407–412, 2016.

[173] Daniel M Sforza, Christopher M Putman, and Juan R Cebral. Computational fluid dynamics in brain aneurysms. *International journal for numerical methods in biomedical engineering*, 28(6-7):801–808, 2012.

[174] Daniel M Sforza, Christopher M Putman, and Juan Raul Cebral. Hemodynamics of cerebral aneurysms. *Annual review of fluid mechanics*, 41:91–107, 2009.

[175] Akram M Shaaban and André J Duerinckx. Wall shear stress and early atherosclerosis: a review. *American Journal of Roentgenology*, 174(6):1657–1665, 2000.

[176] Yuji Shimogonya, Takuji Ishikawa, Yohsuke Imai, Noriaki Matsuki, and Takami Yamaguchi. Can temporal fluctuation in spatial wall shear stress gradient initiate a cerebral aneurysm? a proposed novel hemodynamic index, the gradient oscillatory number (gon). *Journal of biomechanics*, 42(4):550–554, 2009.

[177] M. Shojima, M Oshima, Kiyoshi Takagi, Ryo Torii, Motoharu Hayakawa, Kazuhiro Katada, Akio Morita, and Takaaki Kirino. Magnitude and Role of Wall Shear Stress on Cerebral Aneurysm: Computational Fluid Dynamic Study of 20 Middle Cerebral Artery Aneurysms. *Stroke*, 35(11):2500–2505, 2004.

[178] Judith C Sluimer and Mat J Daemen. Novel concepts in atherogenesis: angiogenesis and hypoxia in atherosclerosis. *The Journal of Pathology: A Journal of the Pathological Society of Great Britain and Ireland*, 218(1):7–29, 2009.

[179] Fattah Sotoodehnejadnematalahi and Bernard Burke. Human activated macrophages and hypoxia: a comprehensive review of the literature. *Iranian journal of basic medical sciences*, 17(11):820, 2014.

[180] Robert M Starke, Nohra Chalouhi, Muhammad S Ali, Pascal M Jabbour, Stavropoula I Tjoumakaris, L Fernando Gonzalez, Robert H Rosenwasser, Walter J Koch, and Aaron S Dumont. The role of oxidative stress in cerebral aneurysm formation and rupture. *Current neurovascular research*, 10(3):247–255, 2013.

[181] W E Stehbens. Histopathology of cerebral aneurysms. *Archives of neurology*, 8(3):272–285, 1963.

[182] William E Stehbens. Etiology of intracranial berry aneurysms. *Journal of neurosurgery*, 70(6):823–831, 1989.

[183] Hans-Jakob Steiger. Pathophysiology of development and rupture of cerebral aneurysms. *Acta Neurochir Suppl*, 1990.

[184] Shin-Ichiro Sugiyama, Hui Meng, Kenichi Funamoto, Takashi Inoue, Miki Fujimura, Toshio Nakayama, Shunsuke Omodaka, Hiroaki Shimizu, Akira Takahashi, and Teiji Tominaga. Hemodynamic analysis of growing intracranial aneurysms arising from a posterior inferior cerebellar artery. *World neurosurgery*, 78(5):462–468, 2012.

[185] Michael J Taggart and Susan Wray. Contribution of sarcoplasmic reticular calcium to smooth muscle contractile activation: gestational dependence in isolated rat uterus. *The Journal of Physiology*, 511(1):133–144, 1998.

[186] Hiroyuki Takao, Yuichi Murayama, Shinobu Otsuka, Yi Qian, Ashraf Mohamed, Shunsuke Masuda, Makoto Yamamoto, and Toshiaki Abe. Hemodynamic differences between unruptured and ruptured intracranial aneurysms during observation. *Stroke*, 43(5):1436–1439, 2012.

[187] Takashi Tarumi, Muhammad Ayaz Khan, Jie Liu, Benjamin M Tseng, Rosemary Parker, Jonathan Riley, Cynthia Tinajero, and Rong Zhang. Cerebral hemodynamics in normal aging: central artery stiffness, wave reflection, and pressure pulsatility. *Journal of Cerebral Blood Flow & Metabolism*, 34(6):971–978, 2014.

[188] Cormac T Taylor and Sean P Colgan. Regulation of immunity and inflammation by hypoxia in immunological niches. *Nature Reviews Immunology*, 17(12):774, 2017.

[189] Yasutaka Tobe. *Pathological Engineering for Predicting Transition of Human Cerebral Aneurysms*. PhD thesis, Waseda University, 2016.

[190] Yasutaka Tobe, Takanobu Yagi, Yuki Iwabuchi, Momoko Yamanashi, Kenji Takamura, Takuma Sugiura, Mitsuo Umezu, Yoshifumi Hayashi, Hirotaka Yoshida, Atsushi Nakajima, et al. Relationship between pathology and hemodynamics of human unruptured cerebral aneurysms. In *The 15th International Conference on Biomedical Engineering*, pages 44–47. Springer, 2014.

[191] H Ujiie, Y Tamano, K Sasaki, and T Hori. Is the aspect ratio a reliable index for predicting the rupture of a saccular aneurysm? *Neurosurgery*, 48(3):493–495, 2001.

[192] Hiroshi Ujiie, Hiroyuki Tachi, Osamu Hiramatsu, Andrew L Hazel, Takeshi Matsumoto, Yasuo Ogasawara, Hiroshi Nakajima, Tomokatsu Hori, Kintomo Takakura, and Fumihiko Kajiya. Effects of size and shape (aspect ratio) on the hemodynamics of saccular aneurysms: a possible index for surgical treatment of intracranial aneurysms. *Neurosurgery*, 45(1):119–130, 1999.

[193] Kristian Valen-Sendstad, Kent André Mardal, Mikael Mortensen, Bjørn Anders Pettersson Reif, and Hans Petter Langtangen. Direct numerical simulation of transitional flow in a patient-specific intracranial aneurysm. *Journal of Biomechanics*, 44(16):2826–2832, 2011.

[194] Kristian Valen-Sendstad, Kent André Mardal, and David A. Steinman. High-resolution CFD detects high-frequency velocity fluctuations in bifurcation, but not sidewall, aneurysms. *Journal of Biomechanics*, 46(2):402–407, 2013.

[195] Kristian Valen-Sendstad, Marina Piccinelli, and David A Steinman. High-resolution computational fluid dynamics detects flow instabilities in the carotid siphon: Implications for aneurysm initiation and rupture? *Journal of biomechanics*, 47(12):3210–3216, 2014.

[196] Alvaro Valencia, Hernan Morales, Rodrigo Rivera, Eduardo Bravo, and Marcelo Galvez. Blood flow dynamics in patient-specific cerebral aneurysm models : The relationship between wall shear stress and aneurysm area index. 30:329–340, 2008.

[197] Alvaro Valencia and Francisco Solis. Blood flow dynamics and arterial wall interaction in a saccular aneurysm model of the basilar artery. *Computers and Structures*, 84(21):1326–1337, 2006.

[198] Nicole Varble, Jianping Xiang, Ning Lin, Elad Levy, and Hui Meng. Flow Instability Detected by High-Resolution Computational Fluid Dynamics in Fifty-Six Middle Cerebral Artery Aneurysms. *Journal of Biomechanical Engineering*, 138(6):061009, 2016.

[199] Prem Venugopal, Daniel Valentino, Holger Schmitt, J. Pablo Villablanca, Fernando Viñuela, and Gary Duckwiler. Sensitivity of patient-specific numerical simulation of cerebal aneurysm hemodynamics to inflow boundary conditions. *Journal of neurosurgery*, 106(6):1051–1060, 2007.

[200] David A Vorp, Paul C Lee, David HJ Wang, Michel S Makaroun, Edwin M Nemoto, Satoshi Ogawa, and Marshall W Webster. Association of intraluminal thrombus in abdominal aortic aneurysm with local hypoxia and wall weakening. *Journal of Vascular Surgery*, 34(2):291–299, 2001.

[201] David HJ Wang, Michel S Makaroun, Marshall W Webster, and David A Vorp. Effect of intraluminal thrombus on wall stress in patient-specific models of abdominal aortic aneurysm. *Journal of Vascular Surgery*, 36(3):598–604, 2002.

[202] Zhijie Wang, John Kolega, Yiemeng Hoi, Ling Gao, Daniel D Swartz, Elad I Levy, J Mocco, and Hui Meng. Molecular alterations associated with aneurysmal remodeling are localized in the high hemodynamic stress region of a created carotid bifurcation. *Neurosurgery*, 65(1):169–178, 2009.

[203] Bryce Weir. Unruptured intracranial aneurysms: a review. *Journal of neurosurgery*, 96(1):3–42, 2002.

[204] Bryce Weir, Christina Amidei, Gail Kongable, J Max Findlay, Neal F Kassell, John Kelly, Lanting Dai, and Theodore G Karrison. The aspect ratio (dome/neck) of ruptured and unruptured aneurysms. *Journal of neurosurgery*, 99(3):447–451, 2003.

[205] Charles R. White, Hazel Y. Stevens, Mark Haidekker, and John A. Frangos. Temporal gradients in shear, but not spatial gradients, stimulate ERK1/2 activation in human endothelial cells. *American Journal of Physiology-Heart and Circulatory Physiology*, 289(6):H2350–H2355, 2005.

[206] Megan M Wood, Lorene E Romine, Yauk K Lee, Katherine M Richman, Mary K O'Boyle, David a Paz, Pauline K Chu, and Dolores H Pretorius. Spectral Doppler signature waveforms in ultrasonography: a review of normal and abnormal waveforms. *Ultrasound quarterly*, 26(2):83–99, 2010.

[207] J Xiang, AH Siddiqui, and H Meng. The effect of inlet waveforms on computational hemodynamics of patient-specific intracranial aneurysms. *Journal of biomechanics*, 47(16):3882–3890, 2014.

[208] Jianping Xiang, Sabareesh K. Natarajan, Markus Tremmel, Ding Ma, J. Mocco, L. Nelson Hopkins, Adnan H. Siddiqui, Elad I. Levy, and Hui Meng. Hemodynamic-morphologic discriminants for intracranial aneurysm rupture. *Stroke*, 42(1):144–152, 2011.

[209] Jianping Xiang, Markus Tremmel, John Kolega, Elad I Levy, Sabareesh K Natarajan, and Hui Meng. Newtonian viscosity model could overestimate wall shear stress in intracranial aneurysm domes and underestimate rupture risk. *Journal of NeuroInterventional Surgery*, 4(5):351–357, 2012.

[210] Lijian Xu, Lixu Gu, and Hao Liu. Exploring potential association between flow instability and rupture in patients with matched-pairs of ruptured-unruptured intracranial aneurysms. *BioMedical Engineering Online*, 15(s2):461–477, 2016.

[211] Lijian Xu, Fuyou Liang, Lixu Gu, and Hao Liu. Flow instability detected in ruptured versus unruptured cerebral aneurysms at the internal carotid artery. *Journal of Biomechanics*, 72:187–199, 2018.

[212] Takanobu Yagi, Ayaka Sato, Manabu Shinke, Sara Takahashi, Yasutaka Tobe, Hiroyuki Takao, Yuichi Murayama, and Mitsuo Umezu. Experimental insights into flow impingement in cerebral aneurysm by stereoscopic particle image velocimetry: transition from a laminar regime. *Journal of The Royal Society Interface*, 10(82):20121031, 2013.

[213] Greg Zaharchuk, Alastair J Martin, Guy Rosenthal, Geoffery T Manley, and William P Dillon. Measurement of cerebrospinal fluid oxygen partial pressure in humans using mri. *Magnetic Resonance in Medicine: An Official Journal of the International Society for Magnetic Resonance in Medicine*, 54(1):113–121, 2005.

[214] Hasballah Zakaria, Anne M. Robertson, and Charles W. Kerber. A parametric model for studies of flow in arterial bifurcations. *Annals of Biomedical Engineering*, 36(9):1515–1530, 2008.

[215] Christopher K Zarins, Michael A Zatina, Don P Giddens, David N Ku, and Seymour Glagov. Shear stress regulation of artery lumen diameter in experimental atherogenesis. *Journal of Vascular Surgery*, 5(3):413–420, 1987.

[216] Tibor Zemplenyi, Donald W Crawford, and Mark A Cole. Adaptation to arterial wall hypoxia demonstrated in vivo with oxygen microcathodes. *Atherosclerosis*, 76(2-3):173–179, 1989.

[217] Z. Zeng, D.F. Kallmes, M.J. Durka, Y. Ding, D. Lewis, R. Kadirvel, and A.M. Robertson. Hemodynamics and anatomy of elastase-induced rabbit aneurysm models: Similarity to human cerebral aneurysms? *American Journal of Neuroradiology*, 32(3), 2011.

[218] Zijing Zeng. *Novel methodologies for investigating the pathophysiology of cerebral aneurysms*. PhD thesis, University of Pittsburgh, 2011.

[219] Chi Zhang, Sheng Xie, Shuyu Li, Fang Pu, Xiaoyan Deng, Yubo Fan, and Deyu Li. Flow patterns and wall shear stress distribution in human internal carotid arteries: The geometric effect on the risk for stenoses. *Journal of Biomechanics*, 45(1):83–89, 2012.

[220] Xixi Zhao, Meide Zhao, Sepideh Amin-Hanjani, Xinjian Du, Sean Ruland, and Fady T. Charbel. Wall Shear Stress in Major Cerebral Arteries as a Function of Age and Gender-A Study of 301 Healthy Volunteers. *Journal of Neuroimaging*, 25(3):403–407, 2015.

[221] Lu Zheng, Wen Jie Yang, Chun Bo Niu, Hai Lu Zhao, Ka Sing Wong, Thomas Wai Hong Leung, and Xiang Yan Chen. Correlation of adventitial vasa vasorum with intracranial atherosclerosis: A postmortem study. *Journal of stroke*, 20(3):342, 2018.